Mathematical Sciences School, QUT

Cell Migration and Proliferation on Homogeneous and Non-homogeneous Domains: Modelling on the Scale of Individuals and Populations

Brodie A. J. Lawson

Bachelor of Applied Science (Mathematics/Physics), QUT

Bachelor of Applied Science (Hons.), QUT

Principal Supervisor: Professor Graeme Pettet

Associate Supervisor: Associate Professor Dann Mallet

This thesis is submitted for the degree of Doctor of Philosophy in the Science and Engineering Faculty, Queensland University of Technology

2013

Keywords

adhesion, cell tracking, cellular automata, cellular Potts model, chemokinesis, chemotaxis, contact inhibition of locomotion, contact inhibition of migration, contact inhibition of proliferation, CPM, diffusion, finite volume method, flux limiting, GGH model, Glazier-Graner-Hogeweg model, heterogeneous domain, invasion, lattice anisotropy, Metropolis algorithm, mitosis, non-linear, proliferation, random motility, scrape assay, scratch assay, travelling waves, volume-filling, wound healing assay

Abstract

Cell migration is a behaviour critical to many key biological effects, including wound healing, cancerous cell invasion and morphogenesis, the development of an organism from an embryo. However, given that each of these situations is distinctly different and cells are extremely complicated biological objects, interest lies in more basic experiments which seek to remove conflating factors and present a less complex environment within which cell migration can be experimentally examined. These include in vitro studies like the scratch assay or circle migration assay, and ex vivo studies like the colonisation of the hindgut by neural crest cells. The reduced complexity of these experiments also makes them much more enticing as problems to mathematically model, like done here.

The primary goal of the mathematical models used in this thesis is to shed light on which cellular behaviours work to generate the travelling waves of invasion observed in these experiments, and to explore how variations in these behaviours can potentially predict differences in this invasive pattern which are experimentally observed when cell types or chemical environment are changed. Relevant literature has already identified the difficulty of distinguishing between these behaviours when using traditional mathematical biology techniques operating on a macroscopic scale, and so here a sophisticated individual-cell-level model, an extension of the Cellular Potts Model (CPM), is been constructed and used to model a scratch assay experiment. This model includes a novel mechanism for dealing with cell proliferations that allowed for the differing properties of quiescent and proliferative cells to be implemented into their behaviour. This model is considered both for its predictive power and used to make comparisons with the travelling waves which result in more traditional macroscopic simulations. These comparisons demonstrate a surprising amount of agreement between the two modelling frameworks, and suggest further novel modifications to the CPM that would allow it to better model cell migration. Considerations of the model's behaviour are used to argue that the dominant effect governing cell migration (random motility or signal-driven taxis) likely depends on the sort of invasion demonstrated by cells, as easily seen by microscopic photography.

Additionally, a scratch assay simulated on a non-homogeneous domain consisting of a 'fast' and 'slow' region is also used to further differentiate between these different potential cell motility behaviours. A heterogeneous domain is a novel situation which has not been considered mathematically in this context, nor has it been constructed experimentally to the best of the candidate's knowledge. Thus this problem serves as a thought experiment used to test the conclusions arising from the simulations on homogeneous domains, and to suggest what might be observed should this non-homogeneous assay situation be experimentally realised. Non-intuitive cell invasion patterns are predicted for diffusely-invading cells which respond to a cell-consumed signal or nutrient, contrasted with rather expected behaviour in the case of

random-motility-driven invasion. The potential experimental observation of these behaviours is demonstrated by the individual-cell-level model used in this thesis, which does agree with the PDE model in predicting these unexpected invasion patterns. In the interest of examining such a case of a non-homogeneous domain experimentally, some brief suggestion is made as to how this could be achieved.

Contents

Statement of Original Authorship

The work contained in this thesis has not been previously submitted to meet requirements for an award at this or any other higher education institution. To the best of my knowledge and belief, the thesis contains no material previously published or written by another person except where due reference is made.

Signed,

Brodie Lawson

Date:

Acknowledgements

Many thanks to my family and friends for their continued support, and especially my lovely girlfriend Rimi. I owe alot to the fantastic teaching staff of the QUT mathematics department for showing me the real joys of the field and of course to my supervisory team of Prof. Graeme Pettet and Assoc. Prof. Dann Mallet for their patience, assistance and inspiration. Thanks also to those who have or will review this thesis for their helpful suggestions and commentary. I'm not good with this but you all deserve acknowledgement and gratitude.

Chapter 1

Introduction

The workings of any biological object are fantastically complex, an incredibly dynamic system constructed from large numbers of extremely sophisticated building blocks, biological cells. Indeed, cells are so complex that they can move of their own accord, possess rudimentary intelligence and replicate themselves many times over. By the time the nearly innumerable interactions of cells in different states and of different types are taken into account, it is easy to understand why scientific problems in biology have for the most part remained rather impenetrable to physics and chemistry to this day. This is despite these problems indeed being built from the workings and rules of those very disciplines.

Abstracting away from these intricacies somewhat by considering cells as the "elementary units" of a biological system does alleviate some portion of the complexity of cells and their interactions, but the massive remaining complexity has allowed biology to remain a verdant and active scientific field. Indeed, working experimentally with such complicated objects makes it difficult for experiments to be perfectly repeated and possible for key effects to be obscured or even mistakenly attributed due to the abundance of conflating factors. Modern biology has to some extent become focused on this massive number of interacting players, very capable of identifying what these players are and how they might impact cell behaviour in one certain circumstance, but making little contribution to the big picture. This might seem a harsh criticism, but it is one that has been levelled at biologists from mathematicians many times (for example [129]). As is argued in that work, biological experimentation is absolutely necessary, but could strongly benefit from a more systematic approach. Of course, biologists can easily criticise mathematical models for their artificiality and the necessity for simplifying assumptions which immediately reduce them to not dealing with real cells - however what mathematics *can* do is work to inform the 'plan of attack' that experimentalists can use to make broader conclusions with their work. Painting the 'big picture' with brushstrokes instead of going pixel-by-pixel.

Mathematical modelling is capable of far more than simply simulating already understood problems, although its use in avoiding significant numbers of possibly expensive or lengthy experiments is certainly one of its virtues. Really, mathematical modelling can almost be seen as simply another approach to experimentation. Just as traditional experimentation works from simplifying assumptions and a chosen methodology, so too does proper mathematical modelling, and both are most powerful and informative when they are answering or even proposing questions, as opposed to simply proving the hypothesis or re-creating previously demonstrated results. The goal of mathematical modelling should not be to get closer and closer to perfectly simulating a given problem in mathematical language (a nigh-impossible goal), but to explore how and why a set of model(s) and assumptions predicts what it does, and what can be learned from this.

Therefore, the goal of the modelling presented in this thesis is not to perfectly capture cells and their myriad behaviours, and indeed many are knowingly ignored. Instead, the focus is placed specifically on some of the most basic of cell behaviours - migration and proliferation - and *in silico* simulation of how these behaviours work in combination to generate cellular invasion patterns. When these models have been demonstrated as capable of appropriately re-creating *basic* experimental results, they can then be extended to the novel thought experiment presented in this thesis as a means of proposing a new biological experiment and how different experimental observations that might be seen in such an experiment might be interpreted in terms of which elements of cellular behaviour are dominant. A model cell type (osteoblast-like MG63 cells) is chosen here for the availability of mathematically-relevant experimental results which can be used to determine parameter values, but those experimental results are not sought to be perfectly reproduced. The applicability of the simulated results and conclusions of the modelling to other cell types outside the specific chosen model cell is also considered.

Due to the fact that proliferation and migration are key components of cellular behaviour in countless biological situations, properly understanding them is critical. Without these behaviours there could be no transition from embryo to formed baby, to adult. Wounds would not heal (indeed proliferation is required for the constant cell turnover exhibited by our bodies). Cancer is characterised by unbounded proliferation, and it is the migration of these cancerous cells that makes the disease particularly dangerous and difficult to defeat. In each of these examples, however, it is unclear what exactly is driving the migration in the first place, and more importantly, how to control it. Cells can migrate in response to changes in chemical concentration, pressure, temperature and electric current, and yet this is not their only means of movement - active cells can also migrate randomly. How do cells detect open space and crawl into it? How important is the amount of pushing being done by other cells as they proliferate within crowded colonies? Separate to the cell cycle, how exactly do cells elect when to proliferate? The answers surely depend on the type of cell and situation being considered, and are hardly obvious. There is certainly a significant amount of understanding still to be gained even at a most basic level.

Taking a step back to the basics of cell proliferation and migration and focusing solely on those behaviours does prevent any direct application of the mathematical results discussed in this thesis to the aforementioned problems of wound healing, morphogenesis and cancer and its spread. However, the understanding potentially gained by the experiments (and the means to analyse their results) put forward by this thesis is expected to be more general and thus applicable to all sorts of biological situation. This choice of simplification also makes the mathematical modelling easier, but does not sacrifice experimental validation. Biologists use assays like the scratch (or scrape, or wound healing) assay and other related experiments [110] specifically to measure migration-driven healing of an artificial wound, attempting to recreate *in vivo* conditions but removing a good number of conflating factors involved with actual wound healing or other *in vivo* experiments. A more involved discussion of this experiment (and related experiments) along with the rationale for choosing it as the experiment to simulate is provided in Chapter 6.

The modelling strategies applied to cell migration problems can mostly be separated into two main categories of model - those that consider populations of cells simply according to concentrations and those that work at the level of individual cells, considering their behaviours as individuals instead of their averaged, macroscopic behaviours. Of course, within these two schools of thought there is still a wide range of existing and potential strategies, but the distinction is an important one, given the very different philosophies employed by each. Notably, there are also models which successfully combine the philosophies of both, for example by considering cells as individuals but modelling the behaviour of signalling substances in terms of their concentration. However, work that seeks to compare the two approaches, instead of merely utilising them, is far less developed. Comparing results between the two scales (population level and individual cell level) raises many questions and provides great opportunity for refining models.

A large portion of this interest comes from the way various cell behaviours and interactions can or cannot easily be captured by the two different overarching strategies. There are many examples of behaviours that can be modelled via widely accepted means at one scale, but remain rather untouched or at least unjustified at another. These are discussed throughout the thesis, with summaries of previous work, and explorations of how the models at both scales used here compare, presented.

The means of modelling cells at the population level is a system of partial differential equations (PDEs), which are derived from conservation of mass (of cellular material or signalling substance). A review of existing PDE systems that have found use in modelling cell migration problems is used to synthesise a modified model which seeks to better represent how cells block one another, an effect which is easily represented by most individual-cell-level models including the one implemented here. Chapter 2 presents the literature review of existing techniques, before explaining the numerical method used to solve the synthesised equations and demonstrating its successful performance on a series of test problems.

At the individual cell level, the advanced form of the cellular Potts model, the GGH (Glazier-Graner-Hogeweg) model is used to capture cells and their individual behaviours. This technique is an example of a Cellular Automaton (CA) in that it works from a grid of sites, with each occupying one of a finite number of states. The CPM and GGH model are distinguished by their representation of cells as occupying many sites at once, allowing their individual shapes to be clearly defined. Chapter 3 summarises the GGH model and attempts to contextualise it within the general field of CA techniques, examining what considerations must be taken in using an approach like this to represent biological cells given the method's roots actually lie within statistical physics.

Given that the GGH model is less established compared to the PDE approach used to represent cells on the macroscopic scale, it is analysed more deeply in this thesis. Chapters 4 and 5 examine how the behaviours of chemotaxis and proliferation respectively have been incorporated into the GGH model in the past, and make claims about how they *should be*. Chapter 4 presents a novel verification that the dominant technique for GGH model chemotaxis is indeed appropriate, casting some doubt on the few remaining papers which do not use that approach. The GGH model's ability to simulate chemotaxis as a singular behaviour (instead of as one component of a model capturing some certain specific biological effect) is then also explored, including the question of the potential existence of contact inhibition of migration, the effect which stops cells from encroaching onto one another, inherently built into the framework itself. Chapter 5 discusses proliferation in the GGH model, a topic on which there is far less consensus. Some review of existing techniques is presented before the novel technique used in this thesis is described and argued for. This technique is then used to demonstrate that it allows the GGH model to naturally predict logistic growth in a space-limited cell population.

Both models operating at the two different scales are applied to the scratch assay in Chapter 6, which simulates what the modified PDEs predict for macroscopically-observed invasion operating under a number of possible dominant migration effects. The GGH model's ability to accurately simulate a scratch assay in the first place is questioned, with solid comparison to experimental data being presented by using a novel but simple technique to avoid the nebulous nature of parameters in the CPM/GGH model. This ends up highlighting a seriously lacking behaviour in the GGH model which to the author's knowledge has not been presented in the literature, and was not implemented here because it's necessity was not known until after those simulations. A comparison of how the PDE model and GGH model predict invasion driven by the response of cells to a chemical signal allows for a conclusion to be drawn regarding the question of whether or not guided or unguided migration drives cell migration in these problems, a question that has been considered in the literature (e.g. [178]) but remained open.

This conclusion leads directly into the next chapter, where a unique thought experiment that has not been realised biologically is used to further consider the differences between the two modelling frameworks, and between the various potential drivers for cellular invasion considered here. Somewhat surprisingly, without any artificial modification of either of the PDE or GGH models, both suggest the same expected observations which might be seen experimentally for the various invasive regimes considered. This result does not further strengthen the conclusion drawn in Chapter 6 that cell migration in a scratch assay is likely dominated by their random motility as opposed to a chemical response, but *does* provide a direct means of testing it, should the experiment be physically realisable. Some suggestions of how a similar experiment might be realised are briefly presented and justified.

Chapter 2

Cells As Populations

2.1 Mathematical Modelling of Cell Populations

2.1.1 Partial Differential Equations as a Framework

A Very Brief History

The mathematical modelling of cells as populations is well developed, but the majority of work on the topic has only come in the past 60 or so years with the general development of mathematical biology. That said, population-level models tend to work from the well-worn framework of continuity equations which express conservation of substances which vary with space and time and date back to Maxwell's equations of electrodynamics [60]. Even before that work, ODEs were being used to model dynamic processes, such as the very biologically-relevant work of Verhulst expressing the growth of a population of organisms via the now well-known logistic equation [201]. However, it was the revolutionary work of Turing in 1952 [195] which demonstrated the power of mathematical equations as biological pattern generators and thus inspired what might be argued as the 'true' birth of the field of mathematical biology. The next development reaching a similar level of importance was not until the Keller-Segel model of chemotaxis in 1970 [94], which allowed mathematical models to capture the dynamic responses of cells to their environment. As Semple *et al.* point out [168], also very limiting to this field in the past was the lack of computational resources and speed, essentially preventing any sort of major simulation of cells via these models and restricting work to those situations where the resulting PDEs permitted analytical analysis. With computer power now much more freely available, limitations of working purely analytically are greatly eased, allowing for both the easy simulation of the predictions of these PDE models and the freedom to include more refined considerations of various cell behaviours without concern for how they might impact on the ability to do pen-and-paper analysis. Of course, the rise of this 'new' approach (numerical mathematics) does not supersede analytical analysis, though it is primarily numerical simulation that is presented in this thesis for macroscopic models. Additionally, while the numerical methods are here described as allowing for easy simulation of PDEs, they are certainly not without their own pitfalls and are naturally also a still developing area of research. Both of these points are demonstrated in detail by the following literature review. A strong summary of how PDE approaches have been used to model developmental biology, including their strengths and weaknesses and questions still left open is presented by Baker *et al.* [16], though the focus there is largely on pattern formation, of which the scratch assay considered in this thesis is not the greatest example.

The key to modelling cell populations with PDE models is the fact that it is indeed the population being considered. The continuity equation (or equations) that much of population-level cell modelling is based around makes sense only for some continuous conserved quantity. This is no different to physics, where the ubiquitous conserved quantities (for example, heat, charge, density/mass) are all considered as continuous. Just as the Navier Stokes equations do not consider every molecule of fluid and instead reduce the fluid to a continuous field of density, so too can cells be considered not as individuals but as continuous fields of density or concentration. The model must then consider not what individual cells are doing but instead how they behave as a large group. Of course, 'zooming out' like this and hence losing the distinguishability of individual cells must be done carefully, as this section discusses. On the positive side, by approaching the modelling from a populations-as-concentrations mindset, continuity equations and the resulting PDEs quickly become quite natural to use. A prime (and early) example of this sort of thinking in a biological context is Fisher's equation, which in 1937 was developed in order to model the spreading of a mutant gene through a population [49], considering neither individual genes or individual organisms but simply working with a continuous density of mutant gene 'concentration'.

Even with the technology of PDEs to represent the evolution of cell populations, there was still the issue of how something as complicated as cells could be adequately represented. Even at the population level, morphogenesis demonstrates the necessity for these mathematical models to be able to predict complicated and unexpected patterns and structures. It was for this reason that Turing's 1952 work was so revolutionary. He demonstrated that two interacting chemicals (interpreted as continuous concentrations and modelled via continuity equations) could produce non-uniform steady states despite only diffusion and reaction (resulting in production/consumption) being the represented behaviours [195]. This only occurred for certain choices of diffusive rates and reaction kinetics, with the key necessity being one chemical acting as an 'activator', and the other an 'inhibitor' of the activator. Examples of this phenomenon have come to be known as "Turing instabilities" or "diffusion-driven instabilities". While Turing's modelling was not actually concerned directly with cells, the chemicals considered were general and so could certainly be thought of as morphogens able to trigger cellular response. A prime example of such pattern formation in response to chemical signals is the myriad patterns that can be seen in animal skin, which PDE models have since been used to predict. Patterns in animal markings like snakeskin, zebra, big cats and fish have all been mathematically recreated via Turing instabilities with a compelling degree of success. A good explanation of how these varying patterns can be produced using this one framework is provided by Koch and Meinhardt [98], and both this review and the aforementioned review of Baker *et al.* [16] explain in good detail how this modelling can be related to the underlying biology and present illustrations of its success. The latter also presents an example where Turing-style PDEs have correctly predicted what is experimentally observed in mouse hair follicle patterning when the activator (here the Wnt signalling pathway) is artificially stimulated or an inhibitory gene (Dkk2) is over-expressed (represented by changes of parameters in the PDEs) [175]. This is a powerful validation of diffusion-driven instabilities as a biological mechanism, made more compelling by this experimental 'robustness' to mathematical variation.

The second major evolution in mathematical modelling of cell populations also came from an influential paper not directly considering cells, in Keller and Segel's work on migratory and pattern formation behaviours of the slime mould *Dictyostelium Discoideum* [94]. The connection to cellular behaviour is far more apparent here, however, given that *D. discoideum* is widely recognised as a very suitable model organism for eukaryotic cells [32, 148]. The primary contribution of Keller and Segel's work was the inclusion of chemotactic movement, providing a mathematical means of representing the guided motion of cells in response to signalling chemicals. Although the earlier work of Patlak [150] presented an equivalent model derived from a biased random walk, the emphasis is placed here on the Keller-Segel model because it was their publication that prompted the great deal of further exploration in this area. Indeed, some authors refer to the model as the Patlak-Keller-Segel model to give Patlak retrospective credit for his original presentation and derivation of the model, though this is not a consistent trend. Tactic effects have also shown a great ability to generate spatial patterns, a fact which is best demonstrated in the recent work of Painter and Hillen who used a simple, one-dimensional Keller-Segel model to generate a wide variety of patterns including temporally repeating structures and even spatio-temporal chaos [145]. The previously mentioned models of animal skin patterning have indeed in some cases used chemotactic effects to generate these patterns.

Of course, if cells are responding to chemical signals (whether their concentration or gradients in concentration), then the concentrations of these chemicals must also be modelled. Just as with the interacting chemicals of Turing's work, signalling substances can be modelled via the same continuity equation framework that cells are. With chemotaxis and diffusion now both able to be expressed as fluxes within the framework of interacting continuity equations, and proliferation (production) and/or death (consumption) of cells (signalling substance) easily interpreted as source/sink behaviour, the building blocks for a very wide range of PDE models for cell populations were in place. By varying the number of interacting species (each modelled by continuity equation), and the exact nature of the terms within these continuity equations (and the associated parameter values), a very wide range of situations within cell biology have been modelled at the scale of cell populations and interacting concentrations. Of course, mathematical modelling has not been limited to just this approach, and modifications to the basic continuum framework have been used to represent behaviours other than migration or proliferation/death. However, the primary focus of this introduction is on standard continuum equations, as these are what are used in the thesis. The mechanisms for including the behaviours listed above in continuum PDEs are covered in Section 2.1.2.

The consideration of mechanical forces between cells and their extracellular matrix (ignored by most other models) led to the development of the influential Tranquillo-Murray model [193], modelling wound healing by considering the ECM as a viscoelastic solid and allowing it to respond to the traction forces derived from myfibroblasts. A thorough consideration of the model is presented by Hall [73] in his thesis, retaining the focus on dermal wound healing. Also presented is a sizable review of extensions and variations of the model that had since been presented in the literature, along with other population-level approaches considering mechanical forces as a key component. Other models have also used these *mechano-chemical* ideas to model for example pattern formation in morphogenesis [136] and in skin patterning [36]. However, given that the models used in this thesis are purely mass-conservation-based, models featuring mechanical considerations are not reviewed beyond this extent except where judged as relevant. Given that the 'substrate' that cells crawl over in the scratch assay is not deformable, disregarding mechanical models is somewhat reasonable. However, a type of mechanical healing driven by cables of actin across multiple cells can be observed for small wounds even in a simple scratch assay situation [71].

Continuity Equations

A continuity equation, expressed generally, takes the form

$$\frac{\partial Q}{\partial t} + \nabla \cdot \mathbf{J} = f, \tag{2.1}$$

where Q is some continuous quantity, $\mathbf{J}$ is the vector flux of the quantity at any point and f is a source/sink term expressing the rate of generation or removal of the quantity Q. As mentioned previously, equation (2.1) is an ubiquitous equation in electrodynamics [60], fluid modelling and heat transfer [149] and many other scientific disciplines, given the flexibility in choosing Q to be any physical conserved quantity and in defining $\mathbf{J}$ and f in order to reproduce its physical behaviour. By choosing these terms to depend on other dependent variables (also likely defined by continuity equations), complex systems of interacting agents can be modelled via coupled PDEs with physical interpretations and established approaches for solution. Cell populations and the chemicals with which they interact (the quantity Q representing a continuous density/concentration) are only one example of such a system, the result of considering conservation of mass (and occasionally momentum) within a field of cellular concentration.

A very important subclass of these continuity equations are reaction-diffusion equations and advection-reaction-diffusion (sometimes termed ARD) equations. These simply refer to those cases where the form of the flux $\mathbf{J}$ in (2.1) is solely diffusive, or diffusive and advective, respectively (these terms are explained later in this section). The models in this thesis are indeed examples of these types of equation, as are essentially all cell population models which work from a continuum basis. However, this is a classification of the mathematical form of the equation(s), and so is not specific to biology. Key behaviours and solution techniques for diffusion-reaction and ARD equations have been considered mathematically within a wide range of applied contexts.

Solutions of PDEs (or systems of PDEs) sourced from the continuity equation(s) do not often permit exact analytical solution, certainly including those arising in cell biology. However, even in such cases these PDE systems often permit mathematical consideration via techniques such as travelling wave or phase plane analysis. Simulation via approximate numerical simulation is also very powerful and widespread, and both analysis techniques are discussed in Section 2.1.3 Arguably these are merely means to an end, however, and more important is the determination of how various biological effects (or observed, big-picture cell behaviours) can be properly represented mathematically. Given the immense complexity of cellular systems, this has of course been and continues to be a very active topic.

Working from the population scale is best regarded as a simplifying assumption, in that the complexities of individual behaviour are being either disregarded or averaged over the population in what is essentially a prescribed way. Using the continuum framework (2.1) has found considerable success even with very simple models and as is described in the next section all kinds of cell behaviour can be represented on the population-scale. However, working at this unique perspective and ignoring individual interactions risks the glossing over of emergent behaviour which cannot be easily predicted. The following section discusses the use of continuum PDEs in modelling various situations in cellular biology, and demonstrates the strengths and weaknesses of this approach. Other population-level approaches (such as PDEs not fitting into the continuum framework) are considered only briefly.

2.1.2 Cell Behaviours in the PDE Framework

Especially given their respective mathematical interpretations, it is beneficial to consider two main types of cell behaviour here - those involving some sort of migration and those involving proliferation (mitosis) or cell death (apoptosis, necrosis). These two types of behaviour correspond to the $\mathbf{J}$ term and the f term in equation (2.1), respectively. Of course, which behaviours are observed and to what extent depends strongly on the type of cell and the environment being considered. For this reason, there does not exist, nor surely can there exist, some sort of perfect form of (2.1) that will capture the wide variety of behaviours (and their combinations) that can be observed in any biological or experimental situation. This is not to take away from modelling via continuity considerations using equations of form (2.1), but simply highlights the importance of properly considering the situation being modelled. The wide range of publications featuring applications of the various models discussed here are not reviewed in any real detail, this section instead focusing on the mathematical 'tools' that fit into the continuity framework, how these tools have been modified or refined, and what cellular behaviours they might fail to adequately capture. The actual construction of a continuity-based model for use in this thesis is left for Chapter 6, which deals with the chosen biological context - the scratch assay.

Migratory Behaviours - Random Motility

Perhaps the most elementary of cell behaviours, yet one that is also disputed and always under consideration is that of their 'random' motility, often termed diffusion given the similarities between this behaviour and the random spread of other diffusive quantities, such as heat or large numbers of molecules suspended in fluid. The issue is, cell behaviour at a fundamental level is surely not random. However, just as Brownian motion came about from the seemingly-random net result of thermal forces on a suspended object [35], the complex nature of cells and the signals and environments they respond to could easily result in a similar seemingly-random, diffusive movement, especially when observed on the scale of an entire population. Random motility is a behaviour sometimes observed in individual cells both prokaryotic [76] and eukaryotic [192] and in eukaryotic cell model organism *D. discoideum* [161], though the magnitude of such behaviours is very situation-dependent. Moreover, as is discussed in those references such observations are the net result of a series of movements in single directions that are seemingly randomly oriented. That is, the cells demonstrate directional persistence (memory) and so being able to consider their motion as random is another advantage of the big-picture view offered by population-scale modelling. Observations of cellular 'flow' from regions of high density to regions of low density (the key qualitative effect of random motility on a macroscopic scale) are readily observed [1], though also at work in those observations is the restriction of movement via cell-cell contact (contact inhibition of migration). The difference between a diffusive flow arising from unhindered random movement and one arising from the impedance of cells on each other's movement is discussed below.

Diffusive movement was a concept already established mathematically, at the continuum level, via Fick's law [35]. A Fickian flux (which would be the $\mathbf{J}$ or a constituent part of it in equation (2.1), the continuity equation) is given by

$$\mathbf{J} = -D\nabla Q, \tag{2.2}$$

where D is the "diffusion coefficient" describing the speed of the diffusive behaviour and need not necessarily be a constant. Indeed, its choice as some sort of functional form (typically dependent on concentration) has allowed for a more realistic representation of true cell motility, capturing a variety of additional known cell behaviours as is discussed here. It can be reasoned by inspection that a flux of form (2.2) results in a flow of quantity Q from areas of high concentration to areas of low concentration, the key macroscopic consequence of Abercrombie's experimentally observed contact inhibition of migration [1]. This suggests that even in the constant D case, a diffusion term of form (2.2) does possibly demonstrate a contact inhibition effect. Given that different fluxes are additive, a flux of form (2.2) can be combined with other fluxes (most notably those of directed motion) and reaction terms to produce a wide variety of emergent behaviour, even when D is chosen simply to be constant.

When D does not take a functional form, using the definition of a diffusive flux (2.2) as the flux in the continuity equation (2.1) results in the much simpler PDE

$$\frac{\partial C}{\partial t} = D\nabla^2 C + f, \tag{2.3}$$

after relabelling the quantity Q to C to increase consistency with what follows. Choosing $f = 0$ gives exactly a population-level representation of individual cells undergoing a random walk [16, 134], demonstrating that if this subset of cellular motile behaviour can be considered truly random, a flux like (2.2) is correctly recreating its macroscopic consequences. Incorporating some type of mitosis and/or apoptosis/necrosis by choosing a non-zero f does not impact on this random movement behaviour. Thus *diffusion-reaction equations*, equations of form (2.3) remain a flexible tool for modelling a broad range of situations when cell motility can be regarded as essentially random. Given that chemical transport via Brownian motion occurs on a yet smaller scale, equation (2.3) is even more naturally suited to representing evolution of cell-relevant chemicals, with the reaction term f expressing how these chemicals are produced or consumed, whether by cells or the environment itself. It is coupled sets of reaction diffusion equations that Turing demonstrated can produce complex patterns, despite their simplicity [195]. Their use has remained relevant still to today, their ability to predict complex patterns arising through morphogenesis summarised by the aforementioned reviews [16, 98].

When cell densities are high, they collide and contact inhibition prevents cells from encroaching onto one another, suggesting a deviation from the purely random movement modelled by linear diffusion. The first proposed modelling of contact inhibition in PDEs, by Sherratt [173], in fact argued that linear (constant D) reaction-diffusion equations were suitable for close-packed cells when only one species was present. This is supported by the work of Abercrombie [1] where contact inhibition resulted in a trend of overall migration from regions of high concentration towards regions of low concentration, qualitatively equivalent to a linear diffusive flux. Sherratt pointed out that when considering multiple species, however, uncoupled diffusive fluxes would allow each population to spread out independently, which will certainly not occur if cells from the other populations are impeding this spread via contact inhibition. By weighting the amount of diffusive flux by how the population of one species compared to the total population (here N), namely choosing

$$\mathbf{J}_i = -D\frac{C_i}{N}\nabla N \tag{2.4}$$

for all cell populations C_i, the correct mixing behaviour was obtained. Here D could be a constant, or take a functional form like those next discussed. In fact, Sherratt worked with a non-dimensionalised form of (2.4) which had $D = 1$. Working loosely within the context of tumours, Sherratt used these contact-inhibited diffusive fluxes to perform an extensive analysis of travelling waves of invasion that propagated through closely packed two-species populations, demonstrating that the two cell species were correctly impeding the other's movement.

However, despite Sherratt's original assertion that reaction-diffusion equations could adequately model even closely-packed populations of only one cellular species, there have since been suggestions for modelling contact inhibition with more advanced diffusive fluxes anyway. Cai *et al.* [25] and Painter and Sherratt [146] argued that close cell-cell contact necessitates a non-linear diffusion term (even for a singular cell species) and that a decreasing amount of migration as population density increased was appropriate ($\frac{dD}{dC} < 0$), due to contact inhibition restricting movement in dense areas. The opposite case, in which D increases with cellular concentration has also been considered in a cellular context. Physically, this represents the effect of "population pressure" frequently used in models of insect and animal dispersion/invasion [25]. Simpson *et al.* considered both an increasing and decreasing coefficient for the sake of completeness in their studies of invasive waves of neural crest cells [179] and Maini *et al.* briefly discussed this type of diffusion coefficient for the sharper travelling wavefronts they generate, which would better match their experimental observations of a scratch assay [114]. However, neither work suggested a physical basis for an increasing diffusion coefficient. It was later pointed out by Sengers *et al.* [169] that a certain simple example of an increasing diffusion coefficient corresponds to the cell velocity being proportional to (and directed along) the 'gradient of free space' and thus does not contradict with the intuition that contact inhibition should cause higher cell densities to restrict motile effects [169]. They considered two types of cells in a cell invasion experiment and found that for one type of cell a linear diffusion term (constant D) better matched the experiment, whereas for a second type of cell the increasing diffusion coefficient produced a better agreement with the experimental data. Kowalczyk [100] reduced a set of PDEs arising from a fluid momentum-conservation argument to a set of coupled PDEs in continuity form like those discussed in this section. The inclusion of a pressure term representing the physical forces between cells resulted in an increasing diffusion coefficient. The form of this pressure term was justified by a phenomenological argument but care must be taken when a term representing intercellular forces is used in a macroscopic model - for example, the pressure term considered by Kowalczyk disallows adhesive effects and thus would be likely inappropriate in some biological contexts. In the paper, the increasing diffusion coefficient was used to regularise a chemotactic aggregation effect.

Recent works that have demonstrated how functional forms for diffusion coefficients can be derived from individual-based models (which can more naturally represent the effects of cell-cell interactions) are very interesting. Represented in such models are effects like adhesion between cells, or the repulsive effect implied by contact inhibition (recalling that some observations have cells not actually stopping, but deliberately changing direction after colliding with another cell [1]), and this is achieved simply by biasing cell moves which form or break contact with neighbouring cells. Anguige and Schmeiser [9] derived a quadratic, and hence non-monotonic expression for the diffusion coefficient, and under certain conditions (sufficiently strong adhesion) D could even take negative values. Fernando *et al.* [48] discussed a variety of possible "exclusion process" agent-based models that all handled cell-cell interactions differently and derived the associated diffusion coefficients in the macroscopic limit. The functional forms of these diffusion coefficients were also non-monotonic in most cases and again adhesive effects allowed for the possibility of negative diffusion coefficients and hence shock fronts in solution profiles. The bias probability(ies) which govern these nonlinear, non-monotonic diffusion effects are not parameters that could be experimentally determined directly, however they could easily be chosen phenomenologically according to which behaviours have been observed as important for a given type of cell in a given context.

When a functional form is used for D in (2.2), carrying out the differentiation expressed by the $\nabla \cdot \mathbf{J}$ term in equation (2.1) via the chain rule suggests functional choices for D result in both a diffusive *and* advective flux contribution, as pointed out for example by Murray [134] when discussing travelling waves. This can be important for questions of classifying or solving the resulting PDEs but in terms of cellular behaviour, the functional form is still capturing random motility, and should be interpreted as such. The varying D represents a variation in cellular motile activity, for example membrane ruffling. A single cell's movement might only be inhibited in certain directions, but when cells are considered as an entire population there cannot be such a thing as an 'inhibited direction'. Instead, any net guided movement will emerge due to different concentrations of cells at different points in space, the core behaviour still unguided. Thus, contact inhibition of migration is a behaviour naturally represented by a (nonlinear) diffusive flux, because it directly impacts the level of membrane ruffling activity but does not inherently have a specific directional effect.

Migratory Behaviours - Chemokinesis

Also modelled using diffusive fluxes of basic form (2.2) is the behaviour of *chemokinesis*, which is a response of cells to their external chemical situation though unlike tactic behaviours is not active in a specific direction. Although cells become polarised in a certain alignment and display directional persistence, polarities change over time and if polarisation directions are random the net behaviour remains a random walk. The presence of the chemokinetic signal simply encourages the cells to move at all, or with a greater velocity. Thus the behaviour of chemokinesis is separate to the directional response of cells to gradients in chemical signals, and is instead best thought of as a chemical dependence of the random motility just discussed.

Mathematical modelling utilising chemokinetic fluxes typically take the diffusion coefficient of (2.2) to be an increasing function of chemical concentration (for example [179, 23]), however it should be noted that chemokinetic responses in cells are not so simple. Abrupt changes in ambient concentration can sometimes trigger an initial 'cringe' response where all cell motion stops, and will generally be adapted to with populations eventually returning to the original behaviour despite the higher concentration of 'activator' chemical [192]. Moreover, when chemical concentration is strong enough to over-encourage extension of crawling apparatus, cell motility is actually *decreased* because these extensions are no longer mostly restricted to the cell anterior, hindering the polarisation necessary for migration. These experimental observations strongly suggest a simple increasing function $D(S)$ is not appropriate, and determination of a more realistic function is not a simple task at all.

Despite this criticism, models which have implemented chemokinetic diffusion terms have seen good success and have recreated experimental results using these simple increasing functions. Perhaps the ranges of chemical concentration where receptor saturation occurs and motion is actually hindered overall are not encountered in the experiments in question. Moreover, the chemicals inducing a chemokinetic effect need not be the same as those inspiring a chemotactic effect (see below). The leukocytes considered by Byrne *et al.* [23] responded to the experimentally supplied attractant gradient in a Boyden chamber, but also produced a different chemokinetic factor themselves which caused an increase in diffusion when the cell population was high. This chemical signal can therefore be thought of as a means of cells detecting whether they are in a highly-populated area or not, and the increase in diffusion in such regions might be capturable simply by using a concentration-dependent diffusion coefficient just like those suggested for contact inhibition. This highlights the sort of caution that must be taken when working with these ‘zoomed out’ population-level approaches, because different behaviours are much more difficult to distinguish at this scale.

Migratory Behaviours - Chemotaxis

The directed motion of cells is at first glance more intuitive than the undirected motion described above. While diffusive fluxes have been argued here as a useful mathematical tool rather than a representation of some specific cell behaviour, directed motion in response to stimulus is more quantifiable and direct. That said, there is again no consensus on the exact nature of appropriate flux terms, and the situation being modelled remains of utmost importance, let alone the general complexity associated with any cellular behaviour. Again, just as with diffusion, it is macroscopic observations of this directed motion that attempts are being made to capture, and intricate specificities will be smeared over in the process.

There is a wide range of stimuli that cells respond to, and this detection and response comes about through a variety of complex mechanisms that are not entirely understood. Among these stimuli is chemotaxis, the directed migratory response of cells to diffusible chemical signals [15]. The complex process where cells detect these chemical signals through a finite number of receptors designed to pick up specific molecules need not be considered to such a great level of detail when working with population-scale PDEs, though as will be discussed the macroscopic effects of this process can be important. The responses of cells to other stimuli (for example haptotaxis or thermotaxis, the responses of cells to adhesive factors and temperature, respectively) also occur on similarly small scales, and thus their modelling can be simplified in much the same way.

A key trend observed in the way cells respond to many of these environmental stimuli is that it is actually the *gradient* as well as the present amount of stimulus material that cells respond to. Eukaryotic cells are capable of detecting gradients corresponding to a difference in concentration of 2% across their bodies, and becoming polarised along these gradients in order to inform their motion [148]. However, the details of this process are not fully understood, and dependencies on factors like cell shape are very real and highly complex [83]. Devreotes and Zigmond presented several possible behavioural models for how gradient detection might occur in eukaryotic cells [42] from a more phenomenological point of view, and a more recent consideration by Parent and Devreotes suggested a combination of these behaviours best explained various experimental observations [148]. A review of the biological and chemical specificities of chemotaxis for the cases of *D. discoideum* and neutrophils is given by Bagorda and Parent [15].

Mathematically, Keller and Segel's (and Patlak's) equations modelling the chemotactic motion of the slime mould *D. discoideum* [94] are regarded as one of the major breakthroughs in continuum modelling of cells and their migration [168], and have become the general framework for tactic migration. This general framework is most succinctly expressed as a contribution to the flux term dependent on the gradient of a stimulus substance, the concentration of which is here labelled S,

$$\mathbf{J} = \chi C \nabla S. \tag{2.5}$$

Here χ fulfils a similar role as the diffusion coefficient D in (2.2). That is, it represents the overall rate of movement or strength of chemotactic effect and just like D can be taken either as constant or dependent on cell concentrations and/or outside factors. Although the original Keller-Segel model was proposed for modelling aggregation of *D. discoideum*, it was soon after used by its authors and countless others to model bacterial chemotaxis, as is reviewed by Tindall *et al.* [191].

The use of a flux term of form (2.5) to model chemotactic responses has a serious issue when modelling cell aggregation via a chemical signal, because they are well known to result in an infinite blow-up within finite time under certain conditions [81, 82]. Physically, this represents all of the cells migrating to a single point, which due to each cell occupying some amount of space is obviously unrealistic. This does provide a nice example of how spatial effects can easily be lost when working at the macroscopic level, and that care must be taken when assuming that they are irrelevant at this scale.

Thus there is a strong motivation to represent spatial effects such as inhibition of migration resulting from cell-cell contact not only for the pure sake of realism but as one possible technique for preventing this infinite blow-up. This can be achieved via modifications to the form of χ to make it concentration-dependent in order to prevent cells from migrating tactically when they have no room to move [21, 43, 77, 200]. The primary form used to achieve such an effect resembles a logistic growth term (and indeed this is sometimes referred to as logistic chemotaxis) and is

$$\chi(C) = \chi_0 \left(1 - \frac{C}{C_{\text{max}}}\right). \tag{2.6}$$

Such a form for the chemotactic sensitivity has in fact been derived from a 1D random walk model considering spatial effects using a continuum limit [144]. This type of term is commonly referred to as a 'volume filling' term, but given that it is a hindrance of movement that increases with the concentration of cellular material present at a certain point it can also be thought of as a representation of contact-inhibition. Indeed, at a basic level contact inhibition simply prevents cells from encroaching onto one another and thus is simply the behavioural reason for a space filling effect to exist. This simplified view is especially appropriate for the 2D context of the scratch assay considered in this thesis.

Interestingly, the common forms of non-linear diffusion coefficients and non-linear chemotaxis coefficients representing cell collisions are completely different, and many models using a volume-filling effect apply it only to the diffusive or chemotactic portions of cell motion. This point is raised by Wang [207] who also uses a macroscopic limit of random walk transition probabilities to derive and explore a series of Keller-Segel models featuring possibly nonlinear diffusion and chemotaxis coefficients, the difference between the models coming down to what assumption was made about the physical interaction between cells. These models were earlier presented more briefly by Wang and Hillen [208] but the more modern reference is recommended by the author. A slightly different model which simply uses a multiplicative factor of $1 - C$ for both movement terms was explored by Burger *et al.* [22] and Byrne and Owen [24] considered cells and extracellular fluid (in which the signalling chemical is suspended) as a multiphase model in order to derive a Keller-Segel model with complex, nonlinear coefficients for both movement terms. Given the earlier statement that the contact-inhibition-like non-linear diffusion coefficients don't tend to match the volume-filling chemotactic coefficients, the author considers it pertinent to mention that the non-linear diffusion used by Painter and Sherratt [146] did actually take such a form, and the diffusion-adhesion model of Anguige and Schmeiser also uses the same basic principle [9]. These two models do not feature any kind of tactic effect along with this nonlinear diffusion, however.

A separate effect which also can be used to remove the issue of infinite blow-up in finite time is the saturating nature of tactic responses due to the limited number of receptors on a cell surface. By using a functional form for χ which depends on S, the cells' response to chemical can be reduced as more signalling substance is present (often with reference to a certain point S_{max}, or $S = 1$ if scaling has taken place). This results in a saturation effect that seeks to represent the limited number of receptors for signalling substance on a cell surface, and indeed can also prevent the previously discussed issue of finite time blow-up in some cases (for example [139]). Again the ignorance of receptor dynamics (and other intricacies) of the chemical signalling process has made for simpler equations but resulted in a potentially unphysical model, and at least the macroscopic effects of this saturation of chemical response should be taken into account. Indeed, as is reviewed by Murray [135], experiments comparing macroscopic observations of bacteria populations obtained via laser scattering [38] best matched a choice of χ term including a saturation effect presented by Lapidus and Schuller [107]. A much wider review of various choices of chemical concentration dependent χ is presented by Ford and Lauffenburger [52]. If the chemotactic velocity $\mathbf{v}$ is derived from cells sensing not the gradient of the chemical concentration field but instead the logarithm of its gradient, this is easily shown to be equivalent to a concentration-dependent χ taking the form

$$\mathbf{v} \propto \nabla(\ln S) \quad \rightarrow \quad \chi(S) = \frac{\chi_0}{S}. \tag{2.7}$$

This form was in fact considered by Keller and Segel themselves [95] in modelling the formation of band patterns in bacterial colonies, and because the cell velocity is no longer proportional to ∇S but instead $\nabla S/S$, this form represents cells detecting the *relative* gradient as opposed to the *absolute* gradient. This is a behaviour which matched some experiments of the time period [167] and matches modern experiments under certain conditions [93]. Moreover, it provides a sense of the adaptability of a cell's sensing mechanisms already discussed above in the chemokinetic case. However, a chemotactic response of form (2.7) does not correctly predict observations that the cell response actually saturates completely when cell receptors are at maximum occupancy, or that for small concentrations the sense of the gradient is lost to random noise. Thus a more sophisticated form known as the "receptor law" came into favour, originally proposed by Lapidus and Schiller [107] when they showed it matched the experiments of Dahlquist *et al.* [38] who specifically sought to explore the concentration dependence of chemotactic response. This dependence takes the form

$$\mathbf{v} \propto \frac{KS}{(K+S)^2}\nabla(\ln S) \quad \rightarrow \quad \chi(S) = \frac{K\chi_0}{(K+S)^2}, \tag{2.8}$$

which demonstrates that the strength of the response does indeed vanish for very small or very large concentrations. The maximal chemotactic velocity occurs at $S = K$, and K is the disassociation constant for receptor-ligand binding, though is sometimes interpreted as just a constant. However, inspection of the actual form for $\chi(S)$ demonstrates that cell velocities (weighted by the chemical field gradient) are actually maximised when S is zero or very small, and thus care must be taken with whether or not the assumption that cells sense the *relative* gradient remains valid for very small concentrations of signal where random noise has an impact. Golding *et al.* [67] point out this fact, and also provide an easily understood derivation of the form (2.8) from a receptor-based argument whilst sparing the biological detail.

Experiments have clearly shown that bacteria display the ability to sense temporal changes in the concentration of signalling chemical at their location, explaining how they are capable of following gradients despite their small size and the effects of random noise in the signalling mechanism [113]. This effect is clearly not represented by equation (2.5), however it can be argued that on a macroscopic scale this form of a flux could intrinsically represent memory effects. Indeed, a model which features temporal sensing by bacteria has been shown to correspond to the Keller-Segel equations with complex non-constant diffusion and chemotaxis terms [165] and a set of different PDEs (though not all in continuity form) has also been derived from individual cell behaviours featuring temporal sensing of chemotaxis [44].

As will be discussed more thoroughly in Section 2.2, tactic flux terms can make PDE systems far more difficult to solve numerically and greatly increase the importance of a robust numerical solution technique, due to their hyperbolic nature [7]. This is a concern even for simple terms where χ is kept constant, though functional forms for χ like (2.8) can further complicate matters. In addition to the aforementioned effect of infinite blow-up in finite time, tactic movement terms are capable of producing varied spatial patterns, perhaps the most interesting example of which is the ability of a simple chemotaxis model to produce spatio-temporal chaos even on a one-dimensional domain [145].

Cell Kinetics

The second group of behaviours represented in continuity equations (2.1) are the 'reaction terms', representing creation or destruction of material and hence also referred to as source terms (creation) or sink terms (destruction). In the cases of cells, these behaviours represent processes such as mitosis, apoptosis and necrosis, and for chemicals they represent the effects of chemical reactions which alter the concentration of relevant molecules at a location. These terms are incorporated into the function f in equation (2.1), and multiple effects can be included by simply summing together their independent contributions. Just like with the migratory behaviours already discussed, when working from this macroscopic point of view many of the complexities involved in these kinetic processes can be safely disregarded. Factors like the mitotic cycle, complex enough on its own to inspire a great deal of research [202], are typically (and legitimately) ignored, or used simply to determine parameter values. With the shapes of cells (and their finite size in general) usually not considered when modelling at the scale of populations, the spatial effects of proliferation are typically not explicitly considered either, a point which is elaborated on and explored in the scratch assay context in Chapter 6. However, the fact that only a finite number of cells can occupy and survive in a finite amount of space is easily represented macroscopically via approaches like the one discussed below, which is ubiquitous in cell modelling.

The shapes of individual cells are not considered when looking at a population, so the spatial effects of proliferation are not explicitly considered either (this is elaborated in the scratch assay context in Chatper 6). Additionally, evidence that proliferating cells behave differently in terms of migration [85] and adhesion [12] is difficult to take into account, though models which do distinguish between proliferating and migratory cells have been examined. Pettet *et al.* used different PDEs for the quiescent and proliferating cell populations in their model, with only quiescent cells displaying a chemotactic effect [155], and Landman *et al.* explored how the introduction of a proliferating cell subtype that did not migrate affected the invasive wavespeed compared to Fisher's equation [103].

Incorporating cell proliferation and death into the continuity framework (2.1) via the term f is not particularly difficult. Although mitosis, apoptosis and necrosis are certainly distinct behaviours, in a given biological situation typically at least one can be disregarded as only negligibly present. Moreover, as is explained below the net product of these effects can often be successfully represented macroscopically via only a single term for f. In order to achieve basic realism for a chosen form of f, it must satisfy certain key properties, and the simple culmination of these necessary properties results in the most prominent example of an f term representing both births and deaths.

Firstly, if there are zero cells at a point, then there should be no mitosis or death occurring there either. That is to say, there is no source of cells and so $f(C = 0) = 0$ is a requirement of the function. There will also be a maximum number of cells that can be supported, depending on the availability of space, or possibly nutrient. If this maximum is reached, then there must also be no further mitosis (or perhaps more precisely, the balance between cell deaths and mitosis results in equilibrium). Regardless, this consideration implies that $f(C = C_{\text{max}}) = 0$, where C_{max} may depend on nutrient concentration. Determination of this maximum may not be simple - even if nutrient is not a concern for cells the issue of space (and when it is available) is hardly simple when the modelling framework features no consideration of cells occupying space at all. However, through non-dimensionalisation this maximum can be scaled out (provided it is a constant), avoiding the issue so long as actual cell counts are not needed.

The simplest source term that satisfies the aforementioned conditions is

$$f = \lambda C\Big(1 - \frac{C}{C_{\text{max}}}\Big), \tag{2.9}$$

where λ is a rate constant controlling the speed of proliferation. This type of source/sink term results in the ubiquitous behaviour of logistic growth, and thus a term of form (2.9) is often called a logistic growth term. If a simple linear diffusion is chosen for the flux (D in equation (2.2) is taken as constant), then using (2.9) with a dimensionless concentration (obtained by scaling with C_{max}) results in Fisher's equation,

$$\frac{\partial C}{\partial t} = D\nabla^2 C + \lambda C(1 - C). \tag{2.10}$$

This equation has been used to model cells proliferating and migrating in wound healing assays (for example [114], see Chapter 6 for review) and is a model for many kinds of *bistable media* and thus the generation of travelling waves as is discussed in Section 2.1.3.

The inclusion of a space-filling effect which prevents cells from proliferating beyond a certain maximal density is already built into a term like (2.9) as has been discussed, however this term is only a basic possible example. With the extracellular matrix itself occupying 3D space, this would also hinder cell proliferation and thus a modified term in which the carrying capacity is reduced according to the amount of present ECM was used by Perumpanani and Byrne [151] when modelling tumour cells and their interactions with tissue.

Especially in work regarding bioreactors, it is well known that the presence of nutrient is a significant determinant of cell growth, an effect which is represented in their mathematical modelling as well [33]. Galban and Locke compared and contrasted various forms of nutrient-dependent growth term, comparing their predictions to experimental data [55].

Other Cell Behaviours

Other behaviours not fit for such simplistic classification as simply migratory or proliferative/depletive do exist. Adhesion between cells, or between cells and the underlying substrate, is a key behaviour, and the actions of cell adhesion molecules have been demonstrated as an integral component of contact inhibition [86]. While contact inhibition has been represented using modifications to migratory terms as discussed above, other PDE models have included sensing integral contributions to flux terms in order to specifically consider adhesion at a population scale between cells [10, 11], or between cells and also between cells and medium [58, 143, 28]. Additionally, a modified diffusion coefficient (possibly negative) can also be used to model the effects of cell-cell adhesion, with a PDE being derived from the transition probabilities of a modified random walk including an adhesive effect [9]. Haptotaxis was previously described as a tactic response to chemicals which are bound to the substrate as opposed to freely diffusing. It is worth noting here, however, that this substrate-bound 'chemical' can be the number of adhesive sites available to cells, the haptotactic motion in some senses the mechanical result of a gradient of adhesiveness. That said, the majority of population-scale modelling of haptotaxis is via the typical representation of tactic effects in continuum equations, equation (2.5). Adhesion can be much more naturally represented and simulated at the scale of individuals (via the Cellular Potts model, presented in Section 3.2).

A different type of contact guidance, not to be confused with haptotaxis, is *durotaxis*, which is the cellular response not to the adhesive availability of substrates but simply their rigidity [111], and the shapes of substrate surfaces can also impact on cell motile velocity and chosen directions of migration [92], however modelling specifically incorporating these effects via terms in continuity equations has not been performed to the author's knowledge. Care is here advised that durotaxis may not actually be a 'tactic' behaviour in the sense of obeying (2.5), despite its name. Guiding or otherwise impacting cell movement via the substrate is a simple experimental method for exploring the ideas later presented in this thesis, and Chapter 7 explains how emergent ideas in mathematical modelling can be very applicable to the problem of heterogeneous substrates.

Cells can also be passively migrated by the movement of the underlying substrate that they are attached to or crawling over, an effect that has been mathematically represented in various models. Given that this is a movement term, it is easily incorporated into the cellular flux $\mathbf{J}$, however the velocity of the substrate is a separate quantity that must also be tracked, typically achieved by an additional PDE which captures mechanical effects. The aforementioned Tranquillo-Murray model for wound healing [193] is a good example of this type of model, showing that the PDE for mechanical effects can be very complicated and need not fit into the continuity form (2.1).

Chemical Spread and Kinetics

This section has so far discussed only cellular behaviours, and yet has referenced their interactions with chemicals and nutrient several times. Naturally, these chemical species must be given their own mathematical description, and the conservation of mass represented by the continuity equation (2.1) remains perfectly valid and applicable. Moreover, given that molecules of these chemical species operate at a scale even *smaller* than that of the individual cells which are also being averaged over in the macroscopic limit, behavioural specificities can be disregarded more safely. As in the cellular case, the equation(s) are constructed by encoding movement behaviours into the flux, $\mathbf{J}$ and kinetics into the source/sink term f. However, molecules of chemical possess no active motile behaviour and thus any flux of chemical will be the net effect of random dispersal (a diffusive flux) and passive transport. The inclusion of a diffusive flux for chemical species is widespread in mathematical modelling of cell biology, and moreover the previously discussed considerations of non-linear diffusion to represent cell behaviours like contact-inhibition or chemokinesis are inapplicable here so that the diffusivity can easily be taken as a constant. Also rather readily observed in the literature is the representation of substrate-bound chemicals by choosing a diffusion coefficient of zero. These chemicals could represent adhesive factors (or the amount of immobile ECM to adhere to) and thus Keller-Segel models using a cellular response of form (2.5) to a non-diffusing signalling chemical have been used to model haptotaxis [152, 153, 116]. It should be noted however that the PDE models in those references do feature other chemical species (e.g. proteases) which degrade the ECM and do diffuse.

Chemical kinetics depend entirely on how the specific chemicals being considered interact with cells, and thus a range of models for chemical behaviour can be seen in the literature depending on the biological situation being considered. For example, the different kinetic terms that have been used in a wide range of bacterial chemotaxis models is summarised in the appendix of Tindall *et al.*'s review article [191]. The models reviewed there do not represent the full extent of utilised forms, either, and no effort to comprehensively review is made here. This is a choice the author feels is justified because the scratch assay has been chosen specifically because of its simplicity. However, two very common forms are listed here and briefly explained as an illustrative example.

The first form of chemical kinetics takes

$$f_S = \alpha C - \beta S, \tag{2.11}$$

where f_S is the f from the continuity equation (2.1) corresponding to the chemical species, and as before C is the cell concentration and S the chemical concentration. Such a form corresponds to cells producing the chemical species at a rate α, and the chemical decaying exponentially at rate β, sometimes termed dilution. Kinetics of form (2.11) apply in cases where the cells themselves produce a chemical signal, such as cAMP produced by *D. discoideum*. Of course, the kinetics involved in generating the periodic waves of cAMP observed *in situ* are more complex and may involve incorporation of additional interacting chemical species [166, 123].

The second type of kinetics takes

$$f_S = -\gamma(S)C, \tag{2.12}$$

where again f_S is the source/sink term in the continuity equation. Here the cells consume or otherwise convert the signalling chemical to an unusable form, and there is no active production of chemical. It may be supplied at a boundary of the problem domain (for example [33]) or simply present at the beginning of a simulation and consumed as the simulation progresses. The function $\gamma(S)$ is a rate coefficient of the consumptive process, with possible dependence on the chemical concentration. The simplest choices are to have $\gamma(S) = \gamma_0$ or $\gamma(S) = \gamma_0 S$, which correspond to a constant rate of decay per cell or a rate of decay per cell proportional to the amount of chemical. The second term is arguably more realistic, given that increasing the amount of chemical will increase the reaction rate. However, if reaction dynamics are considered, then a term capturing Michaelis-Menten kinetics, $\gamma(S) = \gamma_0 S/(k + S)$, is preferable and indeed the most widespread choice [172, 52]. Chemical kinetics of form (2.12) are generally seen in the macroscopic models of bacterial chemotaxis [191] although a considerably more complex form featuring consideration of bound and extracellular chemical has been used in a model for neutrophils in the Boyden chamber [172].

Conclusions

This section has summarised various types of cell behaviour and the common means of representing those behaviours within the continuum framework operating from the principle of conservation of mass. This has included the primary behaviours discussed in the introductory chapter, Chapter 1, at least those which operate at the scale of populations and thus readily lend themselves to modelling via this framework. Some of the issues inherent in neglecting individual behaviours have been raised, and these and others are further considered throughout the thesis, at least those which are relevant to the scratch assay.

The primary movement behaviours of cells can be separated into those which are essentially random, or diffusive, and those which are guided by an external signal. The typical flux term governing diffusive behaviours is given by equation (2.2) (or for multiple cell species perhaps (2.4)), where the diffusion coefficient might depend on either the concentration of cells and/or chemical signal(s) present, representing the effects of contact inhibition of migration, chemokinesis and rarely, adhesion. Guided movement of cells is represented using fluxes of the form (2.5), where the signal being responded to must also be modelled with another PDE (forming a coupled system). The coefficient determining the strength of the chemotactic effect may also be varied in order to incorporate the macroscopic effects of contact inhibition of migration and saturation of a cell's receptors for chemotactic signal. Reasonably well-accepted means of incorporating both effects have been presented and reviewed, though interestingly little presented work has used the two in conjunction.

Cell and chemical kinetics have also been considered, if broadly, and their consequent effects have been discussed. Due to the highly situation-dependent nature of these types of terms, no single kinetic form has been espoused as superior, and indeed the scratch assay context from which the main part of the thesis operates within is chosen for its simplicity and thus does not seem to dictate complex kinetic forms.

For the sake of readability and later reference, this brief section is concluded with an illustrative pair of coupled PDEs which might represent a cellular population,

$$\begin{aligned} \frac{\partial C}{\partial t} &= \nabla \cdot (D\nabla C - \chi C \nabla S) + \lambda C(1-C) \\ \frac{\partial S}{\partial t} &= D_S \nabla^2 S - \gamma C S. \end{aligned} \tag{2.13}$$

Where D and χ might take functional forms, causing the equations to become nonlinear. These equations have been generated simply by substituting into $\mathbf{J}$ and f the terms representing the discussed behaviours, and serve both as a lead in to the next section by demonstrating what sort of equation needs to be solved, and to define the notational choices that have been made in this thesis.

2.1.3 Solution Approaches

In general, the types of PDEs discussed in the previous section, including equation (2.13), do not easily permit direct analytical solution, whether in a closed or series form. However, their solutions may be approximated by using numerical approaches, or by making use of exploratory mathematical techniques such as perturbation methods or travelling wave analysis which can unlock critical information about solution behaviour. Both types of approach are discussed in this section, though only briefly, before the chosen numerical approach in this thesis (the finite volume method) is covered in a greater level of detail in Section 2.2.

Travelling Wave Analysis

A travelling wave is essentially an observed mathematical phenomena, though one that is typically easily related to the underlying problem being modelled. The technical definition of a travelling wave is a solution profile which moves through space but displays a pattern with no temporal variation. At least, that is how they are generally considered, though in this thesis the definition is broadened to include those patterns which do feature a temporal variation but in a consistent manner or to a degree that can be considered insignificant at the scale of interest. This new definition allows invasion patterns arising from stochastic individual-based models (like the GGH model used in this thesis) to also be termed travelling waves. The velocity of a travelling wave must be constant, or at least have a constant average velocity (in the stochastic case).

When working at a macroscopic scale, a travelling wave is simply a solution which takes the form

$$C_i(\mathbf{x}, t + \Delta t) = C_i(\mathbf{x} - \mathbf{v}\Delta t, t) \qquad \forall i, \tag{2.14}$$

where $\mathbf{v}$ is the vector velocity of propagation and each C_i is an interacting species in the problem (in this case different types of cells and the chemicals they respond to). The implicit dependence between position and time can also be expressed in a characteristic form as

$$C_i(\mathbf{x}, t) = C_i(\mathbf{x} - \mathbf{v}t) \qquad \forall i, \tag{2.15}$$

which is in fact often used as the definition of a travelling wave itself. The two equations (2.14) and (2.15) express the same thing, namely that the solution profile is advancing (but retaining its shape) through time at a speed and direction specified by $\mathbf{v}$. It is very possible that a stable solitonic pattern can evolve from different initial data in a problem that supports travelling waves, and thus it should be noted that the two equations used here to define travelling waves need not be satisfied for all t.

Travelling wave phenomena are typically generated via the property of *bistability*, in which the problem equations permit two (or perhaps more) steady states. The travelling wave is then a moving effect which serves to perturb the solution from one state to the other, and thus this is most easily realised when one steady state is unstable and the other stable. A different behaviour in which a travelling effect temporarily perturbs a solution away from a stable state which is then recovered does technically satisfy definition (2.14) but is usually termed a travelling *pulse* or soliton. These phenomena are the ubiquitous result of mathematical simulation of a diverse range of physical situations, typically those featuring some kind of invasive effect. An easily visualised and illustrative example is that of a spreading forest fire, in which a tree will have two possible steady states. A tree which has burnt down can no longer support fire and will remain that way. A living tree will also remain living in the absence of external influence, however when it is exposed to fire it will begin to burn down. That is to say, the state of being dead is a stable steady state, in that it cannot be affected, whereas alive trees represent an unstable steady state that is vulnerable to perturbation. The moving region of trees currently burning is the wavefront, the travelling wave resulting in an 'invasion' of burnt trees. A review of the types of equation which can predict travelling waves is provided for example by Gilding [62].

Travelling waves remain an important and easily observed phenomena within the specific context of cell biology. Here the stable steady state is a maximal population of cells, and the unstable steady state is a complete lack of cells. Obviously if conditions allow for cells to proliferate, then even the introduction of a small number of cells will be enough to eventually fully populate an uninvaded region and thus the problem is bistable and macroscopic mathematical models will often predict travelling waves of migrating and proliferating cells. This behaviour of proliferation up to some maximal occupancy is expressed for example by the aforementioned choice of source term f, equation (2.9). Travelling waves have been observed and mathematically explored in contexts of tumour invasion [171], dermal wound healing [40, 50], and in migration assays like the scratch assay considered in this thesis [114]. More general explorations of travelling wave phenomena arising from the types of equations that arise in cell biology and discussed in this review have also been performed and these have made important contributions like determining how shock-fronted waves can be explained via phase plane [154] or what the conditions are for non-monotonic wavefront profiles to form [105].

The characteristic relation (2.15) allows the dimension of the underlying problem to be reduced, and from the simplified problem phase plane analysis (for example with chemotactic waves [154]) or even an analytic solution [2] permit further mathematical exploration. This is the key idea behind travelling wave analysis, which uses the predicted or known existence of travelling wave solutions to search for solutions of form (2.15) and thus determine their properties. Properties usually easy to observe experimentally like the speed of invasion can often be determined analytically [49, 106]. Here the concept of a travelling wavespeed is especially important because clear observations of the wave profile remain somewhat difficult in a cellular context, but the speed of a wave itself is macroscopically observable over a large enough timeframe.

The focus in this thesis is the simulation and interpretation of cellular invasion models operating at different physical scales, and thus although travelling waves are a core concept in the interpretation of simulated results, actual analytical travelling wave analysis is not performed here. For this reason, the review here of travelling waves in mathematical modelling of cell biology has not been made comprehensive. However, specific results which are deemed relevant to the scratch assay considered by this thesis are discussed in Chapters 6 and 7 as they become important.

Numerical Simulation

When equations do not permit the determination of an exact solution, the other alternative approach is to instead generate an approximate solution via one of a group of approaches referred to as *numerical methods*. In the case of PDEs, these methods typically work by first using a means of approximating the derivative terms in a set of equations, thus reducing the problem to a (possibly nonlinear) set of equations in the dependent variables to be solved. Given that these methods are approximate, care must be taken as to the validity of these approximations and how they operate within a numerical method. Thus, numerical methods remain a developing field, with a rather rich history in the literature for each different approach.

Section 2.1.2 has summarised the various types of term arising in continuity representations of cell populations and the chemicals they respond to, concluding with a set of equations (2.13) which represent at a basic level the equations to be solved in this thesis. It should be recalled that the terms D and χ are potentially non-linear. The two equations (2.13) are advection-reaction-diffusion equations, and this classification allows for the unification of different approximate solution processes.

The method used here to solve the PDEs operating at a macroscopic level is the finite volume method, a numeric scheme which is especially appropriate for the solution of conservation equations (of course including the continuity equation (2.1) which was used as the basis to derive (2.13)). The finite volume method is discussed in Section 2.2.

2.2 The Finite Volume Method

2.2.1 Basics of the Method

This section describes how the finite volume method (FVM) works as a numerical method to solve PDE (and some ODE) problems, especially those arising due to conservation arguments. The method is discussed here in general without too much reference to the specific types of problem that are being solved in this thesis, though in several places this could hardly be avoided due to flexibility of the framework itself. Historical and modern references are provided but this is not a comprehensive literature review. Section 2.2.2 then explains how specifically the FVM has been implemented for this thesis, focusing on the specific equations that need to be solved in this thesis. The contextual place of the finite volume method amongst other numerical schemes has been discussed in Section 2.1.3.

Like many methods for approximately solving PDEs, the finite volume method begins by first discretising the spatial domain the problem is being solved on. That is, the domain is split up into a set of smaller domains, called control volumes or cells (though here referred to only as control volumes so as to avoid potential confusion with biological cells). Each control volume has associated with it a vertex, and these vertices are the points within the domain where information is known, just like the grid points used by other numerical solution techniques for PDEs. Fundamentally, there are two possible approaches for mesh generation. A cell-centred approach defines control volumes first and then places vertices at their centroids, whereas a vertex-centred approach defines vertices first and then cell boundaries are located at the centres between these nodes. The differences between the two schemes are more pronounced for meshes which are irregular, especially triangular. The method used here is a vertex-centred approach.

The control volumes themselves can be any shape, so long as they fit together to cover the entire domain, and there is no requirement that each be the same shape or size. Of course, the shape must be dealt with in formulating the algorithm, so should not be made too complex without good reason. In considering a rectangular (cuboidal) domain, the simplest choice of control volume shape is rectangular (cuboidal) control volumes, which tile together rather obviously. This choice of shape also leads to the simplest mathematical formulation. The other popular choice which deserves a mention, but is not dealt with further here, is triangular control volumes. These come with a more complicated mathematical formulation but also offer increased flexibility (and are essentially a necessity for domains with more complex shapes which cannot be tiled with square or cuboidal volumes).

The finite volume method is especially effective for the solution of conservation equations, because the method works from the concepts of flux and sources/sinks of a conserved quantity. Indeed, the conservation of quantity should remain true not only over the entire problem domain but each individual discretised control volume as well. The method is formulated by enforcing the condition that the conservation of substance(s) involved must be satisfied over each control volume. The following derivation works from the example of a single multi-dimensional continuity equation (2.1), describing the conservation of some quantity Q. Restated here for convenience,

$$\frac{\partial Q}{\partial t} + \nabla \cdot \mathbf{J} = f,$$

where $\mathbf{J}$ is the vector flux of substance and f is a source/sink term representing substance produced or consumed. The finite volume method requires that the underlying conservation described by (2.1) be satisfied not only within the entire domain but within each smaller control volume. Referring to these control volumes as Ω_i, this condition then requires that

$$\int\limits_{\Omega_i} \frac{\partial Q}{\partial t}\, dV + \int\limits_{\Omega_i} \nabla \cdot \mathbf{J}\, dV = \int\limits_{\Omega_i} f\, dV \qquad \forall i. \tag{2.16}$$

This condition can be restated via Gauss' theorem, replacing the flux integral with a surface integral to get

$$\int\limits_{\Omega_i} \frac{\partial Q}{\partial t}\, dV + \sum_k \oint\limits_{\sigma_{i,k}} \mathbf{J} \cdot \hat{\mathbf{n}}_k\, dS = \int\limits_{\Omega_i} f\, dV \qquad \forall i, \tag{2.17}$$

where $\sigma_{i,k}$ describes the k different surfaces of control volume i and $\hat{\mathbf{n}}_k$ are the normal vectors for these surfaces. This formulation is useful for irregular shaped control volumes. Returning to (2.16) and considering the case of a rectangular control volume (pictured in Figure 2.1), the condition for one control volume becomes

$$\int\limits_{y_s}^{y_n} \int\limits_{x_w}^{x_e} \frac{\partial Q}{\partial t}\, dx\, dy + \int\limits_{y_s}^{y_n} \int\limits_{x_w}^{x_e} \nabla \cdot \mathbf{J}\, dx\, dy = \int\limits_{y_s}^{y_n} \int\limits_{x_w}^{x_e} f\, dx\, dy, \tag{2.18}$$

where x_e,x_w,y_n and y_s are the various positions of the control volume boundaries, as shown in Figure 2.1. The derivation proceeds by dividing both sides of (2.18) by the area of the control volume, $\Delta x \Delta y$, and reversing the order of integration and derivation in the first term to get

$$\frac{\partial}{\partial t}\left(\frac{1}{\Delta x \Delta y} \int\limits_{y_s}^{y_n} \int\limits_{x_w}^{x_e} Q\, dx\, dy \right) + \frac{1}{\Delta x \Delta y} \int\limits_{y_s}^{y_n} \int\limits_{x_w}^{x_e} \nabla \cdot \mathbf{J}\, dx\, dy = \frac{1}{\Delta x \Delta y} \int\limits_{y_s}^{y_n} \int\limits_{x_w}^{x_e} f\, dx\, dy. \tag{2.19}$$

The first and last terms in this equation are seen to be the integral of a quantity over a region divided by the area of that region - the average. Taking advantage of this notation (and realising that the average is independent of space variables), equation (2.19) is reduced to

$$\frac{d\bar{Q}}{dt} + \frac{1}{\Delta x \Delta y} \int_{y_s}^{y_n} \int_{x_w}^{x_e} \nabla \cdot \mathbf{J} \, dx \, dy = \bar{f}. \tag{2.20}$$

By writing the vector flux in terms of its horizontal and vertical components as

$$\mathbf{J} = J_x \mathbf{i} + J_y \mathbf{j}, \tag{2.21}$$

the second term in (2.20) can be split off into two integrals corresponding to the two terms in the dot product $\nabla \cdot J$, to get

$$\frac{d\bar{Q}}{dt} + \frac{1}{\Delta x \Delta y} \int_{y_s}^{y_n} \int_{x_w}^{x_e} \frac{\partial J_x}{\partial x} \, dx \, dy + \frac{1}{\Delta x \Delta y} \int_{y_s}^{y_n} \int_{x_w}^{x_e} \frac{\partial J_y}{\partial y} \, dx \, dy = \bar{f}. \tag{2.22}$$

Here the integral formulation of the Mean Value Theorem,

$$\int_a^b f(t) \, dt = f(\xi) \, (b - a) \qquad a \leq \xi \leq b \tag{2.23}$$

is invoked on both integral terms (on the integral that is not counteracted by a derivative) to result in

$$\frac{d\bar{Q}}{dt} + \left[\frac{\Delta y}{\Delta x \Delta y} \int_{x_w}^{x_e} \frac{\partial J_x}{\partial x} \, dx \right]_{y=\xi_y} + \left[\frac{\Delta x}{\Delta x \Delta y} \int_{y_s}^{y_n} \frac{\partial J_y}{\partial y} \, dy \right]_{x=\xi_x} = \bar{f},$$

where $x_w \leq \xi_x \leq x_e$ and $y_s \leq \xi_y \leq y_n$ are the unknown values from the Mean Value Theorem. After some simplification and application of the Fundamental Theorem of Calculus to handle the counteracting integrals and derivatives, the exact equation for the finite volume method with 2D rectangular control volumes,

$$\frac{d\bar{Q}}{dt} + \left[\frac{1}{\Delta x} \left(J_{xe} - J_{xw} \right) \right]_{y=\xi_y} + \left[\frac{1}{\Delta y} \left(J_{yn} - J_{ys} \right) \right]_{x=\xi_x} = \bar{f}, \tag{2.24}$$

is derived. Here J_{xe} denotes the horizontal flux, J_x, evaluated at the East face $x = x_e$, and so on for the other fluxes. Equation (2.24) cannot be used in this exact form, however, because information will only be known at the node points. This means the averages cannot be evaluated, the fluxes are unknown on the faces and ξ_x and ξ_y are still indeterminate. From here, several approximations must be made so that (2.24) can be expressed (approximately) in terms of concentration information only at node points.

The specific approximations made here separate the various finite volume methods from each other. Almost universal is approximating the average terms, $\frac{d\bar{Q}}{dt}$ and $\bar{f}$ by using the node point for the control volume being averaged over. $\bar{Q}$ is replaced by Q_{P} (denoting Q at the point P in Figure 2.1) and $\bar{f}$ is replaced by f evaluated at the point P. Similarly, the quantities ξ_x and

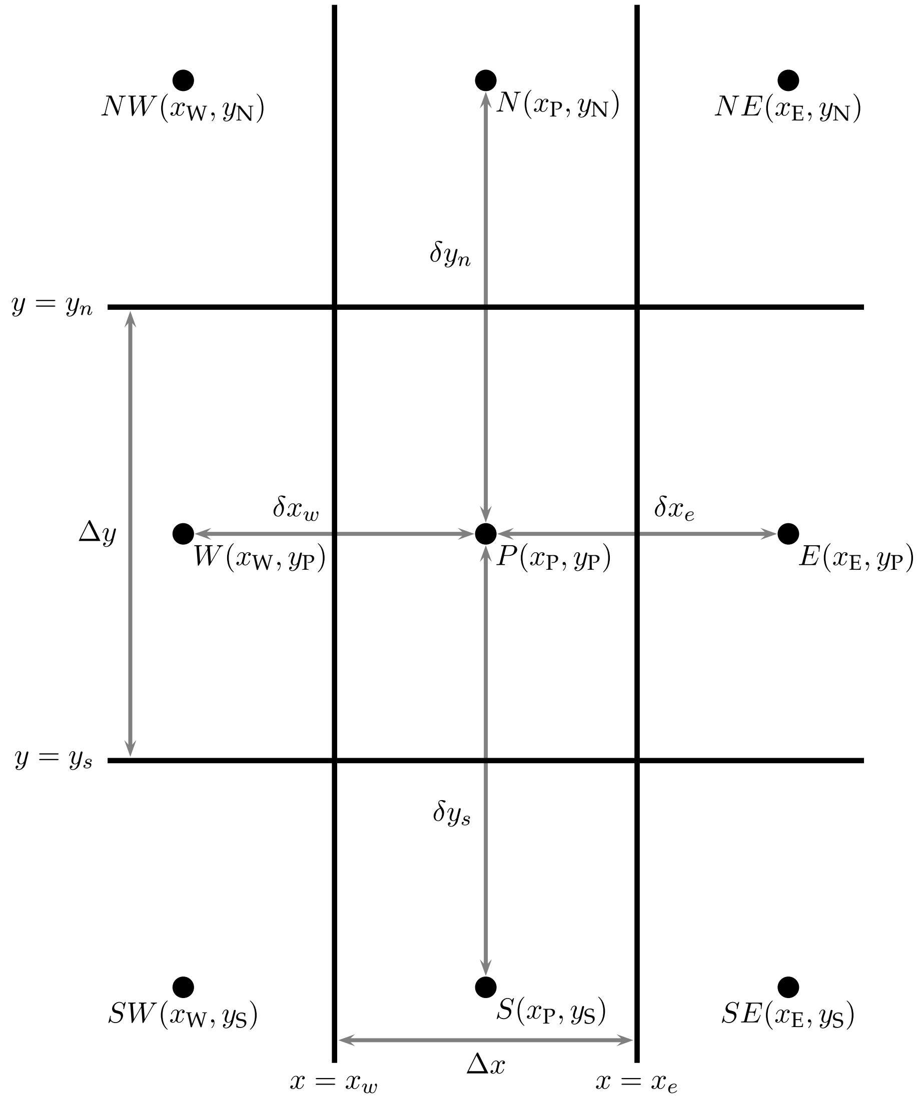

Figure 2.1: A rectangular control volume. Heavy lines indicate the boundaries of the control volume, quantities in brackets refer to co-ordinates.

ξ_y from the Mean Value Theorem are also approximated using the node point P, becoming x_P and y_P, respectively. Making use of these approximations, (2.24) becomes the approximate

$$\frac{dQ_{\mathrm{P}}}{dt} + \left[\frac{1}{\Delta x}\left(J_{xe} - J_{xw}\right)\right]_{y=y_{\mathrm{P}}} + \left[\frac{1}{\Delta y}\left(J_{yn} - J_{ys}\right)\right]_{x=x_{\mathrm{P}}} = f(x_{\mathrm{P}}, t, Q_{\mathrm{P}}). \tag{2.25}$$

From here, the notation that the flux terms are evaluated at the centre of the control volume (for one co-ordinate) is dropped for simplicity.

What remains is approximating the flux terms using only information from nodes, and advancing through time by approximating the time derivative. How the flux terms should be approximated depends on the nature of the problem and the amount of accuracy required - there is a wide variety of options and this is the biggest point of variability amongst finite volume approaches. As discussed in Section 2.1 and demonstrated by the example equation (2.13), the two types of flux that are used in modelling cell migration are diffusive and advective, both possibly non-linear. The next two sections detail how both types of flux can be approximated in the finite volume method, working from the two types of fluxes (2.2) and (2.5) applied to the continuity equation (2.1).

With the flux terms approximated, the time derivative becomes the only information not represented in terms of the node points, and so (2.25) reduces to an ODE problem (often referred to as a *semi-discrete* problem) that can be integrated using many different types of timestepping method.

Diffusive Fluxes

Diffusive fluxes can typically be identified by the presence of the derivative of the conserved quantity, and the following approximations will work from the general form discussed in Section 2.1.2 which is restated in its 1-D form here for convenience,

$$J_{\text{diff}} = -D\frac{\partial Q}{\partial x}. \tag{2.26}$$

Here Q remains simply a conserved quantity, and D is the diffusion coefficient, not necessarily constant. Referring back to the general equations (2.13) which are to be solved, it is seen that both the cell concentration and chemical concentration feature a diffusive flux in their respective PDEs. It is seen in equation (2.25) that this flux must be evaluated at the boundaries of control volumes. However because information is known only at the node points, an approximation is necessary.

An easy choice to make is to approximate the derivative at the control volume face using the two points on either side of the face. Applying this approximation to the form of the flux (2.26) gives

$$-D\frac{\partial Q}{\partial x}\bigg|_{x=x_e} = -D|_{x=x_e}\left(\frac{Q_{\mathrm{E}} - Q_{\mathrm{P}}}{\delta x_e}\right) + O(\delta x_e^2), \tag{2.27}$$

where the error of $O(\delta x_e)$ is easily proven via combining two Taylor series in different directions both centred at $x = x_e$, however only in the vertex-centred case. Applying (2.27) to the diffusive flux at faces on either side of the control volume, in the case of constant D and equally spaced node points, equation (2.27) recovers the standard finite difference approximation for a diffusive term

$$D\frac{\partial^2 C}{\partial x^2} = D\frac{C_{i-1,j} - 2C_{i,j} + C_{i+1,j}}{\Delta x^2} + O(\Delta x^2). \tag{2.28}$$

However, in the case where the diffusion coefficient is not constant, things cannot be handled so simply. If the diffusion coefficient depends on independent variables x, y and/or t, then these will be known at the boundary and although the system cannot be reduced to (2.28) there is no additional complication because (2.27) can still be used without change. However, if the diffusion coefficient depends on either or both of the dependent variables, C and S, and it often does (recall Section 2.1), then this information is not known at the cell boundaries (only at node points) and a further approximation is required. The most obvious approach is to use some kind of averaging, though there are two possible ways to take such an average. Taking the diffusion coefficient to be dependent on Q, the quantity $-D_C|_{x=x_e}$ could be approximated either by

$$D|_{x=x_e} = \begin{cases} D\left(\dfrac{Q_\mathrm{P} + Q_\mathrm{E}}{2}\right) & \text{Evaluating the function at average concentration} \\[2ex] \dfrac{D(Q_\mathrm{P}) + D(Q_\mathrm{E})}{2} & \text{Averaging the function itself.} \end{cases} \tag{2.29}$$

It should be noted that the arithmetic average is presented in (2.29) merely as an example, and that other averages like the harmonic or geometric average can also be used. Moreover, when the mesh is not generated using a vertex-centred approach, the distances to the face for the two node points may be different and thus equation (2.29) must be changed to an appropriate weighted average to reflect this.

Which option of the two options presented in (2.29) makes a better choice depends on the nature of the function D and the problem being solved itself, and their respective performance on a non-linear test problem is explored in Section 2.3. As mentioned in the next section, it is possible that more involved considerations than merely averaging via (2.29) are desirable here, especially when a high degree of spatial accuracy is required.

Advective Fluxes

Advective fluxes are considered separately here because they are well-known for causing problems when not handled correctly [109]. That is, even simple advective fluxes, such as those representing a simple constant velocity in one direction, cause the finite volume scheme to not be Total Variation Diminishing (TVD) when simply averaged via the previously discussed approach used for diffusive fluxes. The concept of a scheme being TVD or not was first established by Harten [75], and is not delved into in any great detail here. Essentially, if a scheme is not TVD, any minor oscillations in solutions do not diminish but can instead grow into major inaccuracies, a clearly undesirable property and especially so when working with sharp fronts. This section discusses some simple and ubiquitous approaches which generate TVD approximations of advective fluxes. Other conditions of numerical 'safeness' have also been suggested, and it has in fact been proven that no TVD scheme can be second-order spatially accurate in 2D [68] - thus 'weaker' conditions of monotonicity like Spekreijse's positivity condition [182] are also relevant. These numerical analysis results are reviewed here for interest and context, though they are considered slightly outside the scope of this thesis.

The discussion of an advective flux here follows the form discussed in Section 2.1.2 and again uses a one-dimensional form for simplicity. Restated here for convenience, the flux to be approximated is

$$J_{\text{adv}}|_{x=x_e} = \left[\chi C \frac{\partial S}{\partial x}\right]_{x=x_e}, \tag{2.30}$$

using the east face as an example.

The derivative term in equation (2.30), $\partial S / \partial x$, can be approximated using the same finite difference-like approach used in the case of diffusive fluxes (2.27). However, the other terms cannot be averaged in a manner like equation (2.29) if the resulting scheme is to remain TVD [108]. The simplest approach which is TVD is known as *upwinding*, or more accurately, *first-order upwinding* because higher-order versions do exist. The exact nature of upwinding is discussed as a special case of the more sophisticated *flux limiting* approach implemented here. An averaging approach like (2.27) is effectively second-order in terms of spatial accuracy, and so first-order upwinding trades the accuracy of simple averaging for the numerical stability associated with a TVD scheme. More specifically, upwinding is known to artificially introduce diffusion, smoothing any numerical instabilities that might form. Flux limiting seeks to indeed limit this artificial diffusion, localising it in order to recapture second-order spatial accuracy when away from trouble points in the solution.

With the nodes labelled as in Figure 2.2, the basic flux limiting strategy approximates a quantity G evaluated at the face according to

$$G|_{x=x_e} = L(G) = \begin{cases} G_{\text{up}} + \dfrac{\Delta x_{\text{up}}}{\Delta x_{\text{down}}} \dfrac{\psi}{2} \left(G_{\text{down}} - G_{\text{up}}\right) & 0 \leq \psi \leq 1 \\[2ex] G_{\text{down}} + \dfrac{\Delta x_{\text{down}}}{\Delta x_{\text{up}}} \dfrac{2-\psi}{2} \left(G_{\text{up}} - G_{\text{down}}\right) & 1 < \psi \leq 2 \end{cases} \tag{2.31}$$

recalling that the example case of the east face is still being considered. Equation (2.31) still represents an average of known information on either side of the face where the flux is being approximated, but this average is now weighted by a parameter ψ which controls how important information at the point upstream from the flux is as opposed to the information at the point downstream from the flux. The Δx terms refer to the widths of the two neighbouring cells, used to appropriately weight the average according to the non-uniform mesh. In the case

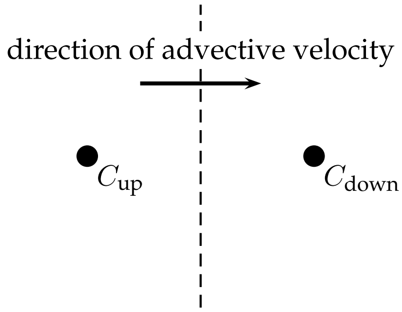

Figure 2.2: Labelling of upwind and downwind points

$\psi = 1$, (2.31) reduces to

$$G|_{x=x_e} = \frac{G_{\text{up}} + G_{\text{down}}}{2},$$

which is (arithmetic) averaging and more spatially accurate. The case of $\psi = 0$ reduces equation (2.31) to

$$G|_{x=x_e} = G_{\text{up}},$$

which is the aforementioned first-order upwinding and more numerically stable. The weighted average of flux limiting dynamically chooses between these two extremes (and in some cases, also the other extreme of downwinding), and because ψ varies from face to face and timestep to timestep the appropriate scheme can be chosen even as the solution profile changes spatially and temporally.

Not yet discussed is what composes G, and this is deliberate, because it is actually a point of flexibility in the finite volume implementation here. Previous works which proved the desirable properties of flux limiting (and the necessary conditions to obtain them) used (2.31) to calculate C at the face and then used this value in functional terms [182]. However, Turner and Perre mention flux limiting all terms separately [196]. Three possible choices of G (all of which result in approximation of $[\chi C]_{\text{face}}$ in equation (2.30), recalling that the derivative term is being approximated using standard differencing) are explored in Section 2.3, and these are, with the function $L(G)$ defined by equation (2.31),

$$\begin{aligned}
&[\chi C]_{\text{face}} = \chi(C_{\text{face}}, S_{\text{face}})C_{\text{face}}, \qquad C_{\text{face}} = L(C), \qquad S_{\text{face}} = L(S),\\
&[\chi C]_{\text{face}} = L\Big(\chi(C,S)\,C\Big),\\
&[\chi C]_{\text{face}} = L\Big(\chi(C,S)\Big)\,L(C).
\end{aligned} \tag{2.32}$$

That is, the flux limited weighted average can be used either to determine appropriate values of the conserved quantities, which are then used to evaluate the functions (the first option), or a weighted average can be taken of the functions themselves, either together (the second option) or separately (the third option). To briefly recap, the first approach seems to be favoured in the literature, but all are tested in this thesis for completeness in Section 2.3.

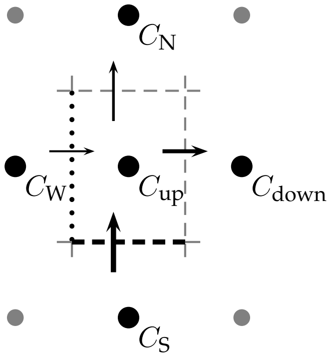

Figure 2.3: Selecting an upwind face for the flux through the eastern face, which is to the right. Arrows indicate direction and strength of flux. The greatest flux flows to point C_{down} (C_{P}) through the bottom face (darkened), so using the maximum flow method will choose this face as the upwind face and $C_{2\mathrm{up}} = C_{\mathrm{S}}$. If using the 1D approach, the upwind face will be the west face (dotted) and $C_{2\mathrm{up}} = C_{\mathrm{W}}$.

The parameter ψ is actually chosen according to a function known as a flux limiter, $\psi(r)$, where r is a sensor designed to locate problem areas like developing shocks or sharp fronts. Many different choices for $\psi(r)$ have found use, and this issue is discussed after the sensors they are based on are covered. A recent work suggests a re-interpretation of the sensor and corresponding limiter functions in order to make properties like forward-backward symmetry and behaviour on non-uniform meshes more transparent [209], but the 'traditional' notation and definitions have been used here for better consistency with the general literature.

The sensors r considered here have in common the feature of examining the solution behaviour at the face where flux is being approximated and at an 'upwind face'. In the case of more than one spatial dimension, it is not obvious which face this should be. In the sense of it being an *upwind* face, it should be chosen according to where the 'flow' of flux is most strongly flowing from. This approach is referred to as the maximum flow method and has seen use in the literature, for example by Turner and Perre [196] or Flegg *et al.* [50, 189] where the finite volume method is applied to a wound healing problem very relevant to those in this thesis. However, other authors have suggested that breaking down a 2D problem into two 1D problems does result in a spatially second-order and conservative scheme [182], though this does require identification of specifically positive and negative fluxes. In the finite volume implementation presented here, both approaches are available, either selecting the upwind face according to the maximum flow method or simply using the face 'behind' the upwind node, as would be done in one dimension. Both approaches are demonstrated graphically in Figure 2.3. Notice the introduction of new notation, $C_{2\mathrm{up}}$, referring to the new point on the other side of the upwind face.

There are two different types of sensor implemented here, both of which have appeared in the literature previously. Both use a ratio of information at the upwind face to the face being currently considered, but said information differs between the two. The first sensor uses a ratio of the derivative of the conserved quantity between the two faces. The derivative is not exactly known but is easily approximated with finite differences. Expressed mathematically, that is

$$r = \frac{C_{\text{2up}} - C_{\text{up}}}{C_{\text{up}} - C_{\text{down}}} \frac{||\mathbf{r}_{\text{up}} - \mathbf{r}_{\text{down}}||}{||\mathbf{r}_{\text{2up}} - \mathbf{r}_{\text{up}}||}, \tag{2.33}$$

where the various $\mathbf{r}$ are the position vectors of the points in question and thus the differences are the appropriate distances δx and δy values when using a rectangular mesh (see Figure 2.1). The second sensor instead uses a ratio of

$$r = \frac{\mathcal{J}_{\text{up-face}}}{\mathcal{J}_{\text{face}}}, \tag{2.34}$$

where $\mathcal{J}$ refers to some flux-related quantity evaluated at the indicated control volume face. Several slightly different measures are used for $\mathcal{J}$, as discussed in Section 2.2.2, though all are strongly related to the flux through the face. The two sensors (2.33) and (2.34) presented here have both already been presented in the literature, though the author believes that the consideration of possible $\mathcal{J}$'s in equation (2.34) is new work. This sensor was originally presented by Turner and Perre [196], with $\mathcal{J} = \mathbf{v} \cdot \hat{\mathbf{n}}$ though their conclusion was that in the case of their wood-drying problems, the sensor was appropriate only for flux limiting what were referred to as the "mobility terms", and that the conserved quantities of material (densities) were best handled using a sensor like (2.33). The applicability of both sensors to the types of IBVP encountered in modelling the scratch assay is examined in Section 2.3.

Equation (2.33) refers to values of C at node points, which are known, but equation (2.34) on the other hand requires information about the fluxes between node points at the control volume faces, which are indeed what is being approximated in the first place! Thus, old information must be used in order to determine the values of the sensor r as needed, however this information could either be updated at every timestep, or after every Newton step. In a similar sense, sensor (2.33) can be evaluated explicitly (using information updated after every timestep or Newton step), or implicitly (using 'new' information, that is, using the variables that are being solved for in the calculation of the sensor also). The method of Turner and Perre [196] used a fully implicit approach, presumably including their calculations of the sensor r via equation (2.33), but Thackham *et al.* argue that an explicit approach is preferable because it reduces the non-linearity of the problem, suggesting that simulations ran better when the values from the beginning of the timestep were used to evaluate equation (2.33). More information about the timestepping process and how these approximations are updated are discussed in Section 2.2.1.

Both sensors, (2.33) and (2.34) are made use of by Turner and Perre [196] with the conclusion being that the derivative-based sensor was appropriate for conserved quantities (in their wood-drying case an example is phase densities) and that the flux-based sensor was appropriate for 'mobility terms' like permeabilities. The applicability of both sensors for the types of problem in this work is explored in Section 2.3.

Remaining is the choice of the flux limiter function, $\psi(r)$, itself. However, theory regarding suitable choices of this function for 1D problems is already well-developed (most importantly

Limiter Name	$\psi(\mathbf{r})$
Averaging (not TVD)	1
First-order upwinding (less accurate)	0
Minmod	$\max\Big(0, \min(1, r)\Big)$
Superbee	$\max\Big(0, \min(2r, 1), \min(r, 2)\Big)$
van Leer	$\frac{r+\lvert r\rvert}{1+\lvert r\rvert}$
Parabolic	$\max\Big(0, \min(2r - r^2, 1)\Big)$
Koren	$\max\Big(0, \min(2r, (1 + 2r)/3, 2)\Big)$

Table 2.1: A few possible choices for $\psi(r)$

culminated by Sweby [186]). The two conditions that the solution must be TVD and must offer the higher accuracy of averaging where possible result in two restrictions on the shape of the function $\psi(r)$. A list of some popular flux limiters, many satisfying these shape conditions, is presented in Table 2.2.1. In two dimensions, the previously mentioned work demonstrating how a 2D problem can be broken down into two 1D problems which are limited in the normal way does provide second-order spatial accuracy but satisfies a slightly weaker stability condition of *positivity* [182]. That is to say, the same sorts of limiting function successful in one dimension should continue to be successful in multiple dimensions so long as the choice of sensor, r, is correctly identifying which parts of the solution profile require artificial diffusion.

With a sensor chosen between (2.33) and (2.34), and appropriate flux limiter such as those in the second section of Table 2.2.1 also decided upon, flux limiting for the system is completely defined. At each control volume face where there are advective fluxes to approximate, the upwind and downwind nodes and faces are found so that (2.31) can be applied, making use of the chosen limiter function and sensor. This application of the flux limiter also depends on the chosen 'averaging' scheme, some possibilities listed in equation (2.32).

Boundary Conditions

The handling of boundary conditions in the finite volume method as described above is actually rather simple, provided the mesh the problem is solved upon is set up in a certain way. That is, the control volumes on the boundaries must have their node point lying along the boundary, making them half the size and with their nodes not centred. The idea is demonstrated graphically in Figure 2.2.1. Given that these are still control volumes being dealt with, equation (2.25) can still be used. Indeed, flux through all of the faces excepting the boundary face can be approximated as discussed in Sections 2.2.1 and 2.2.1. With the node point on this boundary face, the most common types of boundary condition can all be represented with just one equation,

$$J_b = k(C_b - C_\infty). \tag{2.35}$$

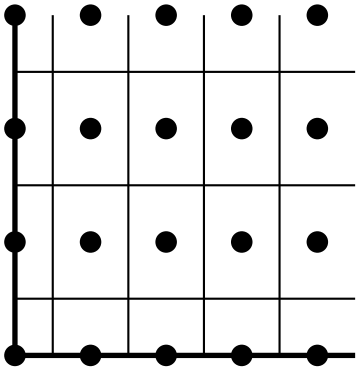

Figure 2.4: The differences between boundary and interior control volumes. Darker lines indicate a boundary of the problem domain.

It is seen here that setting $k = 0$ gives zero-flux (Neumann boundary), and that setting $k =$ large generates a high degree of restoring flux when C_b is away from C_∞, essentially forcing $C_b = C_\infty$, a Drichlet boundary condition. Robin boundaries are implemented using intermediate values for k.

Timestepping

The problem (2.13) has now been redefined as a set of coupled ODEs, two for each node point, after all of the discussed approximation techniques for flux terms have been applied. If flux limiting will be implemented, then in the course of these approximations the sensor, r, and limiter function, $\psi(r)$, must also be chosen. The key now is to construct a complete approximate solution by integrating out the time derivative in (2.25). However, the time dependencies of the other quantities in this equation are unknown, and so a numerical ODE integration scheme must be implemented. There is a wide range of ODE integrators that find application in finite volume problems. Indeed, given the form of equations (2.25), any approach that can accommodate systems of coupled ODEs can be used. Described here is a very common approach which allows easy specification of whether speed, stability or accuracy is most important, and this is the approach implemented in the code. However, if accuracy is very important then higher-order timestepping schemes should be considered.

Starting from equation (2.25) where the time derivative is to be approximated, it is beneficial to assume that the flux terms have already been approximated (removing any spatial dependence) and to gather terms to get an equation

$$\frac{dQ_{\mathrm{P}}}{dt} + A(t) = 0,$$

where $A(t)$ represents the remaining terms with flux terms approximated using some technique like those discussed in the previous sections,

$$A(t) \approx \left[\frac{1}{\Delta x}\left(J_{xe}(t) - J_{xw}(t)\right)\right]_{y=y_{\mathrm{P}}} + \left[\frac{1}{\Delta y}\left(J_{yn}(t) - J_{ys}(t)\right)\right]_{x=x_{\mathrm{P}}} - f(x_{\mathrm{P}}, t, Q_{\mathrm{P}}).$$

The time integration is handled by taking a series of finite steps, so that there will always be 'current' information to work from. Considering one such step, of length Δt, the new time will be $t + \Delta t$ and the already known information is for time t. For generality, an arbitrary linear combination of equation (2.36) for current and future information is used to build the time integration scheme,

$$(1-\theta)\frac{dQ_{\mathrm{P}}}{dt}\bigg|_{t} + \theta\frac{dQ_{\mathrm{P}}}{dt}(t)\bigg|_{t+\Delta t} + (1-\theta)A(t) + \theta A(t+\Delta t) = 0. \tag{2.36}$$

The linear combination has been taken here such that the equation directly corresponds to the above in the limit $\Delta t \to 0$.

The time derivatives in equation (2.36) are approximated by Taylor series in very similar fashion to the way the spatial derivatives were handled above. The Taylor series for the two different derivative terms will be centred around different points in time (current and future), resulting in

$$\frac{Q_{\mathrm{P}}(t+\Delta t) - Q_{\mathrm{P}}(t)}{\Delta t} - (1-\theta)\frac{\Delta t}{2}Q_P''(t) + \theta\frac{\Delta t}{2}Q_P''(t+\Delta t) + (1-\theta)A(t) + \theta A(t+\Delta t) = O(\Delta t^2).$$

A final Taylor series can be used to approximate one double derivative in terms of the other (incurring further $O(\Delta t^2)$ error which is simply absorbed into the existing error term), resulting in

$$\frac{Q_{\mathrm{P}}(t+\Delta t) - Q_{\mathrm{P}}(t)}{\Delta t} + (2\theta-1)\frac{\Delta t}{2}Q_P''(t) + (1-\theta)A(t) + \theta A(t+\Delta t) = O(\Delta t^2),$$

or equivalently,

$$\frac{Q_{\mathrm{P}}(t+\Delta t) - Q_{\mathrm{P}}(t)}{\Delta t} + (1-\theta)A(t) + \theta A(t+\Delta t) = (2\theta-1)O(\Delta t) + O(\Delta t^2). \tag{2.37}$$

Equation (2.37) is the equation that must be solved for the values $Q_{\mathrm{P}}(t+\Delta t)$ in order to step the equations through time - all values at time t are already known. However, because the spatial approximations $A(t+\Delta t)$ will depend on other unknown dependent variables, the problem to be solved is actually a set of $2N$ potentially non-linear equations in $2N$ variables, where N is the number of node points. The individual equations comprising this set arise from considering equation (2.37) for each node point and for both dependent variable (C or S). The only time the equations are not coupled and can be solved simply is when $\theta = 0$.

The multi-dimensional Newton's method is used, which solves the system

$$\mathbf{F}(\mathbf{x}) = 0. \tag{2.38}$$

Choice of β	**Type of timestepping**	**Advantages**
$\theta = 0$	Fully explicit	No solves needed, fastest computation time
$\theta = \frac{1}{2}$	Crank-Nicolson	Most accurate, eliminating $O(\Delta t)$ error in (2.37)
$\theta = 1$	Fully implicit	Greatest numerical stability

Table 2.2: Important possible choices for θ

The set of equations represented by (2.37) is already in this form if the right hand side is set to zero, incurring an $O(\Delta t)$ error unless $\theta = \frac{1}{2}$, which incurs an $O(\Delta t^2)$ error. The parameter θ is arbitrary, but the important cases for θ are summarised in Table 2.2.1.

Newton's method works by taking a starting iterate, $\mathbf{x}_0$, which is preferably close to the solution, and updating the iterate according to

$$\mathbf{x}_{i+1} = \mathbf{x}_i + \delta\mathbf{x}, \qquad \delta\mathbf{x} = -J^{-1}\mathbf{F}. \tag{2.39}$$

That is, each step involves solving the matrix system $\mathbf{J}\delta\mathbf{x} = -\mathbf{f}$ for the update $\delta\mathbf{x}$, and then using this update to generate a new approximate solution. Given that the goal is to find a zero of the system (2.38), iterations are terminated when $||\mathbf{F}(\mathbf{x})||$ becomes sufficiently small according to some criteria. Newton's method tends to converge to a zero of the equation relatively quickly, however it is also possible that it fails to converge completely. For this reason, the method is often modified to be *globally convergent* by preventing overly large steps $\delta\mathbf{x}$ where necessary [96]. For details of the simple global convergence implemented here, see Section 2.2.2.

So, the set of coupled equations given by application of (2.37) to equation (2.25) is solved for $\mathbf{x}(t + \Delta t)$ via Newton's method, (2.39). This solution vector $\mathbf{x}(t + \Delta t)$ then contains the list of concentrations of both $C(t + \Delta t)$ and $S(t + \Delta t)$ at all of the node points, and so the timestep has been taken. The information at $t + \Delta t$ can now be used to take a further timestep, until the desired timeframe of the simulation has elapsed. With each timestep being a separate process, there is no reason that timesteps must all be the same size. Indeed, some implementations utilise an adaptive time step that seeks to prevent overly large timesteps being taken if they would result in solution instabilities or failure of the Newton method to converge.

Summary of the Method

In summary, the finite volume process as interpreted here is:

- Discretise the problem domain into a number of control volumes, here rectangular (see Figures 2.1 and 2.2.1)
- Use the finite volume framework to reduce the PDEs to be solved (2.13) to a coupled set of ODEs at each node (2.25) and apply the previously discussed flux approximations.
- Step through time as required by the simulation:

  - Choose a timestep Δt
  - Approximate the time derivatives in (2.25) via (2.37) applied to each equation. Recall that the P referred to in (2.37) is the right hand side of one equation in (2.25).
  - Rearrange the resulting system of equations into the form $\mathbf{F}(\mathbf{x}) = 0$, and then solve via Newton's method (2.39). A good choice for the initial guess $\mathbf{x}_0$ is the state of the problem before timestepping, given by $C(t)$ and $S(t)$ at each of the points. On taking the first timestep, this would be the initial condition.
  - The root $\mathbf{x}$ located by Newton's method contains the values of $C(t+\Delta t)$ and $S(t+\Delta t)$ at all of the node points - the timestep has been taken.
- Visualise or interpret results as necessary

2.2.2 Implementation

Although the previous sections describe how the finite volume method is used to solve PDEs, and cover some possible variations in its use, there is still a great deal of flexibility in the construction of a working finite volume implementation. This section details and justifies the choices made in creating the finite volume code used in this thesis. The finite volume implementation uses the MATLAB programming language, and consists of a set of bundled .m files which call each other during the numerical simulation process. The code is completely run from the *Driver.m* file, however, to maximise usability - the other .m files can mostly be thought of as internal, and only when changing the definitions of the functional forms will a user have to deal with any file other than *Driver.m* (as explained in Section 2.2.2).

Model Equations

Although the approximations for flux terms have already been discussed (see equations (2.27) and (2.31) and surrounding explanations), the forms of the flux terms themselves are flexible. In the implementation here, the known application of cell biology allows a specific form of the advective flux to be chosen to simplify matters, by assuming that it will be a tactic flux arising due to chemotaxis or haptotaxis. Non-linear diffusion may be specified by choosing a non-constant diffusion coefficient, and the chemotactic coefficient may also be chosen as non-constant. That is, the equations solved are

$$\frac{\partial C}{\partial t} = \nabla \cdot \Big(f_1(x,y,t,C,S,D)\nabla C - f_2(x,y,t,C,S,\chi)C\nabla S \Big) + f_3(x,y,t,C,S,\lambda) \tag{2.40}$$

$$\frac{\partial S}{\partial t} = \nabla \cdot \Big(f_4(x,y,t,C,S,D_s)\nabla S \Big) + f_5(x,y,t,C,S,\lambda_s). \tag{2.41}$$

This slightly awkward expression of the equations makes a certain point of the implementation clear. Provided by the user are the five functional forms for the two diffusion coefficients, advective coefficient, and two source terms. However also provided are a list of user-defined constants corresponding to each, $D, D_s, \chi, \lambda, \lambda_s$, which are also inputs in the functional forms. This is done to allow basic changes to be made to the functional forms without the need to open the corresponding separate m-files where the functional forms are defined. For example, if linear diffusion was to be implemented, then in the m-file that specifies the diffusive functional form (*defineD.m*) the choice $f_1 = D$ could be made and this way the user can simply vary the input parameter D to control the strength of the diffusive effect without re-defining the function each time. The various functions f are specified simply using MATLAB's standard mathematical language, and as shown in equation (2.40) the functions are free to depend on both of the independent variables, on the three independent variables (two spatial dimensions, and time) and on each function's corresponding user-provided constant.

In the case where the chemical species S is unchanging in time (i.e. $f_4 = f_5 = 0$) the user can specify this fact and greatly improve the computational time by reducing the number of equations to be solved by half, thus reducing the size of the Jacobian and thus its high computational cost. Otherwise, both equations are solved for every node point simultaneously, and so implicit portions of the timestep are considering this interaction implicitly. The interaction terms are also included in the generated approximate Jacobian matrices.

The model equations are solved using the method as described over the previous sections, with the various possibilities discussed usually selectable by the user. These choices are easily specified by the user along with all the other user-defined parameters in the *Driver.m* MATLAB file. The specifics of some of these choices are explained over the next few sections, and the list of user-defined parameters and their definitions is provided in the readme.txt file coupled with the finite volume implementation.

If the model equations possess a known analytical solution, then a comparison between the known and numerical solutions is made both graphically and in terms of the absolute error between the two vectors. The user can easily specify that an analytical solution exists and will be used for plotting and error calculations, but this must then be specified by the user in the *GetAnalyticalSolution.m* file.

Mesh Specification

The finite volume implementation uses a rectangular mesh for simplicity, matching the formulation presented in Section 2.2.1. The user can specify the number of nodes in both of the two spatial dimensions, and then these will be distributed within the domain according to one of three schemes which the user is free to select, and the scheme used for the two dimensions need not be the same. The first scheme is a uniform mesh, which has all node points evenly spaced across the domain, with points located on all boundaries. The other two schemes use a pair of geometric progressions (GPs) for the differences in the node positions to create a pattern that is symmetrical about the centre of the domain in that direction. Depending on where the GP is started from, the end result is a set of node points focused closer together either at the centre of the domain, or at the two boundaries. This gives the user the ability to possibly focus node points in rapidly varying regions, for example boundary layer effects. The user can specify the ratio parameter for any geometric progressions used. The user must of course also specify the actual physical lengths of the domain in both dimensions, and this is done by nominating a starting co-ordinate and an ending co-ordinate both horizontally and vertically. The choice of rectangular control volumes limits the implementation to rectangular domains.

Handling of Flux Terms

The finite volume implementation uses approximations for flux terms in the manner already discussed. That is, the diffusive portions of the fluxes are approximated using equation (2.27) with equation (2.29) to average the diffusion coefficient if it's non-linear. The user specifies which approximation to approach from the two in (2.29), or in the case where neither diffusion coefficient (f_1 or f_4, or by Section 2.1.2's notation D and D_S) depends on C or S, the user may specify no approximation to be used, allowing for exact values of x and y to be used, because unlike C and S these will be exactly known at the face where the flux is being approximated. The ∇S term in the advective flux is also approximated using the same equation as for the diffusive fluxes, equation (2.27). The C and f_2 which also make up the advective flux are dealt with together using a combination of equations (2.31) and (2.32), the user specifying which type is to be used in the latter.

Recalling that r and $\psi(r)$ must also be defined, the user may select between the two sensors (2.33) or (2.34), and also what quantity is actually used to measure the fluxes from the following options:

$$\begin{aligned} \mathcal{J} &= \mathbf{v}\cdot\hat{\mathbf{n}} = \chi(\nabla S\cdot\hat{\mathbf{n}}) && \text{Advective velocity} \\ \mathcal{J} &= J_{\text{adv}}\cdot\hat{\mathbf{n}} = \chi(\nabla S\cdot\hat{\mathbf{n}})C && \text{Advective flux} \\ \mathcal{J} &= J\cdot\hat{\mathbf{n}} = (\chi C\nabla S - D\nabla C)\cdot\hat{\mathbf{n}} && \text{Total flux} \end{aligned} \tag{2.42}$$

This measure $\mathcal{J}$ is used when calculating the sensor r via fluxes (2.34) and also in determining the upwind face if the maximum flow method is being used (see Figure 2.3). The user nominates if the maximum flow method is to be used, otherwise all 'backtracking' along fluxes will be carried out in one dimension (again, see Figure 2.3). Additionally, the user may choose between updating these fluxes only after each timestep, or after each individual Newton step. The latter case actually causes the set of non-linear equations to change while being solved, however it allows for much less reliance on 'old' information that might cause sensors of type (2.34) to incorrectly determine where upwinding and/or downwinding is necessary.

In the case where the derivative sensor is being used for r, the option is available to either use current information for C_P, C_{up} and $C_{2\text{up}}$, defining the sensor implicitly, or to use the values of C at these points at the beginning of the timestep. As discussed, both have been seen in the literature, with an implicit calculation better at dynamically locating problem areas but also increasing the non-linearity of the problem and possibly hindering convergence of the Newton solver. When using flux limiting with either sensor, the use of information at the upwind face causes dependence in the advective flux on information which is two nodes away, whether directly $C_{2\text{up}}$ when using the derivative-based sensor (2.33) or less directly when using the flux-based sensor (2.34). The calculation of the sensor is the only source of dependence on nodes outside nearest neighbours, and so following Turner and Perre [196] the Jacobian matrix contributions due to these dependencies are ignored in order to reduce the non-linearity and the number of non-zero elements.

The function $\psi(r)$ is defaulted to the van Leer limiter, which satisfies the conditions required for a TVD scheme and second-order accuracy in well-behaved regions (for 1D problems on uniform meshes), and also uses downwinding ($\psi > 1$) to sharpen fronts with artificial anti-diffusion. The other limiters tested here are Koren's third-order limiter [99], to see if it can provide any additional accuracy, and the parabolic limiter, used because it never uses downwinding ($\psi(r) \leq 1$ for all r) and thus tends to be safer [196]. All of the limiters mentioned here are listed in Table 2.2.1.

Implementation of Newton's Method

As described by the procedure 2.2.1, once the equations are established they must be solved, and in the general case they could very well be non-linear, necessitating a non-linear solver. Newton's method has already been discussed in Section 2.2.1 and is the approach used in the implementation to solve the discretised, approximate model equations. In using Newton's method, the Jacobian matrix of the equation set must be generated and given the desire here for a flexible solver which can handle a variety of problems the necessary equation derivatives cannot simply be specified as they will vary between each set of equations solved. Instead an approximation for the Jacobian matrix is constructed using what amounts to a simple finite differencing process, resulting in it being potentially inexact, though so long as the finite difference is small a good equivalence with Newton's method is generally expected [96] and was indeed observed when the file responsible for building the Jacobian matrix, *buildJacobian.m*, was checked for correctness. The matrix is constructed element-wise out of a series of these finite difference approximations, according to

$$\begin{aligned} J_{ij} &= \frac{f_i(\mathbf{x} + \sqrt{\epsilon}\mathbf{e}_j||\mathbf{x}||) - f_i(\mathbf{x})}{\sqrt{\epsilon}||\mathbf{x}||} \qquad && ||\mathbf{x}|| \neq 0 \\ J_{ij} &= \frac{f_i(\mathbf{x} + \sqrt{\epsilon}\mathbf{e}_j) - f_i(\mathbf{x})}{\sqrt{\epsilon}}, && ||\mathbf{x}|| = 0 \end{aligned} \tag{2.43}$$

where J_{ij} indicates the elements of the Jacobian matrix, f_i is the ith equation of the set and e_j is the jth Cartesian standard basis vector. The parameter ϵ is the machine precision (in this case MATLAB's machine precision, $\epsilon \approx 2.2 \times 10^{-16}$), the quantity $\sqrt{\epsilon}||\mathbf{x}$ seeking to represent a perturbation small enough so as to accurately calculate the derivative, yet not so small that rounding error interferes with the approximation. In order to greatly reduce computational time, only the elements which could be non-zero are calculated, which for any given site and equation will be the five-point stencil of nearest neighbours for *both* concentrations, C and S. While the choice of sensor may cause elements outside of this stencil to also be non-zero, as previously mentioned they are not calculated and left as zero. This may increase the number of Newton steps necessary to solve the system, but so long as convergence is still achieved the simulation behaviour will be barely affected because neither the equations to be solved themselves, nor the criteria for having found their solution (see below) have changed. Obviously, boundary sites do not use the full stencil due to some nearest neighbour nodes being missing.

The Newton solver is made slightly more sophisticated in two primary ways, both simple modifications that allow the user more control over convergence and computation time. The first of these is a very simple *global convergence* or *line search* algorithm, which seeks to prevent the problem of solution overshoot that is known to sometimes occur when using Newton's method [96]. The method here simply calculates a full Newton step and the new norm $||\mathbf{f}_{\text{new}}||$ as normal, but then checks this value against the original value before the step was taken. If

$$||\mathbf{f}(\mathbf{x}+\lambda\delta\mathbf{x})|| < (1-\lambda\alpha)||\mathbf{f}(\mathbf{x})|| \qquad \alpha, \lambda < 1 \tag{2.44}$$

is not satisfied using the initial Newton step ($\lambda = 1$) then the method is thought to have overshot and so instead λ is halved and the new norm is recalculated using this new smaller step. This process continues until equation (2.44) is satisfied or λ becomes smaller than the user-defined parameter λ_{min} which is included to prevent the Newton step becoming unworkably small. The parameter α is also user-defined, and the closer its value is to 1 the more the norm must decrease in order for condition (2.44) to deem it sufficient. The value recommended by Kelley, from where this algorithm was taken from, is $\alpha = 10^{-4}$. The user also has the option of not using global convergence at all, in which case the $\lambda = 1$ step is always accepted, corresponding to an unmodified Newton's method.

The second means of giving more control over the non-linear equation solution process (Newton's method) to the user is to allow the frequency of recalculating the Jacobian matrix to be specified. While in the 'true' Newton's method the Jacobian matrix is recalculated after every step is taken, given the high computational cost of constructing this matrix the time required to find a solution can often be reduced by only recalculating the Jacobian matrix every so often, even though this will increase the number of Newton steps required to reach the solution [96]. With the Newton method being calculated after every m Newton steps, $m = 1$ corresponds to the normal Newton's method, $m = \infty$ (or some very large number) is equivalent to the chord method, and intermediate values of m are termed the Shamanskii method, after its creator [170]. The user specifies m along with all the other program parameters and constants. Additionally, if global convergence is being used and a step with sufficient decrease is not found (that is, λ in equation (2.44) reaches λ_{min}), then the Jacobian is immediately recalculated so that a new descent direction is found, a method also suggested by Kelley [96]. When using the Shamanskii method, this rebuild of the Jacobian matrix will reset the number of steps taken since the last matrix re-generation.

The termination criteria used here is one that is generally recommended and accepted for Newton's method [96], and is

$$\text{Stop generating after iteration } \mathbf{x}_k \text{ when} \qquad ||\mathbf{F}(\mathbf{x}_k)|| \leq \tau_a + \tau_r||\mathbf{F}(\mathbf{x}_0)||, \tag{2.45}$$

where again $\mathbf{x}_0$ is the initial guess, and τ_a and τ_r are an absolute error tolerance and relative error tolerance, respectively. The absolute error tolerance is used to allow the algorithm to terminate even when the initial condition is very close to the desired solution itself. The two tolerances τ_a and τ_r are specified by the user, with smaller values for each increasing the accuracy of Newton updates but also increasing the computational cost for each timestep. There is a second termination criteria also used in this implementation. If the Newton solver has executed more than a user-specified number of steps and the norm has not decreased sufficiently to satisfy condition (2.45), then the algorithm terminates and the current solutions for C and S are accepted as the values for the next timestep, though a warning that the Newton method has failed to converge is output to the display window.

Timestepping

The timestepping procedure implemented here has already been described in Section 2.2.1 - that is, a finite difference technique is used to approximate the temporal derivative, but using a combination of old and new information. The user specifies the parameter θ in equation (2.37), selecting either an explicit or implicit scheme, or any compromise between the two. The advantages and disadvantages of notable values of θ have already been summarised in Table 2.2.1. The user also specifies what the total timeframe of the simulation t_{end} and the number of timesteps to be taken n_t, of course resulting in $\Delta t = t_{\text{end}}/n_t$. No sort of adaptive timestep has been implemented here for simplicity, although a basic scheme of reducing the timestep when the Newton method is judged as failing to converge (Section 2.2.2) would be a natural extension. The timestep could also be reduced if the predicted solution after a timestep is not physically reasonable and thus suggests numerical artefacts, although this has not been done here, partially for the sake of the implementation's flexibility. Given the specific inclusion in the modelled equations (2.40) of taxis the implied application is biological cells, for which nonphysical results are easily distinguished (for example negative values of the concentrations C or S), but as is seen in Section 2.3.2 it is not the only possible application these equations can be applied to.

Visualisation

Once the simulation results have been calculated, they can also be visualised. Given the results are in 2D, this is achieved in MATLAB with a simple *surf* command being used to visualise both the C and S concentrations across the domain. The values of the analytic solution will also be visualised on the same sets of axes if the user has nominated that an analytic solution exists and will be provided. Results may be visualised using multiple images or as animations, though animations only show the results for the cellular concentration C. The user selects the frequency with which results are visualised (in terms of the number of timesteps taken), or can simply select to show only the initial and final result. If an animation is being created, the user may also opt to save this as a .avi movie file, though changing the filename of the created .avi file cannot be done through *Driver.m* and so the author's recommendation is to create a movie using the default filename and then rename it manually before the next movie is generated.

2.3 Test Problems and Numerical Results

2.3.1 Linear Diffusion, Advection and Reaction in One Dimension

The first test problem considered was taken directly from a paper by Simpson *et al.* who used it to test their own operator split scheme [177]. Very good results are indeed obtained by their solution method, though it is the author's opinion that this was largely due to the sophistication and power of the underlying numerical scheme (the aforementioned KT scheme presented by Kurganov and Tadmor [101]) and their third-order timestepping - not due to the operator split. Indeed their results remained equally good in the case where no operator splitting was performed, however the point should be made that the operator splitting is what allowed the explicit KT scheme to represent the advective transport without running into the stability issues associated with handling a diffusive flux explicitly. The problem was chosen as a test problem here because it involves all of a diffusive, advective and reactive component and has an easily realised analytical solution, thus presenting a perfect opportunity to verify the full finite volume implementation. The finite volume method is not quite as sophisticated as the KT scheme and at best second-order timestepping has been implemented here, so the comparison to those published results might not be favourable. However, the finite volume implementation had to be demonstrated as sufficiently accurate and without numerical instability. The variety of problems considered in this thesis all handled by the same implementation demonstrates the flexibility of the scheme, something more difficult to realise using the more sophisticated and complex numerical approaches.

The PDE to be solved, as expressed by Simpson *et al.*, is

$$\frac{\partial C}{\partial t} = D\frac{\partial^2 C}{\partial x^2} - v\frac{\partial C}{\partial x} - kC, \tag{2.46}$$

which corresponds to (2.40) with

$$\begin{gathered} f_1 = -D, \quad f_2 = v, \quad f_3 = -kC, \\ f_4 = 0, \quad f_5 = 0, \quad \nabla S = 1\mathbf{i}. \end{gathered} \tag{2.47}$$

Here, D, v and k are all constants, representing the diffusion coefficient, advective velocity and the rate of decay, respectively. Given a suitable initial condition, an analytical solution for (2.46) exists. A simple choice is a Gaussian profile of width l and centred at $x = x_0$,

$$C(x,0) = \exp\left(-\left(\frac{x - x_0}{l}\right)^2\right), \tag{2.48}$$

which leads to a solution to (2.46) in the form of a moving, decaying and spreading Gaussian profile,

$$C(x,t) = \frac{e^{-kt}}{\sigma(t)} \exp\left(\left(\frac{x - x_0 - vt}{l\sigma(t)}\right)^2\right), \qquad \sigma(t) = \sqrt{1 + \frac{4Dt}{l^2}}. \tag{2.49}$$

Although this analytical solution is for an infinite domain $-\infty < x < \infty$, choosing a sufficiently small width of the Gaussian, l, allows the domain to be truncated and assigned boundary conditions,

$$C(0,t) = C(L,t) = 0, \tag{2.50}$$

without incurring much additional error, provided of course that the centre of the Gaussian is within the truncated domain ($0 < x_0 < L$), and remains within for the entire simulation.

The problem is easily incorporated into the framework described in Section 2.2.2, using (2.47). However, because the equation (2.46) is specified only in one dimension, the finite volume solver had to be adapted into a 1D solver before it could be used on this problem. This was achieved simply reducing the number of node points in one dimension to two, and then using no flux boundary conditions on both boundaries in this dimension. Then, so long as the initial condition was also defined as invariant along this dimension, fluxes were zero in this direction and the second dimension could simply be ignored.

The boundary conditions were represented simply by setting $k_b = 10000$, and $C_b = 0$ for both boundaries in equation (2.35). The initial condition was defined simply by evaluating equation (2.48) at each node point. However, because the implemented finite volume solver is designed to solve problems involving a chemotactic or haptotactic response, the advective flux term required a little modification to make it represent a completely linear velocity. The implemented form of the flux for the cell population (see (2.40)) is

$$J = -D\frac{\partial C}{\partial x} + \chi C \frac{\partial S}{\partial x}.$$

In this test problem the PDE variable (already labelled C) can easily be thought of as a cell population, and choosing D as a constant recovers the diffusive component of the flux. However, in order to achieve linear advection matching (2.46), it must be chosen that

$$\chi = v, \qquad \text{and} \qquad \frac{\partial S}{\partial x} = 1. \tag{2.51}$$

This then requires that

$$S(x) = x, \tag{2.52}$$

Parameter	**Definition**	**Value**
D	Diffusion rate	0
v	Linear velocity	1
k	Decay rate	0.1
L	Domain width	2
Δx	Control volume width	0.002
t_{end}	Simulation timeframe	1
τ_a	Absolute Tolerance	1×10^{-4}
τ_r	Relative Tolerance	1×10^{-6}
Δt	Timestep	0.002
x_0	Initial Gaussian centre	0.5
l	Initial Gaussian width	0.04

Table 2.3: Parameter values for the linear test problem, providing values for equation (2.47).

at all times, which was achieved by using this as the initial condition and nominating in the code that the chemical concentration was unchanging. Of course, the boundary conditions must match (2.52) also, but with the chemical concentration unchanging this was easily achieved via equation (2.35) by taking $S_b = 0$ for the left boundary and $S_b = L$ for the right boundary, designating both as Drichlet boundary conditions using $k_b = 10000$.

The choice of parameter values followed Simpson, Landman and Clement [177] who presented the problem, and then these were varied in order to explore the performance of the method in a variety of situations. The chosen base parameters, expressed in the terms used by the finite volume implementation, are described in Table 2.3.

Firstly, fully implicit timesteps ($\theta = 1$) were used simply to verify that the method had been implemented without error. Although the error introduced by using a first-order time integration might be quite significant, Simpson *et al.* presented their simulation of a simple temporally implicit finite difference scheme for comparison with their KT scheme results [177] that could also be used here, given the similarities between the finite difference and finite volume methods for simple problems. The results were entirely as expected, with the schemes of averaging and flux limiting performing better than upwinding due to their higher order of spatial accuracy. Those numerically-solved profiles did match the presentations in the literature of results using the aforementioned equivalent scheme, suggesting the finite volume method has been implemented correctly. A variety of D values were used to ensure that both advection-dominated and diffusion-dominated situations were operating correctly. Just as previously published, the temporally first-order scheme did not perform well for advection-dominated problems, demonstrating the need for the second-order timestepping scheme.

The Crank-Nicholson scheme (using $\theta = 0.5$) was indeed found to handle these more numerically challenging cases better, with considerably less numerical diffusion, as can be seen in the example visualisation Figure 2.5. Given that the travelling pulse had now been much better resolved, it became important to determine which from the variety of potential schemes offered

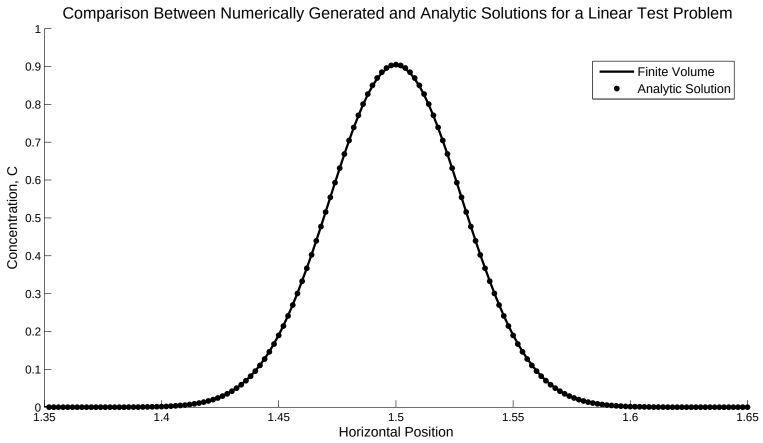

Figure 2.5: Demonstration of the very accurate solution predicted by the finite volume (solid line), as compared to the exact solution (dotted). Parameters are as in Table 2.3, with the visualised region being only the active section of the problem domain.

by the finite volume implementation here showed the best performance.

Several performance criteria were established so that this comparison could be made quantitatively. Given the presence of the exact solution, one natural measure was the relative error, calculated using the norm of the difference between the exact and simulated solutions divided by the norm of the exact solution. The 2-norm was used here, for the role of the ∞-norm is replaced by the more transparent second performance criteria, which was the difference in pulse heights. Determined simply by the maximum concentration values across the domain for both the simulated and analytic solution, this criteria provided a very direct representation of the amount of numerical diffusion that is introduced by the numerical solution process. Thus, a good correlation between these two criteria suggests that the primary source of error in this problem was arising from numerical smearing of the very sharp front. Two other criteria were tracked, but considered less major than the two just mentioned. These were the change in the total amount of mass in the domain (which, given this is a conservation problem largely unaffected by the boundaries, should be zero), and the most negative concentration value (which provides a simple measure of the extent of numerical oscillation). The performance of the various schemes according to these benchmarks is presented in Table 2.4.

Here, the velocity coefficient $\chi = 1$ was constant and thus the various choices for the flux limited quantity (2.32) were equivalent. The simulations presented in Table 2.4 used a Van Leer flux limiter (see Table 2.2.1), with the performance of different flux limiters being explored below. It is easily seen that in terms of the overall error and the amount of incurred numerical smearing, upwinding is the scheme which performs the worst, just as was observed for the $\theta = 1$ case because of its first-order spatial accuracy. Averaging, with second-order spatial accuracy, did provide a much better resolution of the travelling front, though at a cost of introducing numerical oscillations as evidenced by the presence of not insignificant negative

Scheme	**Error (rel.)**	**Pulse Height**	**Mass Gain/Loss**	**Most Negative**
Averaging	5.99×10^{-2}	-4.77×10^{-3}	-1.13×10^{-8}	6.12×10^{-4}
Upwinding	4.49×10^{-1}	-4.21×10^{-1}	-1.05×10^{-8}	$\ll \epsilon$
Sensor (2.33), 'explicit'	2.08×10^{-3}	-2.90×10^{-3}	-1.09×10^{-8}	$\sim \epsilon$
Sensor (2.33), 'implicit'	2.05×10^{-2}	-3.72×10^{-2}	$+3.85 \times 10^{-3}$	$\sim \epsilon$
Sensor (2.34), 'explicit'	3.13×10^{-2}	$+3.24 \times 10^{-4}$	-1.04×10^{-8}	$\sim \epsilon$
Sensor (2.34), 'implicit'	3.10×10^{-2}	-2.47×10^{-3}	-1.12×10^{-8}	$\sim \epsilon$

Table 2.4: Test results for various possible finite volume schemes according to several performance criteria. Values closer to zero are desirable for all criteria, and the most successful scheme in terms of each criteria has been highlighted. $\epsilon \approx 2.2 \times 10^{-16}$ indicates the machine epsilon, and values close to or smaller than this are considered inappreciably different from zero. Van Leer flux limiting has been used in all flux limited cases, with different flux limiters considered below.

concentration values. The magnitude of these oscillations was not overly large, but examination of the solution profile confirms that they are a numerical artefact situated directly behind the travelling pulse, and would probably be more pronounced if a larger spatial grid size was being used. These results neatly highlight the importance and necessity of flux limiting, for without its use the solution was either subject to severe artificial diffusion (upwinding) or numerical oscillation (averaging). Depending on the type of flux limiting, however, the results were very different.

All four flux limited methods demonstrated lower error values, but significantly lower than the other schemes was that using the sensor (2.33) and having this sensor calculated using the values of C from the beginning of the timestep, instead of those most up-to-date. If the most recent values were used instead, the error increased by an order of magnitude, owing both to an increase in artificial diffusion and a larger degree of violation of conservation. When sensor (2.34) was used instead, the choice of using more recent information (updated every Newton step) or less recent information (updated every timestep) seemed to make less difference, although again using the most recent information resulted in a larger amount of artificial diffusion, the 'explicit' version of the scheme in fact *over-estimating* the peak height, suggesting an abundance of numerical anti-diffusion. This is indeed a possibility because the Van Leer flux limiter does allow for downwinding ($\psi > 1$). Interestingly, when the performance of the two different sensors is compared (using the better-performing explicit case for both), the derivative-based sensor (2.33) shows a smaller amount of error despite incurring a larger amount of artificial diffusion. Graphical examination of the solution profiles revealed that this was due to the peaks being in slightly different locations, the movement of the pulse lagging behind slightly when using the flux-based sensor (2.34). It was found that in general, the numerical prediction of a slightly incorrect pulse movement speed or shape was the other large contributor to bigger error norms, along with numerical diffusion.

The performance of the flux limiting schemes when using different flux limiters is presented in Table 2.5, using the same judgement criteria as before. It is seen that the trend of implicitly using the derivative-based smoothness sensor (2.33) results in a violation of mass conservation much more significant than in the other cases, regardless of which limiter is chosen. In terms of overall error, the derivative-based sensor performed slightly better, and the best case found indeed used this limiter, explicitly. Not all limiters listed in Table 2.2.1 were considered, however three important cases were explored. The first is the popular Van Leer limiter, with results already presented above but shown again here for ease of comparison. This limiter satisfies the requirements for being TVD and second-order away from trouble spots, and allows for anti-diffusive downwinding in order to sharpen fronts. Also considered was the parabolic limiter used and recommended by Turner and Perre [196], which is also TVD and second-order but is restricted to never downwind. Their results suggested its predicted solutions were equivalent to the Van Leer limiter, but the computational time was significantly decreased. This result has not been observed here. Instead, the parabolic limiter led to increased error for all cases considered. A lack of downwinding to sharpen fronts might be expected to cause an increase in unwanted smearing of the pulse, but this was not observed. Instead, graphical examination reveals the increase in error norms results from pulse velocities being measured less accurately, with the numerical solution often ‘lagging’ behind the true solution by a very slight amount, an effect which was more pronounced when using the parabolic limiter. The parabolic limiter was also found to be associated with an increase in oscillations when used explicitly, indicated by the larger negative concentrations observed. Koren’s limiter, which does allow downwinding, was found to perform badly in all cases considered, except for when sensor (2.33) was used implicitly. Even then, the performance was at best comparable to the Van Leer limiter, and as mentioned above using this sensor implicitly results in a not insignificant violation of mass conservation. In the other cases, Koren’s limiter resulted in significant oscillations in the solution (notice the maximum concentration of 30 for the case of the flux-based sensor), or a complete failure to converge. Koren’s limiter is considered again in the next test problem, but here it has been seen to struggle with this numerically challenging problem.

Overall, the method that performed the best on this test problem was flux-limiting, which was found to be a necessary improvement over the two simpler to implement schemes of upwinding or un-weighted averaging. However, care must clearly be used in the choice of limiter function, with the Van Leer limiter showing the best performance. A choice of sensor (2.33) evaluated explicitly (using values of C at the beginning of the timestep) showed the best overall performance, with an error norm an order of magnitude better than any other approach trialled here. The next test problem will be used to examine how general or problem-specific this conclusion might be, so that an appropriate choice of scheme can be made for the cell invasion simulations later presented for which an analytical solution is not so readily available.

2.3.2 Non-linear Diffusion and Advection in One Dimension

The next considered test problem made use of a non-linear yet exactly solvable PDE in order to test the performance of the different flux-limiting methods and ensure that the implemented

Scheme	Error (rel.)	Pulse Height	Mass Gain/Loss	Most Negative
Sensor (2.33), ‘explicit’				
Van Leer	2.1×10^{-3}	-2.9×10^{-3}	-1.1×10^{-8}	$\sim \epsilon$
Parabolic	5.0×10^{-2}	-9.3×10^{-4}	-1.1×10^{-8}	-2.7×10^{-8}
Koren	2.9×10^{0}	6.4×10^{-1}	-2.2×10^{-7}	-1.3×10^{0}
Sensor (2.33), ‘implicit’				
Van Leer	2.1×10^{-2}	-3.7×10^{-2}	$+3.9 \times 10^{-3}$	$\sim \epsilon$
Parabolic	5.8×10^{-2}	-5.4×10^{-2}	-8.1×10^{-3}	$\sim \epsilon$
Koren	2.2×10^{-2}	-1.9×10^{-2}	-8.3×10^{-3}	-4.9×10^{-7}
Sensor (2.34), ‘explicit’				
Van Leer	3.1×10^{-2}	$+3.2 \times 10^{-4}$	-1.1×10^{-8}	$\sim \epsilon$
Parabolic	5.6×10^{-2}	-7.5×10^{-3}	-1.2×10^{-8}	-9.8×10^{-9}
Koren	6.9×10^{0}	3.0×10^{1}	-3.6×10^{-6}	-1.3×10^{0}
Sensor (2.34), ‘implicit’				
Van Leer	3.1×10^{-2}	-2.5×10^{-3}	-1.1×10^{-8}	$\sim \epsilon$
Parabolic	5.6×10^{-2}	-7.7×10^{-3}	-1.1×10^{-8}	$\sim \epsilon$
Koren	Newton method failed to converge at all timesteps			

Table 2.5: Test results for various flux limiting approaches with varying flux limiters $\psi(r)$ according to several performance criteria. Values closer to zero are desirable for all criteria, and the most successful scheme in terms of the two main criteria has been highlighted (other criteria are too similar in multiple cases, so are unmarked). $\epsilon \approx 2.2 \times 10^{-16}$ indicates the machine epsilon, and values close to or smaller than this are considered inappreciably different from zero.

code could handle non-linear problems correctly. This problem also involved a non-linear diffusion coefficient, so that choices like that of equation (2.29) could now be examined. Again, this problem featured only one spatial dimension, so the 2D code was modified in the same manner as before to apply it to the problem. The analytical solution of the original PDE was presented by Fokas and Yortsos [51], and the use of the PDE as a test problem for a finite volume scheme came from Awad and Turner [13].

The problem is a non-linear PDE, presented by Fokas and Yortsos [51] as

$$\frac{\partial S}{\partial t} = \frac{\partial}{\partial x}\Big(\frac{1}{(\beta S + \gamma)^2}\frac{\partial S}{\partial x}\Big) + \frac{\alpha}{(\beta S + \gamma)^2}. \tag{2.53}$$

S here is the saturation of oil in a multiphase (oil and water) flow problem through porous media, with equation (2.53) deriving from Darcy’s law. The choice of the two functional forms is a deliberate one to ensure exact solvability of the PDE, though it is also argued by Fokas and Yortsos to be physically reasonable [51] given appropriate choice of β and γ. These are the parameters that are somewhat free, with α defined by

$$\alpha = -\beta \frac{\Big(\beta S_{or} + \gamma\Big)\Big(\beta(1 - S_{wr}) + \gamma\Big)}{1 - S_{wr} - S_{or}}. \tag{2.54}$$

S_{wr} and S_{or} are the minimum saturations of water and oil respectively, and the values used in

Fokas and Yortsos' work of $S_{wr} = 0.0375$ and $S_{or} = 0.15$ are also used here.

The problem of course requires the definition of boundary and initial conditions also, which are as follows.

$$\begin{aligned} S(x,0) &= 1 - S_{wr} \\ \left.\frac{\partial S}{\partial x}\right|_{x=0} &= \frac{\alpha}{\beta}(\beta S + \gamma) + \frac{\delta}{\beta}(\beta S + \gamma)^2 \\ \lim_{\xi \to +\infty} S(\xi, t) &= 1 - S_{wr} \end{aligned} \tag{2.55}$$

Here δ is a constant defined by the parameters β and γ according to

$$\delta = \beta - \frac{\alpha}{\beta(1 - S_{wr}) + \gamma} \tag{2.56}$$

Notable here is that the boundary condition for $x = 0$, the specified flux condition, can be shown to correspond to a net flux through the left boundary of -1 when substituted into (2.53).

Again, this problem is only one-dimensional but was solved via application of a two-dimensional finite solver. The same approach described in Section 2.3.1 remains equally valid here, namely using only two grid points with no-flux boundary conditions in one dimension. The conservation equation formulation the finite volume method operates from, equation (2.1), requires 'movement' terms to be cast as a flux. This was achieved by integrating the second term of the PDE in (2.53) with respect to x and absorbing it into the differentiated bracket of the first term. Relabelling S as C, the PDE becomes

$$\frac{\partial C}{\partial t} = \frac{\partial}{\partial x}\left(\frac{1}{(\beta C + \gamma)^2}\frac{\partial C}{\partial x} - \frac{\alpha}{\beta(\beta C + \gamma)}\right),$$

which matches the form (2.1) by taking

$$J = \frac{1}{(\beta C + \gamma)^2}\frac{\partial C}{\partial x} - \frac{\alpha}{\beta(\beta C + \gamma)}. \tag{2.57}$$

The first term here can be thought of as a diffusive flux, given the inclusion of the $\frac{\partial C}{\partial x}$ term, albeit a non-linear diffusion that still may pose problems. The second term does not formally match the definition of advection, but appears similar and may require careful numerical handling. Written in terms of the finite volume functions, this problem is expressed

$$\begin{aligned} f_1 &= \frac{1}{(\beta C + \gamma)^2}, \quad f_2 = \tfrac{1}{C}\tfrac{\alpha}{\beta(\beta C + \gamma)}, \quad f_3 = 0, \\ f_4 &= 0, \qquad f_5 = 0, \qquad \nabla S = 1\mathbf{i}. \end{aligned} \tag{2.58}$$

The analytical solution to the problem (2.53) is, not surprisingly, quite complicated. Unlike in the linear test problem, where the function could easily be stated explicitly, the transforms involved here in determining the solution force it to be implicitly defined. The means of obtain-ing the analytical solution are explained in the paper of Fokas and Yortsos [51], who present the solution as

$$S(x,t) = \frac{1}{\beta}\Big(\frac{\partial \bar{x}}{\partial x} - \gamma\Big), \tag{2.59}$$

where $\bar{x}$ is the solution to

$$\begin{aligned} e^{\alpha x} &= \phi(\bar{x},t) \\ &= \frac{1}{2}\mathrm{erfc}\left(\frac{\bar{x}}{2\sqrt{t}}\right) + \frac{1}{2}\exp\left(-\delta\bar{x} + \delta^2 t\right)\mathrm{erfc}\left(\frac{\bar{x}}{2\sqrt{t}} - \delta\sqrt{t}\right) - \frac{1}{2}\exp\left(-\beta\bar{x} + \beta^2 t\right)\mathrm{erfc}\left(\frac{\bar{x}}{2\sqrt{t}} - \beta\sqrt{t}\right) \\ &\quad - \frac{1}{2}\exp\left(-(\delta-\beta)\bar{x} + (\delta-\beta)^2 t\right)\mathrm{erfc}\left(\frac{\bar{x}}{2\sqrt{t}} - (\delta-\beta)\sqrt{t}\right) + \exp\left(-(\delta-\beta)\bar{x} + (\delta-\beta)^2\right). \end{aligned} \tag{2.60}$$

The first issue with this solution is the derivative $\dfrac{\partial \bar{x}}{\partial x}$, which is unknown, at least in that form. Using the chain rule,

$$\frac{\partial \bar{x}}{\partial x} = \frac{\partial \bar{x}}{\partial \phi}\frac{\partial \phi}{\partial x}.$$

The first derivative term can be determined by swapping the variables and taking the reciprocal, and the other is easily obtained from (2.60). Using these in (2.59) gives the solution to the original variable $S(x,t)$ as

$$S(x,t) = \frac{1}{\beta}\Big(\alpha e^{\alpha x}\frac{1}{\frac{\partial \phi}{\partial \bar{x}}} - \gamma\Big). \tag{2.61}$$

The derivative here can be taken, but after that $\bar{x}$ will still be unknown. While equation (2.60) cannot be solved analytically for $\bar{x}$, given a value of x and t it can be solved numerically, for example via Newton's method. Once this value of $\bar{x}$ has been determined, the derivative $\frac{\partial \psi}{\partial \bar{x}}$ can be evaluated and so (2.61) gives the solution. Thus, although it has a complex form, the solution can still be generated at any discrete point in space and time and hence numerical schemes can be tested against it. However, at each timestep a Newton solve at *each* node point will be required.

For the simulations presented here, the 'analytical' solution was generated using Newton's method manually programmed into the MATLAB file *generateAnalyticSolution.m*, using the same type of stopping criteria used for the Newton solver in the finite volume implementation (2.45), including the same user-specified tolerance values and maximum number of iterations. However, it was found that when the problem parameters are varied from those used by Awad and Turner [13] to make the problem more difficult to numerically solve, the generation of the 'analytical' solution often actually failed to converge to the correct result or at all, even if a simple global convergence routine was used. However, as is elaborated on when these cases are considered, mathematical arguments can be made about the properties of the exact solution as was originally done by Fokas and Yortsos [51] when they presented the exactly-solvable PDE in the first place. In the cases where the analytical solution was able to be successfully generated, the relative error could be calculated as before in order to test the finite volume scheme's performance on this non-linear PDE, however in this case there are less guarantees about the

Parameter	Definition	Value
β	Model parameter	5
γ	Model parameter	0.12
S_{wr}	Minimum water saturation	0.0375
S_{or}	Minimum oil saturation	0.15
L	Domain width	2
Δx	Control volume width	0.05
t_{end}	Simulation timeframe	0.6
Δt	Timestep	0.01
τ_a	Absolute Tolerance	1×10^{-4}
τ_r	Relative Tolerance	1×10^{-6}

Table 2.6: Parameter values for the nonlinear test problem, providing values for equation (2.58).

nature of the exact solution, preventing the direct testing of performance properties like the amount of peak smearing as was possible for the linear test problem.

The first tests performed followed those of Awad and Turner [13], choosing $\beta = 5$ and $\gamma = 0.12$, from which α and δ were calculated according to equations (2.54) and (2.56) respectively. Parameters used are specified in Table 2.6. As in the linear case, firstly the basic options for schemes were all considered to determine if flux limiting was indeed a necessary consideration for this problem. The results are displayed in Table 2.7. Due to this being a non-linear problem, some of the previously discussed options for the finite volume scheme that were not relevant for the linear test problem do become relevant here, though the effects of varying these are explored in a manner informed by these preliminary results. When the advective terms are averaged or upwinded, little in the way of choices need to be made to fully define the scheme. However, no matter how the advective terms are handled, the approach for the diffusive terms remains flexible according to the two approaches already described in equation (2.29). The performance of all the basic schemes were tested using both methods of approximating diffusion coefficients.

In the case of the advective term, the initial averaged quantity at the control volume face is done using the weighted average (2.31) used for linear advective terms. Varying how this average is calculated gives the different tested schemes of averaging, simple upwinding, and flux limiting, as already discussed and tested for the linear problem in Section 2.3.1. However, there are several choices for what this averaged quantity might be and how it is then used to approximate the advective flux through the face, as described by equation (2.32), and unlike in the linear problem these three approaches are no longer equivalent. In these preliminary tests, the first approach in (2.32) (flux limiting the concentration, then applying this to the functional form of the advective flux) has been used. In the case of the flux-based sensor (2.34) the chosen sensed flux $\mathcal{J}$ was the advective flux, the second choice listed in equation (2.42). All flux limiting simulations in Table 2.7 used the Van Leer flux limiter.

The results immediately demonstrate the necessity of flux limiting, given that the performance

Scheme	**Average Concentrations**	**Average Coefficients**
Averaging	3.72×10^{-3}	2.83×10^{-3}
Upwinding	1.18×10^{-2}	1.41×10^{-2}
Sensor (2.33), 'explicit'	1.44×10^{-3}	2.96×10^{-3}
Sensor (2.33), 'implicit'	1.49×10^{-3}	3.09×10^{-3}
Sensor (2.34), 'explicit'	5.97×10^{-3}	2.42×10^{-3}
Sensor (2.34), 'implicit'	5.71×10^{-3}	2.25×10^{-3}

Table 2.7: Test results for various approaches to handling the advective term when solving the non-linear PDE, with the relative error for each scheme listed. The two pairs of columns refer to the method used to approximate the diffusion coefficient at control volume faces, with the two methods listed in the order they appear in equation (2.29). The best performing scheme for each type of diffusive averaging is shaded.

of the upwinding scheme showed a significantly larger amount of error compared to the other trialled schemes. While averaging did demonstrate roughly equivalent overall performance here, it is generally not numerically stable and thus not reliable as a general approach. The two different types of flux limiting sensor showed considerable difference in performance, though which made the better choice depended on how the diffusive terms were handled. In the cases of both types of sensor there was no major difference between the explicit and implicit versions, suggesting that the explicit scheme is preferable due to its simplicity. However, all of these results were generated using the first averaging approach for advective terms listed in equation (2.32), and the other possibilities were also tested for this nonlinear problem where the choice does have an impact on the scheme. Using the case of the most successful Van Leer limiter, the results across the possible choices of averaging approach for advective functions (2.32) is provided in Table 2.8.

There are definite trends in the performance of the various schemes, but the interdependence between variables is very complex. One choice of averaging approach for either diffusive terms or advective terms was never unconditionally better. However, on average the best performing schemes were limiting all terms for advective fluxes (the third type in (2.32)) and averaging values of the diffusion coefficient itself for diffusive fluxes (the second type in (2.29)). More worthwhile is picking out the best-performing schemes and considering whether they are also the best performing schemes under other conditions or for different problems. Here the best scheme overall was found to be using a flux-based sensor (2.34) with the sensor chosen as the advective velocity, evaluated implicitly. The diffusive fluxes are approximated by averaging the diffusion coefficients themselves. However, for the previously considered linear PDE (Section 2.3.1) the best performing scheme used the other type of sensor for flux limiting, equation (2.33), evaluated explicitly. Here, the explicit version of this sensor again outperformed the implicit version, and given that an implicit handling of the sensor is associated with increased non-linearity in the equations to be Newton solved, it can be discarded as a potential scheme for further simulations. Overall, the derivative-based sensor showed good performance for all combinations of options, and under optimum conditions performed almost as well as the best

Diffusion - Averaged Concentrations			
Scheme	**Advective Average 1**	**Advective Average 2**	**Advective Average 3**
Averaging	2.76×10^{-3}		
Sensor (2.33), 'explicit'	1.44×10^{-3}	1.57×10^{-3}	3.08×10^{-3}
Sensor (2.33), 'implicit'	1.49×10^{-3}	1.71×10^{-3}	3.20×10^{-3}
Sensor (2.34), 'explicit'			
$\mathcal{J}$ type 1,	7.35×10^{-3}	6.05×10^{-3}	3.95×10^{-3}
$\mathcal{J}$ type 2,	5.97×10^{-3}	4.59×10^{-3}	2.45×10^{-3}
$\mathcal{J}$ type 3,	4.46×10^{-3}	3.14×10^{-3}	1.39×10^{-3}
Sensor (2.34), 'implicit'			
$\mathcal{J}$ type 1,	7.09×10^{-3}	5.77×10^{-3}	3.63×10^{-3}
$\mathcal{J}$ type 2,	5.71×10^{-3}	4.31×10^{-3}	2.17×10^{-3}
$\mathcal{J}$ type 3,	4.27×10^{-3}	2.97×10^{-3}	1.38×10^{-3}

Diffusion - Averaged Coefficients			
Scheme	**Advective Average 1**	**Advective Average 2**	**Advective Average 3**
Averaging	2.83×10^{-3}	3.42×10^{-3}	4.76×10^{-3}
Sensor (2.33), 'explicit'	2.96×10^{-3}	4.06×10^{-3}	5.78×10^{-3}
Sensor (2.33), 'implicit'	3.09×10^{-3}	4.18×10^{-3}	5.88×10^{-3}
Sensor (2.34), 'explicit'			
$\mathcal{J}$ type 1,	3.52×10^{-3}	2.48×10^{-3}	1.18×10^{-3}
$\mathcal{J}$ type 2,	2.42×10^{-3}	1.52×10^{-3}	1.66×10^{-3}
$\mathcal{J}$ type 3,	1.53×10^{-3}	1.51×10^{-3}	2.85×10^{-3}
Sensor (2.34), 'implicit'			
$\mathcal{J}$ type 1,	3.31×10^{-3}	2.27×10^{-3}	1.15×10^{-3}
$\mathcal{J}$ type 2,	2.25×10^{-3}	1.45×10^{-3}	1.89×10^{-3}
$\mathcal{J}$ type 3,	1.55×10^{-3}	1.69×10^{-3}	3.07×10^{-3}

Table 2.8: Comparison of test results for various averaging approaches for the advective flux listed in equation (2.32), for the various possible finite volume implementations. Data for both types of diffusion term approximation listed in equation (2.29) is listed. $\mathcal{J}$ refers to the quantity taken as a flux measure when using the flux-based sensor, the choices listed in equation (2.42).

scheme using the flux-based sensor. This combined with its good performance for the linear test problem suggests it is the optimal choice to use when applying the finite volume method in Chapters 6 and 7.

The cellular invasion problems considered in this thesis include chemotactic problems with sharp-fronted waves, and thus it was important to determine how the finite volume solver performed on a non-linear problem that featured less compensatory diffusion than the one presented here. As discussed by the original presenters of the analytically solvable PDE, Fokas and Yortsos [51], the sharpness of the wavefront could be increased by increasing the value of the problem parameter β, so long as the ratio γ/β remains constant. For $\beta \to \infty$, the problem possesses a much simpler analytic solution of a shock front connecting the same uninvaded and invaded states observed for the 'standard' value of β, $1 - S_{wr}$ and $S = S_{or}$ respectively. The shock front travels at a constant speed of $\dfrac{1}{1 - S_{wr} - S_{or}} \approx 1.23$ and thus the performance of the finite volume solver in this more challenging case could also easily be tested by direct comparison with a shock front moving at this speed. Thus a very large value of $\beta = 5000$ was chosen, with γ then appropriately chosen as $\gamma = 120$ to preserve the ratio γ/β.

It was seen that the finite volume method did correctly predict a moving front which was very sharp and correctly moving at the expected speed of 1.23 when a sufficient number of gridpoints and sufficiently small timestep were used. Given this is a non-linear, numerically challenging problem, it was heartening to see that the finite volume method did perform suitably well. However, the wavefront was not a perfect shock but occupied a width of a few gridpoints, and given the sharpness of the front the norms are larger than in the previous problems despite the simulated solution indeed displaying a very sharp front in the correct position. The various methods were also tested for this more difficult problem, with the results summarised in Table 2.9. These results were simulated using a grid size of $\Delta x = 0.005$ and $\Delta t = 0.01$, still on a domain of $L = 2$ and over a timeframe of 0.6. It was seen that in this case the flux-based sensor resulted in much better performance.

2.3.3 An Illustrative 2D Problem

A linear and non-linear problem have been used to demonstrate the necessity of flux limiting and determine how best it should be applied in situations relevant to this thesis, however both of these test problems worked in one dimension and the 2D nature of the code has not yet been properly examined. In addition, there is a point still in question regarding the determination of the second upwind face for which two methods have been discussed here. To briefly recap, one approach simply follows back in one dimension, whereas the other approach called the maximum flow method locates the node from which the largest flux is coming from and uses that. This simple problem is used to test these two approaches and generally examine the method for a 2D problem.

The problem used is rather numerically challenging and features pure advection with no dif-

Scheme	**Advective Average 1**	**Advective Average 2**	**Advective Average 3**
Upwinding	3.27×10^{-2}	3.27×10^{-2}	3.27×10^{-2}
Averaging	Oscillations in all cases		
Sensor (2.33), ‘explicit’	2.69×10^{-2}	2.88×10^{-2}	3.20×10^{-2}
Sensor (2.33), ‘implicit’	2.74×10^{-2}	2.91×10^{-2}	3.20×10^{-2}
Sensor (2.34), ‘explicit’	Incorrect solution for all cases and sensor types		
Sensor (2.34), ‘implicit’			
$\mathcal{J}$ type 1,	3.72×10^{-3}	2.94×10^{-3}	2.76×10^{-3}
$\mathcal{J}$ type 2,	3.72×10^{-3}	2.94×10^{-3}	2.76×10^{-3}
$\mathcal{J}$ type 3,	3.72×10^{-3}	2.94×10^{-3}	2.76×10^{-3}

Table 2.9: Comparison of test results for various averaging approaches for the advective flux listed in equation
(2.32), for the various possible finite volume implementations. Data for both types of diffusion term approximation listed in equation (2.29) is listed. $\mathcal{J}$ refers to the quantity taken as a flux measure when using the flux-based sensor, the choices listed in equation (2.42).

fusion and a very sharp solution profile in order to examine the finite volume solver's performance in a sort of ‘worst case’ scenario. This choice of problem also allowed the solution to be easily specified. Starting from equations (2.13), a simple first-order hyperbolic problem is easily formulated by taking $\chi(S) = \chi$, and $D_C = D_S = f_C = f_S = 0$. Making these substitutions results in

$$\frac{\partial C}{\partial t} = \nabla \cdot \Big(-\chi C \nabla S\Big), \tag{2.62}$$

with S pre-determined and unchanging in time. If S is a linearly varying function in space, ∇S is then essentially a constant and the solution profile follows this linear gradient at a constant speed, with no change in shape. While a purely hyperbolic PDE can pose problem enough, the methods were further tested in this case by using a turning ‘track’ of constant increasing chemical gradient S to force the solution profile to turn sharp corners and thus compare how the two approaches for determining the 2up point performed in comparison to each other. One method will detect the incoming flux along the track from before the turn, while the other which only checks in one dimension will not. Defining the distance along this track with a parameterised variable l, the problem (2.62) becomes 1D, expressed as

$$\frac{\partial C}{\partial t} = \frac{\partial}{\partial l}\Big(vC\Big) \qquad\qquad v = \chi\frac{dS}{dl} = \text{constant}. \tag{2.63}$$

This is easily solved via the method of characteristics, and with an initial pulse placed at the start of the track,

$$C(l,0) = \delta(l),$$

the overall solution is then

$$C(l,t) = \delta(l - vt). \tag{2.64}$$

That is, the initial pulse follows the track at a speed of v and retains its shape.

Initial simulations on this problem used a small number of grid points in order to ensure fast runtimes, and while these small-scale simulations were not appropriate for making comparisons against the exact solution (2.64), in several cases it was immediately apparent whether a given method could correctly solve this type of problem or not. Based on the previous results displaying the importance of a second-order timestepping scheme, Crank-Nicholson timestepping was used in all simulations discussed here unless otherwise mentioned. In these initial simulations, not unexpectedly, it was quickly apparent that using averaging to approximate advective fluxes ($\psi = 1$ in (2.31)) results in a great deal of spurious oscillation, not surprising because the scheme is not TVD. Both first-order upwinding ($\psi = 0$ in (2.31)) and gradient-based flux limiting (using a sensor of form (2.33)) resulted in simulations which featured no spurious oscillations but did involve a great deal of smearing of the pulse. Sensors of the form (2.34) were found to perform differently according to the specifics of the sensor and how it was updated. If the velocity is used as the detected quantity, the resulting scheme is essentially equivalent to averaging. This is because $\chi \nabla S$ is constant along the path, and thus all ratios are unity ($r = 1$ along the path). For all limiters considered here $\psi(1) = 1$ (and this is a very desirable property for limiters, see Section 2.2.1 or [186]). Thus the use of the cell velocity as a determinant of the flux to be sensed was seen not to be appropriate. If the actual flux is sensed instead of just the velocity, then the values of ψ vary with the travelling pulse and so the flux limiter might be able to correctly detect where artificial diffusion is required. It was found that the limiter did successfully prevent oscillation and resulted in proper peak transport but only in the case where the fluxes were updated dynamically (after every Newton step).

2.3.4 Conclusions

The finite volume method, implemented as discussed in Section 2.2.2 has been tested on a variety of problems in order to determine its applicability to model equations that might arise in modelling the scratch assay at a macroscopic scale, and given the implementation's flexibility, an effort has been made to find which approach within the implementation is correct.

Across all problems, flux limiting has been shown as a necessary inclusion, with first-order upwinding schemes proving to be numerically stable but inaccurate, and averaging schemes shown to break down when applied to the more numerically challenging problems. Of course, higher-order upwind schemes could also correct the over-dissipation present when using the basic upwinding implemented here, and other high resolution schemes like the KT scheme [101] would also be appropriate.

Two different sensors for detecting 'trouble spots' in the domain have been tested, a derivative-based sensor (2.33) and a flux-based sensor (2.34). Both showed good performance under circumstances suited to them, although in the linear problem the derivative-based sensor did perform better. More importantly, when the non-linear PDE test problem was made more numerically challenging by increasing the dominance of advection over diffusion, the flux-based sensor was found to cause the Newton's method to either fail to converge (when the sensor was calculated implicitly) or converge to incorrect solutions (when the sensor was calculated explicitly). This matches the observations of Turner and Pierre [196] who also considered a sensor of form (2.34) but found it was useful for limiting mobility tensors but not concentration terms. The point of flexibility in choosing exactly what type of flux was sensed from those listed in equations (2.42) was found to affect performance in the cases where this sensor was well behaved, but did not affect whether or not the scheme outright failed to correctly converge in the more difficult nonlinear problem. Flux limiting with a sensor defined by equation (2.33) is the chosen form of the implementation used in the remainder of the thesis, due to its good performance and relative safety across both the linear and nonlinear test problems, including the harder case of the nonlinear problem.

Performance of this sensor did not depend to any significant degree on whether it was calculated explicitly or implicitly. Therefore, for the sake of simplicity and reducing the non-linearity of the problem to be Newton solved at each timestep, the sensor (2.33) is calculated using information from the beginning of the timestep, as was also done by Thackham *et al.* when using a finite volume method to simulate travelling waves of cellular invasion [189]. The limiter function of Van Leer (see Table 2.2.1) was selected after it demonstrated the most accurate and stable performance amongst the three tested here.

The nonlinear problem raised further questions about how functional forms for diffusion and advection should be evaluated, for the case of both diffusive terms (2.29) and advective terms (2.32). However, no specific combination of selections from among these options stood out as superior to a significant degree, with the interactions between various choices in fact being very complex. Given the results for the challenging (strongly hyperbolic) linear problem, the derivative-based sensor was chosen for use in the subsequent simulations of the scratch assay. Importantly, the non-linear problem was also made strongly hyperbolic using a change of parameter, with the finite volume implementation demonstrated as very capable of successfully solving the numerically difficult, nonlinear equation.

The maximum flow method espoused by Turner and Pierre [196] has been here considered using a simple 2D problem that turned out to be entirely illustrative. This was a highly hyperbolic problem including a sharp change in advection direction which quickly demonstrated that the maximum flow method was prone to numerical instability for one type of sensor and provided no performance increase in the case of the other, also requiring it to be evaluated implicitly. Given this increased complexity, it was decided as an inappropriate choice for the PDEs solved in the simulation of the scratch assay.

The finite volume method, with the outlined choices for sensor, flux limiter and function evaluation method, has now established as suitable for solving even difficult numerical problems including dominant linear or nonlinear advection terms. This renders it perfect for use on the PDEs which are used to macroscopically model the scratch assay in Chapter 6. A wide range of potential implementations have been checked to ensure that the one used here is best suited for application to hyperbolic problems within those allowed by the flexible implementation.

Chapter 3

Cells As Individuals

3.1 Mathematical Modelling of Individual Cells

Individual cell-level modelling typically assigns overall rules to determine how a system of individuals behaves, and then continues to evaluate and re-evaluate those rules for every cell involved in the system as the model progresses through time. These rules can often be very simple and still result in very complex and/or unforseen emergent behaviour and it was the examples of this hidden complexity demonstrated by von Neumann [204] and via Conway's "Game of Life" [56] that essentially kicked off the concept of *Cellular Automata* (CA). Due to the fact that model behaviours in CA are typically emergent, and often defined by rules which feature a random component, individual-cell-level modelling is largely limited to simulation as opposed to mathematical analysis. This does little to invalidate it as a modelling approach, and indeed the simplicity of inherent rules typically makes for easier implementation when compared to numerical solvers for PDEs. The reliance on simulation does explain the field's relative slowness to take off until computers became sufficiently powerful and available [168].

Cellular automata involve the discretisation of time and space just like numerical techniques for solving PDEs, however this is not true of all techniques composing individual-cell-level modelling. The discretisation of space results in some finite number of sites (often referred to as cells but not here in order to prevent confusion between cellular automaton cells and biological cells), and each site is considered as being in one of a finite number of possible states. In the simplest case, a binary system, each volume is either in a state of 0 or 1 which in a cell biology context would typically correspond to whether or not that site was occupied by a cell. With a system defined in this manner, the temporal evolution of the system is enacted via repeated applications of the cellular automaton rules at each timestep. A recommended introduction to the concept of cellular automata is provided by Dormann [45], and a demonstration of the core concept of a set of simple rules producing complex emergent behaviours is perhaps best given by a graphical representation of the Game of Life, easily available in javascript form via a web browser [124]. Wolfram's book [210] argues strongly for cellular automata as a scientific revolution which all but supersedes traditional mathematical modelling, though these bold claims have been denounced as unfounded [72]. Nevertheless, that review rightly points out that Wolfram's book does present a fantastic compilation of applied CA as featured in a wide variety of disciplines.

Different types of cellular automata have found application to a very wide range of fields, certainly including cellular biology. The modelling framework as a whole has been used for example to simulate excitable media like the Belousov-Zhabotinsky chemical reaction [57], sexual reproduction [203] and its coexistince with asexual reproduction [27], the interactions of gas particles [74] and synchronisation [127]. In cellular biology, CA models are greatly useful, because they can easily operate on the scale of individual cells, argued by Walker and Southgate as a suitable point to use a 'middle-out' approach for biological modelling [206]. Choosing a middle point and working outwards avoids the issues obviously inherent in trying to make predictions of large systems based on interacting genes (bottom-up) or predicting component behaviours solely based on the physical properties and behaviours of organisms (top-down).

Two specific types of cellular automata that can be viewed as modelling frameworks in themselves are the Lattice Gas Cellular Automata (LGCA) and Cellular Potts Model (CPM), and both have been used rather extensively in the simulation of biological cells as demonstrated by the summary presented by Alber *et al.* [5]. Of course, other models fitting the general CA mould but not falling into either of those frameworks have found and continue to find success in modelling cell biology problems, due to the powerful flexibility offered by simply being able to 'make up your own rules'. Some examples of such 'freeform' CA include the modelling of tumour growth [3] and their interaction with the immune system [117], the formation of the ubiquitous vessel structures in biology (seen for example in angiogenesis or the invertebrate trachea) [122], or modelling HIV infection in the body [87]. Another somewhat independent school of thought is that of agent-based models, which like the cellular automata models described here operate by treating cells as individuals (referred to as agents) and defining a set of rules governing their behaviour which can be iterated to simulate the evolution of the system. The general point of differentiation between agent-based models and cellular automata is that agent-based models are *off-lattice*, whereas CA models operate on a pre-defined lattice of possible occupation sites. Some good examples of agent-based modelling in cell biology include those of the slime mould *D. discoideum* [147], and especially relevant are the models of Bindschadler and McGrath [18] and Walker *et al.* [205] who specifically model the healing of wounded cell monolayers, albeit with different models applied to different biological problems.

The LGCA modelling strategy was originally used to model the behaviour of individual particles of ideal gases and liquids on a lattice. Since the founding work of Hardy, de Pazzis and Pomeau [74], many extensions to the strategy have been implemented, allowing LGCA to find application to a more diverse range of fields including the behaviours of interacting biological cells. In the basic LGCA, the shape of each particle (in this case cells) is not considered, only its velocity and location. Each site can contain multiple particles, but typically an exclusion principle restricts the system so that no two particles with the same velocity can occupy the same site at once. Each timestep is composed of two phases, an interaction phase followed by a movement phase. In the interaction phase, particles may change their movement direction at random, but also through collisions with other particles in the simulation - how colliding particles change direction on collision is defined by a set of rules chosen to best represent what is known about the behaviour of the particles being modelled. In the movement phase, each particle moves to the neighbouring site in the direction of the movement channel it currently occupies (or remains in its current location if it occupies a rest channel). An important extension to the strategy is a more complicated lattice structure [54] (hexagonal as opposed to square), used to cut down on anisotropy. While the basic framework of a LGCA is a series of movements and collisions of agents, reaction kinetics have been included [31], and thus the two primary types of behaviour seen in relevant PDE models (flux and source/sink) can indeed be represented as a LGCA. Indeed by introducing a chemically-guided bias to the collision and/or movement behaviours of LGCA agents, a model for cellular chemotaxis can be constructed [41]. Thus despite its origins as a model for gas particles, this framework has evolved to also simulate biological cells, and given the approach's history and development mathematical analysis techniques have already been established for LGCA models.

The cellular Potts model (CPM), or in fact an extension of it, is the chosen framework for individual-cell-level simulations used in this thesis. For that reason, the method is not briefly summarised here but instead reviewed and considered to a much greater level of detail just below in Section 3.2. At a simple level, this technique also takes inspiration from statistical physics like LGCA and defines cell behaviours in terms of the total free energy of the system, which is to be minimised. The primary advantage of the CPM is the way it represents cells as occupying multiple sites, allowing for a natural way to track deformations in cell shape and size. A good summary of where the cellular Potts model sits in the context of theoretical biology, including an introductory review of its application, is provided by Glazier and Merks [129].

3.2 The Cellular Potts Model

3.2.1 History of the Model

The cellular Potts model (CPM) is a cellular automata (CA) modelling strategy which is in fact an example of a large-Q Potts model modified in order to model cell behaviour (hence its name), and was originally referred to as such. The Potts model, in fact an extension of the earlier Ising model [138] is a model which considers the total energy of some number of interacting 'spins', which originally referred to electron alignment. This allowed the model to consider the formation and destruction of magnetic domains in ferromagnetic materials, however various alternate interpretations of 'spin' have allowed for application to a wide variety of topics. A particularly pertinent example is in the Potts model's use in modelling coarsening of soap bubbles [66], because this was what inspired its adaptation to modelling biological cells. In the soap bubble case, each unique spin represents a different bubble, allowing a bubble to be specified by a group of sites all with the same spin. The CPM works in the same way, with sites occupied by matching spins containing elements of the same cell. It is this exact specification of shape that primarily differentiates the cellular Potts model from the great majority of other individual-cell-based methods.

The cellular Potts model began in 1992 as a model of cell sorting in multi-cellular clusters [70], demonstrating via a cellular automata approach the predictions of Steinberg's Differential Adhesion Hypothesis (DAH) [183]. That is, cells of different types behaving like immiscible fluids, a behaviour that has indeed been experimentally observed [53]. From there, the model was explored, such as the determination of critical temperatures for realistic cell behaviour [64] or the more recently published book which gives physical meaning to all of the CPM parameters [63, 118], including many of its extensions. The most notable extensions in fact lead to a renaming of the model, the GGH model. This name comes from the CPM's two original creators, François Graner and James Glazier, and its subsequent biggest contributor, Paulien Hogeweg, and hence somewhat suggests a direct improvement over the earlier CPM. Indeed the modifications associated with the GGH, negative adhesive energies and a dissipative cost for state changes, have been argued as more realistic [142]. However, despite this apparent superiority, the CPM without these refinements is still often encountered in the literature. Lastly, the author believes it is worth noting the works of Mombach *et al.* [133] and Mombach and Glazier [132] for the way they were able to verify that using the CPM's thermodynamic approach to model cell biology is indeed reasonable. The first of these works demonstrated that cell sorting does occur according to an exploration of the energy landscape and requires random fluctuations to locate a global energy minimum (complete sorting). This was achieved by treating cellular aggregates with the drug cytochalasin B which inhibits membrane fluctuations and thus demonstrating that the resulting impedance of cell sorting was also reproduced in their CPM simulations with a reduced temperature corresponding to reduced membrane activity. The second important work just mentioned analysed the motion of individual marked cells within an aggregate, demonstrating that they exhibited a biased random walk consistent with statistical mechanics in both experiments and CPM simulations. These observations suggest that the CPM is a very capable tool for representing cell behaviours at the scale of individual cells.

The energy minimisation framework both the CPM and GGH work from (explained in detail in Section 3.2.2) cannot be used to represent all cell behaviours that might need to be included in model simulations. Most notable are the behaviours of tactic response and mitosis, both of which have been previously modelled using modified CPM or GGH models (though rarely are the two encountered together). The simulations in this thesis make use of both behaviours, and so both are explored thoroughly in this thesis and are presented in separate chapters (4 and 5), of course including brief reviews of their appearances in the literature. These successful inclusions of effects beyond the central idea of energy minimisation demonstrate that even within a well-defined framework like this the flexibility offered by the freedom to 'make up rules' in freeform CA is not lost. Of course, these rules must be sensible and justifiable.

The CPM and GGH have been applied to a wide variety of biological problems, including morphogenesis in the growing chick limb [29, 160], the complex life cycle of the slime mould *D. discoideum* [88, 119, 166], the growth and invasion of tumours [17, 157, 185, 197, 198], the development of cellular patterning in *Drosophilia* eyes [90], the formation of vascular networks [17, 130], the growth of biofilms [159] and keratinocyte migration including polarisation [120], among many others. The biological application of this thesis, the healing of wounded monolayers, has seen brief consideration in the CPM/GGH [141], but those simulations did not feature an invasive effect and lacked proliferation.

3.2.2 Basic Framework of the CPM/GGH

In the standard CPM originally proposed by Graner and Glazier [70], the state of the system is described by specifying what currently occupies each site in the CA lattice. This lattice can be one, two or three dimensional and could theoretically be constructed out of any shape which can tile the problem domain. Primarily the CPM uses a square or cuboidal lattice, because a regular structure with consistency of side lengths greatly simplifies calculations of cell volumes and surface areas, and adhesion between cells. The description here uses the most common case of a 2D CPM on a square lattice, visualised in Figure 3.1, and this is the implementation used in this thesis also. The occupation of each site (i, j) is described by $\sigma(i, j)$, each unique positive integer value of σ corresponding to a different cell. Multiple lattice sites may be simultaneously occupied by the same cell, that is $\sigma(i_1, j_1) = \sigma(i_2, j_2)$, and it is because one cell occupies multiple lattice sites at once that the CPM can model deformations of individual cells. The concept of individual cells possessing shapes according to the specification of σ at each site is visualised in Figure 3.1. Cells also belong to one of a set of types, denoted by $\tau(\sigma)$. Two cells of differing species would have different τ and σ, but two cells of the same species would have the same τ but differing σ. The medium between cells is essentially considered as another type of cell, and given a unique value of τ and σ (often the 'starting value', 0 or 1).

This explanation of the CPM starts with its historical root of the Potts model, in which the system is described as above, with a finite number of lattice sites each being in some state from Q possible states [162]. The aforementioned Ising model is the specific case of the Potts model where $Q = 2$ [138]. As in Hamiltonian and quantum mechanics, the total energy of the system is referred to as the "Hamiltonian" or "Hamiltonian interaction energy" and denoted by H. Here this total energy can only depend on the current state of the system (which state each site is currently in). In modelling the original application of the Potts model [162], namely interacting spins in crystal lattices such as ferromagnets, the Hamiltonian was composed as a sum of energy contributions from each 'state mismatch' where two neighbouring sites do not share the same current state. In ferromagnets, groups of identically-aligned electron spins called "domains" form in the absence of an external field due to energy-minimisation behaviours [37], and so by having energy increase with every 'state mismatch' between neighbours, low-energy configurations will feature groups of many sites in the same state (many electrons with

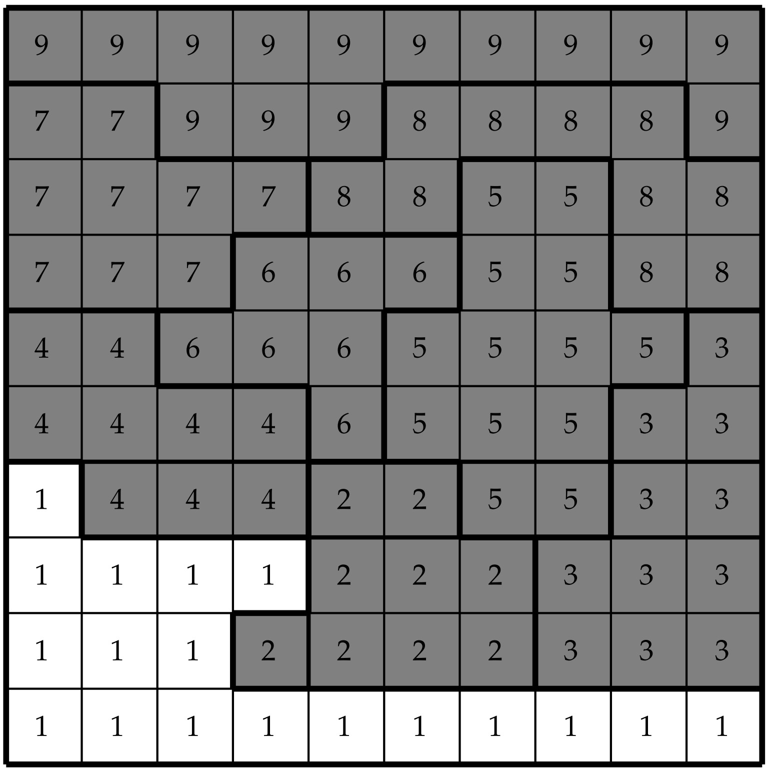

9	9	9	9	9	9	9	9	9	9
7	7	9	9	9	8	8	8	8	9
7	7	7	7	8	8	5	5	8	8
7	7	7	6	6	6	5	5	8	8
4	4	6	6	6	5	5	5	5	3
4	4	4	4	6	5	5	5	3	3
1	4	4	4	2	2	5	5	3	3
1	1	1	1	2	2	2	3	3	3
1	1	1	2	2	2	2	3	3	3
1	1	1	1	1	1	1	1	1	1

Figure 3.1: Demonstration of how definition of unique site occupancies results in specification of cell shapes and positions. The shaded areas indicate regions occupied by cellular mass, and the unshaded region is unoccupied (referred to as 'medium' and assigned index $\sigma = 1$). Dark lines are cell edges.

the same spin alignment). Expressed mathematically, the Hamiltonian is

$$H = \sum_{i,j} \sum_{i',j' \in N(i,j)} \left(1 - \delta_{\sigma(i,j),\sigma(i',j')}\right). \tag{3.1}$$

Here $N(i,j)$ is the set of sites neighbouring the site (i,j) and $\delta_{i,j}$ is the Kronecker Delta, defined as

$$\delta_{i,j} = \begin{cases} 1 & (i = j) \\ 0 & (i \neq j) \end{cases}. \tag{3.2}$$

In (3.1), the entire system is considered by summing over all lattice sites (the first sum over all i and j). For each lattice site, the adhesive contribution between this site and each of its neighbours $N(i,j)$ must be included (the second sum over all $i', j' \in N(i,j)$). The Kronecker delta is included to 'turn off' energy contributions between neighbours which do share a type and hence only mismatches between neighbours will contribute to the total energy. Equation (3.1) essentially ignores the complex interplay of energy contributions in ferromagnets, yet retains the observation of domains as the low-energy state. From here, statistical physics approaches can be used to determine properties of the system via this total energy, or minimum energy configurations can be found.

An application of the Potts model which better demonstrates its extension to the CPM is its use in modelling the growth of domains, such as coarsening of metal grains [8]. In considering the temporal evolution of a system represented like this, a stochastic Monte Carlo process referred to as the Metropolis algorithm [131] is used to capture how the system attempts to reach the minimum energy state defined by H. In the Metropolis algorithm as it is used here, a site is chosen at random and its current state is changed to a randomly selected state. Energy minimisation is achieved by checking how this change affects the value of the Hamiltonian (ΔH), then implementing the change with probability

$$Pr(\text{Trial accepted}) = \begin{cases} 1 & \Delta H < 0 \\ \exp\left(-\dfrac{\Delta H}{T}\right) & \Delta H \geq 0. \end{cases} \tag{3.3}$$

That is, all trialled changes which reduce the total energy of the system are certainly accepted, whilst those which increase the total energy are only possibly accepted. The more a trialled change increases the total energy, the less likely it is to actually happen. T is the 'temperature' of the system, with higher T's making unfavourable changes more likely to be accepted. The form of (3.3) used here is the one appropriate to the CPM for consistency with what follows, and it should be noted that when a physical energy is being considered as in the Potts model, the temperature T should in fact be replaced with $k_B T$, where $k_B = 1.38 \times 10^{-23}$ J K^{-1} is Boltzmann's constant. There is a clear parallel between the exponential term in (3.3) and Boltzmann factors of statistical physics, which also relate probability to energy.

The overall effect of the Metropolis algorithm is to produce a gradual evolution of a system represented by some total energy toward its minimum energy state, loosely informed by statistical physics. If only changes which decreased the energy were accepted, then the system could quite easily become 'stuck' in a local minima of energy and never reach the true minimum energy configuration. By allowing energistically unfavourable evolutions to *possibly* occur but having them be less likely than energistically favourable evolutions, given enough time the evolving system should be able to get itself out from these minima and reach its true lowest-energy state. The temperature then represents the strength of this effect, an interpretation which remains valid in the case of the cellular Potts model where the temperature T in equation (3.3) is not the physical temperature and indeed has no easy physical interpretation at all. The actual updates that the Metropolis algorithm trials must also be changed for use in the cellular Potts model. Once a random site to update has been chosen, instead of selecting a new state at random, the new state is chosen from one of its neighbouring sites. By doing this, each trialled update then represents a cell stretching its membrane into the new site, whether it is free space or occupied by another cell which it is encroaching upon. In the case where medium chooses to 'expand', this can be thought of as a retraction of the cell it expands onto.

The original biological application of the CPM was the sorting of mixed cells, an observable behaviour apparently explained by Steinberg's Differential Adhesion Hypothesis (DAH) [183] which states this behaviour arises from types of cells minimising surface energy associated with their adhesion to other cells or the medium they occupy. Given that the Potts model's Hamiltonian (3.1) is a total surface energy of the system, it appears to be appropriate in this context also. However, in order to model sorting of various cell types, which depends on the differences between the adhesive strengths of these different types, equation (3.1) must be modified by including a type-dependent adhesive strength, $J(\tau_1, \tau_2)$. There is still adhesion between medium and cells, so medium is also treated as another cell.

$$H_{\text{adhesion}} = \sum_{i,j} \sum_{i',j' \in N(i,j)} J\Big(\tau\big(\sigma(i,j)\big), \tau\big(\sigma(i',j')\big)\Big)\left(1 - \delta_{\sigma(i,j),\sigma(i',j')}\right). \tag{3.4}$$

All other terms in (3.4) are exactly as described in (3.1). Again the total energy here is a sum over all boundaries between sites, with a contribution to the energy coming from any boundary where this is a state mismatch (that is, any edge of a cell). When $\delta_{\sigma(i,j),\sigma(i',j')} = 1$, the two neighbouring sites are occupied by the same cell and there is no energy contribution because there is no adhesion within a single individual cell. It is worth noting here that if the neighbourhood is defined in all directions, each boundary between sites is actually counted twice (for example the boundary between sites (m, n) and $(m+1, n)$ would be considered both when $i = m, j = n, i' = m+1, j' = n$ and when $i = m+1, j = n, i' = m, j' = n$. This essentially causes the values of J to effectively be doubled by being counted twice, which one should be aware of when choosing and interpreting parameter values. The adhesive energies are best interpreted in terms of the resulting *surface tension* which equation (3.4) introduces into a simulation trying to minimise the value of H. The surface tension between two cell types i and j is denoted γ_{ij}

and is defined [70] as

$$\gamma_{ij} = J_{ij} - \frac{J_{ii} + J_{jj}}{2}. \tag{3.5}$$

If the surface tension is negative, the cells will disassociate into a ‘checkerboard’ pattern because boundaries between different cell types are energistically favoured compared to boundaries between matching cell types, and if the surface energy is positive then cells will prefer to adhere to other cells of their type and thus clusters of each type will form.

Another critical difference between the cells modelled by the CPM and the various situations modelled by the original Potts model is that cells have some certain volume, whereas soap bubbles, for example, are free to grow or recede in order to minimise the total surface energy of the system. Expressed another way, “cell sorting occurs through the movement of cells, not cell growth” [70]. In order to prevent cells from growing or shrinking at will, they are assigned a (possibly type-dependent) “target volume”, $V(\tau)$. The meaning of this quantity is the volume (measured in number of lattice sites occupied) that a cell would tend to be in the absence of other factors. If the lattice sites have physical dimensions, then this target volume would similarly have physical meaning. By including a second term into the Hamiltonian which increases the energy when cells are not at their target volumes, energy-minimisation behaviour will effectively induce a force causing cells to want to be at this target volume. This might seem rather arbitrary, but can be interpreted as an elastic energy associated with cells stretching or being compressed. The mathematical form of this elastic energy originally used by Graner and Glazier [70], and essentially universally adopted, is

$$H_{\text{volume}} = \lambda \sum_{\sigma>1} \big(v(\sigma) - V\big(\tau(\sigma)\big)\big)^2 . \tag{3.6}$$

Here $v(\sigma)$ is the volume of the cell with index σ and $V\big(\tau(\sigma)\big)$ is the target volume of a cell of that type. The sum is taken over all values of $\sigma > 1$, adding up the energy contribution from each cell and discounting the volume of the medium, which is unconstrained. The term is squared to ensure the contribution is positive regardless of whether the cell is smaller or larger than its target volume - both situations should be unfavourable in terms of minimising H in order to have cells prefer to be the designated size. The constant λ defines the ‘strength’ of the volume constraint (the higher the value of λ, the more unfavourable it is for a cell to be away from its target volume), and so resembles an elasticity constant. However, given that larger values of λ result in more rigid cells, in this thesis λ terms are sometimes referred to as “inelasticities”, or as volume or surface constraints.

The overall Hamiltonian is simply defined as the sum of the Hamiltonian contributions from the different factors determining cell behaviour. That is,

$$H_{\text{total}} = H_{\text{adhesion}} + H_{\text{volume}}.$$

Using the definitions above, equations (3.4) and (3.6), the total Hamiltonian is

$$H_{\text{total}} = \sum_{i,j} \sum_{i',j' \in N(i,j)} J\Big(\tau(i,j), \tau(i',j')\Big) \left(1 - \delta_{\sigma(i,j),\sigma(i',j')}\right) + \lambda \sum_{\sigma} \left(v(\sigma) - V\big(\tau(\sigma)\big)\right)^2, \quad (3.7)$$

and this is the quantity that the system will seek to minimise as it evolves over time. Additional factors controlling cell behaviour can be included simply by adding additional terms to (3.7), taking care that their relative importance is represented mathematically through multiplicative strength constants, in the same way λ is used for the volume constraint.

The form of the Hamiltonian (3.7) is equivalent to the earlier Potts model studies (3.1) if J is a constant and λ is zero. Mathematical results from these earlier simulations cannot be interpreted well in a CPM context, however, because an unconstrained size ($\lambda = 0$) is not physically reasonable for biological cells. Eukaryotic cells, complete with central nucleus, cannot simply be removed by reducing their volume to zero, which is what occurs with unconstrained volume (domains growing at the cost of others). If the biological processes for cell death (necrosis and apoptosis) are to be included in the CPM framework then this should be achieved through some trigger resulting in cell death. Without careful justification, one should be careful assuming that any cell that reaches zero volume has died, because this is not an expected behaviour in the CPM and could be the result of an improper choice of parameter values or error in the implementation. Given the nature of trial updates in this framework (3.3), a cell which disappears can never reappear.

3.2.3 Interpreting the CPM/GGH

Given the stochastic nature of the CPM introduced by the Metropolis algorithm (3.3), simulations run with identical parameter choices and initial conditions will still differ. Whether running simulations until steady state or considering transient behaviours, there will still be significant differences between subsequent runs. However, when considered macroscopically there will be some kind of emergent behaviour which will remain consistent across simulations. A reasonable analogy can be found in marking patterns in animals - while the exact patterns found within a single species will differ between individuals, every leopard can be recognised for their distinctive spotted pattern, and so on. Indeed, the minor variation within a macroscopic pattern that the CPM naturally predicts via its stochastic nature is if anything an argument in its favour, though thinking along those lines raises interesting questions about just where determinism lies in biological processes that are well beyond the scope of this thesis. A quantitative measure is still quite necessary in order to provide something solid with which different stochastic simulations can be compared, and examples of such include the average number of sides a cell has [64], boundary lengths between different cell types [133], calculated diffusion coefficients [142], the volume of cellular material (when this is allowed to vary significantly by including mitosis) [185] or invasive velocities [17].

With random updates being accepted or rejected according to the Metropolis algorithm (3.3), it is clear that more favourable than unfavourable updates to the system state will be made, leading to a general trend of reducing the value of H. Increasing the model parameter, T, increases the probability that an unfavourable move will be accepted, and so T can be seen as a 'willingness' of the system to go against its overall goal of lowering the Hamiltonian free energy. T is referred to as the temperature, because of its similarities to physical temperature (consider for example how increasing the temperature of ice can change it from an ordered solid to a chaotic gas). When the temperature is zero, the system can only move in ways that reduce its energy, and when the temperature is infinite, the system will accept all updates and hence completely ignore the value of the Hamiltonian free energy and behave entirely at random. Negative temperatures lead to probabilities greater than one in (3.3) and so are both mathematically and physically unreasonable. While the similarities between the simulation temperature and the thermal temperature have been mentioned here, they are of course *not* the same thing, with one controlling the energy of individual molecules and the other the 'energy' of cell membranes.

Graner and Glazier define two different critical temperatures [64] that, when either is exceeded (or nearly exceeded), lead to unphysical behaviours. One governs cells remaining whole (by considering survival chances of small pieces surrounded by mismatched spins, and the other governs how willing cells of different types are to sort in order to minimise adhesive energy. Graner and Glazier also suggest that the temperature is low in the "biological limit" compared to these calculated critical temperatures (at least for their choice of parameters). It has also been suggested that the temperature can be thought of as the amplitude of fluctuations of cell membranes [133]. Given that each update is the expansion or retraction of a single piece of cell, it can certainly be seen as a cell's membrane fluctuation, and given that a higher temperature will cause more fluctuations to be accepted, this view is certainly rather feasible. It has been shown that the effects of cytochalasin-B (a drug inhibiting membrane fluctuations) on cell sorting were modelled reasonably well in the CPM through a reduction in temperature [133]. However, using the Metropolis algorithm (3.3), the simulation temperature does not have an impact on trialled updates which result in a decrease in the total energy of the system, and thus it cannot be directly interpreted as a direct control of 'membrane activity'. Indeed, a temperature $T = 0$ does *not* correspond to zero membrane movement in the CPM.

Further conflating matters, cells in fact do cease membrane activity when the thermal temperature becomes too small [133], however in almost all biological experiments careful control of temperature is maintained and so the simulation temperature T need not be considered in a thermal sense. Interestingly, novel results in this thesis do suggest that the chemokineitc effect of increasing cellular activity in the presence of activator chemicals [42] could be very conveniently represented in the CPM by specifying T to depend on chemical concentration S with $T(S)$ an increasing function (see Section 4.3.3).

The author believes that the claim that a value of T can be determined from experimental measurements of membrane fluctuations or diffusion coefficients [214] is rather idealistic, although trial and error matching of diffusion coefficients for a given set of parameters might succeed.

It seems far more reasonable to consider temperature as a model parameter that can be varied as necessary to ensure realistic behaviours. Indeed, sometimes different Monte Carlo steps within a simulation use different temperatures, usually in the form of zero-temperature annealing steps used to stabilise a system by forcing it to find a local minimum of the Hamiltonian [64, 133] before visualising results or making statistical calculations. These zero-temperature steps will not produce long-range or large-scale behaviours, but can be used to 'clean up' a system, removing energetically unfavourable and biologically unrealistic aspects of a simulation like small pieces of cells that have broken off.

3.2.4 Extensions to the CPM/GGH

The cellular Potts model has seen many extensions since its introduction in 1992, including those that operate within the framework of minimising the total energy and those that work alongside it. Given the flexibility of cellular automata approaches like the CPM and the wide range of problems it has been applied to, the review presented here does not attempt to summarise every last change that has been made to the CPM within its history. Many of these are specific to the cell biology problem they have been developed to simulate and are thus not directly relevant to this thesis. Instead, this section focuses on those changes which have been suggested as means of improving the framework as a whole, allowing it to better simulate cell biology problems *in general*.

As mentioned in the brief discussion of the history of the CPM (Section 3.2.1), a new name directly crediting the originators of the CPM and its subsequent biggest contributor was coined, the GGH (Glazier-Graner-Hogeweg) model. This name is typically applied to a more advanced version of the CPM, featuring certain extensions that have been demonstrated to allow it to more realistically capture cell behaviour [142]. The first of these extensions is the use of negative energies to represent adhesion between cells, put forward by Ouchi *et al.* [142]. So long as the value of J between cells and medium is lower than the value of J between cells, the general trend predicted by the GGH model will be cells sticking together, demonstrating cell-cell adhesion. However, the preference of cells to stick together is not simply an energy-minimisation behaviour but a real chemical effect, and thus energistically should be represented with a negative contribution to H, such that breaking up these cell-cell adhesive contacts correctly requires a cost. Of course, if H is decreased for each cell-cell contact, the minimal energy configuration will be one which maximises cells' contact with each other, and cells will thus take on very ruffled and disjoint shapes in order to maximise contact. For this reason, just as the volumes of cells are constrained to prevent unphysical shrinking or swelling by an appropriate Hamiltonian contribution (3.6), their surface area (or perimeter in 2D) can also be constrained to prevent the unrealistic deformations introduced by negative values for J using a very similar contribution to H,

$$H_{\text{surface}} = \lambda_2 \sum_{\sigma>1} \big(a(\sigma) - A\big(\tau(\sigma)\big)\big)^2 . \tag{3.8}$$

Here $a(\sigma)$ is the surface area of a cell, measured simply by counting the number of exposed surfaces by checking for mismatches with neighbouring sites. $A\big(\tau(\sigma)\big)$ is the 'target' surface area for a cell of that type, and the strength of the membrane constraint effect is controlled by λ_2 in the same fashion as λ in the volume constraint (3.6). Indeed from this point on, the volume constraint λ is re-labelled as λ_1 to highlight the fact that these are both inelasticity constants, the difference being one is for cells themselves (λ_1) and the other specifically for their membranes (λ_2). The value of $A(\tau)$ is free to choose, but must be chosen with the constrained volume in mind for realistic cell behaviour. Ouchi *et al.* suggest that in a 2D simulation, assuming that cells naturally want to be circular and then allowing an additional 20% of membrane slack,

$$A(\tau) = 1.2\sqrt{\pi V(\tau)}, \tag{3.9}$$

is a good choice [142].

Using equation (3.8) as an additional Hamiltonian contribution and taking J between adhesive cells as negative was demonstrated by Ouchi *et al.* to now correctly predict the movement of one cell within an aggregate of another type of cell (the less cohesive cell should move faster, which did not happen when J's are all positive) [142]. They also pointed out that what is being done here is a decoupling of the two separate behaviours of cell-cell adhesion and a fixed membrane length, which were previously both encoded solely into the choice of adhesive strengths J. Applying this extension makes the expression of H more complex and introduces additional parameters, but also allows for a more natural interpretation of the values of J and more realistic cell behaviour. A further suggestion to improve realism by taking into account the mechanical physics and recovering classical elasticity for cells has been suggested by Poplawski [156], using a surface area constraint of form

$$H_{\text{surface}} = \lambda_2 \sum_{\sigma>1} \left(a(\sigma)v^{2/3} - A(\tau)V(\tau)^{2/3} \right)^2,$$

with λ_2 defined in terms of physical cell properties in the referenced work. However, the use of this more complex form has not caught on in the CPM/GGH literature.

The second important extension to the CPM which comprises its relabelling to the GGH model is the inclusion of a dissipation effect when cells deform. This represents the energy required to actually enact any kind of cell movement, and thus introduces an energistic penalty to any update which is trialled. The technique was first introduced by Hogeweg [79] in order to reduce random fluctuations in the CPM, making modifications directly to ΔH by adjusting the Metropolis algorithm like so

$$Pr(\text{Trial accepted}) = \begin{cases} 1 & \Delta H < -H_{\text{bond}} \\ \exp\left(-\dfrac{\Delta H + H_{\text{bond}}}{T} \right) & \Delta H \geq -H_{\text{bond}}. \end{cases} \tag{3.10}$$

The inclusion of this effect was demonstrated to improve directional persistence in CPM cell movements by Ouchi *et al.*, however the values used for H_{bond} there differed greatly to those used by Hogeweg. The effect of H_{bond} is also weighted by the value of the simulation temperature T as can be seen from (3.10) and so should be chosen as appropriate for a given simulation. Due to it being an energistic penalty, the larger the value of H_{bond}, the less active overall a CPM simulation will be. In a sense increasing H_{bond} is like lowering the simulation temperature T, because both affect only the probability of trial updates being accepted, though in a slightly different way which also changes the proportion of updates which are automatically accepted.

Many other possible extensions to the general CPM framework have also been considered. The fact that the CPM operates on a square grid means that it can be quite prone to lattice effects, arising from the difficulties a square lattice has representing and interpreting smooth objects. This effect is referred to as lattice anisotropy and affects the CPM in terms of its ability to accurately measure surface tensions and perimeters, which take place at the edges of cells. Demonstrations of the effect at work can be seen in the ability of a simple cell cluster to take on a round shape, which it should do naturally due to its desire to minimise the inherent surface tension which arises when the value of J between cells and medium is larger than that between cells [63]. The more prevalent the effects of anisotropy are, the less round the resulting shape will be. Lattice anisotropy has been corrected by basing perimeter and adhesion energy calculations off a larger number of neighbours [90, 142], or by using a hexagonal lattice for its ability to better represent circular shapes whilst still tiling space [118, 188].

The viscosity of the fluid medium is not captured in the typical CPM framework, with the medium being free to deform in any way due to its unconstrained volume and surface. While the viscous regime cells operate in seems to be rather well captured by the standard CPM, judging by its widespread success, in situations where the advection of the fluid is important (most notably for its transport of chemicals like signal or nutrient) this basic approach might not suffice. Dan *et al.* demonstrated that by representing the medium as a series of 'fluid cells' also bound to the constraints on standard CPM cells, a viscosity effect could be incorporated [39]. They then went on to couple a CPM using this modification with an off-lattice finite difference formulation of an advection-diffusion equation that could be used to track chemical transport, allowing cell-driven advection of chemical signals to be captured in the CPM.

Although working in a specific context of angiogenesis, the extension of Merks *et al.* to track and constrain cell lengths [128] is a general modification that could be made to any CPM. This approach introduces a length constraint of essentially the same form as equations (3.6) and (3.8), except that here the constrained quality is the length of a cell along its longest axis. A means of approximating this length is detailed in the referenced work. The specification of a 'target length' and then penalising cells for deviating too far from this length is not however the representation of some physical effect but instead used to control the shapes of cells. If a cell has a very long target length in comparison to its target volume, then that cell will take on an elongated shape. Thus a constrained length is an important tool for accurately representing cell types which have a highly elongated shape, which has indeed been demonstrated to potentially be an important determinant of their migratory behaviour [176]. This approach has been shown by Backes *et al.* to allow the CPM to naturally predict intercalated structures via its usual energy-minimisation behaviours applied to cells which desire a highly elongated aspect ratio [14].

A physical effect which goes largely ignored in CPM and GGH model is that of gravity. For the most part, this is because this modelling tends to take place in 2D, either because the situation being modelled involves cells crawling along some kind of substrate they are attached to, or simply for the sake of reduced complexity. However, the means of including a gravitational effect into the CPM framework has been put forward by Glazier and Uphadyaya [65]. Additionally, a rather artificial inclusion of a gravity-like effect was used by Savill and Hogeweg in their modelling of the *D. discoideum* life cycle to cause the mound to topple over when it reached a certain size [166]. However, as is pointed out in that work, in experimental observations of *D. discoideum* behaviour the petri dish can be turned upside down without affecting the formation of the mound and so this suggests gravity might not be the driving effect here. Savill and Hogeweg's implementation of gravity simply biases cell updates which occur in the fall direction via direct modification of each considered ΔH.

Two key extensions which represent general cell behaviours that have not yet been discussed here are proliferation and tactic response to signals. These features are indeed critical to the application of the GGH model here to the scratch assay, and thus these two behaviours are discussed separately in their own chapters, chemotaxis in Chapter 4 and proliferation in Chapter 5. Those chapters review the relevant literature and then present the chosen approaches used in the GGH model implemented here, and for this reason they are not discussed in the following section regarding the GGH model implementation.

3.2.5 Implementation

The GGH model implementation here works from the basic CPM approach discussed in Section 3.2.2, combined with the extensions comprising the GGH model described in Section 3.2.4. Combining the standard CPM Hamiltonian contributions (3.4) and (3.6) with the additional constraint on cell perimeters (3.8), the overall Hamiltonian energy that the system tries to minimise is

$$H = \sum_{i,j} \sum_{i',j' \in N(i,j)} J\Big(\tau(i,j), \tau(i',j')\Big) \left(1 - \delta_{\sigma(i,j),\sigma(i',j')}\right) \\ + \lambda_1 \sum_{\sigma>1} \big(v(\sigma) - V\big(\tau(\sigma)\big)\big)^2 + \lambda_2 \sum_{\sigma>1} \big(a(\sigma) - A\big(\tau(\sigma)\big)\big)^2 . \quad (3.11)$$

The system is evolved using the modified Metropolis algorithm including a binding energy, (3.10).

As with the finite volume solver discussed in Section 2.2.2, the GGH model is implemented here using the MATLAB programming language, as a series of bundled .m files. The entire function of the code is not discussed here, but the general framework is outlined and specificities are explained. Simulations are run using the file *Driver.m*, where all parameters used by the GGH model are specified, including the values of cell adhesions J, inelasticities λ_1, λ_2 and target volumes V for all cell types, the value of the dissipation energy H_{bond} and the simulation temperature T. Parameters regarding chemotaxis and proliferation are also defined here if they are to be included in the simulation. The user also nominates the number of grid points to be used in the simulation, the physical lengths these represent, and the number of Monte Carlo steps to run the simulation over, by defining the physical time each MCS is worth and nominating a total timeframe of the simulation. The frequency and means of results visualisation are also chosen by the user.

Simulations are run on a 2D rectangular lattice composed of square sites. The number of sites and the physical domain widths should be balanced so that all sites are square, with the implementation not designed to handle rectangular sites due to the differences in the calculation of adhesion energy and cell perimeters and volumes. The mesh is defined by a separate file *MeshGenerate.m* that generates a list of which sites are neighbours to each site, using either the standard Moore or von Neumann set of neighbours (the user chooses, though a Moore neighbourhood is highly recommended and is used for all simulations presented in this thesis). However, modification to the mesh-generation file would allow for meshes of different shapes (still composed of small square sites) to be defined and these should operate correctly without any further modification to the rest of the MATLAB code.

The other aspect of the GGH model simulations here that is user-defined is the initial condition, which is specified in the file *generateIC.m* and simply consists of nominating an initial occupation value σ for each site in the simulation domain. Of course, this must be chosen in a fashion that generates a realistic initial condition, and elements with matching $\sigma > 1$ should be simply connected so that no individual cells begin in separate, disconnected pieces. Initial conditions used in this thesis use simple square or rectangular cells, though the slightly artificial nature of this kind of initial condition is counteracted by letting a cell system evolve to a more realistic configuration before the real simulation begins (e.g. a scratch occurs, or the cells are subject to the chemical gradient). In the later simulations involving chemotaxis, the initial chemical concentration at each lattice site is also defined in *generateIC.m*.

There are no boundary conditions of the traditional sort in the GGH model, but a choice must still be made as to how to deal with the edges of the domain. Here, any site which has a number of neighbours less than the full number in the interaction neighbourhood is recognised as being a site on the edge of the domain. The difference between those two numbers is tracked so that calculations of perimeter and adhesive energy are still made correctly, with the adhesion to the edges of the boundary being defined by a parameter $J_{\text{walls}}(\tau)$. To minimise the effect of the boundaries, here all cell types are given a value of $J_{\text{walls}} = 0$ so that no type of cell (or absence of cell) prefers to occupy an edge location. Given that the flexible implementation here allows for the specification of internal 'holes' or obstacles in the domain if carefully specified when defining the list of sites and neighbours in *meshGenerate.m*, the stickiness of these obstacles for cells of different types could be controlled by choosing values for $J_{\text{walls}}(\tau)$ which did indeed vary with τ.

Each Monte Carlo step is enacted by a repeated process of selecting a site at random from the entire domain, and then choosing one of its neighbouring sites at random and trialling the update made by copying the 'spin' (value of σ) of the first site into the chosen neighbouring location. A number of trials equal to the number of sites in the simulation is performed for each MCS, though it should be noted here that trials which do not update the system at all are indeed possible, when a cell selects a neighbouring site also occupied by the same cell. In these cases, ΔH does not need to be calculated, saving a great deal of computational time, however these meaningless trials do still count to the total number of trials comprising a single MCS. When a trial does result in a change to the system, the effect on the Hamiltonian is calculated. Although the formulation technically works from the total free energy of the system, it is too computationally expensive to recalculate H with every trial, given that the effects on the system energy which result from any trial can only have a short range effect. A single expansion of cell can affect at most the areas and perimeters of two individual cells, and there might be a change in adhesion energy contributed by that site. Thus, these small differences are all that is calculated when a new trial update is considered, resulting in a direct calculation of ΔH to be used by algorithm (3.10) to accept or reject the update.

All calculations using J operate from the basis that both cells adhering together will feel the effects of the adhesive bond, and thus a single bond between two cells of types τ_1 and τ_2 contributes $2J(\tau_1, \tau_2)$ to the total value of H. Surfaces are detected using the Moore neighbourhood, and this does indeed mean that diagonal mismatches between cells do still count as an exposed boundary and contribute to the adhesive energy, in order to reduce lattice anisotropy. However, despite the use of the Moore neighbourhood in calculating adhesive connections, the perimeter is determined only be considering mismatches in the four cardinal directions, thus corresponding directly to the length of the line drawn around the boundaries of a given cell's occupied sites. These choices certainly retain some lattice anisotropy compared to the more advanced techniques discussed in Section 3.2.4, however the choice is made here for the sake of simplicity. The impacts on chemotactic cell migration of any remaining lattice anisotropy is explored in Section 4.3.2.

The MATLAB implementation works from a series of functions in separate files which call each other, the details of which are not covered here. However, those files which are most likely to be important for modification or customisation of the implementation are briefly listed. The file *runMainCode.m* controls the overall process of performing the MCS and determining the trial updates, and thus could be modified to use a different scheme for trial update selection, perhaps like cluster selection methods which attempt to update multiple sites at once to allow a more rapid location of minimal energy states. The actual trialling of updates according to algorithm (3.10) is controlled by *trialConsider.m* and so modifications to that equation should be represented there. The calculation of each ΔH is performed by the file *deltaHamiltonian.m*, and so this file should be modified if the form of H (3.11) is changed, though these changes must be represented in terms of ΔH directly, instead of fully calculating H before and after the trial update. The visualisation approach draws a series of figure objects corresponding to each occupied site and the boundaries between cells, as specified in *visualiseResults.m*. If additional cell types were included, their colours could be selected here, and additional features (like the scratch location markers seen in Chapters 6 and 7) can also be added to the produced figures by modifying this code.

Chapter 4

Chemotaxis in the Cellular Potts Model

4.1 Chemotaxis in the CPM framework

Chemotaxis and haptotaxis have been modelled in many implementations of the cellular Potts model through a small variety of approaches, and these various approaches have been used in CPM and GGH models to simulate a wide variety of biological applications. This chapter seeks to review and analyse these various approaches *as* approaches, and to explore their proper incorporation into a CPM/GGH framework. For this reason, a complete review of chemotaxis and other tactic behaviours in the CPM is not presented here, instead the focus is specifically on different implementations and their applicability. Previous work that *has* also focused specifically on chemotaxis as a model component (instead of simply including it in order to obtain a desired qualitative effect) is considered in detail.

The implementation of chemotaxis at the population scale using PDEs has already been discussed in Section 2.1.2. The behaviour is represented using a flux term of the form

$$\mathbf{J} = -\chi C \nabla S,$$

which corresponds to the cellular material (concentration C) being advected at a velocity

$$\mathbf{v} = \chi \nabla S. \tag{4.1}$$

In order for correspondence between the individual-cell-level and population-level models considered in this thesis, it is desirable that the cellular Potts model displays results also consistent with equation (4.1). That is, the velocity should depend linearly on both the chemotactic strength and the slope of the concentration field of the signalling substance. The various approaches that have been used to model chemotaxis in the CPM or GGH (and a few possible modifications) considered in this chapter are judged largely on their ability to demonstrate this desirable linear trend, with the method best demonstrating the relation (4.1) then considered in a far greater level of detail.

Recalling that the cellular Potts model behaves according to the defined total free energy (the Hamiltonian H), the natural first thought for incorporating chemotaxis is to modify the definition of H with a term that introduces a chemotactic tendency. Indeed, this approach has been used with a Hamiltonian contribution of the form

$$H_{\text{chemo}} = -\sum_{i,j} \mu\Big(\tau\big(\sigma(i,j)\big)\Big) S(i,j), \tag{4.2}$$

for example by Zeng *et al.* [214] to model haptotactic attraction in chick limbs, or by Jiang *et al.* [88] to model chemotaxis in bud formation of *D. discoideum*. Those authors do not include the negative sign in (4.2), instead negating μ (reversing the effects of positive or negative μ as discussed below), however writing the chemotactic contribution this way allows for consistency of sign between the cell-level chemotactic strength, μ, and the population-level chemotactic strength, χ. In equation (4.2) the sum is taken over every lattice site (here all i and j, corresponding to a rectangular 2D lattice), S is the concentration of signalling substance at each lattice site and μ is a weighting factor often referred to as the chemical potential. If μ is positive, then the Hamiltonian is decreased when the concentration S is increased and thus cells prefer to be in regions with higher concentration (the signalling substance is an attractant). If μ is negative, the Hamiltonian increases in regions of higher concentration and the signalling substance is a repellent. Lastly, the quantity μ is type-dependent, allowing for different types of cells to respond differently to the signalling substance - most notably the medium will have no response ($\mu(\tau = 1) = 0$). There is nothing to prevent other dependencies from also being built into μ, such as a concentration dependence capturing the saturation of tactic response with increasing chemical concentration [63] or temporal effects like the refractory nature of *D. discoideum*'s response to cAMP [59].

The approach (4.2) is not without issues. If the concentration field S is modified by adding or subtracting a constant, its gradient ∇S (and hence the equation (4.1) predicted cell velocity) is unaffected and yet (4.2) certainly does change value. This lack of additive invariance is a serious issue because the strength of chemotaxis is not only dependent on the gradient of the concentration field but its value as well. If cells move up a gradient of chemical attractant, they will feel the effects of (4.2) more strongly, and thus the response will surely not be linear. By considering a cell stretching in the opposite direction to the chemotactic gradient, it is seen that the Hamiltonian free energy is still decreased (if μ is positive) because another lattice site is now included in the sum in (4.2). Thus, although stretching up the gradient of attractant is most preferable for cells, they still prefer stretching down the gradient to not stretching at all, resulting in a general trend of growth in cell size. This growth continues until the quadratic nature of the volume constraint eventually balances this effect, causing the typical cell size to become considerably dependent on μ. The opposite case where the chemical signal is a repellent will cause cells to shrink in order to minimise the number of sites they occupy (because each occupied site results in more detected repellent). Thus although chemotaxis using equation (4.2) has been used in various CPM implementations, and has even been argued as being equivalent in one spatial dimension to the Keller-Segel equations in the macroscopic limit [4], the approach has serious issues which appear to invalidate its use. The performance of this chemotaxis approach is tested directly in Section 4.3.1.

Another approach suggested by Glazier and Uphadyaya is to use only the exposed parts of each cell as chemotactic sensors, perhaps better matching biological observations that cells detect gradient only at their edges [65]. The referenced work specifies this contribution to the Hamiltonian only as an integral around the cell boundary for each cell, though one possible interpretation within the framework being discussed here would have such a term would take the form

$$H_{\text{chemo}} = -\sum_{i,j} \sum_{i',j' \in N(i,j)} \mu\Big(\tau\big(\sigma(i,j)\big)\Big) \frac{S(i,j) + S(i',j')}{2} \left(1 - \delta_{\sigma(i,j),\sigma(i',j')}\right). \tag{4.3}$$

That is, at each site the cell borders are located (using the Kronecker delta, just like was done for adhesion in equation (3.4) and each cell border contributes chemotactically to the total Hamiltonian in a fashion similar to (4.2). Here an averaging of concentration over the two neighbouring sites has been used (representing a linear interpolation for the concentration at the boundary itself), though generally sites should be small enough and chemical concentration fields smooth enough that simply considering only the "interior" concentration would make little difference.

Of course, the form (4.3) suffers from similar problems to those with terms of the form (4.2). Just as an addition over sites caused cells to want to occupy more sites, an addition over edges will cause cells to want more edges and thus deform to occupy a larger surface area (perimeter in 2D). This is equally undesirable and may lead to individual cells breaking into pieces simply to increase their surface area, certainly an unphysical behaviour. Equation (4.3) suffers from the same lack of invariance under addition in S, its contributions to H increasing in magnitude as S increases, even when the gradient remains unchanged. Thus this approach (also tested in Section 4.3.1) is expected to at least fail to predict the desired linear trend (4.1). The approach (4.3) has not been used in an actual CPM simulation to the best of the author's knowledge, however it remains an interesting case because it does capture the biological fact that cells interact with a chemical gradient via their membrane, that is, at their edges, and has been suggested as a potential form to use. Indeed the review work of Glazier *et al.* [63] also comes to the conclusion that a boundary-sensing effect is phenomenologically appropriate but then presents the ΔH-based scheme discussed below as the accepted alternative.

Having worked through the serious issues with these two possible chemotaxis schemes (4.2) and (4.3) and briefly considered a few potential modifications (not shown here because they were soon determined ineffective in one way or another), the entire idea of simply adding a term to H which produces chemotactic movement seems somewhat futile. The majority of the literature does agree with this view, using the alternate approach which is described below. However, to the author's knowledge the arguments presented here which actually refute these approaches have not been presented, nor verified via simulation as is done in Section 4.3.1. Given that approach (4.2) still sees occasional use and approach (4.3) has been touted as a potentially more realistic approach, the demonstration of the failings of these methods is still considered important.

With no contribution to the Hamiltonian seeming to be appropriate for modelling chemotaxis, and yet all cell behaviours defined in the CPM via the Hamiltonian, there needs to be a change in thinking. As it turns out, what is necessary is not so much a change, as a return to the original basis of the cellular Potts model and its connections with statistical physics. Using the fact that the negative gradient of a potential field is the force, or a loose application of Hamiltonian mechanics, it can be argued that in a similar manner the forces experienced by cells relate to the negative gradient of the Hamiltonian energy utilised by the CPM [118]. Furthermore, given that a regular grid spacing has been used in the implementation here, the gradient can essentially be thought of as simply $-\Delta H$ within a constant. Determining the forces associated with the direct Hamiltonian contributions like (4.2) and (4.3) is not easy, because ΔH cannot be simply determined from H. However, forces can be incorporated instead by directly modifying ΔH, and that is the key for this next representation of chemotaxis. Adjusting ΔH does impact on the CPM in that it no longer behaves simply according to minimising some pre-defined H, but because it is always the value of ΔH that is checked by the CPM when trialling any cell protrusions or retractions via equation (3.3), the overall approach of punishing or rewarding cell behaviours according to the change in energy associated with each trial update is indeed retained. This also means that including a modification to ΔH into the computer implementation discussed in Section 3.2.5 is quite trivial.

A ΔH contribution to model chemotaxis was first utilised by Savill and Hogeweg, and by Maree and Hogeweg, in their respective modelling of *D. discoideum* behaviour [166, 119]. This took the rather natural form,

$$\Delta H = \Delta H_{\text{trad}} - \mu(S_{\text{neigh}} - S_{\text{site}}). \tag{4.4}$$

Here, ΔH_{trad} refers to the 'traditional' ΔH calculated by comparing H before and after the trial change is made without including chemotactic effect, using an equation like (3.11). S_{neigh} and S_{site} refer to the concentrations of chemical at the site being expanded into and the site being expanded from, respectively. Thus, it is easily seen that (4.4) decreases ΔH if a cell's expansion is occurring up a gradient, and increases ΔH if a cell's expansion is down a gradient (so long as μ is positive, meaning the signalling substance is an attractant). Thus expansions up a gradient of attractant (or down a gradient of repellent) are more likely to be accepted when checked by equation (3.10), as desired. Again, μ is dependent on cell type and could easily incorporate other dependencies in the same manner as the previously discussed approaches.

It is worth considering how cell recessions (expansion from sites occupied by medium) should be handled when operating with a chemotactic approach like (4.4). While it was previously mentioned that sites occupied by medium do not contribute to chemotactic calculations, this is not necessarily true when using a Hamiltonian along with (4.4). When considering ΔH, μ remains the chemotactic strength and associated with cell types, but it behaves somewhat differently. Even if the current chosen site is occupied by medium (and hence the μ used would be that for medium), an expansion from this site into a cell-occupied site represents a retraction of cell, which due to its constrained volume also promotes the cell's movement. It is retractions *up* a gradient that push a cell's centre of mass in the correct direction, so there is actually an argument for medium using the chemotactic coefficient of the cell it is encroaching on to.

Savill and Hogeweg's representation of chemotaxis (4.4) is now somewhat accepted as standard [63], and this is one of the major contributions of Paulien Hogeweg that surely contributed to her appearing in the name of the extended CPM model, the GGH (Graner-Glazier-Hogeweg) model. In addition to avoiding the issues with the other chemotaxis schemes discussed here, the aforementioned arguments tying physical force to the cellular Potts model have been used to argue that chemotaxis using (4.4) matches typical population-level chemotaxis in the sense that cell velocity is directly proportional to the gradient [118]. Using the relation $F \propto -\Delta H$,

$$F_{\text{chemo}} \propto \mathbf{v} = \mu(S_{\text{neigh}} - S_{\text{site}}) \ \propto \ \nabla S. \tag{4.5}$$

This makes use of the fact that cells and the CPM tend to operate under the Aristotelian regime [118] where force is proportional to velocity, and so it is seen that cell velocities are directly proportional to the signal gradient and the 'strength' parameter μ. This matches the desired relation (4.1) and because the two are interchangeable this equation (4.5) will now be referred to when discussing the linear trend between chemotactic effect and velocity. Of course, this is not the only force experienced by cells in a CPM simulation, given the other also-varying terms that make up H. It cannot be assumed that the chemotactic 'force' can be separately considered, as all behaviours in the CPM operate via acceptance or rejection of trialled updates and thus even effects like constrained volume can induce or hinder movement-like behaviours. This is in contrast to PDE formulations of cell behaviour where various behaviours all contribute to the time derivative but can generally be interpreted separately. That the CPM using chemotaxis scheme (4.4) does behave according to relation (4.5) has been verified via simulation by Maree *et al.* [118] but there were no parameter values provided and it seems that other extensions comprising the GGH model (as opposed to the standard CPM) were not included. This result only holds "within a realistic range of parameters". A far more in-depth exploration of how well this type of chemotaxis adheres to relation (4.5) under the full GGH framework is undertaken in the following sections.

Other work which does somewhat focus on chemotaxis as a behaviour, and not merely as a tool for modelling some specific application exists in the literature. The original, concentration-sensing chemotaxis (4.2) was examined by Zeng *et al.* and shown to be a predictor of cell aggregations into spots or stripes, despite the lack of a Turing-like mechanism [214], and Merks [130] demonstrated the very interesting result that simply contact-inhibiting chemotactic response can lead to self-reinforcing instabilities that can grow into web-like structures. This is a very different result to the aggregation behaviour typically demonstrated by cells moving chemotactically toward an attractant they themselves produce. Käfer *et al.* explored how the interaction between chemotaxis and differential adhesion effects could actually cause clusters of one type of cell to be pushed *down* the gradient despite both cell types responding equally to the signal [91]. Depending on the balance of adhesive energies, the direction of this push can potentially differ for clusters or individual cells of the second cell type. This effect is a pressure-driven effect that occurs only when cells have a limited amount of space to invade, that is they are being pushed by chemotaxis up against a solid boundary. Nevertheless, it highlights some of the complexities of CPM/GGH model chemotaxis that are not initially obvious.

It is worth noting that none of these discussed chemotaxis approaches seek to properly model the exact mechanisms of chemotaxis in a migrating cell, their focus simply on producing a chemotactic velocity preferably obeying the relation (4.5). The methods involving direct contribution to the Hamiltonian do not easily lend themselves to biological interpretation, but the ΔH contribution method (4.4) now in widespread use can be physically interpreted to a certain extent. With each ΔH being generated by a specific extension or retraction of a cell, this approach resembles “scheme B” described by Devreotes and Zigmond [42] where cell detection of gradients occurs specifically via/during extension of lamellipodia/pseudopodia. It is pointed out in that work that the locality of such a scheme prevents it from properly predicting rapid changes in orientation of entire cells that can be observed in situations where sharp and/or strongly temporally varying gradients are involved. This suggests that incorporation of specificities of chemotaxis into the CPM framework to be beneficial, especially when the chemotactic response can rapidly vary in direction or strength. A key example is *D. discoideum* aggregation via sharp pulses of cAMP. Without proper consideration of polarisation and/or directional persistence the movement of cells within these sharp, symmetrical waves of attractant can actually induce a net movement *away* from the source [78]. The previous representations of *D. discoideum* aggregation simulated using the GGH framework have used phosphodiesterase degradation [121, 119] or simply a spatially decaying signal ($1/r$ dependence) [166] to break the symmetry of waves and avoid this issue. These solutions are certainly reasonable (a single cAMP pulse emitted by one cell must decay as it expands, and phosphodiesterase degradation has been shown to be a critical part of the aggregation process [211]), but the unexpected result of pulsed waves potentially causing *dis*-aggregation still highlights the potential importance of implementing the peculiarities of chemotaxis. The original solution to this ‘chemotactic wave paradox’ presented by Hofer *et al.* [78] for PDE models has not seen an equivalent CPM implementation to the author’s knowledge.

Extensions to the chemotactic effect beyond equation (4.4) with a potentially non-constant μ are not common. Maree *et al.* presented a model which featured polarisation of cells [120], using a complicated approach coupling the CPM to differential equations directly modelling actin and G-protein dynamics. Not only is cell polarisation an important facet of chemotactic migration and more naturally representable in individual-cell-based models like this, it is also an interesting extension to the GGH model because it allows for the introduction of active cell movement even in the absence of a chemical gradient. By comparing the direction of trialled cell expansions to the current direction of a cell’s polarisation vector using a ΔH adjustment like equation (4.4), a cell will be biased to move in the direction of its polarisation. The direction of the polarisation vector could then be informed by the concentration and/or gradient of a chemical signal(s), but could also simply be chosen randomly with some degree of directional persistence in order to recreate the random motility that cells do exhibit. This is an extension not implemented in this thesis, but the importance of which becomes even clearer in Chapter 6.

The inclusion of multiple chemical signals is easily represented simply by using multiple terms of the chosen chemotaxis implementation, presumably equation (4.4). Each of these would use its own cell response strength μ_i and stimulus concentration function S_i. Another simple extension which has been presented but not widely used in the literature is the effects of receptor saturation [118]. This was suggested as achievable in the same fashion as is done for PDE models with χ like in equation (2.8), simply modifying μ by an appropriate multiplicative factor. This is indeed the approach used here for the GGH model in Chapters 6 and 7, for consistency with the population-level chemotaxis term used in that work.

In the simulations used in this chapter to examine chemotaxis as a core behaviour, none of these “chemotactic specificities” have been incorporated into the GGH model. This is to avoid overcomplicating the issue, with the focus of this chapter being to test basic chemotaxis using equation (4.4) to ensure it satisfies desirable properties so it can be used in the GGH model simulations of the scratch assay in Chapters 6 and 7. The effects of varying parameter values on the chemotactic response are then considered to inform parameter choices in those scratch assay models also.

4.2 Implementation and Simulation Details

In order to properly examine and compare how each of the three methods represents chemotactic behaviour in the cellular Potts model, several simple simulations were constructed and then run multiple times and for various parameter values. This is in stark contrast with the majority of CPM simulations utilising chemotaxis - those which seek to model a certain experiment or biological process feature much more complex interplay of cell positions and behaviours, as well as often nontrivial and dynamic concentrations of signalling substance. The specific behaviour of the cells’ response to gradient is somewhat masked by the complexity of the simulations in question, and so chemotaxis has simultaneously been included in a wide variety of CPM or GGH simulations whilst remaining arguably untested at a core level. Indeed, as will be demonstrated here, even in the absence of any kind of cell sorting or external behaviours (excepting chemotaxis), simulations vary wildly and in many different ways depending on parameter values.

All simulations were carried out using the standard GGH Hamiltonian, (3.11), combined with chemotaxis included via the standard ΔH adjustment (4.4) except as mentioned in Section 4.3.1 where the different methods of including chemotaxis are considered. The standard update scheme, trialling expansions or contractions of a random cell into one of its neighbouring sites and accepting or rejecting according to the Metropolis algorithm with dissipation energy (3.10)

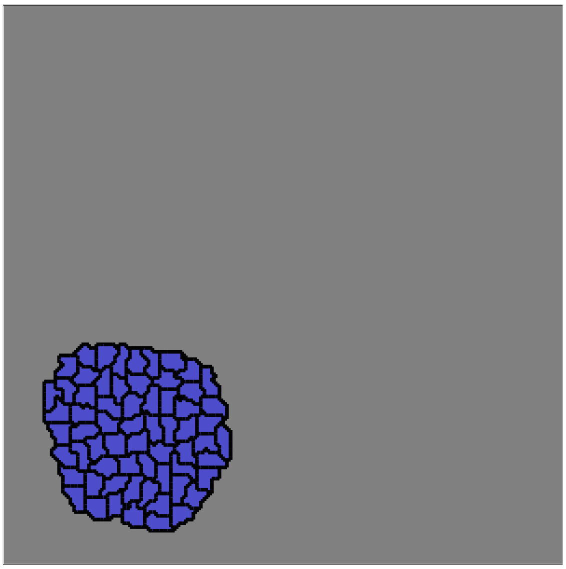

Figure 4.1: The base initial condition used in the simulations in this chapter. A cluster of 64 cells starts in the bottom left of the domain, and responds to a permanent gradient pointing towards the upper right.

was used to evolve simulations through time. This time is measured in MCS (Monte Carlo Steps), with each MCS being made up of a number of random trials equal to the number of sites in the system. The following simulations were all run on square grids, with a standard size of 150×150 sites, however more sites were used as necessary and less sites where possible to improve computational performance. All sites in this grid were given effective side lengths of 1 for simplicity, a valid choice here where there is no physical length scale to be used.

Given the difficulty of creating a realistic initial condition, instead the system was initialised as a cluster of 64 square-shaped cells (forming a larger square) that is allowed to evolve into a round cluster through adhesion-driven surface tension effects. Once a certain time had passed (here 500 MCS), the chemotactic gradient was 'switched on', and the now more realistically-shaped cluster could respond to the signalling substance. This way the unrealistic nature of the rather artificial initial condition chosen here could not affect the nature of the chemotactic response. An example of the initial condition after this 500 MCS 'settling period' is shown in Figure 4.1.

Velocities were measured by tracking the centre of mass of clusters, and determining how this varied between each Monte Carlo step. Where velocities are quoted in this section considering chemotaxis, what is actually being measured is the average velocity over a large period of time, taking the difference in positions of the centre of mass between the end of a simulation and some reference point. This displacement vector is then projected into the direction of chemotaxis, so that random movement in other directions does not contribute to the measured velocity. The use of a long-term displacement vector to calculate velocity means that the observed speeds essentially represent an *effective* chemotactic velocity, because motion back down the gradient will reduce the calculated speed, no matter how fast the movements of individual cells might be. Given that the primary goal is to test equivalence with the macroscopic chemotactic velocity (4.1), this measure of effective velocity is thought to be highly appropriate. However, in cases where random motion of clusters is significant and causes them to move a great deal, large values of velocity might be recorded despite this motion not necessarily being chemotactic. This is only an issue for very high temperatures which cause increased diffusion, and so does not play a part except when the effects of high temperatures are being considered.

The parameter values used for the following simulations are for the most part drawn from the two sets defined in Table 4.1, except where otherwise explained. The first set described is actually a rather arbitrary and simplistic choice of parameters, albeit a set suitable for the GGH model (that is, featuring a constrained surface area and negative surface adhesions between cells). Given that simulations run here are being used as explorations of the GGH model and not as a representation of any specific physical situation, this arbitrariness is somewhat forgivable. The second set in Table 4.1 are parameters taken from the work of Ouchi *et al.* demonstrating the increased realism of the GGH's constrained surface areas and of a nonzero bond dissipation energy [142]. This second set of parameters is not necessarily more physically realistic for a given biological situation, however it has been sourced from published work specifically considering the GGH. It was found (especially without reducing lattice anisotropy by taking many more neighbours) that this model produced cells that were rather immobile, and hence not so suited to chemotactic movement. This is why the strengths of cell-cell and cell-medium adhesion were lowered here compared to that work, to allow for increased migration of cell clusters. In the second set of parameters, a higher value for the temperature, $T = 20$ was chosen. This increased value of temperature is chosen because when using these parameters the values of each ΔH are larger and the value interpreted by the Metropolis algorithm (3.10) is $\Delta H/T$. Particularly worthy of note in Table 4.1 is the choice $H_{\text{bond}} = 0$, though brief testing not presented here did show that the discarded methods in Section 4.3.1 demonstrated the same failings for nonzero H_{bond}, and for the accepted method the effect of adjusting H_{bond} is explored in Section 4.3.5.

The apparent failings of the H-based (as opposed to ΔH-based) approaches to chemotaxis were already detailed in Section 4.1, with the simulations run here intended to demonstrate that these issues do indeed manifest themselves in practical usage (and examine how readily they manifest). This is best achieved by using moderately high values for chemotactic response μ, so that the effects of the chemical gradient are not masked by the core behaviour of the GGH model. However, smaller values of μ were also considered, and this quickly highlighted the failure of equation (4.2). The problem uses a simple, linearly-increasing chemical gradient in

Parameter	Value - Set 1	Value - Set 2
J_{cm}	3	5
J_{cc}	-2	-5
λ_1	2	10
V	25	64
λ_2	2	5.5
A	21	34
T	10	20
H_{bond}	0	0

Table 4.1: Parameters used for chemotaxis test cases in the GGH model

one direction, diagonally up and to the right,

$$S(x, y) = 0.05(x + y). \tag{4.6}$$

This concentration field has been chosen to isolate the chemotactic response as a behaviour, avoiding the additional complications of a change in gradient direction or dynamic chemical concentration. The diagonal direction has been chosen to involve both spatial dimensions, however the effects of a one-dimensional gradient on the successful chemotaxis implementation are explored in Section 4.3.2.

4.3 Simulations and Analysis

4.3.1 Comparison of Chemotaxis Methods

As discussed before, out of the three main chemotactic modelling approaches that have been used or discussed, Hogeweg's ΔH adjustment, equation (4.4) is now favoured and is argued to properly result in a force with linear dependence on chemotactic strength, corresponding to the dissipative conditions within which cells operate. First presented here is evidence via simulation of the failings of the approaches which use a direct modification to H, equations (4.2) and (4.3). Then preliminary tests of the ΔH-based chemotaxis (4.4) are performed.

The predicted failings of equation (4.2) were soon seen when a high value of chemotactic response $\mu = 50$ was used in the GGH model implementation. The cells did initially expand up the gradient when the chemotaxis is switched on, but then after this initial swelling there was no further movement up the gradient at all. This was not an expected behaviour, but can be easily explained. Once the cells have expanded up the gradient as far as their constrained volume will allow, the only way the cell cluster can move is if its back end moves, and as the chemotactic coefficient becomes larger the energy cost of removing occupied sites from the back end of the cluster becomes more prohibitive. Indeed, when the chemotaxis coefficient was lowered to a value of $\mu = 5$ the cluster in fact displayed a faster rate of movement. This effect is displayed in Figure 4.2, which shows the structure and position of two cell clusters after the same amount of time, one with a weak chemotactic response and the other a strong chemotactic response. Clearly the problem of cells swelling beyond their normal size is not the only issue with chemotaxis implemented using the method (4.2), because a positive linear response of cluster velocity to the level of chemotactic response has clearly not been demonstrated - indeed the response is not increasing at all. Simulating with the second set of parameters from Table 4.1 demonstrated the same trends observed here. The results here are clearly in stark contrast with biological and mathematical expectation, demonstrating the failure of the direct sensing method (4.2) despite its argued equivalence with the Keller-Segel equations [4]. Clearly the assumptions used there are too optimistic to remain applicable to actual cells being simulated by the CPM/GGH model.

When the chemotactic sensing of cells is instead restricted to their surfaces, as specified by equation (4.3), similar problems are expected to occur. However, whereas previously cells would try to maximise their volumes in order to “detect” more chemical and hence minimise energy, when only the edges contribute cells will now try to maximise their surface areas. This is still undesirable, and even simulations using a low value of μ demonstrated the hypothesised issues with this approach to chemotaxis. At first the cluster moved up the gradient as expected, but because the Hamiltonian contribution (4.3) directly operates from the value of S as the cluster moves up the gradient the chemical effect becomes stronger and cell shapes become unrealistic as they deform to increase their boundary length. This is demonstrated visually in Figure 4.3, which uses a constant value of $\mu = 5$ but at two different points in time. When the value of μ is increased, the severity of this effect is also increased, although the overall cluster velocity up the gradient does indeed get faster. Thus if the issue of cells taking unrealistic shapes by wildly increasing their boundaries could be addressed, this method might in fact be a reasonable choice. For this reason, the same simulations were trialled again using stiffer cell membranes by choosing $\lambda_2 = 10$, and it was found that this greatly reduced the flexibility of cells but when a sufficiently high value of μ was used to attract cells up the gradient to larger concentrations, unphysical cell shapes did again develop. Moreover, it was found that the velocity displayed by a cluster as it migrated up the gradient did not remain constant, and a brief exploration of the trend between the value of μ and the cluster velocity also demonstrated a nonlinear relationship. Thus although the chemotaxis scheme (4.3) has demonstrated better performance than the previous scheme (4.2), this is still not an appropriate means of including chemotaxis into a CPM or GGH model, due to the lack of a predictable, linear response and the very real possibility that any significant amount of chemotactic effect can result in the creation of unphysical cell shapes.

It is worth noting that all simulations detailed here were performed using positive values of μ, corresponding to a signalling substance that acts as an attractant. Given that both methods have been demonstrated to have serious flaws, simulations with negative values of μ are not presented to the same level of detail because the direct sensing methods (4.2) and (4.3) have already been shown as highly unsuitable for modelling attractants. However, brief simulations did confirm that using a negative value of μ to simulate a repellent chemical indeed introduced

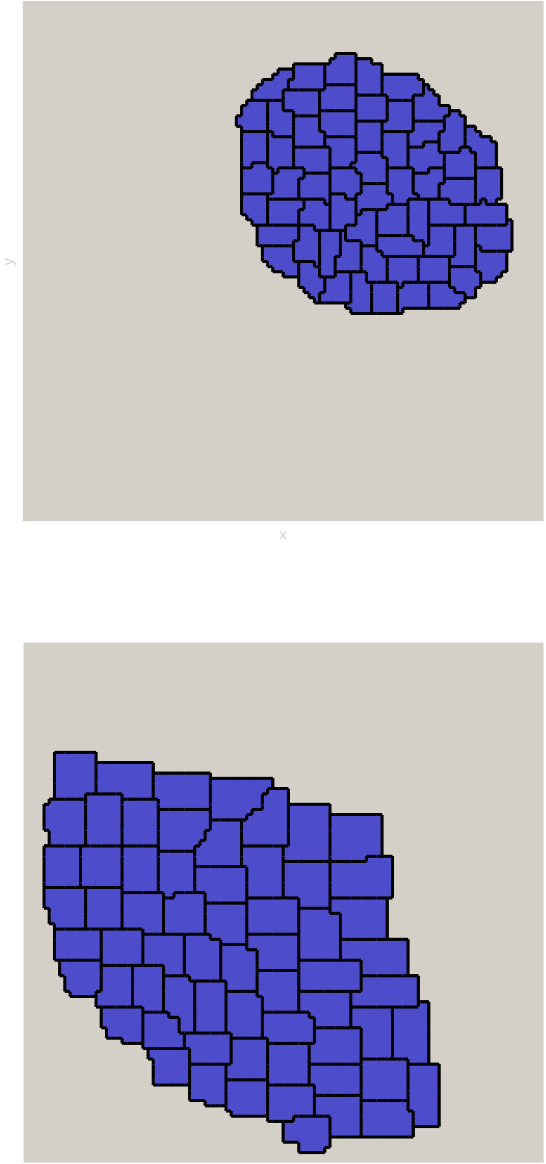

Figure 4.2: Example simulation of chemotaxis using equation (4.2) and a low value ($\mu = 5$, top figure) and a high value ($\mu = 50$, bottom figure) of chemotactic response. Simulations are run on a 100×100 grid (full region shown in grey) with cells exposed to chemotaxis for 7500 MCS and parameters are the first set in Table 4.1. The decrease in velocity for a larger value of μ, against mathematical and biological sense is clearly seen.

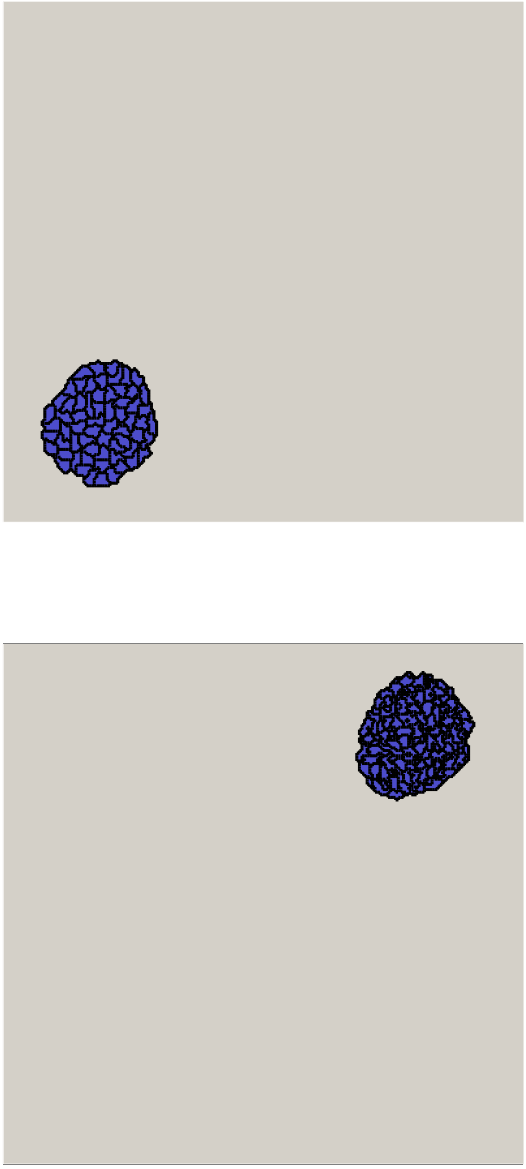

Figure 4.3: Example simulation of chemotaxis using equation (4.3) and a low value of chemotaxis ($\mu = 5$) and visualised after 750 and 7500 MCS of chemotaxis respectively. Simulations are run on a 200×200 grid and parameters are the first set in Table 4.1. The loss of realistic cell shapes as S increases is clearly demonstrated.

the opposite undesirable behaviours to the ones demonstrated above. That is, cells exposed to a repellent with equation (4.2) chemotaxis reduced their size, and if the chemical response was strong enough cells disappeared completely. A sufficiently strong repellent with equation (4.3) chemotaxis caused cells to try to minimise the lengths of their boundaries, and upon quickly finding a shape that achieved this all cells stopped membrane fluctuation altogether (and thus cluster movement stopped as well). These schemes which make direct contributions to H in order to attempt to model chemotaxis are clearly inappropriate, as expected.

As reviewed previously, the better accepted implementation of chemotaxis in the CPM or GGH model directly adjusts the values of ΔH calculated for each trial update directly, instead of adjusting H itself. Using this approach makes meaningful tracking of H over time very difficult but ΔH adjustments allow the *direction* of each update to be compared to the gradient, which is essential. The briefly discussed idea of considering cell polarisations would also be implemented in this way, except in that case it would be a comparison between polarisation vector and expansion direction that informed the ΔH contribution. The general success of this accepted method for CPM chemotaxis, (4.4), was reaffirmed here briefly before its properties were examined more thoroughly in the following sections.

Using the first set of parameters in Table 4.1, the desirable behaviours of this ΔH-driven chemotaxis were readily observable. Even when μ was increased to a value of 1000, the cells still remained as a cluster and moved (quickly) up the gradient. When μ was further increased to 10,000, some breaking up of the cluster was observed, but cells themselves retained realistic shapes and moved rapidly up the gradient. Reasonable negative values for μ were also tested, with a regular movement down the gradient of repellent confirmed. Without any sort of modification, equation (4.4) appears to provide suitable results for both problems in which chemotaxis is a dominant behaviour and those where it is not, for both attracting and repelling signals. Additionally, a preliminary varying of the chemotactic response μ did indeed appear to demonstrate a linear relationship between chemotactic effect and chemotactic velocity, at least for smaller values of μ, which is consistent with the result published for the basic CPM [118]. However, there should be a much deeper look into the workings of GGH model chemotaxis using ΔH-based approaches, because as previously discussed despite their widespread use in modern CPM/GGH implementations they still have not been fully explored as a behaviour themselves, at least in the author's opinion. Thus, the impacts of many factors on the chemotactic effects simulated by approach (4.4), and whether it truly predicts a linear response, are considered in the following sections, in order to properly test this ubiquitous approach and determine both how it is best implemented and how it might be improved. An example simulation of a cluster operating under equation (4.4) with strong chemotaxis is visualised in Figure 4.4.

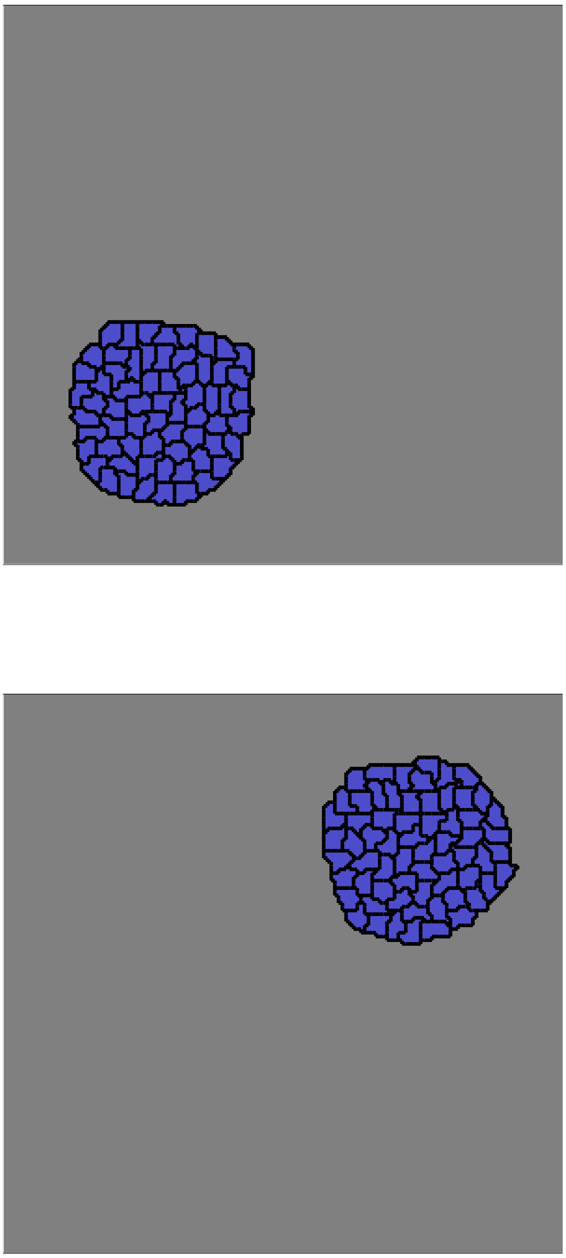

Figure 4.4: Example simulation of chemotaxis using equation (4.4), using a high value of chemotaxis ($\mu = 40$) and visualised after 750 and 7500 MCS of chemotaxis respectively. Simulations are run on a 200×200 grid and parameters are the first set in Table 4.1. Movement of the cluster up the gradient whilst individual cells maintain realistic shapes is observed.

4.3.2 Lattice Anisotropy

The first important thing to consider was the effect of the lattice itself. Given that most CPM simulations are run on a square lattice (including those used in this thesis), the effects of lattice anisotropy as described in Section 3.2.4 could also have an impact on the chemotactic behaviours examined here. In order to determine if there was any direct impact of lattice anisotropy on chemical-directed movement, simulations run using gradients which promoted tactic movement in one and two spatial dimensions were compared. These two chemical fields were

$$S(x,y) = \begin{cases} 0.05(x+y) & \text{2D movement - `diagonal'} \\ 0.05y & \text{1D movement - `vertical'} \end{cases},$$

with comparison of ∇S suggesting that the velocity of cells should be $\sqrt{2}$ times larger in the diagonal case compared to the vertical case, at least if only chemotaxis is considered. Both parameter sets from Table 4.1 were investigated to see if this result was indeed obtained, with a failure to demonstrate this result suggested here as the impact of lattice anisotropy.

The results discovered here were actually rather complex. For moderate values of chemotaxis $\mu = 20 - 40$, the ratio was observed to be $\sqrt{2}$ just as expected. However, for larger values of chemotaxis (e.g. $\mu \sim 150$), the ratio became lower than this value, suggesting that straight moving clusters moved faster than diagonally moving clusters. Thus lattice anisotropy is indeed an issue which can be observed in GGH model simulations of chemotaxis, but only when the chemical response is rather extreme. For small values of μ the effects of chemotaxis are harder to distinguish from random migration and the effects of surface tension. In those cases the value of the velocity ratio was larger than $\sqrt{2}$. However, when a value of $H_{\text{bond}} = 10$ was trialled to reduce random migration, the velocities did demonstrate a ratio of $\sqrt{2}$.

To ensure that the effects of surface tension (known to be affected by lattice anisotropy) were not the cause of the lattice anisotropy seen above for large μ values, surface tension was switched off by setting all J values to zero and simulations re-run. Although the anisotropy was indeed reduced in this case, unfortunately ratio remained lower than $\sqrt{2}$ when μ values were very large. This trend was also found to persist when various changes to parameters were considered, including changes to membrane elasticity and adhesion strengths, including the use of the second parameter set outlined in Table 4.1.

Given the variation in the velocity ratio between diagonally- and vertically-moving clusters for different μ values, it is hard to make a simple conclusion about how exactly chemotaxis in the GGH model is affected by lattice anisotropy. For moderate values of μ it has been seen to be not a major concern, but the large-μ case which should theoretically overpower the effects of the lattice on surface tension has demonstrated that lattice anisotropy as a limitation of the framework which should be considered. Surface tension can be eliminated from adhesion calculations by choosing additional neighbours [142], however the suggestion here is that chemotactic response of cells is impacted by the lattice independent of how the lattice also affects this surface tension. Presumably the choice of a hexagonal lattice [188] would significantly rectify this [63].

4.3.3 Temperature

The impact of temperature on chemotactic migration is not easy to predict and was indeed found to be rather complex in simulations here. The key issue is the existence of critical temperatures which disrupt the ability of cells in the CPM to behave appropriately and hence can have a significant impact on their response to chemical gradients. If the temperature is too low, movement is restricted by a lack of accepted trial updates, and if the gradient or the cell response to it is not sufficiently strong cell clusters can become stuck. On the other hand, if the temperature is too high, cells will not retain their shapes and while a movement up the gradient can be seen, the erratic updates can cause the amount of cluster surface 'exposed' to the gradient to vary more significantly and in some cases individual cells or small clusters can break off from the original cluster. With a higher temperature meaning more trial updates are accepted by the Metropolis algorithm (cell membranes are more active in general), extensions *down* the attractant gradient become more likely, despite the energistic penalty (4.4). This suggests that although a low temperature will lead to no or greatly reduced migration due to cells being inflexible and easily stuck, a higher temperature will also reduce migration speeds. In the most extreme case of very high T, all trialled updates are accepted, and no actual cell behaviours specified by the Hamiltonian (and ΔH in the case of chemotaxis) are observable at all. Instead, all cell movements and shape changes are entirely random. The critical temperatures referred to here of course depend on how flexible and adhesive the cells are, but how differing amounts of chemotaxis might impact on these critical temperatures is hard to predict.

In order to confirm or deny these hypotheses, simulations as described in Section 4.2 were performed with a variance in temperature used to determine how this affected cell behaviours. As before, conclusions were drawn by considering both how the clusters behaved in terms of shape (including whether or not the initial cluster broke apart) and the velocity measured by tracking the cluster's centre of mass. Temperatures used varied between the two parameter sets used (see Table 4.1), because the critical temperatures are different between parameter sets. Critical temperatures were approximately determined by repeated trialling for a small selection of chemotactic strengths, in order to explore how critical temperatures were affected by strong or weak chemotaxis. In all cases, cluster velocities over the range of 'acceptable' temperatures (those satisfying all critical temperatures) were also calculated. The intention was to determine how temperature might best be selected in GGH simulations involving chemotaxis, including those modelling the scratch assay presented in Chapters 6 and 7.

Using the first parameter set, initially the situation of no chemotactic response ($\mu = 0$) was considered. This provided determination of the 'typical' critical temperatures, namely those valid in the absence of chemotactic effects and hence somewhat similar to those discussed in the original presentations of the cellular Potts model [64, 70]. It was found that when the temperature was below $T = 4$, cells were too inflexible to move much at all, and the cluster did not demonstrate rounding to any notable degree. For temperatures $T > 4$, clusters rounded and further increasing the temperature did not make very much difference until the next critical temperature was reached. This was found to be about $T = 13$, and as the temperature increased beyond this point the round shape of the cell cluster was gradually lost to an increasing degree as cells became more flexible in general and less constrained by the 'rules' encoded into minimising H. However, up until temperature values of about $T = 70$ clusters tended to remain adhesively connected, with a single cell or small group occasionally breaking off but retaining shape and size. Beyond this value, small pieces of individual cells would separate from the cluster, which has no physical interpretation. Further increases in temperature lead to the possibility of cells disappearing entirely, due to the fact that despite this being highly unfavoured energistically, smaller cells have fewer sites to regrow from and a cell occupying no sites can never reappear due to the nature of trial updates. Before considering how chemotaxis affects these critical temperatures, it is worth noting that $T = 13$ is not strictly a critical temperature. While the simulations using a temperature value lower than this (and greater than or equal to $T = 4$) were the most orderly, cells with more active membranes and erratic movements could be modelled by temperatures between $T = 13$ and the true upper limit for biological realism, $T = 70$. Of course, the further the temperature is increased towards that upper limit, the more small, undesirable issues like cells not always being simply connected are exacerbated.

When a moderate amount of chemotaxis was introduced by setting $\mu = 10$, it was actually seen that the behaviour at lower temperatures was almost entirely unchanged. For temperatures lower than 4, cell membranes were too inflexible to allow rounding and this inflexibility also completely hampered any chemotactic movement. As the temperature was increased beyond this point, the cluster began to demonstrate both rounding and response to the chemical gradient. The next critical temperature is that which causes the cluster to lose its structured, round shape, and this was found to also be unaffected by the chemotactic movement, remaining at about $T = 13$. However, despite cluster shapes remaining rather consistent within this region of temperature, the chemotactic velocity was found to vary, and this effect is discussed below and shown in Figure 4.5. For temperatures above 13, the general behaviours of cluster shape still remained consistent. As temperature grew larger the cluster became less round and sometimes small pieces would break off. As the temperature was raised above the earlier found level of $T = 70$, a motion up the gradient could no longer really be observed, with clusters showing essentially random motion due to stretching updates in all directions generally being accepted.

Including a strong chemotactic force by increasing the cell response to $\mu = 40$ or even $\mu = 150$ there were still no major effects of chemotactic migration on general cell behaviours. Even with chemotaxis as a more dominant behaviour, the effects of the H-defined behaviours (and hence the critical temperatures also) remained unchanged to any observable extent. However, the random motion resulting from high temperatures was less able to mask the more pow-

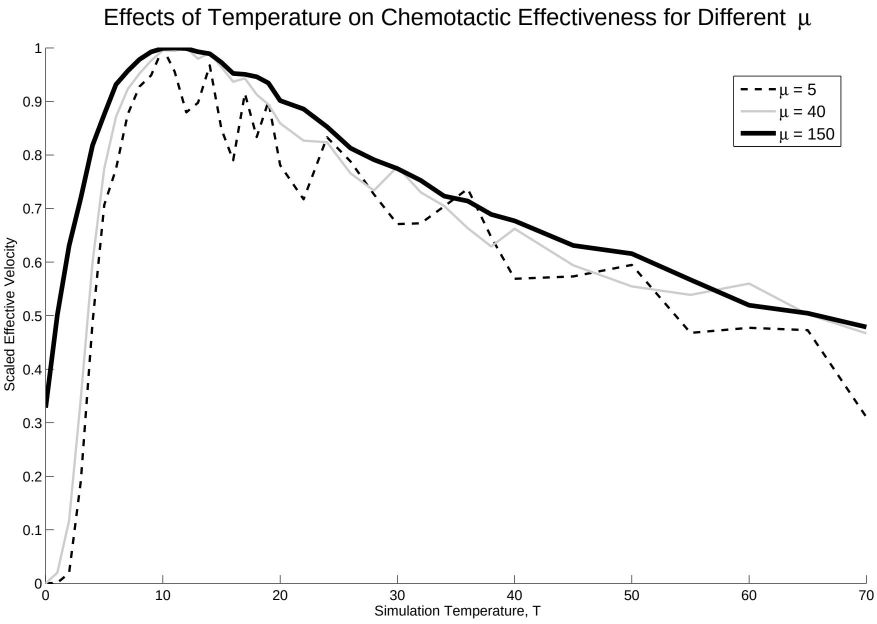

Figure 4.5: Impact of temperature T on chemotactic effectiveness for various values of μ. Velocities are scaled against the maximum velocity observed for each different μ value, allowing the results for different values of μ to be compared despite the overall differences in actual velocity.

erful chemotactic migration in these simulations, and so even for high temperatures slightly exceeding the recommended critical temperature of $T = 70$ a general trend of movement up the gradient remained observable, especially in the $\mu = 150$ case. This is hardly a surprising result, that the effects of random motion are less observable as directed motion increases in intensity, although it was not expected that the temperature dependence of general shapes and cell morphologies would be the same for fast-moving clusters and stationary clusters. It is clearly seen in Figure 4.5 that as μ is increased, the results profiles become smoother. This is simply because with a higher amount of chemotactic velocity, random fluctuations due to the stochastic nature of the GGH model become less significant. For this reason, results presented throughout this section typically use rather large values of μ, to make identifying trends easier, although smaller values of μ were also tested to ensure overall trends remained consistent.

One counterexample was discovered, however, in that rigid clusters for very low or zero temperatures subjected to a very strong chemotactic force would deform entirely in response to the gradient, forming shapes otherwise not seen. An example of this is shown in Figure 4.6, where a temperature of $T = 0.01$ and $\mu = 120$ generates a cluster with a very differently shaped front and back end. As the temperature is increased, shapes gradually return to the expected circular cluster, with clusters at a temperature as low as $T = 1$ showing roughly circular shapes as expected due to surface tension.

In all cases, as can be seen in Figure 4.5, the maximum velocities are obtained once the temperature is large enough to appropriately free membranes but not so large that random fluctuations

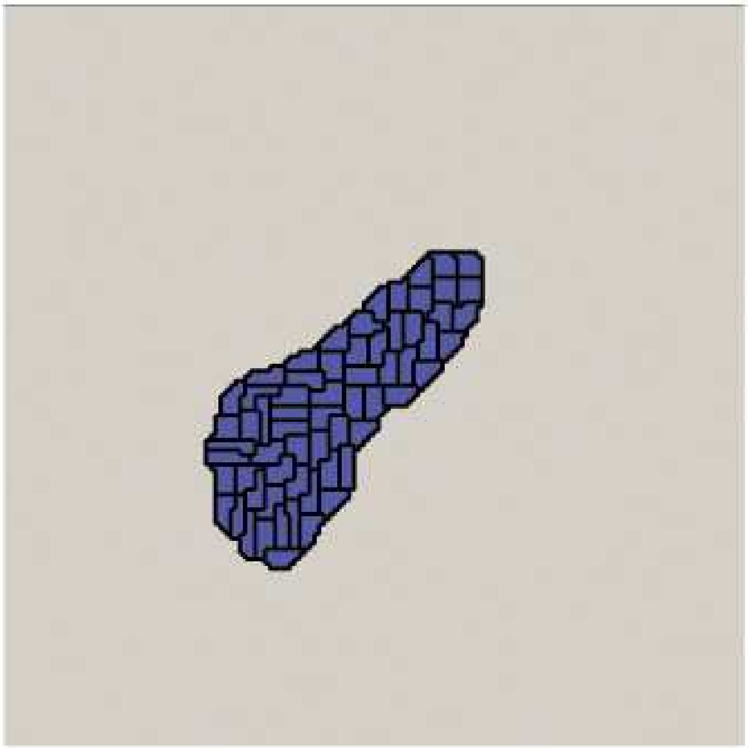

Figure 4.6: An example of cluster deformations observed when temperature is restrictively low (here $T = 0$) but chemotactic migration still feasible ($\mu = 120$).

hamper cell shaping and cluster migration in the expected direction up the gradient. It should be recalled that the velocities measured here refer to overall distance travelled in a simulation, an effective velocity up the gradient as opposed to an average instantaneous speed. That is, the speed in terms of frequency of movement might not actually be strictly slower in high-temperature cases, but the increased degree of random motion does hamper the chemotactic effect of guiding a cluster up a gradient of attractive signal and is hence recorded as a lower speed in Figure 4.5. It is clearly seen that the trend between velocity and simulation temperature is almost entirely unaffected by μ, with an increase of μ simply effecting a reduction of the stochastic noise. It should be recalled however that the results shown there are scaled according to the maximum velocity observed for each μ value, the figure demonstrating the similarity of *trend*, not a similarity between actual velocities. Below certain temperature values, conditions were too restrictive to allow for any chemotactic movement, though in the case of the very strong chemotaxis the 'stiffness' of the simulation can indeed be overcome, as demonstrated by the different y-intercept on the figure for the $\mu = 150$ line. The primary conclusion to be drawn here is that chemotactic effectiveness is actually maximised in the case where cells behave most realistically, below the critical temperature where cluster rounding starts to be lost. This conclusion holds over different μ values, but was also tested using a different set of parameters (set two from Table 4.1).

Under the second parameter set, the important critical temperatures are of course different, and so as before they were first determined in the absence of chemotaxis in order to come up with appropriate temperature ranges to use in simulations. As before, below a certain temperature cells were too inflexible for any sort of cluster rounding to be observed. The critical temperature in this case was determined to be about $T = 7$, reflecting the increased inflexibility of cell volumes and membranes under these parameters. The second critical temperature, beyond which cluster rounding was lost to random fluctuations in cell shape, was found to be much larger under this parameter set, with clusters remaining relatively round up until a value of about $T = 45$. Again individual cells generally retained their shapes even as clusters lost their round structure, until the temperature was much larger. In this case, the temperature at which individual cells were seen to regularly demonstrate breaking off of individual cell pieces was found to be a value as high as about $T = 320$. These critical temperatures again serve to inform over what temperature ranges chemotactic simulations should be considered, provide insight when interpreting the generated velocity data, and verify that the chosen value of $T = 20$ already chosen and listed in Table 4.1 is reasonable. Attempts were then made to verify that the previously observed effects of temperature variation on cluster shapes and chemotactic velocities were unchanged working under this new parameter set.

Indeed, the same general behaviours were observable under these parameters as well. As is demonstrated in Figure 4.7, velocities showed the same general trend of increasing with increasing temperature up until a point at which cells could deform freely, but not wildly. From there, as simulation temperature was increased further, migration back down the gradient was made more likely and so overall velocity showed a decrease, though because cells are more stiff under these parameters the decrease in velocity occurs more slowly. Again, the temperature range for maximal directed migration was found to occur within the critical temperatures as defined here, with decreases in average velocity if the temperature was too low or too high (even if it fell between the critical temperatures). The behaviour of overall cell and cluster shapes for varying temperatures was again found to be unaffected by chemotaxis, as with the first set of parameters. The one counterexample where a very rigid (low temperature) cluster demonstrated an observable change in shape resulting from inclusion of very strong chemotaxis remained for this second parameter set.

Overall, it has been demonstrated that the behaviours from the first parameter set are equally as reproducible here, and that it is therefore expected that the conclusions previously drawn are indeed valid for any reasonable parameter set without specific extreme behaviour. For any simulation where chemotaxis is to be included, it can be given maximum effect by choosing a temperature value that would cause proper cluster rounding in the chemotaxis-free case, probably a little less than halfway between both. Perhaps more importantly, it has also been demonstrated that increasing temperature actually does have an impact on chemotactic effect, and not just due to the increase in diffusive behaviour. Diffusive random motion considered as a separate effect will average to no net contribution up or down the gradient, and so is not the source of the decrease in velocity. This is an important result, because for comparison between the GGH model and diffusion-advection PDE approaches one must take into account that vary-

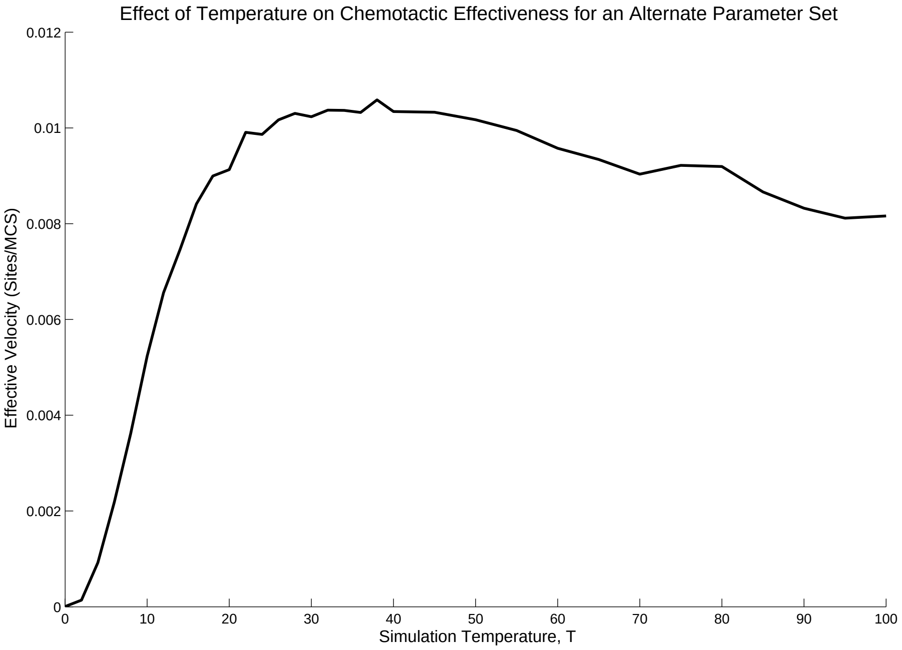

Figure 4.7: Impact of Temperature on Chemotactic effectiveness for the second parameter set listed in Table 4.1, with $\mu = 120$.

ing the amount of diffusion at the cell level by varying T *does* affect the strength of effective chemotaxis. This is in stark contrast to the PDE approach, where diffusion and chemotaxis are regarded as separate behaviours, and any relationship between the parameters D and χ must be defined by a dependence on cell concentration seeking to represent cell-level interactions such as adhesion.

It has been seen that chemotactic movement does not appear to have any real effect on other cell behaviours like inelasticity of cell material and membranes (given the critical temperatures remain unchanged). This suggests that when constructing a GGH model simulation which will include chemotaxis, the values of parameters like cell inelasticities and adhesive strengths can be chosen and trialled along with the simulation temperature until a parameter set producing realistic deformations is settled upon, and then chemotaxis can be introduced to such a simulation without concern about changing the parameter set.

There is one last point of interest with the temperature-velocity relationships discovered here. Qualitatively, the trends match observations in cells where the degree of lamellipod extension is controlled chemokinetically [192], in that those cells show a decrease in motility when the chemical concentration becomes large enough that lamellipod activity becomes chaotic and less guided - the same effect observed here as temperature increased. The parameter T has already been argued as possessing a physical interpretation as the amount of membrane ruffling [133], and thus a chemokinetic effect could perhaps be represented in the GGH model by allowing the simulation temperature T to in fact be a concentration-dependent function which increases with the increasing concentration of signalling chemical. This novel idea would simultaneously capture cells remaining fixed and rounded up for low concentrations, and eventually losing some of their guided sense of direction for high chemical concentrations. It would necessitate a cell-dependant T value, which could be included by modifying the check against the Metropolis algorithm (3.3) by changing T according to the chemical sensed by the cell currently extending a lamellipod (represented by the CPM/GGH model's trial update).

4.3.4 Inelasticities and Surface Tension

To a small extent the differences in chemotactic behaviour observable when these cell properties change have already been considered, simply by way of using two different parameter sets to test the conclusions made in this section. However, the impact of individual parameters within this category was also considered by using the parameter sets in Table 4.1 as a base point and then varying appropriately. Given that cells should tend to be in states where their volume and surface area is equal to or close to what they desire, any stretching required for chemotactic migration will most likely represent a positive contribution to H and so larger values of λ_1 and λ_2 will make these updates less likely to be accepted. This is however a little less clear with λ_2, which controls the inelasticity of membranes, because the suggestion of Ouchi *et al.* [142] to include 'slack' by using a larger-than-circular desired membrane length has been included here. That is, it's possible chemotactic stretching might actually cause the membrane to grow closer to its target length and so larger values of λ_2 could actually increase observed velocity. As for the surface tension γ, controlled by the adhesive strengths J and defined by equation (3.5), again it is expected that a larger surface tension would impede chemotactic movement, since in general an expansion of a cell in 'equilibrium' will push it further from the circular shape which minimises the Hamiltonian contribution due to surface tension (cell-cell and cell-medium adhesion).

The effects of varying λ_1, λ_2 and γ were seen to be as predicted, although it was found the different parameters did impede chemotactic motion to different degrees, as can be seen in Figure 4.8. The simulations with pictured results were run using the first parameter set (Table 4.1) with a value of $\mu = 40$, a significant amount of chemotaxis chosen to make any trends more visible. However, simulations with a smaller value of μ, and matching simulations for the second parameter set (with appropriately adjusted μ values), were also performed and the overall trends remained consistent. It is worth noting that simulations with very small values of λ or γ, especially the case where they are zero, do lead to unrealistic shapes which lends less weight to those results.

The impact of adjusting λ_2 is the most interesting, due to the fact it seems to have an increased impact at larger values than λ_1 does, and that observed velocities do not simply monotonically decrease as λ_2 increases. Both of these observations are explainable. The additional impact of λ_2 is thought to come about because of the way a single trial update will only ever change a cell's volume by one, but can change a cell's surface area by up to four, making elasticity of membranes far more impactful on whether updates required for chemotactic stretching are accepted or not. The initial increase in observed velocity as λ_2 increases is due to how it affects the balance between volume and surface area conservation. The non-monotonicity seen in the profile of velocity as λ_2 does match the hypothesis that the slack introduced in membranes might mean that larger values of λ_2 will result in an expansionary force and hence enhance chemotactic motion, however this is likely not the actual explanation. After all, as λ_2 continues to increase (which should further increase the effect of such an expansionary force), the velocity drops sharply. Also, the non-monotonic region occurs for very low values of λ_2 where cell shapes are in fact not very realistic, and the complex behaviour surely results from the fact that cells take on strange, non-physical shapes in this case.

Overall, the larger the inelasticity or surface tension the less flexible cells are, as is demonstrated in Figure 4.8 and was tested for other values of μ. No unexpected behaviours are observed, so long as the values of λ_1, λ_2 and γ are such that cell shapes remain realistic. This suggests that these forces of rigidity and surface tension can be calibrated to generate appropriate cell shapes independent of chemotaxis, and then chemotaxis separately included. While it is obvious and natural that cells less able to deform will show less migratory behaviour, PDE interpretations of this sort of effect are not well developed and on the scale of cell populations the two behaviours can not be simply separated like they are in the GGH model.

4.3.5 Dissipation Energy

The dissipation energy, H_{bond}, is an additional cost added to each considered ΔH associated with a trial update, and so affects *all* trialled updates equivalently. Given that chemotaxis is a migration of cells (and the 'effective' chemotaxis measured here is a movement of a cluster's centre of mass), the effect of including a dissipation energy is easy to predict - a general reduction in accepted updates should lead to a general reduction in any kind of overall movement and hence chemotactic effect. However as previously mentioned, given the rather extreme variance in implemented values for H_{bond}, the exact nature of this reduction is worthy of determination. Also interesting are the results presented by Maree *et al.* [118] where the addition of a dissipation energy (there referred to as a 'yield' and denoted by Y) affected the relationship (4.5) simply by a constant, maintaining a linear relationship between the value of μ and the chemotactic velocity. The details of their simulation were not presented but it was believed by this author that such results applied only to the CPM and not the full GGH model. Considering a sufficiently large value of H_{bond}, it is obvious that no motion will be accepted as no update will lead to a ΔH comparable to this value - unless μ is also very large in order to allow chemotaxis to overcome this strong resistance to cell activity. That is, there will be a critical value of μ before which no motion is seen, and such behaviour could very well exist even when the value of H_{bond} is not so prohibitively large. If this would turn out to indeed be the case, then it could contradict those presented results.

The effect of including a cost of dissipation was indeed seen to restrict chemotactic movement,

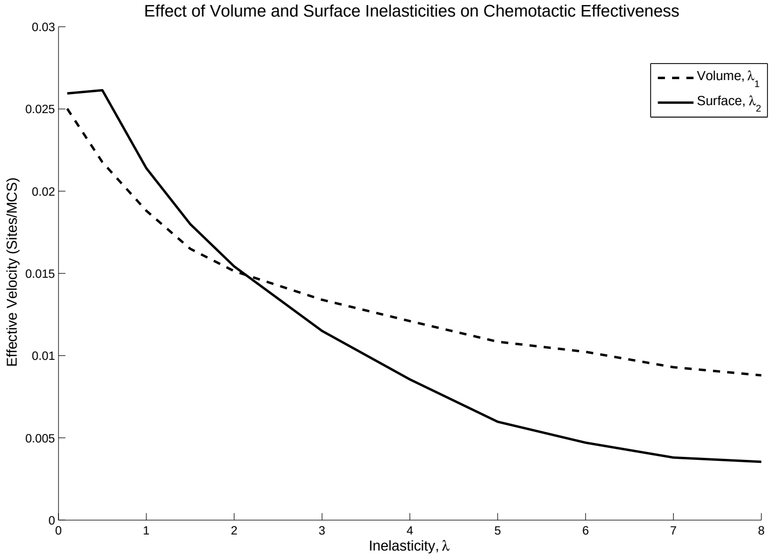

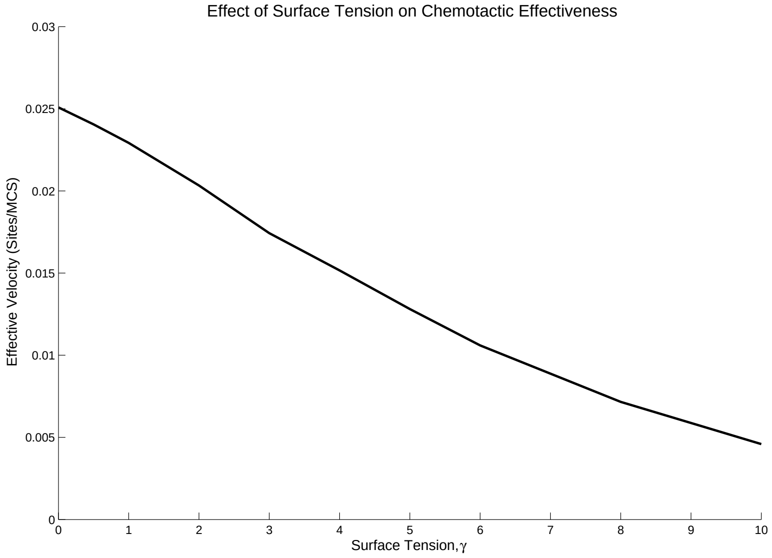

Figure 4.8: Impact of inelasticity (λ_1, λ_2) and surface tension (γ) on chemotactic effectiveness. Parameters are the first set in Table 4.1 apart from those listed on the figure. Here $\mu = 40$. The expected decreases in velocity with increasing rigidity and surface tension are seen, albeit with interesting behaviour for small values of λ_2.

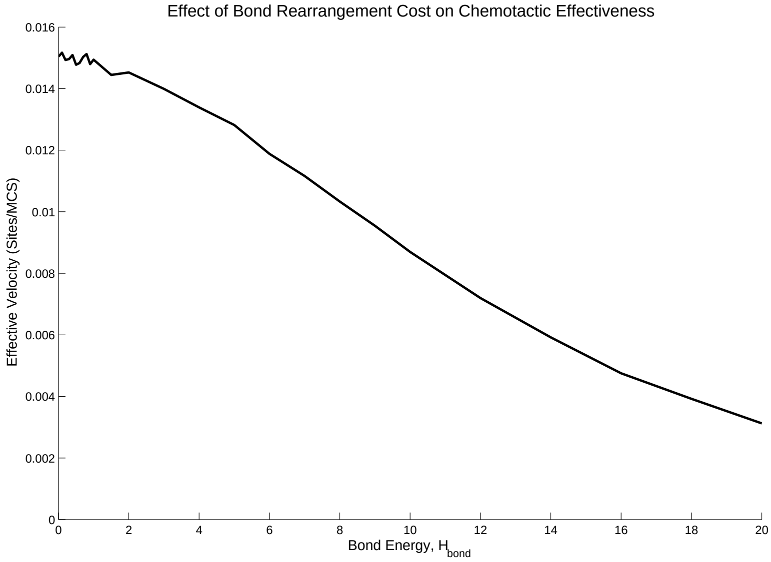

Figure 4.9: The impacts of an energy cost for bond breaking over small and large scales. Parameters are those in the first set of Table 4.1, except for H_{bond} which is as marked. Here $\mu = 40$.

although in the simulations run there was found to be an initial period where increasing the value of H_{bond} did not decrease the velocity and seemed to keep it constant. These observations for smaller values of dissipation energy were subject to a larger amount of stochastic variation, making it difficult to determine the exact nature of the behaviour. The increase in stochasticity likely explains the effect too, because for lower values of H_{bond} diffusion is more prevalent in simulations and while clusters are more free to move at these low values, the present diffusion also lowers the net chemotactic effect just as was seen for large values of T. As seen in Figure 4.9, the magnitude of the effect is rather small, so it is not a concern in terms of selecting parameters. However, the behaviour exhibited here is in clear contradiction to the suggestions of Maree *et al.* that a dissipation energy simply reduces the rate of chemotactic movement. The question of whether modifications to H_{bond} preserve the linear relationship between μ and effective velocity (also posited by Maree *et al.*) is explored in Section 4.3.7.

It is important to put into context this dissipation energy cost. While its inclusion does reduce fluctuations that could be biologically unrealistic (such as its initial use by Hogeweg [166]) and it has been argued that it should actually be a very strong effect ($H_{\text{bond}} = 80$) to maximise realism [142], the 'energy' referred to is the Hamiltonian energy utilised by the CPM/GGH, not some physical energy. When considering PDE models, or even other agent-based or cellular automata models, there is no need to seek to represent this effect - it is better interpreted as a modification to the GGH model with great potential to improve its simulated results. The simple physical nature of cells indicates there would indeed be some 'energy cost' involved in any deformations in their shapes, however this should be representable in terms of cell elasticity when using a model other than the GGH. At the population level, a wide-ranging restriction on movement could be incorporated simply by adjusting the coefficients of all flux terms, like D and χ, given it should generally apply to all cells equally.

4.3.6 Cluster Size

One of the more interesting factors affecting CPM/GGH chemotaxis is the interactions between individual cells. Here this is examined by varying the size of the cell cluster and exploring how this affects its ability to respond to the chemical gradient. The exact nature of cell-cell interactions and how they impact upon chemotaxis is not well established at all, as was pointed out in Section 2.1.2 by the reviewed continuum models which have suggested both increasing and decreasing rates of migration for more densely concentrated cell populations. Modelling specifically of chemotaxis has strictly used a decreasing term like equation (2.6) to capture the effect of cells blocking one another, and the form of that equation has been derived from simple individual-cell-based models [144]. Here however, cells might not only block the path of others but also pull along nearby cells with them via adhesion, and adhesive effects were not included in those simple CA models used to arrive at equation (2.6). Varying the size of the cell cluster which responds to the chemical gradient is a simple means of checking how contact inhibited cells differ to those which are free of contact inhibition of migration, because a larger cluster will have a greater proportion of its cells in internal locations, and thus supposedly contact inhibited. If increasing the cluster size results in a decrease of effective velocity, then this suggests that internal cells are indeed less able to respond to the gradient and contact inhibition has been represented by the GGH model. On the other hand, an increasing trend in velocity would suggest that adhesive dragging is the dominant effect.

Simulations were run for a variety of cluster sizes, using initially-square clusters for the initial condition as previously described, but now with a varying number of cells. Again the initial condition was allowed to settle into a more realistic shape before switching on the chemotactic gradient. It was found through cursory explorations that varying this initial condition (for example by using an initially rectangular cluster of cells) did have an impact on the observed amount of chemotactic velocity, and that is why simulations presented here only use a square number of cells, allowing for consistency of the initial condition. All results presented here were considered for both a ‘weak’ and ‘strong’ chemotaxis strength, and under both parameter sets in Table 4.1. The presented results are those using $\mu = 40$ and the first parameter set, but overall trends persisted for smaller values of μ also.

Figure 4.10 demonstrates how recorded velocities varied with cluster size, the results made robust by completing many repeated runs. The general trend was one of increasing velocity with increasing number of cells, albeit with an initial dip in velocity for very small cell counts. This dip is in fact the key to explaining what is occurring here, and reveals that the trend of increasing velocity is not a result of reduced diffusion in clusters. The flexibility of a cluster to move is indeed hampered by the presence of additional cells, and this is seen both for chemotactic and diffusive movement, causing the initial dip in velocity (the difference between an individual cell and a cluster). However as the cluster size is further increased, the velocity

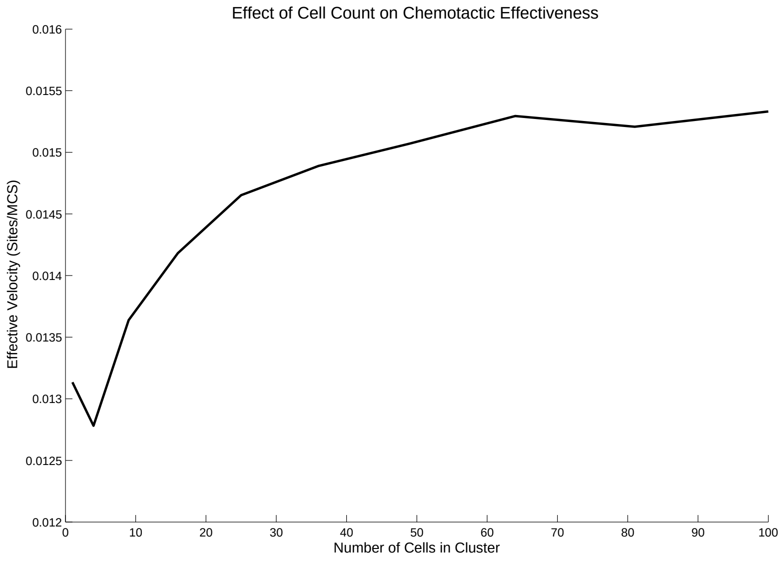

Figure 4.10: Chemotactic velocity dependence on cell 'concentration' (number of cells in a cluster). Parameters are the first set in Table 4.1 and $\mu = 40$.

actually increases for a reason other than decreased diffusion. To determine what was going on here, further simulations were run by varying different parameters of the GGH model, in order to determine how things like reducing diffusive effect would affect this trend and narrow down what was causing the increase in velocity. The issue of a possible adhesive tugging effect was explored by turning off adhesion altogether by setting all J values to zero, an option only available to the more advanced GGH model.

Random diffusive updates were restricted via two different approaches. Decreasing the temperature indeed restricts diffusive movement, although it also impedes chemotactic migration (as demonstrated by Figure 4.5) and so results would be expected to be more susceptible to stochastic noise. In a similar vein to reducing the temperature, increasing the bond dissipation energy cost, H_{bond} also reduces fluctuations and limits diffusive and chemotactic movement. More interesting, however, is the approach of completely turning off adhesion by setting all values in J to zero. Removing adhesion like this gives no energistic reason for individual cells to remain clustered, though all will still be moving in the general direction governed by the gradient and the nature of trialled updates only using neighbouring site occupations does mean that cells will largely remain as a cluster. Removing adhesion altogether allows for a determination of how important the apparent dragging effect is towards cell movement in tightly packed populations. Such a thing cannot be done in the standard CPM, only in the GGH model where the additional constraint on cell membrane lengths maintains their realistic shapes.

It was found that general trends were unaffected by reducing the frequency of 'diffusive' updates or by removing adhesion, leading to a more thorough investigation, the results of which are summarised in Table 4.2. It was quickly realised that adhesion was not the factor respon-

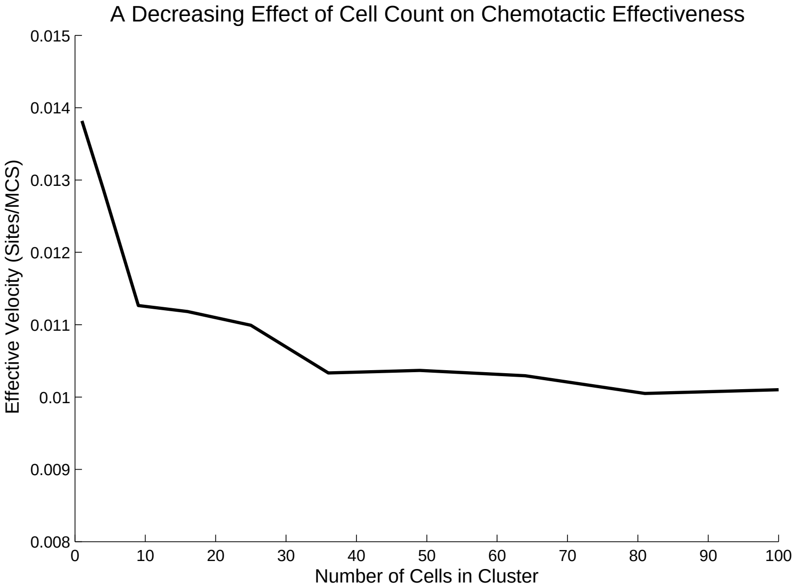

Figure 4.11: Impact of cell 'concentration' (number of cells in a cluster) on chemotactic effectiveness demonstrating a decreasing trend. Parameters are the first set in Table 4.1 but without adhesion, $H_{\text{bond}} = 10$ and $\mu = 40$.

sible for producing a tugging effect which causes the increase of migration as cell numbers increase, this behaviour still observable even with adhesion removed. Indeed, thinking this through from the perspective of trialled updates in the CPM, the real way this adhesion might cause such an effect would be if it helped to close gaps between cells in a cluster when a front cell moves. However, in the CPM, cells can only expand or contract by copying a neighbouring site, and so gaps between cells in a cluster will never form if the cluster begins tightly packed. Adhesion does keep the cluster together, but the assertion here is that larger clusters move slower, and so the increase in velocity for larger clusters must not be an adhesive effect.

The results in Table 4.2 indicate two key trends for how cluster size affected chemotactic effectiveness. The first of these was the behaviour exhibited in Figure 4.10, where increasing cell number caused a quick increase in cluster migration up to a saturated level, albeit with single cells typically faster than small clusters. The other observable trend was one where increasing cell concentration led to a decrease in migratory ability, again up to a certain cell number beyond which little change in velocity was seen. An example of this is shown in Figure 4.11. This trend was certainly more present when adhesion was not included, though as pointed out simply switching off adhesion alone did not actually generate the behaviour.

In all cases, no matter whether an increasing or decreasing trend was observed, there was an apparent 'saturation velocity' beyond which increasing the cluster size further did not cause any noticeable change to the ability of cells and clusters to migrate. This is in sharp contrast to the forms of $\chi(C)$ used in PDE models for chemotaxis, where either the cellular concentration does not have an impact, or chemotactic migration shuts off completely for densely-packed cells. Contact inhibition of migration is generally interpreted as a complete shutting off of cell expansion onto occupied sites, and indeed when it was modelled in the CPM framework by Merks *et al.* this was done by automatically switching off all chemotactic contribution to ΔH when one cell was expanding onto another [130]. However, the original proposition of contact inhibition of migration by Abercrombie [1] was simply that cells which came into contact changed directions and avoided encroachment, not that they strictly stopped all movement. Indeed in scratch assay situations small protrusions into areas occupied by other cells have been experimentally observed [47], and cells in a fully packed monolayer do still demonstrate some motility [190]. As the cluster size increases in the simulations here, the proportion of the cluster which is contact-inhibited approaches one, and thus if contact inhibition entirely removed chemotactic response the velocity of the cluster should approach zero. This has not been observed here, however testing of the additional contact inhibition effect used by Merks *et al.* [130] in the GGH model simulations used here did indeed result in velocity approaching zero for large cluster sizes. This demonstrates that in the GGH model implementation here, contact inhibited cells are still able to migrate to some extent, and indeed in the cases where the trend of velocity with size is *increasing*, this suggests that contact-inhibited cells are actually more active than those on the edges of the cluster!

This line of thinking reveals the critical behaviour at work here. The trend in velocity comes down to how actually ‘contact inhibited’ the internal cells are, and in the context of the GGH model this is represented by how likely updates which feature a cell pushing onto another are likely to be updated. In the standard GGH model (and as implemented here), the values of J between cells are negative and equal, whereas between cells and medium they are positive. This means that the effective value of γ that a cell within the cluster experiences is zero, whereas a cell on the edge of the cluster experiences a nonzero γ and hence a surface tension force which hinders movement up the gradient (as seen in Figure 4.8). This is the primary reason that internal cells are actually able to move faster than external cells in most cases, and explains why when adhesion is switched off primarily decreasing trends are observed. The ability of internal cells to encroach onto others, compared to the ability of external cells to encroach onto empty space, is naturally defined by some choice of GGH model parameters, and this has been shown here to introduce either a contact inhibition effect, or the opposite.

This conclusion was easily tested in a variety of ways, confirming the realisation that the ability of cells to push against one another was the key behaviour affecting which trend was observed. Other means of restricting the ability of cells to push against one another were implemented as seen in Table 4.2. First tried was the change of removing the 20% slack provided to membranes. This makes cells less willing to deform in general, but especially so when a cell is encroaching onto another cell, typically increasing the membrane lengths of both. Of course, the same effect can be achieved by reducing the flexibility of membranes outright, by increasing λ_2. Making either of these changes did indeed produce a decreasing (contact inhibited) dependence of velocity on cluster size. On the other hand, increasing λ_1 instead did not cause a switch from an increasing to a decreasing trend. This is because λ_1 affects more the overall rigidity of cells,

Parameter Changes	**With Adhesion**	**Without Adhesion**
No change	I (0.016)	I (0.016)
$H_{\text{bond}} = 10$	N (0.009)	D (0.010)
$T = 3$	I (0.006)	D (0.007)
No 20% Slack	N (0.007)	D (0.007)
$\mu = 10$	N (0.3)	D (0.4)

Table 4.2: Results for various parameter combinations. D indicates a decreasing behaviour (like in Figure 4.10), I an increasing behaviour (like in Figure 4.11), and N indicates no strong dependence. The figures in brackets are estimations of the observed speed (sites/MCS) once the size-dependence effects saturates. $\mu = 40$ and all other parameters are as described in Table 4.1 except where mentioned.

thus affecting external cells in much the same way as internal cells. When an internal cell encroaches onto another cell this will change the volumes of both, as compared to the stretch of an external cell which will only affect the volume of a single cell. However, a cell which has already stretched up the gradient can actually support encroaching movement from behind because its own volume is currently larger than the target volume dictates.

The contrast between the different effects of the two inelasticities λ_1 and λ_2 on size-velocity trends demonstrates that it is indeed the ability of internal cells to push against one another that controls whether an increasing or decreasing size-velocity trend is observed. This point is further highlighted by the fact that an increase in either type of inelasticity results in a decrease in velocity as shown in Section 4.3.4 - decreasing elasticity of cell volumes or just their membranes causes them to slow down, but only changing the membrane elasticity (which more significantly affects internal cells) can impact on how and if 'contact inhibition' of migration is exhibited by the GGH model.

Now that an increasing size-velocity trend has been seen to result not due to adhesive tugging but because cells actually push into occupied space more easily than unoccupied space, this is a serious point of concern with the GGH model framework, because it is entirely physically unrealistic. Indeed, this effect is essentially a *reverse* contact inhibition of migration where cell-cell encroachment is actually encouraged as opposed to being restricted, in direct opposition to experimental observation and common sense. However, despite this issue being inherent to the GGH model framework with standard choices for adhesion energies J and dictating that parameters are chosen to prevent its inclusion, it has not at all been discussed in the literature.

When the size-velocity trend is decreasing, this *can* be argued as a sort of naturally-included contact inhibition of migration, because cells more easily expand into empty space as opposed to on top of other cells in a monolayer. However, this is a different sort of contact inhibition to the one used by Merks *et al.* [130], where cells which are attempting to expand into sites already occupied by cell matter ignore chemotactic effects completely. The basic biological understanding of contact inhibition of migration does suggest that encroachment is entirely shut off and indeed cells change direction upon collision in order to avoid it [1]. Despite that, the aforementioned observations of Timpe *et al.* that contact inhibition of migration in a packed monolayer is not fully effective at halting movement [190] do imply that a naturally-occurring trend of cells being less likely to (but not prevented from) encroaching onto one another is biologically realistic. Careful choice of parameters, or perhaps an inclusion of a separately enforced contact inhibition of migration like the one used by Merks *et al.* [130] but with only a reduction instead of a full switching off of chemotactic response could then be used to match specific biological observations of reduced movement in blocked-in cells.

However, these expansions of 'contact inhibited' cells have been seen to not be completely switched off, a different effect to the one used by Merks *et al.* [130] to include contact inhibition and somewhat in contrast to the biological definition which does suggest a lack of encroachment and indeed cells changing direction to avoid it [1]. However, the aforementioned observations of Timpe *et al.* that contact inhibition of migration in a packed monolayer is not fully effective at halting movement [190] do imply that a naturally-occurring trend of cells being less likely to (but not prevented from) encroaching onto one another is biologically realistic.

Certainly in a 2D GGH model like the one used here, the simple constraint of volume prevents cells from haphazardly encroaching onto one another, whilst still allowing for subtle movements and sorting within a fully confluent cluster or monolayer, and thus contact inhibition of migration (or potentially *reverse* contact inhibition as seen here) can be a naturally observed effect in the GGH model without its specific separate inclusion. This is why a proper exploration like the one performed here is very important. An interesting extension would be cases where cell-cell collisions are frequent but cells are not simply limited to a single cluster.

4.3.7 Linearity of Behaviour

The final exploration of GGH chemotaxis was of the exact nature of the actual chemotactic force induced, in terms of how it varied with the strength of gradient/chemotactic response parameter μ. It is preferable that chemotaxis obeys the linear relationship (4.5), to have consistency with population-level thinking and simplify the inclusion of other dependencies like saturation. As already summarised, the linear trend has been demonstrated in the literature but not with a great deal of detail, and apparently using the CPM as opposed to the full GGH model [118]. Moreover, their suggested impact of introducing a dissipative energy cost does not match expectations given that it has been shown in Section 4.3.5 that for migration-resistant parameters a critical value of μ exists before which little to no migration is observed, whereas their results suggested this energistic penalty simply changed the slope of the linear trend. Perhaps their included energistic penalty was not significant enough to severely restrict migration for their choice of parameters. The effects of a dissipative energy cost on chemotactic effectiveness have been discussed in Section 4.3.5 but not specifically how it impacted the trends between velocity and μ, which is considered in this section. Lastly, in the previously published work [118] a saturation effect breaking the linear trend was observed for very large μ values, and this makes perfect sense and is expected to be observed in simulations here as well. Eventually a value of μ will be reached where all trial updates up the gradient will be accepted (and all those down the gradient rejected) and this results in a maximum possible velocity inherent to the CPM, beyond which a linear trend certainly cannot continue.

In order to check the success of the GGH implementation and the use of equation (4.4) for chemotaxis, the response parameter μ was varied to introduce different chemotactic strengths and the velocity was compared against these values of μ to see if a linear trend like (4.5) was observed. Simulations were run using the first set of parameters in Table 4.1, with the usual averaging over repeated simulations to minimise the impact of stochastic effects on the data. It was found that for lower velocities, these fluctuations were more significant and difficult to remove entirely, because for low chemotactic velocities diffusive migration in random directions has more of an impact. Despite these fluctuations, general trends were still very visible in recorded results. Figure 4.12 demonstrates the determined relationship between effective velocity and μ, over both a range of smaller and larger μ values. When μ is not too large, a linear trend is indeed observed, however for very large values of μ the velocity does start to level off to some threshold value presumably corresponding to all trial updates in the direction of the gradient being accepted, and all those in the opposite direction being rejected. However even before this point was reached, the very high μ simulations demonstrated unrealistic cluster behaviours, with cells being compressed into unrealistic shapes by the wild and rapid movement up the gradient. Thus, although a saturation effect between response and chemotactic strength is essentially built in the CPM and GGH model, this should *not* be interpreted as a way of modelling saturation effects arising due to cells' finite number of receptors, because it occurs at a point beyond correct cell behaviour. If this effect was deigned important, it should be implemented using a multiplicative factor (and indeed this is done in Chapters 6 and 7.

The question of how the introduction of a bond dissipation energy $H_{\text{bond}} > 0$ affected the linearity of the chemotaxis-velocity relationship was also considered. It was found that for values of H_{bond} up to about 10, the trend did indeed remain linear, but with a slower overall velocity. This observation agrees completely with the results of Maree *et al.* [118]. However, larger values of H_{bond} do not demonstrate a linear trend, because they impede cell motility enough that low amounts of chemotactic response do not cause any real directed migration to occur. There is a threshold level of chemotactic effect that must be present in order to see any kind of response to the gradient, as also observed in Section 4.3.5.

4.4 Conclusions

With chemotaxis (and other types of taxis) being a critical cell behaviour in a wide range of biological and experimental situations, its incorporation into the CPM framework is extremely important and thus many examples of this can be seen in the literature. However, it has been argued here that the established means of implementing chemotaxis have been made use of without fully considering how exactly they function when considered simply as single behaviours. Given this lack of sufficient consideration, this chapter has reviewed and then examined vari-

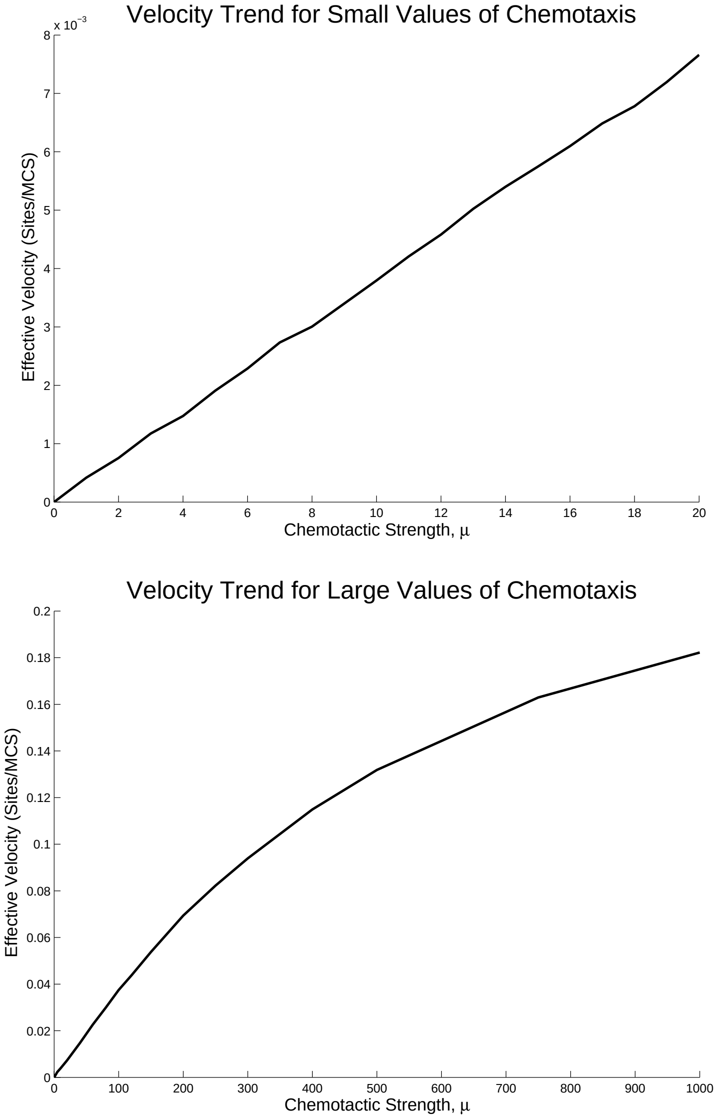

Figure 4.12: The observed trend between effective chemotactic velocity and the chemotactic sensitivity parameter μ, over both reasonable values of μ, demonstrating the linear trend, and for overly strong values of μ for which the trend saturates.

ous means of incorporating chemotaxis to consider how truly successful they are, and also to explore how they interact with other base cell effects in the GGH model in order to inform what might be appropriate parameter choices.

The three basic methods for representing chemotaxis that can be found in the literature are a direct sensing of concentration by cells (4.2), a direct sensing by cell surfaces (4.3), and the sensing of gradients by trialled extensions (4.4). Despite claims that the first method equates to the Keller-Segel equations (most recently [112]), this has required significant assumptions which have been demonstrated here to be inapplicable to actual simulations of chemotaxis of cell clusters using the GGH model. Indeed both methods for chemotaxis which involve direct modification of the definition of the Hamiltonian free energy, H, have been shown here to be certainly incorrect, explaining their lack of wide adoptance in the literature. The alternate method based around making modifications directly to the value of ΔH associated with each update, equation (4.4), has been verified here as significantly more appropriate for handling chemotaxis and then tested in-depth.

It is desirable that the parameter controlling the strength of chemotaxis in the GGH model, μ, can be interpreted and used in essentially the same way that χ is used in PDE models to define chemotactic flux at the population scale. For this to be the case, it is necessary that chemotactic force translates linearly into velocity as per the Aristotelian regime. Given that the chemotactic force is proportional to μ, this necessitates a linear relationship between the effective cell velocity and the value of μ, a trend that has been demonstrated by Maree *et al.* [118] except for an apparently simpler model and without simulation detail. This linear trend has here been demonstrated as correctly exhibited by the full GGH model, so long as the value of μ was not made unrealistically high, those values resulting in unrealistic cell behaviours anyway. Thus it has been concluded here that chemotaxis using equation (4.4) as a basic approach for chemotaxis to be possibly built off of is entirely appropriate, so long as the chemotaxis not so strong as to result in unphysical cell behaviours.

The technique as stated here seeks not to represent all the specificities of how cells detect gradients themselves, though it does serve as a phenomenological predictor just as the Keller-Segel equations use a phenomenological flux term to represent chemotaxis at a larger scale. This ignorance of tactic behaviours' inner workings has been seen here as apparently equally valid at this scale of individual cells, except in those cases where these inner workings are responsible for larger scale effects, such as with the chemotactic wave paradox [78].

The effects of different parameter values and simulation details on chemotactic migration of cell clusters have also been examined, and this has been used to inform the modelling in the later Chapters of this thesis. It has been shown that chemotaxis can be thought of largely as a separate effect in the GGH model, in the sense that parameter values can be decided on first to create realistic behaviours and then chemotaxis incorporated after that. Lattice anisotropy does not have any significant effect on chemotactic movement for moderate chemical response strengths, with diagonally moving and vertically moving clusters showing the same rates of velocity. The effects of lattice anisotropy could prove a concern for strong chemotactic responses. More notably, diffusion and chemotaxis have been seen to not be separate behaviours in the GGH model, and an abundance of diffusive effect (such as that occurring for individual, unconnected cells or for large simulation temperature T) does actually hinder the chemoctatic response. If diffusion was a separate effect (as it is considered at the population level), then it should have no impact on chemotactic migration because over a long timeframe a diffusive effect results in no net movement in any direction. This is a consequence of all behaviours in the GGH model being represented via the Metropolis algorithm (3.3) in a non-linear fashion, and the conflation of movement effects should be carefully considered. Thus despite the evidenced linear relationship between cell velocity and chemotactic response parameter μ, tying this parameter to the macroscopic parameter χ should only be done with great care and only within a specific problem context.

Very interestingly, it was found that the negative surface energies between cells which the GGH model uses result in an effect where cells are more able to encroach upon other cells as opposed to empty space, a direct violation of experimental observation and the principle of contact inhibition of migration. It is thus important to check and adjust parameter values in order to prevent this unphysical effect from occurring in GGH model simulations featuring chemotaxis. This is not an effect that has been previously discussed in the literature, again because CPM chemotaxis has been predominantly used as a means to an end as opposed to carefully examined, especially in the context of the extended model, the GGH model.

The individual-cell-level simulations presented in the following chapters use a parameter set very similar to the first set in Table 4.1, now that the behaviour of such a set in a chemotactic context has been thoroughly explored. However, given the issue of 'reverse contact inhibition' which has been shown to arise here, the value of the dissipation energy is set to $H_{\text{bond}} = 10$. As can be seen in Table 4.2, the trend observed for normal adhesive parameters and this value of H_{bond} results in an essentially neutral trend of velocity against cluster size, suggesting that cells can push equally well against other cells or open space. Contact inhibition can then be introduced by using no adhesion ($J = 0$ in all cases), and this is indeed an idea used to create the adhesive regimes listed in Chapter 5 and used throughout the remainder of the thesis. Additionally, to further reduce movement within clusters, the slack provided to cell membranes is also reduced in the remaining simulations in the thesis, from 20% to 10%.

With these changes decided upon and the method properly considered, chemotaxis can now be included to measure the response of cells in the scratch assay to some kind of chemical signal, including the possibility of a substrate-bound nutrient that drives the healing effect. This is presented in Chapter 6. The next chapter is used to define, implement and explore a method for handling the other major effect added to the GGH model, proliferation.

Chapter 5

Proliferation in the Cellular Potts Model

5.1 Previous CPM/GGH Models Featuring Proliferation

The issue of incorporating cellular mitosis into the cellular Potts model has not yet been discussed for two reasons. Firstly, cell proliferation is not ubiquitous in cellular Potts model implementations, although it has appeared in several places within the literature (as is reviewed here). Moreover, there is no consensus on its implementation, which tends to be specific to the biological situation being simulated. Secondly, proliferation does not fit well within the core framework of energy minimisation the CPM operates from. Just as it was demonstrated with chemotaxis, proliferative events can not simply be incorporated directly into the Hamiltonian energy H to be minimised. Indeed, because they rely on the creation of new cells (new values for σ), the Metropolis algorithm alone will never create any extra cells, and so creation events must come about through additional rules specifically constructed for this purpose. The structure of these rules requires consideration of cell biology (specifically the mitotic cycle) and of the specific situation being modelled, though as with all modelling the necessary level of detail is open to interpretation and argument. Indeed a variety of models all using differing levels of detail have been presented in the literature, ranging from simply checking cell volumes (e.g. [79]) to a complex multiscale model which takes into account the specific networks of regulatory factors underlying the cell cycle itself [89].

The problem of including mitosis in a CPM/GGH implementation can be somewhat broken up into two separate questions that must be answered. Firstly, there is the question of what causes a cell to make the 'decision' to proliferate, and second, the actual proliferation processes must be determined in coding terms. The second question is actually quite easily answered, with a general consensus on what should happen found in the literature and supported by experimental observation. That is, cells divide along their shortest diameter due to the interplay of microtubule forces on the centrosomes [80]. Thus, with a cell's minor axis determined, all that remains is to re-label one half of the cell's constituent sites with a new index, thereby creating two cells. Many publications do not mention how they determine the minor axis, though one paper admits to using the approximation of calculating a cell's centre of mass and determining the length of diameters passing through the centre of mass in four primary directions (horizontal, vertical, and the two diagonals) [197]. Although not in the context of proliferation, a method for determining minor and major axes of 2D CPM cells by assuming they are ellipses is presented by Zajac *et al.* in the Appendix of their work [213].

The first question, regarding the factors triggering a proliferative event (or the onset of one) has been answered in various ways by previous implementations of proliferation in the CPM/GGH model. The most common factor encountered is simply a cell's volume, and this remains a compelling choice for the sake of both modelling and realism. If volume is not checked and smaller cells are allowed to proliferate, they will split into daughter cells that are unrealistically small. Experimental evidence also indicates the importance of cell volume, as demonstrated by the seminal experiments of Chen *et al.* [30] proving that it was size/shape itself, and not the amount of cell-substrate contact, that appeared to control proliferation. Even amongst GGH models which directly check cell volume to control proliferation, the specific implementations are far from alike. While basic models which simply include a steadily growing or initially large target volume to allow cells to expand to proliferative size have been used, and with success [17, 29, 79, 160], other models have had the target volume of cells (or its rate of change) depend on other cell properties, thus controlling which cells are capable of reaching the larger volume necessary to divide. In this way, external factors like nutrient availability [160, 185] can have their effects incorporated without jeopardising the physical realism offered by requiring a certain target volume for division. The in-depth approach of Jiang *et al.* [89] explicitly models the key components of the cell cycle's regulatory system but does not allow these regulatory factors to impact on the target volume. Instead they use a large target volume and allow cells to proliferate only if they successfully pass through the 'chemical' checkpoint of the G1-S phase transition *and* are able to grow at a reasonable rate to the size necessary for completing mitosis. The GGH model presented here, discussed below, does use volume as the key determining factor for cell proliferation, but in a unique way.

Different triggers for proliferation apart from cell volume have also been used. One example of an alternate choice is the area-to-perimeter ratio (the 2D equivalent of the volume-to-surface area ratio), the argument being that this ratio represents a cell's ability to exchange nutrients and waste with its environment, motivating mitosis [97]. However, the aforementioned geometric studies [30] (see the review article of Huang and Ingber [84] for some very illustrative images) suggest this might not be the case, for the rounder cells (largest volume-to-surface area ratio) show less proliferative activity than those allowed to spread and stick to the substrate material - and when attachment to substrate was created via separate islands of adhesive material, cell shapes were not very round, even in a 2D sense. Some work using the CPM to model tumours made no consideration of cell size or shape at all, using a random probability of undergoing mitosis affected by cell type (technically a relative measure of how much cells liked to stick to the ECM compared to other cells, though the $J(\tau_1, \tau_2)$ values defining this ratio are the same for all cells of a certain type) and the time since the parent cell last divided [197]. Further work from the same group of authors continued to use a stochastic proliferation scheme, though the chance of proliferation there depended solely on the concentration of TGF-β, with no mention of a strict time dependence [198].

5.2 Proliferation Routine Implementation

The approach to proliferation utilised by the GGH models presented in this thesis is unique, and has not been featured in the literature before to the best of the author's knowledge. The key advantage is the introduction of a proliferative cell type which normal cell types can change into when they elect to proliferate, allowing for different properties between quiescent and proliferative cells to be defined. Knewitz and Mombach did use differing properties for normal and proliferative cells in their model of tumour growth [97], but in that model a cell could not transform its type, instead tumours cells were the only ones which proliferated and these expressed different properties to normal cells. In the proliferation routine used here, the volume of a cell is used both to trigger proliferative events, and as a condition for initiating the cell cycle. The proliferation process used here is as follows, with parameter values given in Table 5.1:

Cell growth is driven by a sliding target volume

Cells are assigned a 'true' target volume which is large enough to allow cells to reach the size required to trigger the mitotic cycle (represented by a change in state to a proliferative cell in the model, as explained next). However, cells which change state in the model will experience a sudden change in target volume, which can lead to unrealistic effects. For this reason, an approach like those of Hogeweg [79] and Knewitz and Mombach [97] where the actual target volume is dynamic and different for each cell is also used here. Every Monte Carlo step, the target volume of an individual cell is moved one closer to the 'true' target volume. When a cell changes type, its individual target volume is set to its current size. All cells use a target surface area corresponding to a circular cell of their current target volume, with the inclusion of a 10% slack as discussed in Chapter 4 and informed by the 20% slack used by Ouchi *et al.* [142].

The true target volume is one which is larger than cells initially present in the simulation, and after successful mitosis (because it is more than half the final mitosis size). This means that all quiescent cells will attempt to grow to this size. The true target volume is chosen as two sites larger than the trigger volume for mitosis, found to be necessary to ensure that a reasonable number of cells are able to reach the trigger volume.

Cells which reach their target volume are allowed to become proliferative

Proliferation is not a simple process of dividing in this simulation, so cells which have been selected to proliferate are actually assigned a new type (new τ value) so that different rules may apply to them compared to normal (quiescent) cells. For example, quiescent cells are known to show a much higher degree of response to signalling substances [155, 85] and indeed in the situation of a cellular monolayer proliferating cells can detach and thus will be unable to crawl at all [103]. Following this, in the implementation here quiescent cells are given a μ value governing the chemotactic response but proliferating cells use $\mu = 0$. That said, the simulations exploring proliferation presented in this chapter do not involve any sort of chemotaxis, and this is mentioned here to highlight how proliferation affects chemotaxis in the GGH model featuring both effects used in Chapters 6 and 7. Cells are checked for entering the proliferative state at the end of each Monte Carlo step, though cells meeting the size criteria for beginning their cell cycle will still only enter it with probability $\mathcal{P}$, which is a constant somewhat tied to the proliferation rate. With the size constraint being a requirement for simply *entering* the proliferative state, cells which are too crowded will not be able to reach the necessary size to even enter the cell cycle, thus capturing the nature of contact inhibition of mitosis. However, it should be mentioned that true contact inhibition of mitosis is not simply an inability to expand but involves chemical and electrical signals which inhibit proliferation altogether [34, 126]. Thus the approach used here is somewhat phenomenological, but is demonstrated in Section 5.3 to produce the desired behaviour.

Cells which are proliferative swell in size due to their different parameter values

Cells undergoing the cell cycle are of proliferative type, and thus have a new target volume associated - the volume required to successfully split into two daughter cells. Thus the target volumes of individual proliferative cells increase bit by bit as before, eventually encouraging them to reach the necessary size if not contact inhibited. Further enhancing the growing effect associated with a cell undergoing mitosis, cells in the proliferative state have an increased value for λ_1 (see Table 5.1) to allow them to readily swell if space is available.

Proliferative cells which reach the target size for proliferation undergo mitosis

This condition checks each proliferative cell's size at the end of every Monte Carlo step, though the time since entering the proliferative state is also checked. Cells must remain in a proliferative state for some minimum value of time, representing the time necessary to complete the processes of the cell cycle. Also, if a proliferative cell has failed to reach the necessary size to split after a certain amount of time has elapsed, it is changed back into a quiescent cell. The times used here for these two values are listed in Table 5.1.

Proliferation occurs via a cut along an approximate minor axis

For simplicity's sake, the determination of the minor axis is the approximate approach used by Turner and Sherratt [197] and mentioned above, tracking the centre of mass of each cell and then checking the lengths of cuts along the primary directions and passing through the centre of mass in order to determine which is the shortest and hence an approximate minor axis. One apparent issue was seen with this approach - cell-occupied sites which are passed through by the minor axis can not be split into two, and so must be assigned the index of one new daughter cell or the other. If the new cell given these extra sites is always on the same side of the cut,

Parameter	**Meaning**	**Quiescent Cells**	**Proliferating Cells**
J_{cm}	Adhesion between cell and medium	3	3
J_{cc}	Adhesion between cells of this type	-2	-2
J_{co}	Adhesion between the two types of cell	-2	-2
λ_1	Inelasticity of cell material	2	10
λ_2	Inelasticity of membrane	2	2
A	Membrane Slack	10%	10%
t_{min}	Minimum cell cycle time (MCS)	-	50
t_{max}	Maximum cell cycle time (MCS)	-	200
V	'True' Target Volume	34	60
V_m	Trigger volume for mitotic cycle	32	-
V_p	Trigger volume for proliferation	-	60
$\mathcal{P}$	Proliferation probability	Varies	-
T	Simulation Temperature	10	
H_{bond}	Dissipation energy	10	

Table 5.1: Parameters used for proliferation in the GGH model. Times are measured in MCS (Monte Carlo steps).

then bias is introduced. In order to prevent this from happening, a random offset of the axis (perpendicular to the axis itself) is used so that disputed sites end up as all part of the same daughter cell, but which daughter cell this is varies. It should be noted that this does cause the two daughter cells to have slightly different volumes, though it does result in rounder shapes than would arise by randomly assigning individual disputed sites. The created daughter cells have changed state, so they are reassigned target volumes equal to their current volumes just as is done when a cell starts or stops trying to proliferate. This target volume then gradually increases to the 'true' target volume as previously discussed.

The key features of proliferation as implemented here are the volume-dependent initiation of the cell cycle, and the use of a new cell type to represent proliferating cells and their differing properties. This model of mitosis is perhaps most similar to that put forward by Hogeweg where cells grow due to stretching [79]. In that model cells that manage to exceed their target volume by a certain threshold have their target volume increased, and this process continues until the cell reaches a size large enough for proliferation. This in a sense does represent contact inhibition, because cells that are blocked in will not be able to stretch enough to increase their target volumes. However, it seems cells that begin to stretch retain that increased target volume, even if they are later blocked by other cells, meaning that all cells will not be alike. Certainly, the cell cycle is not being explicitly considered in this stretching approach. The model presented here does include an effective cell cycle, requiring the passing of a contact inhibition "checkpoint" and a certain minimum amount of time for the cycle to complete. No consideration of nutrient impact has been presented here. This is a potential weakness and possibility for extension of this proliferation model, although within monolayers (such as those in the scratch assay, this thesis' chosen biological application) cell-cell crowding interaction is the primary determining factor for proliferation [126].

5.3 Exploration of the Implemented Scheme

Given that the proliferation scheme is not one that has previously been demonstrated in the literature, it was important to test its performance before using it as part of the simulations for the scratch assay. The natural approach was to simply start with a single cell given sufficient room to proliferate and see how the simulation evolved. The results of one such simulation are visualised in Figure 5.1. Viewing the simulation as an animation showed no strange behaviours from cells, and while initially all cells are generally able to proliferate, as the cluster grows central cells no longer have room to expand and so are left unable to proliferate. They are being 'contact inhibited' as desired. With a sufficient simulation timeframe, cells continued to proliferate until they had filled the entire domain, eventually reaching a state where there were no further proliferative events recorded. While it is known that in a real monolayer there is some level of 'background' proliferation, this is only used to sustain the monolayer and is not seen here because no mechanism for cell death has been included. Experimental evidence suggests that a monolayer grown within a limited amount of space should result in an approximately logistic growth curve [194], so the ability of this model to predict such a behaviour was tested. Logistic growth curves were discussed in Section 2.1 and are the solution to the equation

$$\frac{dC}{dt} = \lambda C\Big(1 - \frac{C}{K}\Big), \tag{5.1}$$

which has the closed form

$$C(t) = \frac{KC_0\, e^{\lambda t}}{K + C_0\,(e^{\lambda t} - 1)}. \tag{5.2}$$

Briefly, K is the carrying capacity, here representing the number of cells which can fit in the limited space the monolayer occupies. If the space is completely filled, then K should depend on the amount of space available and the volumes of cells (strongly impacted by V, but affected by changes in many variables). The rate of growth is λ, and so a strong connection between λ and $\mathcal{P}$ is expected, and their relationship was explored here. All parameters used were those given in Table 5.1, and the effects of varying parameters other than $\mathcal{P}$ were not explored, outside of the alternate adhesive regimes considered below.

The overall results of the simulations were largely as expected, and show good fits with logistic growth curves, some of these visualised in Figure 5.2. As the proliferation probability $\mathcal{P}$ was increased, so too was the growth rate, but the general shape of the curve remained largely unchanged. Several things are particularly noteworthy in these simulations, however. Firstly, data for individual runs with lower $\mathcal{P}$ values was quite variable - each cluster demonstrated logistic-like growth behaviour but when the number of cells was still small the simulations were very susceptible to stochastic effects. This resulted in a sort of 'shifting' behaviour in which the time of 'onset' of logistic growth varied according to how long the first few cells took to multiply up to a level where stochastic effects are less impactful, as is demonstrated in Figure 5.3. The second observed issue was that at the top end of the curve where the cell concentration was high and the domain almost entirely filled, proliferation slowed down significantly but did not stop. It was thought that this might be a result of the growing circular cluster of cells

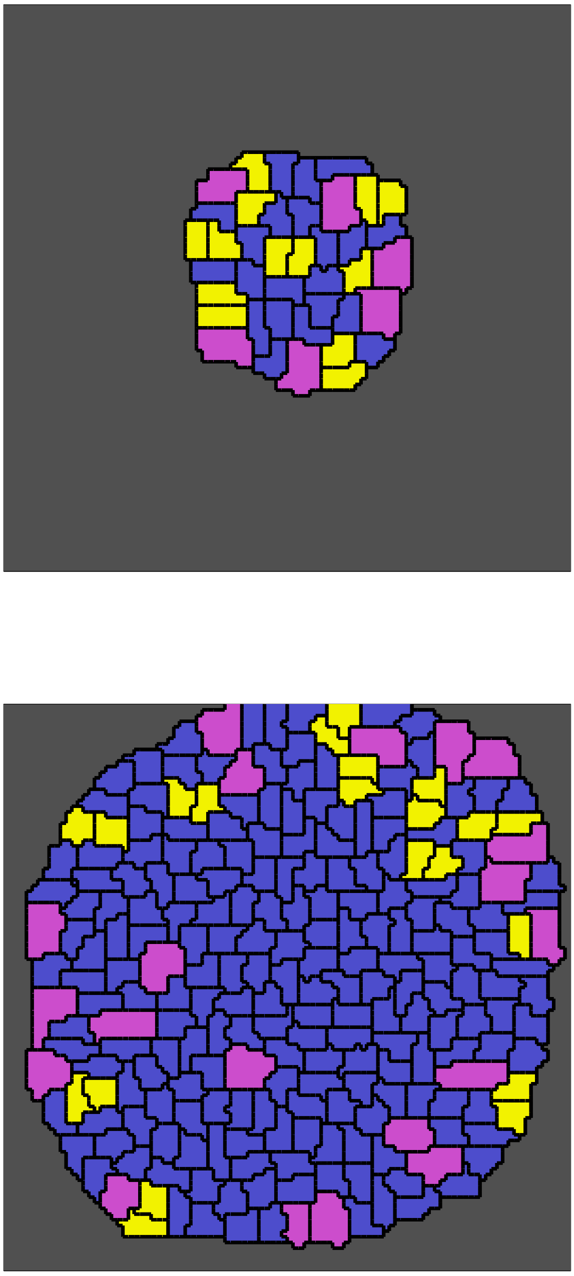

Figure 5.1: Cluster growth beginning from a single seed cell placed in the centre of the domain. Blue cells are normal (quiescent) and magenta cells are proliferative. Yellow cells are normal cells but marked differently to indicate they are recently formed daughter cells of a proliferative event. Simulation snapshots taken after 1000 and 2000 MCS. The shaded grey region indicates the full simulation domain.

Parameter	Adhesion Type	Standard GGH	Non-adhesive	'Reverse'
J_{cm}	Quiescent/Medium	3	0	-3
J_{pm}	Proliferative/Medium	3	0	3
J_{cc}	Quiescent/Quiescent	-2	0	-1
J_{cp}	Quiescent/Proliferative	-2	0	-1
J_{pp}	Proliferative/Proliferative	-2	0	-1

Table 5.2: Parameter sets corresponding to three different adhesive regimes in the GGH model.

interacting with the square domain, but further examination suggested instead that the slower top-end proliferation resulted from small stochastic variations occasionally (but only rarely) allowing further proliferation, presumably when a cell was able to successfully make several expansions despite them being energistically unfavourable and thus reach a proliferative size despite technically being contact inhibited. In the diagrams shown here, the curve fitting is performed simply by taking the maximal cell count as the carrying capacity K and then varying the value of λ until the 2-norm of the difference between the simulated data and the logistic fit is minimised. However, due to the shifting effect, data before the cell population had reached 1% of its maximum is ignored. In the case of the tabulated data shown below (Table 5.3), the growth rates are calculated using the same curve-fitting technique but applied only to the portion of the growth curve between 5% and 99% capacity, in order to prevent the discussed 'non-logistic' effects from impacting on the estimated proliferation rate. The carrying capacity is still the maximal observed cell count, allowing sufficient time for a steady state to be reached.

The determined trend between proliferation rate and observed growth rate was highly non-linear, as is pictured in Figure 5.4. The way the relationship quickly levels out demonstrates that for higher values of $\mathcal{P}$ the other limiting factors like the cell cycle time and the ability of cells to push on others determine the simulated growth rate. This result is published more for interest's sake and to demonstrate the effect of the parameter $\mathcal{P}$. However, it should be noted that the growth rates listed in Figure 5.4 are measured in terms of MCS in the GGH model, and that this does not directly correspond to a physical growth rate. Indeed, in the method used in Chapter 6, varying the proliferation rate $\mathcal{P}$ also affects what length of time each MCS represents so that the proliferation rate matches an experimentally observed rate.

Another point of interest is the effect of different adhesive regimes on the proliferative growth of a single cell or sparse population of cells into a confluent monolayer, for reasons which are discussed in Chapter 6. Three important regimes have been identified here, and are listed in Table 5.2. The first regime is a standard GGH regime featuring a negative interaction energy between cells representing cadherin-driven adhesion, and a positive adhesive energy between cells and medium representing surface tension. The second regime features no adhesive effect at all. The third regime has cells still sticking to each other, but contacts with medium are favoured over contacts between cells in an attempt to promote expansion into empty areas. The interpretations of these effects and their impact upon GGH model simulations of the scratch assay are explored in Chapter 6.

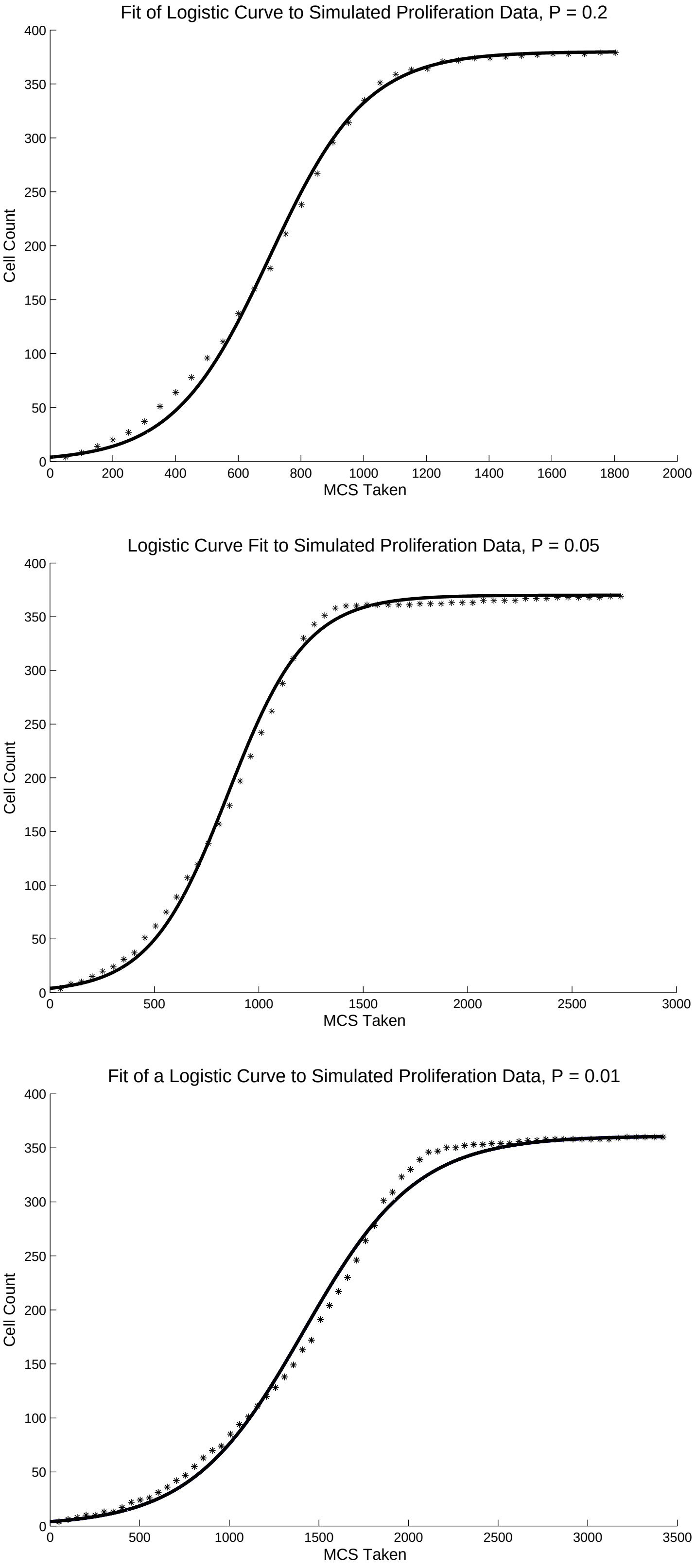

Figure 5.2: Sample fits to logistic curves for simulations with a variety of $\mathcal{P}$ values. Curve parameters are $\mathcal{P} = 0.2$: $r = 6.50 \times 10^{-3}$, $K = 380$; $\mathcal{P} = 0.05$: $r = 5.31 \times 10^{-3}$, $K = 370$; $\mathcal{P} = 0.01$: $r = 3.18 \times 10^{-3}$, $K = 361$.

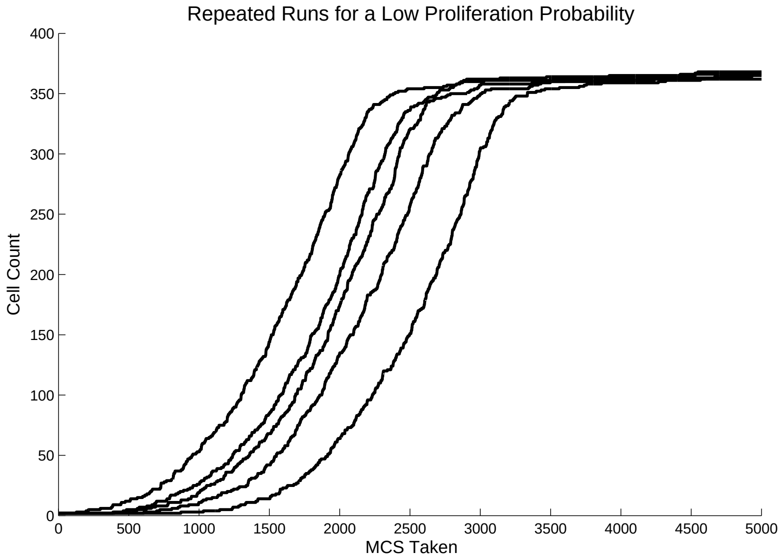

Figure 5.3: Repeated simulations for a low value of the proliferation probability (here $\mathcal{P} = 0.01$) demonstrate a 'shifting' effect resulting from stochastic variation when the cell count is small. The upper portions of each graph all show a roughly equivalent proliferation rate, but the curves are parallel instead of incident because the varying time of onset of logistic growth.

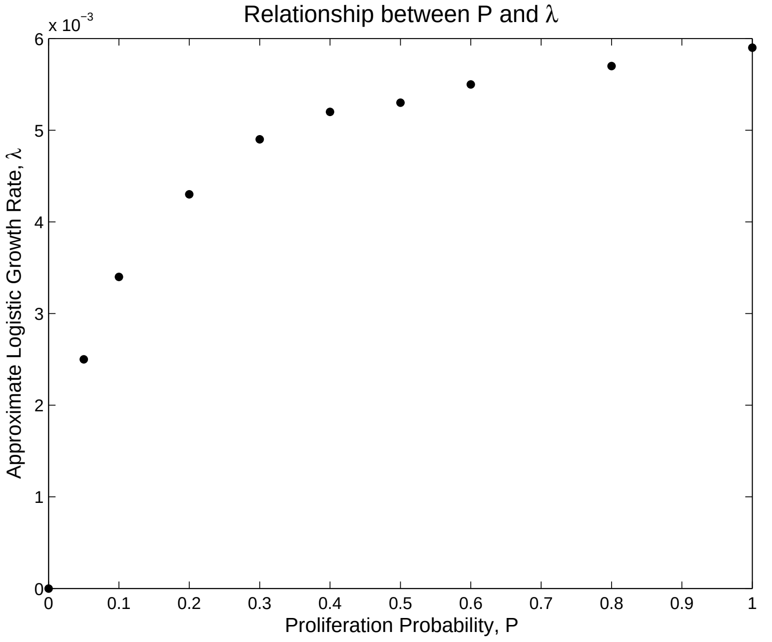

Figure 5.4: Relationship between cell proliferation probability and the simulated growth rate. Parameters are given in Table 5.1. When $\mathcal{P}$ is small it is the limiting factor for the rate of proliferation, but as it is increased the availability of free space and the time required for completion of the cell cycle instead control the mitotic rate.

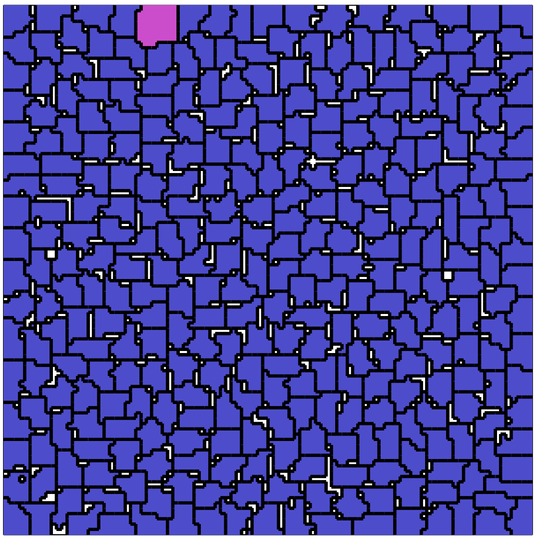

Figure 5.5: State of confluence reached under the reversely adhesive regime. For a sufficiently low value of the proliferation probability (here $\mathcal{P} = 0.01$), the minimum energy state still features gaps between cells.

The effect of changing the adhesive regime was found to have an effect on the proliferative growth curves, as is demonstrated in Figure 5.6. The non-adhesive and reverse adhesive schemes support the initial growth of the colony when it is not limited by space (reduced surface tension promotes cell expansion into unoccupied space), and thus display a much higher rate of proliferation overall. The non-adhesive regime reaches the same steady state of the entire domain being filled with cellular material, but in the reverse adhesive regime contacts between cells and empty sites are favoured, and thus only when the proliferation rate is sufficiently high will these spaces be closed in by cells attempting to proliferate - it is possible for a state with disconnected cells to persist and thus effectively reduce the carrying capacity. This is shown in Figure 5.5. Interestingly, the growth curves for the two non-standard adhesive regimes were very similar apart from this difference in carrying capacity. The normally- and non-adhesive regimes on the other hand show very similar carrying capacities but different growth rates. This is due to the effect just discussed, where space can persist between cells when using the reversely adhesive regime. It should also be noted that this reverse effect is not a general repulsive effect in the same way that adhesion is not a general attractive effect. Even for extreme J values, the confluent population would still only display small gaps between cells.

Values of the calculated proliferation rates and carrying capacity for a variety of $\mathcal{P}$ values under the three different adhesive regimes are given in Table 5.2. The proliferative rate has been calculated by curve-fitting the temporal population data after discarding population values less than 5% and more than 99% of the maximal population, in order to avoid the stochastic

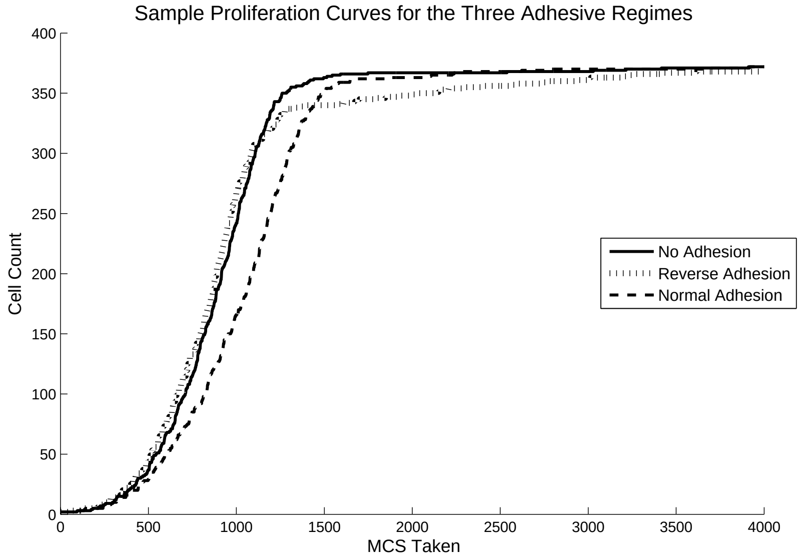

Figure 5.6: Example growth curves (single runs) observed under the three different adhesive regimes listed in Table 5.2. It is seen that the normally- and non-adhesive regimes share a carrying capacity, whereas the reversely- and non-adhesive regimes seem to share the proliferative rate. $\mathcal{P} = 0.05$.

effects which occur at very low cell numbers and the effects of the domain boundaries at high cell numbers. The calculated proliferative rates were averaged over 10 repeated simulations to further minimise stochastic effect. The carrying capacity was calculated by averaging the maximum cell count observed across the same 10 simulations. The results show a trend where the population at confluence reaches a maximal value for a certain proliferation rate, but below that rate proliferation is not sufficiently fast to create a good number of cells still trying to proliferate when the domain is filled. This results in a reduction of the maximum population for lower values of $\mathcal{P}$. In addition, the formation of space between cells in the reversely-adhesive regime for low $\mathcal{P}$ values causes a further reduction in the number of cells which occupy the domain when confluence is achieved.

The proliferation rate is of course reduced when the probability of a cell becoming proliferative is reduced, and is also affected somewhat by the choice of adhesive regime due to the varying abilities of cells to expand into free space in the different regimes. When the proliferation probability is small, it becomes the dominant determinant of proliferation rate and the choice of adhesive regime seems to make little difference. There is nothing particularly surprising about these results, but the data in Table 5.3 is very important for lending physical interpretation to GGH model simulations presented in Chapter 6, and the overall confirmation of a logistic trend validates the proliferation routine created here.

Adhesive Regime	**Value of K**	**Value of λ (/MCS)**
Proliferation Probability $\mathcal{P} = 0.2$		
Standard Adhesion	380	6.07×10^{-3}
No Adhesion	380	7.43×10^{-3}
Reverse Adhesion	379	7.24×10^{-3}
Proliferation Probability $\mathcal{P} = 0.05$		
Standard Adhesion	377	4.96×10^{-3}
No Adhesion	375	6.00×10^{-3}
Reverse Adhesion	375	5.74×10^{-3}
Proliferation Probability $\mathcal{P} = 0.01$		
Standard Adhesion	371	3.06×10^{-3}
No Adhesion	370	3.62×10^{-3}
Reverse Adhesion	360	3.59×10^{-3}
Proliferation Probability $\mathcal{P} = 0.0025$		
Standard Adhesion	363	1.56×10^{-3}
No Adhesion	362	1.76×10^{-3}
Reverse Adhesion	325	1.75×10^{-3}
Proliferation Probability $\mathcal{P} = 0.001$		
Standard Adhesion	360	0.92×10^{-3}
No Adhesion	361	0.93×10^{-3}
Reverse Adhesion	308	0.93×10^{-3}

Table 5.3: Macroscopic parameter values arising from curve fitting of the logistic equation to data produced by GGH model simulation of space-limited proliferation. The effects of the proliferation probability $\mathcal{P}$ and the different adhesive regimes listed in Table 5.2 are demonstrated.

5.4 Conclusions

Proliferation is a key cellular behaviour that has not seen widespread inclusion in the CPM or GGH model and as has been demonstrated here via review, does not possess one single accepted approach for its implementation. It is for this reason that a unique approach for implementing proliferation has been presented here, its primary point of differentiation being the creation of a separate cell phenotype which represents proliferating cells and is used to allow the differing properties of mitotically active cells in the scratch assay context to be captured by the GGH model. Cells enter and leave this alternate phenotype according to how able to grow in size they are, and thus the effects of contact inhibition of proliferation are phenomenologically included by the fact that cells surrounded by other cells will not be able to grow to the required size to become proliferative and/or actually proliferate.

Given the novel nature of the proliferation routine implemented in the GGH model here, verification that it correctly predicts desirable proliferation qualities is of great importance. This has been achieved by demonstrating that for a range of different adhesive regimes, and different proliferation probabilities $\mathcal{P}$, the GGH model simulates logistic growth as desired [194]. The relationship between $\mathcal{P}$ and the observed growth rate has been explored (Figure 5.4) but found to be complex, and the point has been raised that such growth rates are defined in terms of the rather arbitrary simulation parameters of MCS as opposed to any physical timeframe. A means of relating Monte Carlo steps in the GGH model to the passage of physical time for a certain cell type is presented in Chapter 6. This also removes some of the arbitrariness in choosing a value of $\mathcal{P}$.

Three adhesive regimes have been presented as options for use in the modelling of the healing of a wounded monolayer to come. Here all have been seen to maintain logistic growth behaviour or something very close to it, and a reduction in confluence population when simulating under the reverse adhesion regime has been clearly observed and characterised.

With an appropriate and tested means of incorporating proliferation into the GGH model, along with the chemotaxis implemented in the previous chapter, the GGH model has been fully defined and constructed as necessary for its application to the specific biological experiment considered in this thesis, the scratch assay. The GGH model used here represents a powerful means of simulating and exploring cell behaviours at the scale of individual cells, including provisions for contact inhibition of both migration and proliferation, tracking of proliferating cells which behave entirely differently to quiescent cells, and a natural response to chemical signals which matches expectations informed by population-level modelling of chemotaxis.

Chapter 6

The Scratch Assay

6.1 Methodology and Purpose

The scratch assay, also known as the scrape assay or wound healing assay, is an experimental procedure which is used to observe and study the migration of cells with an attempt at replicating *in vivo* conditions. The key idea of the assay is to prompt new migration and proliferation in an already-established population of cells, removing some degree of the artificiality of *in vitro* experimentation. The process is described in experimental detail by Liang *et al.* [110], including a comparison highlighting the strengths and weaknesses of the simple scratch assay compared to other similar experiments that study cell migration. Modifications to the experiment allowing for the tracking of individual cells are also provided in experimental detail in Liang *et al.*'s publication.

The process begins by establishing a confluent monolayer of cells in culture, with the culture dish previously treated with different kinds of serum and coated with appropriate ECM substrate to better resemble the intercellular medium of *in vivo* conditions. From here, a straight scrape is made using any appropriate object (commonly a pipette tip), creating a gap in the cell colony. Repeated photographic images are then taken and used to track the behaviour of the culture as the cells proliferate and migrate to fill in the gap and return to a confluent monolayer. By comparing these photographs, and marking specific locations on the culture dish with an ultrafine marker, the invasion speed can be calculated, and with the addition of a genetic marker and use of a fluorescent microscope the migratory behaviour of individual cells can also be tracked.

The scratch assay is not the only type of *in vitro* experiment that generates simple waves of cellular invasion without incorporating additional complexities. A primary example of an alternative is what is termed here the *circle migration assay* following Sengers *et al.* [169], in which cells are grown within a cloning cylinder in order to form a circular monolayer seeded onto the experimental plate. When the cloning cylinder is removed, the cells now have empty space which they proliferate and migrate to fill, just like the wounded portion in a scratch assay. Both assays treat the culture dish with medium in order to better replicate *in vivo* conditions and thus differ for the most part only in geometry. Although in the scratch assay case the healing is in one direction, the radial expansion of cells in the circle migration assay can also be thought of as a uni-directional cellular invasion problem when considered in polar co-ordinates. Thus experimental examples and mathematical modelling of this second type of assay is considered of essentially equal importance to that of the scratch assay. One key difference is that one type features a physical act of wounding, and the other simply an exposure to empty space, and this has been demonstrated for one cell type at least to significantly affect healing [137].

Scratch and circle migration assays have been performed using several different types of cell including for example airway epithelial cells [212], peritoneal mesothelial cells [114] and mouse 3T3 fibroblasts [26]. Different types of cell tend to show roughly equivalent invasion speeds, although very different invasive profiles, including the results of Sengers *et al.* who showed that two different cell types in a consistent cell migration assay showed notably different invasive wave profiles [169]. One of these cell types, MG63 osteoblast-like cells, was chosen as the model cell in the simulations here in order to inform parameter choices, given the easy availability of experimental data in the work just referenced.

Another relevant experimental setup that demonstrates migrating and proliferating cells and has seen a good deal of similar mathematical modelling (reviewed below) is the colonisation of the hindgut by neural crest cells in chick embryo morphogenesis (for example [181]). The *ex vivo* nature of these experiments invites the possibility of a great deal of extra complexity, however this has not been observed in the related mathematical modelling and thus results relating to these experiments are thought to be very applicable to the scratch assay also.

In addition to the types of experimental setup described above, there are several other types of assay also aimed at examining cellular migration, though these are not explicitly considered here. A review of the various techniques used to analyse both directed and undirected cell migration is provided by Entschladen *et al.* [46].

6.2 The Mathematical Problem

6.2.1 Rationale

Scratch assays present a powerful tool for mathematical analysis, because they can be easily represented mathematically (at least, the features unique to the scratch assay - the general difficulties of truly representing the complexities of cells remain) and are also easy to perform experimentally. In this type of assay there are perhaps no significant cellular behaviours except for cell migration and proliferation. This migration may have a tactic component, for example if seeded fibroblasts establish their own collagen substrate [102] and thus possibly generate a haptotactic gradient, as posited by Cai *et al.* [26]. As has been reviewed in the relevant sections of this thesis, the simulation of tactic and/or random migration and proliferation is possible on the scale of both individuals and a population.

In this work, the experimental procedure serves to inform the mathematical simulations, providing context and data regarding travelling waves of cellular invasion. However, while direct matches between experimental observations and the mathematically simulated results are desirable, what is most important here are the general predictions made by the various models and modelling frameworks, and how these might relate back to the underlying biology. That is, the focus is on the types of travelling wave predicted by PDE models and a specific type of cellular automata (the GGH model) and how the speeds and shapes of these waveforms can be related back to the underlying biology.

To test the conclusions reached, the scratch assay is also considered on a heterogeneous domain (see Chapter 7) and without reducing the problem to one dimension, leading to more complicated travelling waves with different wavefront profiles. Such a thing has not previously been considered using any sort of mathematical model or analysis tool. To the best of the author's knowledge, a scratch assay experiment has not been performed in a heterogeneous environment either, though theoretically could, for example by pre-treating only half a culture dish with ECM, or if an appropriate boundary between regions cannot be constructed, a half-flat half-torturous [92] or half-soft half-rigid [111] base structure could be used to produce different migration velocities in the two regions. Regardless of its experimental feasibility, Chapter 7 demonstrates just why this is a very interesting 'thought experiment' at the very least.

6.2.2 Modelling History

The scratch assay and the aforementioned related experiments have been modelled mathematically in a few different ways, but the general questions which said models uncover and explore are far from answered. Primary are the publications by Maini *et al.* [114, 115], where experimental data from a scratch assay using human peritoneal mesothelial cells were compared to travelling waves predicted by Fisher's equation. However, earlier publications have also used Fisher's equation to simulate *in vitro* cellular invasion situations [187]. Fisher's equation showed a good overall fit with experiments, although Maini *et al.* observed that the fronts predicted by Fisher's equation were more diffuse than those observed experimentally [114]. This was a trend further explored by Sengers *et al.* in a circle migration assay, who discovered that the standard Fisher's equation was appropriate for one type of cell (human bone marrow stromal cells) and that the sharp-front Fisher's equation (using an increasing function of cell concentration for the diffusivity) was appropriate for another type of cell (human osteosarcoma MG63 cells).

A decreasing function of concentration for the diffusion coefficient has also been used to model the healing of an artificial wound in a scratch assay of mice 3T3 fibroblasts [26]. It was found that using this decreasing diffusivity function to model contact inhibition made very little difference to the macroscopic result (including both wavespeed and front shape), but that an individual-cell-based cellular automata showed significant differences in the movements of single cells at different locations within the wavefront. In the same work individual cell tracking in the experimental assay showed that cells in a low-density population did indeed show a significantly greater amount of movement compared to cells in a higher-density population. These observations were made during the formation of a monolayer in the scratch assay experimental setup (but without artificial wounding), and thus support the use of a contact inhibited diffusion term. Cell tracking during the healing of a wound also showed that cells at the front of the wave (where the population density is lower) showed greater movement, but cells behind the wave also migrated biased in the direction of healing.

This work from Cai *et al.* [26] and another publication by Tremel *et al.* [194] including the same group of authors also explored how appropriate the use of the logistic growth term in Fisher's equation is by comparing experimental observations of cell count to logistic growth curves. The agreement was very good, suggesting that this form of the growth term is indeed suitable, at least in the case of a proliferating monolayer. Thus it is at the very least a good starting point for mathematical simulations of the healing process under the same experimental conditions. Following this thought process, any individual-cell-based method which is used to model and simulate the scratch assay should also demonstrate a logistic-like proliferation of cells, at least during the formulation of a monolayer. The GGH model used in this thesis has indeed been shown to satisfy this property in Section 5.3.

Another model of a wound healing assay of mouse 3T3 fibroblasts by Landman *et al.* [103] explored the fact that these cells detach from the substrate they are crawling over while proliferating, and that these proliferations can be seen to occur behind the wavefront. This was achieved using a pair of coupled PDEs, with only attached cells able to migrate (via simple diffusion unimpeded by unattached cells). Two models were developed, one in which only cells with sufficient space elected to migrate, resulting in proliferation occurring at the wavefront, and another where proliferation occurred anywhere but reattachment could only occur where there was sufficient space. In the first case the model reduces to Fisher's equation if the rate of reattachment is sufficiently fast compared to the rate of detachment, whereas the second case does not in any mathematical circumstance. The second case with proliferation possible behind the wavefront matched the experimental observations for this type of cell, and it was found that the travelling waves of invasion generated in this case had a shape strongly dependent on the death rate of unattached cells, and that for careful choice of this parameter the resulting travelling wave almost exactly matched that observed for the general Fisher's equation.

Returning to the work of Sengers *et al.* [169], they explored the idea that cells behind the wave show decreased migration and yet their simulations suggested that a mathematical model with the opposite trend (random motility increasing with cellular concentration) was appropriate at least for one of their cell types. It was pointed out that in cell invasion situations, overall cell migration is towards unoccupied space and thus an increase in cell density in the opposite direction would actually further drive cells in the direction of healing because the amount of movement away from the direction of healing would be reduced. Thus in a sense contact inhibition of migration is perhaps better modelled with an *increasing* diffusivity, and that this form of function can actually be derived by assuming that cell velocity is proportional to the gradient of free space. This interpretation shows that contact-inhibited migration can perhaps be interpreted using an increasing 'diffusivity' function, but that this function and its associated constant does not represent diffusion (or a rate of random cell motility) at all, but instead a macroscopic overall velocity. This is an interpretation favoured here also.

This alternate interpretation of diffusion that seeks to represent the effects of cell-cell collisions still neglects any chemical effects, and the assumption that the cell velocity is directly proportional to the gradient of free space has not been strictly verified. Indeed Sengers *et al.* themselves found that for their other considered cell type, a normal diffusivity function was in fact appropriate [169]. Additionally, using a gradient of free space to drive cell migration results in zero migration behind the travelling wavefront, but for some cell types individuals behind the wavefront do move (and overall in the direction of healing), albeit slower than those within the wavefront region [26, 212].

A very interesting recent publication from Simpson *et al.* suggested that at least the different invasive patterns between the two different cell types of Sengers *et al.* [169] could potentially be explained by including the effect of the cells' aspect ratio into the modelling [176]. They used a CA model featuring rectangular cells and then derived continuum equations from this which demonstrated that roughly-round cells obey Fisher's equation, whereas strongly elongated cells obey a Fisher's equation with degenerate diffusion which would generate sharper invasion fronts like those observed for the MG63 cells of Sengers *et al.* [169] or the peritoneal mesothelial cells of Maini *et al.* [114] which as can be seen in their photographic images are indeed strongly elongated (rod-shaped).

The *ex vivo* studies of the colonisation of the chick hindgut by neural crest cells use the same sort of mathematical modelling, featuring the same key elements of cellular proliferation and migration, and an absence of conflating factors [176, 179, 180, 181]. Moreover, in this situation, donor quail cells can be implanted which then also proliferate and migrate, but can be distinguished in order to determine where cells at the wavefront move in relation to others.

Indeed, this problem has essentially been considered as a general cellular invasion problem by the authors, albeit with *ex vivo* experiments to draw data from. The extra potential complexity of the situation may or may not counterweigh the benefits of comparing simulations to a 'real' biological experiment, but regardless of that these publications are interesting due to the essential equivalence of the mathematical models being used to simulate neural crest cell invasion and the wound healing assay, and the types of questions that the authors are exploring and trying to answer. Indeed, the same authors also considered an unspecified cell migration problem using the same types of mathematical model [178].

The chick hindgut publications sought to explore the difference between models of cell invasion operating at the population level and the individual cell level, including the relation of parameters in a simple cellular automata to a modified Fisher's equation [180]. The two models at different scales were then used to attempt to answer how different migration mechanisms can be distinguished [178], given that at a macroscopic level the different PDE models are essentially indistinguishable [179]. A series of very interesting experiments made full use of these grafted quail cells by placing the graft in different locations and in some cases elminating the proliferative ability of the quail cells genetically, also modelling these situations mathematically [181]. The combination of these experiments served to allow a variety of explanatory models of neural crest invasion to be tested for their ability to explain the experimental results. The conclusion was that proliferation drove the cellular invasion wave, and that cell migration served simply to allow cells to move into empty space to proliferate - behind the frontal part of the wave, cells were effectively stationery and cells behind the 'vanguard' section of the wave remained behind it during the invasive process. The observation that mitosis occurred most significantly at the wavefront was supported by genetic labelling via BrdU demonstrating this fact. The mathematical model used in these simulations was a simple Fisher's equation with two species of cells representing the donor (quail) and host (chick) cells, interacting only through the fact that both cell types contributed to the maximal density in the reaction term. When the donor cells were artificially rendered unable to proliferate before being grafted as a new wavefront (cell vanguard), they failed to colonise the rest of the gut. However, host chick cells from behind the implanted vanguard were able to migrate past it, and then begin to proliferate and eventually colonise the gut despite the 'blockade' of non-proliferative cells. Thus either the grafted population was not dense enough to prevent migration from host cells, or the conclusion in that work that cells behind the vanguard hardly move is not correct. The nature of their diffusive terms assume that the two cell populations are entirely free to mix independently of the presence of the other, and the effect of a diffusion term representing cells blocking others like Sherratt's suggestion [173] would be very interesting to see.

Some cellular automata models of the scratch assay have been discussed above where authors have compared them to PDE-driven approaches, but these have generally been simple models created for the sake of these comparisons, and more complex considerations of the scratch assay and related experiments working at the scale of individual cells can also be seen in the literature. Most important of these are those using the GGH model as discussed immediately below, but a few general examples are also reviewed here. Agent-based models of the healing of monolayers of epithelial cells (and their reaction to calcium) [205] and L1 fibroblasts [18] have used complicated formulations to recreate healing monolayers, the latter using a rather unique concept of two-compartment cells to determine where contact inhibition of mitosis is occurring.

The GGH model has in one case been used to model a scratch assay, by Ouaknin and Bar-Yoseph [141]. However, their model did not feature any kind of proliferation, thus restricting simulations to those which demonstrated fingering expansion into unwounded space but no overall healing or invasive wave behaviour. This fingering expansion was driven by chemotactic response of cells to a chemical they themselves produced when not contact inhibited, and thus is considered here as a variant of the result of Merks who demonstrated a vascular structure (essentially joined fingers) also resulting from a contact inhibited chemotaxis [130], albeit with contact inhibition modelled in a different way. Such fingering patterns have been observed in scratch assay healing [69, 163]. The GGH simulations of invasive waves of tumour cells presented by Turner, Sherratt and Cameron [197, 198] are also of great relevance, because although they operate in a context of cancerous spread, these simulations do not feature behaviours outside of cell interactions (adhesion), proliferation and chemically stimulated migration and thus match the GGH simulations used in this thesis at least in terms of what cellular behaviours are being included. However, those simulations did not use the more realistic form of GGH model adhesion (with negative surface energies) and indeed their presented results for the proliferative case are actually effectively non-adhesive.

Studies of the shapes of travelling waves that do or do not include a guided component to their motion are relevant here, given that one objective is to distinguish between the two types of cell motility, guided and unguided. The specific case of chemotactic invasion waves in cellular populations has been analysed in the literature, leading to the consideration of new phase-plane features like ‘walls’ of singularities and their relation to jump discontinuities often seen in tactically-driven waves [154]. Further exploration of these types of travelling wave [104] culminated in a publication by Landman *et al.* summarising previous demonstrations of tactic invasion and deriving necessary conditions for the existence of non-monotonic wavefront shapes [105]. This was a very important result because it showed some previous demonstrations of non-monotonic wavefronts to apparently be spurious, highlighting the importance of a very accurate and robust numerical scheme for strongly hyperbolic problems like these. The analysed PDEs that generated these non-monotonic wave shapes did not feature any diffusion of cells (random motility) or of attractant species (haptotaxis as opposed to chemotaxis). The conclusions in general of these PDE studies are important because they show how a guided component of motion can modify the shape of the travelling wavefront, and what is very interesting is whether or not the same inclusions of a guided component to motion will have the same effect in individual-cell-level models. Basic equivalence between simple individual-cell-based models and the standard Keller-Segel equations has been demonstrated [6, 184]. Moreover, equivalence between the basic Keller-Segel equations and a simple CPM has also been shown [4], albeit by making rather extreme assumptions such as no interactions between cells. That work also used a term of form (4.2) to incorporate chemotaxis, argued in Chapter 4 as undesirable and thus it is interesting that equivalence between the PDE model and CPM model could be shown using this arguably flawed approach.

6.2.3 Unanswered Questions

The existing mathematical modelling of the scratch assay, circle migration assay and other cellular invasion problems has already been able to show a good qualitative match to experimental observations and with reasonable quantitative agreement. However, generally one or more model parameters have been chosen to best match experimental data, and this freedom of choice can mask the underlying behaviour(s) at work [179]. Different types of cells have demonstrated different invasive patterns, including sharp-fronted and diffuse wavefronts [114], and suggestions that cells behind the invasive wave can be effectively stationary [181] or migratory but with a slower velocity [26]. The region of cells which are proliferatory has also been found to vary, though even in the case of mice 3T3 fibroblasts where proliferation was shown to occur behind the wave, the unattached daughter cells were not always able to reattach due to a lack of space in the monolayer [103]. Thus it can be argued that *feasible* proliferation only occurs at the wave, matching observations from other cell invasion problems [181]. Other cell types have been clearly demonstrated to heal even with proliferative effect completely blocked, due to the fact that monolayer cells at confluence occupy a rather cuboidal or more rounded shape, whereas migrating, crawling cells spread themselves more over the surface they are crawling over [47, 137]. Proliferation (if not chemically eliminated as part of the experiment) is still observed in these situations, but is not limited to the front. All of these different observations show the intense dependence on cell type (and possibly to a lesser extent, the nature of the experiment) on overall invasive behaviour, even though this biological context has been chosen for its apparent simplicity.

Thus, the questions to be answered are how various interactions of basic cell behaviour can result in the different types of invasive wave and proliferative pattern that have apparently been observed across various types of cell. Naturally this analysis must involve modelling at the scale of individual cells, given the aforementioned difficulties in distinguishing between different effects at the scale of whole populations. The GGH model is a natural approach here, given that it naturally incorporates proliferative pressure. Do the conclusions about travelling wave shapes also apply to travelling waves that form in GGH simulations? The question of distinguishing between different migratory behaviours is also approached using the idea of non-homogeneous domains, wherein distinct differences between different invasive phenomena could become apparent even on a macroscopic level.

6.2.4 Models Utilised Here

Partial Differential Equations

The use of PDEs to model cellular behaviours in general has been reviewed in Section 2.1.2, with the approaches used in modelling the scratch assay specifically just discussed in Section 6.2.2. The same basic approach is utilised here, namely a generalised Fisher's equation,

$$\frac{\partial C}{\partial t} = \nabla \cdot \Big(D(C) \nabla C - \chi(C,S) C \nabla S \Big) + \lambda C \Big(1 - C \Big). \tag{6.1}$$

In very brief summary, this is the typical multi-dimensional Fisher's equation, with the inclusion of a chemotactic cellular response and a functional form for diffusion. Following the literature review in Section 2.1.2, the chosen forms for the motility coefficients are

$$D(C) = D_0 C \qquad\qquad \chi(C,S) = \chi_0 \frac{K}{(K+S)^2}(1 - mC). \tag{6.2}$$

Here D_0 and χ_0 are baseline strengths of unguided and guided motility respectively, and m is a parameter referring to the degree to which chemotaxis is impeded by contact inhibition of migration. In previous studies using a 'volume-filling' term like this, this term was not included as a parameter but simply chosen as $m = 1$, corresponding to a complete switch off of chemotactic migration in regions fully occupied by cells ($C = 1$). Given that biased (and thus potentially tactic) migration has been observed behind the travelling wavefront in scratch assay situations [26, 47], the possibility of $0 < m < 1$ is explored in this thesis. To reiterate, the term D_0 does not represent the diffusion coefficient but is instead directly related to the motility of cells in response to cell concentration gradients (representing the net effects of contact inhibition of migration).

In the case of a gradient not consumed by cells and simply passively present to guide cell migration towards the wound space, the concept of saturation does not apply and an alternative form of the chemotaxis coefficient removing saturation effects,

$$\chi(C,S) = \chi_c(1 - mC), \tag{6.3}$$

is used instead.

The chemical concentration must also be modelled via continuum PDE, although various different chemical situations are considered, as is described in Section 6.3.1. The approach used here is standard, namely the continuum equation featuring the possibility of simple, constant-coefficient diffusion, and a source/sink term modelling the production and/or consumption of signalling chemical. Mathematically, that is

$$\frac{\partial S}{\partial t} = D_S \nabla^2 S + f_S. \tag{6.4}$$

The boundary and initial conditions of a scratch assay which is modelled by PDEs are extremely simple and are seen in all of the previously mentioned references. A scratch is being made and cellular debris is washed away, so the unwounded region on one side of the scratch remains at confluence ($C = 1$), and the other side of the scratch is entirely devoid of cellular material ($C = 0$). Expressed mathematically,

$$C\big|_{t=0} = \begin{cases} 1 & (x \le x_b) \\ 0 & (x > x_b), \end{cases} , \tag{6.5}$$

where $x = x_b$ is the location of the scratch. This is an initial condition possessing compact support, a classification important for determining the speed of travelling waves that will evolve from it. The boundary conditions are also very simple, but actually technically correspond not to the scratch assay but to the circle migration assay. That is, no-flux boundary conditions are used so that there is no external source of cellular material, expressed mathematically as

$$\mathbf{J} \cdot \mathbf{n}|_{x=0} = \mathbf{J} \cdot \mathbf{n}|_{x=L_x} = \mathbf{J} \cdot \mathbf{n}|_{y=0} = \mathbf{J} \cdot \mathbf{n}|_{y=L_y} = 0. \tag{6.6}$$

This is important because although a Dirichlet condition can be easily implemented in the macroscopic model, creating a fixed concentration of cells at the boundary in the GGH model is very difficult. This choice of course necessitates care that the healing front does not reach the boundary, to prevent any interference of boundary effects. The domains parallel to the direction of healing also use no-flux boundary conditions, representing an artificial boundary like the edge of the plate in which the scratch assay occurs. This choice ensures that the problem can be treated as one-dimensional in the case of a homogeneous domain, because the initial condition does not vary in the y direction.

It should be noted that this choice of initial and boundary conditions corresponds to only one 'half' of the scratch assay, in the sense that a real healing scratch involves two advancing fronts which meet to close the wound but here only the advance of one front into wounded space is considered instead. This is because the focus is on the travelling waves which develop, not on what happens when they meet.

The initial and boundary conditions for the chemical depend on which chemical situation is being considered, discussed below in Section 6.3.1. The initial conditions are either a specified concentration gradient (constant slope), or the whole domain is initially entirely occupied by chemical, corresponding to the resupply of serum right after the scratch is made in the scratch assay procedure. In the first case, the boundary conditions simply match the specified slope (which doesn't vary temporally anyway) by holding the edges fixed at matching concentrations with Dirichlet boundary conditions. In the case of a dynamic chemical concentration, the boundaries are no-flux, and the nature of the problem means there is almost no flux near boundaries anyway regardless of this condition (even when the chemical is diffusible). These specifications refer to the boundaries parallel to the scratch (here the left and right boundaries, $x = 0$ and $x = L_x$). The boundaries perpendicular to the scratch are always no-flux, allowing for the homogeneous scratch assay to be considered as a one-dimensional problem, just like with the conditions on the cellular concentration, C.

The GGH Model

The GGH model has been used to successfully model other cellular invasion problems in a tumour context, with problems resembling both the scratch assay [197, 198], and the circle migration assay [157, 158] albeit with the incorporation of additional tumour-relevant factors such as necrosis. Thus it is certainly considered to be an appropriate choice of modelling framework here, in representing the scratch assay on the scale of individual cells. Integral to CPM/GGH models due to their emergence from modelling Steinberg's differential adhesion hypothesis

[183] is the contribution to the total energy resulting from adhesion between cells and between cells and the medium. However, an issue barely explored is the concept of an 'adhesion-less' CPM/GGH, where cells are able to deform according to membrane and body inelasticities, respond to chemical gradients and proliferate but do not adhere to each other. When using a constrained membrane length, the surface tension built into the adhesive energy between cells and medium is not required to have cells maintain round shapes. An adhesion-less CPM/GGH model still offers the advantages of representing cell shapes and their pushing forces on each other which most other cellular automata models fail to capture. Moreover, evidence in scratch assay experiments has demonstrated that cells (at least bovine corneal endothelial cells) in fact internalise their cadherin and thus presumably break cell-cell contacts when they become migratory [71]. This would of course be modelled in the scratch assay by setting the value of J between cells to zero. The effect of removing all adhesive effects from the GGH model on chemotaxis has been shown in Section 4.3.6 to hinder the ability of cells to push into each other. However, if cells are not connected (and thus more free to move, as also shown in Section 4.3.6), then turning off adhesion will prevent cells from joining together and thus overall migratory effect would be expected to increase.

The GGH model is used here to model the scratch assay, making use of the advances discussed and explored in Chapters 4 and 5 to include the cell behaviours of chemotaxis and proliferation via the implementations presented in those chapters. The basic choice of parameters used in simulations here is the set listed in Table 5.1. It should be remembered here that the choice has been made that proliferating cells do not respond to the chemical signal, only normal (quiescent cells), as also mentioned in Chapter 4. This choice follows population-scale mathematical models [103, 155] and experimental observation that migration is significantly decreased in proliferating cells [85]. The scratch assay is simulated by first filling the rectangular 2D domain with rectangular cells at a volume slightly lower than that which triggers proliferation (6x5 sites in shape). The overall domain size used is 210x200, thus being initially occupied by 1400 cells. Chemotaxis simulations which involve a larger degree of migration use a domain of double this width. These cells are then allowed to proliferate to a state of confluence, because due to small random fluctuations in cell size some are able to proliferate even with the domain initially fully occupied by cellular material. Once sufficient time was allowed for cells to reach a stable state (500 MCS), a scratch was simulated by choosing a 'wound edge location', a vertical line through the 2D domain. All cellular material on one side of this line were deemed as being removed by the scratch, the sites they occupied having their state changed to medium ($\sigma = 1$). After performing the scratch, cells which fell below a volume of 20 as a result of the cut were determined to have died and been washed away as cellular debris in the process of the experimental procedure [110]. The cells deemed as washed away had all sites they occupied also set to medium ($\sigma = 1$). Any proliferative cells which are scratched but survive revert back to a quiescent state.

One potentially notable omission is the lack of any sort of nutrient dependence of the mitotic behaviour of the cells, though the PDE models also do not consider a nutrient-dependent proliferation. If nutrient can be assumed to be well supplied and thus only lacking in the case of cellular competition, then proliferation would only be limited by this factor when many cells are present. The implementation of proliferation used here does capture this overall effect through its representation of contact inhibition of proliferation, as demonstrated in Chapter 5. Another issue not considered in the GGH implementation here (though surely realisable by an extended model) is the importance of the 3D shapes of cells, capturing the nature of cells to spread more over the substrate when they have sufficient space, and 'round up' otherwise [47]. The 3D nature of cells' lamellipodia extensions pushing under neighbouring cells demonstrated in the same publication might also prove important, and cannot be represented reasonably in a 2D simulation.

The number of cells involved in these simulations might be judged as being too small to allow appropriate comparison to results obtained at a macroscopic scale. However, the larger the simulation domain is (and/or the number of cells in it), the longer each simulation takes to run. Thus the issue of scale was briefly explored in a series of additional simulations where the vertical size of the domain was varied in order to ensure that this did not affect results. Varying the number of cells in this way was found not to affect predicted invasive velocities or structures but did naturally affect the amount of stochastic variation. Using repeated simulations over a moderate scale is faster than a smaller number of large-scale simulations, so that was the approach taken here.

The inclusion of a chemical response as a cell behaviour necessitates a means of handling how the chemical concentration itself varies with the passage of time in the cases where it is dynamic. The goal is to simulate the effects of the equation (6.4) but in the GGH model, thus incorporating the two effects of diffusive spread and consumption by cellular agents. Diffusing acting on a discretised domain requires no special consideration and can be handled in the same manner described in Section 2.2.1. However, the consideration of the source term f_S is a bit different. There is no longer any macroscopic cell concentration to refer to, only the fact of whether a given lattice site is occupied by a cell or not. Thus, an occupied site is considered to correspond to a concentration of $C = 1$ in the functional form $f_S(C, S)$, an unoccupied site similarly corresponding to $C = 0$. Doing this, and labelling the current occupation of each site (zero or one matching C) as γ, the term f_S will always depend linearly on S, and after the application of Crank-Nicholson timestepping approach (chosen for accuracy) the equation (6.4) can instead be written

$$\begin{aligned}
-\left(\frac{D\Delta t}{2\Delta x^2}\right) S^{\text{new}}_{i+1,j} - \left(\frac{D\Delta t}{2\Delta x^2}\right) S^{\text{new}}_{i-1,j} - \left(\frac{D\Delta t}{2\Delta y^2}\right) S^{\text{new}}_{i,j+1} - \left(\frac{D\Delta t}{2\Delta y^2}\right) S^{\text{new}}_{i,j-1} \\
+ \left(1 - \frac{D\Delta t}{\Delta x^2} - \frac{D\Delta t}{\Delta y^2} + \frac{1}{2}\gamma \Delta t \lambda_s\right) S^{\text{new}}_{i,j} = S_{i,j} + \left(\frac{D\Delta t}{2\Delta x^2}\right) S_{i+1,j} + \left(\frac{D\Delta t}{2\Delta x^2}\right) S_{i-1,j} \\
- \left(\frac{D\Delta t}{2\Delta y^2}\right) S_{i,j+1} + \left(\frac{D\Delta t}{2\Delta y^2}\right) S_{i,j-1} - \left(1 - \frac{D\Delta t}{\Delta x^2} - \frac{D\Delta t}{\Delta y^2} - \frac{1}{2}\gamma \Delta t \lambda_s\right) S_{i,j}. \quad (6.7)
\end{aligned}$$

This equation can then be solved as a matrix system, with a simple banded storage approach used here to cut down on memory usage and computational time. The equation (6.7) is solved to obtain the updated chemical concentrations at each lattice site once every Monte Carlo step (MCS). The GGH model implementation here uses square lattice sites ($\Delta x = \Delta y$), as is standard because it greatly eases volume and surface area calculations, though this fact has not been noted in equation (6.7) for generality. The method used to assign physical widths to Δx and Δy and similarly the length of time represented by one MCS Δt is discussed below.

The saturation effect used in some simulations (represented by equation (6.2) at the population level) also needs to be incorporated into the chemotaxis term (4.4) here in the GGH model, and this is done simply by making μ a concentration-dependent function [63]. The concentration values used for the local value of S in order to evaluate this function are the average of the concentrations at the two neighbouring sites selected for each trial update.

The results of all simulations using this framework are presented in Section 6.3.

6.3 Analysis

6.3.1 Scope of This Analysis

On the population scale, travelling waves have been quite deeply explored and so the simulations discussed here serve more as a further test of the finite volume solution algorithm and to provide a solid basis with which to compare the cellular Potts model simulations. On the other hand, while travelling waves of various types have been predicted and generated by the CPM and GGH model, a thorough analysis like the one presented in this section, Section 6.3 has not been presented in the literature. Given that the aim is to answer questions about differentiating between different types of invasive cell migration and proliferation, no single model for the scratch assay is chosen, and instead a variety of different possibilities are all considered.

The CPM/GGH models suffer from the issue of parameter values being far less obvious than is the case for macroscopic models, making comparison between the two scales all the more difficult. It is possible that mean square distances (MSDs) could be calculated and thus used to determine a realistic time measure relative to known MSDs or diffusion coefficients measured macroscopically, however it was anticipated that this would result in GGH simulation times that would be far too long to allow for quantitative comparison with the PDE-generated simulations. Also, given their difference in physical scale, the GGH simulations would also require a staggering number of lattice sites in order to accommodate enough cells to facilitate direct comparison with population-level simulations, which again would be computationally unfeasible. So instead, here the problem of scale is tackled in a more roundabout way, with simulations at both scales here interpreted more as demonstrative cases to be potentially generalised from, as opposed to quantitative predictions. This is perhaps a weakness of the results presented, but given the vastly different approaches of IBVP's and the GGH model the author believes it perfectly valid to focus more on the manifested differences in travelling wave simulations due to the severe differences between how the two modelling frameworks represent (or fail to represent) key cellular behaviours.

The presence of a chemical signal and the cellular response to it was handled in several different ways, resulting in a series of different potential models of a scratch assay which might predict healing behaviour. Each situation is representable (by specifying the initial conditions and evolution behaviours for the chemical concentration S) relatively easily within both the macroscopic PDEs and the individual-cell-based GGH model frameworks. Of course, a 'null' scenario is included, in which there is no tactic migration at all and hence all invasion is unguided. In the simulations featuring a guided component of migration, this is always oriented towards the right, and thus simulations represent the left side of a 'wound' formed by a vertical scratch and how it heals. The different scenarios for attractant behaviour were:

1. There is no chemoattractant present (or equivalently, no cellular response to signalling chemicals), and thus all migration is unguided.
2. The chemoattractant is present in a static concentration field increasing linearly in the x direction, unaffected by cellular interaction. This linear increase begins at a chosen location within the unwounded monolayer. This seeks to simulate simple advection, and thus the chemical response of cells is chosen not to saturate with increasing concentration S.
3. The chemoattractant is present at maximal concentration throughout the entire domain to be consumed by cells, but only after wounding do cells begin to consume the material (consumption before wounding need not be considered because serum is resupplied to the monolayer immediately after the scratch is made). This 'nutrient' which acts as an attractant could be diffusible or substrate-bound.

The second situation listed here might seem somewhat unrealistic, given that it involves a perfectly linear gradient that is suddenly established at the moment of wounding. Indeed it is included here less as a perfect model for the scratch assay experiment and more as a 'pure' example of a guided contribution to cell motility. However, an effect of this type could be considered as a result of a cell polarisation towards the wound arising from a wave of chemical signal, for example the wave of MAPK activation observed in scratch assays involving epithelial cells [137]. The polarisation caused by the passing wave would drive cells in the direction of the wound to heal it, but this is suggested to occur not due to cells following the gradient over any protracted timeframe but instead simply becoming active and polarised and travelling at an innate velocity but biased towards the wound, which is what the 'pure advection' case achieves in a very phenomenological way. Informed by observations that these activation waves penetrate quite deeply into the cell mass behind the wound [137], the beginning of the gradient was positioned either half-way inside the unwounded part of the monolayer, or was allowed to encompass the entire domain and cause all cells to respond. Given this line of thinking, the simulations using this non-dynamic, constant chemical response in fact choose a chemotactic sensitivity function which does not use a receptor-derived dependence on the chemical concentration, equation (6.3). The physical effects of cells blocking each other built into the $(1 - mC)$ term remain important and thus are present in both the saturating (6.2) and non-saturating (6.3) chemical responses.

The general movement of cells into free space is incorporated into the PDE models via the non-linear diffusion term in equation (6.1), but in the GGH model diffusive random motion is not naturally included. Cells in the GGH under these parameters exhibit little random motility, especially when adhesively attached to other cells. Thus it may be necessary to include a chemotactic effect in order to drive migration into unoccupied space. Given that the presentation of empty space to an unwounded monolayer also drives migration [137, 163], this reliance on a chemical signal is a potential issue, though the effects of changing differential adhesions (and thus encouraging or discouraging expansion into empty space) is also considered in simulations below. It should be remembered, though, that because the space occupied by cells is specifically tracked in the GGH model, simply proliferation is enough to drive cells forward and may effectively mimic macroscopic observations despite the lack of any direct migratory effect. Indeed, this would suggest cell clusters remain connected and thus should predict sharp wavefronts that might better match those observed by Maini *et al.* [114].

6.3.2 Unguided Invasion

Population Scale

When there is no chemical presence and complete symmetry in the vertical dimension, equation (6.1) reduces to the ubiquitous one-dimensional Fisher's equation but with a non-linear diffusive term modelling contact inhibition,

$$\frac{\partial C}{\partial t} = \frac{\partial}{\partial x}\Big(D_0 C \frac{\partial C}{\partial x}\Big) + \lambda C(1 - C). \tag{6.8}$$

The chemical equation (6.4) is not needed. The scratch assay initial condition is one possessing compact support, thus the properties of the travelling wave are known [174]. The shape of the wave is

$$C(z) = \begin{cases} 1 - e^{\sqrt{\lambda/2D}(x - x_c)} & (x < x_c) \\ 0 & (x \geq x_c), \end{cases} \tag{6.9}$$

where the wavespeed is $c = \sqrt{D_0\lambda/2}$ and x_c is the shifting location of the sharp front (also travelling at speed c).

The finite volume implementation presented in Section 2.2.2 was used to test this result, with the chosen solution method being the one found as optimal in Section 2.3. That is, Crank-Nicholson timestepping with flux limited advection terms, this flux limiting using the derivative-based sensor (2.33) calculated explicitly with a van Leer flux limiter. This same implementation was used to solve all PDE problems discussed in this chapter and the next, except where specifically mentioned. Both approaches for approximating non-linear diffusive fluxes implemented

Parameter	Definition	Value
D_0	Rate of migration into empty space - unguided invasion	$0.011\,\text{mm}^2/\text{hr}$
	Rate of migration into empty space - guided invasion	$0.001\,\text{mm}^2/\text{hr}$
λ	Cellular proliferation rate	$0.023\,/\text{hr}$
χ_c	Tactic response for supplied gradient (6.3)	$0.08\,\text{mm}^2/\text{hr}$
χ_0	Tactic response to 'fast' consumed signal (6.2)	$0.03\,\text{mm}^2/\text{hr}$
χ_0	Tactic response to 'slow' consumed signal (6.2)	$0.10\,\text{mm}^2/\text{hr}$
m	Coefficient of cell blocking of chemotactic migration	0.9
K	Concentration for maximal chemotactic response	0.5
D_S	Diffusion coefficient for diffusible chemical signal	$0.0018\,\text{mm}^2/\text{hr}$
λ_S	Rate of signal consumption by cells - slow	$0.023\,/\text{hr}$
	Rate of signal consumption by cells - fast	$0.46\,/\text{hr}$
Δx	Width of each control volume in spatial discretisation	0.08mm
Δt	Timestep for temporal discretisation	0.1hr

Table 6.1: Base parameters used for the PDE model of monolayer healing of MG63 cells, some parameters taken from Sengers *et al.* [169] and others derived or chosen as explained in the text.

in the solver and listed in (2.29) were found to produce almost exactly the same result, and from this point on all finite volume simulations used the approach of averaging functional values (as opposed to concentrations).

The ability of the finite volume code to predict the known analytical solution (6.8) was first tested using parameters of $D_0 = \lambda = 1$, corresponding to a scaled form of the equation. Under these conditions, the match between the exact and numerically-determined solutions for both the solution profile and the travelling wavespeed was very good, with the wavespeed being slightly larger than $c = 1/\sqrt{2}$ due to the inability to perfectly resolve the sharp front of the wave when using a moderate number of grid points. The wavespeed was tracked by testing for the first location at which the solution profile reached a certain threshold value when searched from right to left.

The good performance of the numerical solver on the scaled version of the equation is heartening, but using a non-dimensionalised equation actually makes comparisons with the GGH model simulations more difficult and thus for the sake of simplicity and applicability an attempt at choosing a realistic set of parameters to use with the unscaled form (6.8) was made. Sengers *et al.* fit this equation to their experimental data for MG63 cells with very good agreement [169] and thus in this work MG63 osteoblast-like cells are chosen as a model cell and the parameters set forth by Sengers *et al.* are used as a baseline. The full set of base parameters for the population-level models used in this chapter is listed in Table 6.1, with explanations of how they have been determined as they are encountered. The values of D_0 and λ used here are taken directly from Sengers *et al.* [169], with λ sourced from their purely proliferative assay (as opposed to their chosen value giving the best fit with experimental data). The discretisation parameters Δx and Δt have been selected to strike a balance between numerical accuracy and computational speed.

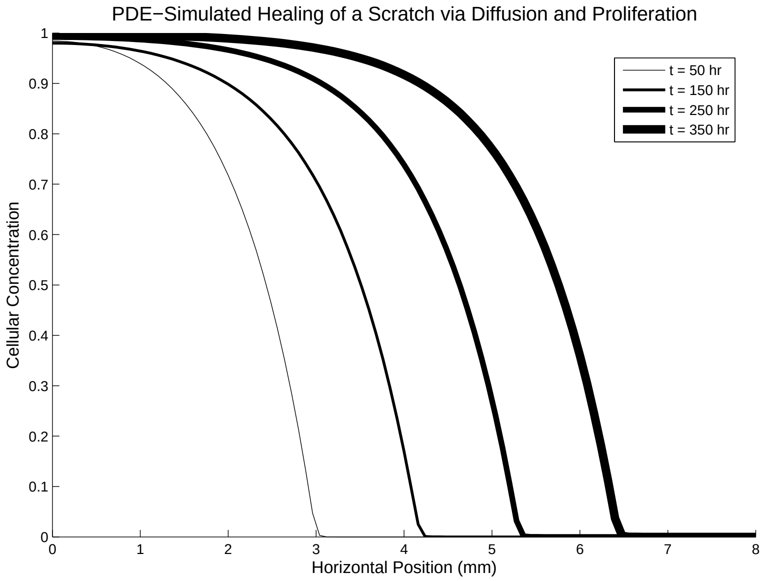

Figure 6.1: Solution profiles for PDE-simulated healing of a scratch of MG63 cells healing entirely via diffusion and proliferation. Darker lines indicate later timesteps, respectively $50\,\mathrm{hr}$, $150\,\mathrm{hr}$, $250\,\mathrm{hr}$ and $350\,\mathrm{hr}$.

The simulated solution profiles obtained here using the discussed parameters and methodology are visualised in Figure 6.1. These simulations did not in fact allow a stationary travelling waveform to form within the simulated timeframe, though when the presented results of Sengers *et al.* were also checked the same observation was found there. This is not largely important, because the rate of expansion into the wounded space in these numerical simulations does quickly reach a constant value after a transitory period from the discontinuous initial condition. The value of this wavespeed was found to match well with what the analytic solution suggests ($c = \sqrt{D\lambda/2} \approx 0.011\,\mathrm{mm/hr}$). This is a slightly lower rate of invasion than the value observed by Sengers *et al.* [169], because the value of λ used here is the one sourced from their cell proliferation data, as opposed to their curve fitting to experimental results. The transitory period before reaching the steady wavespeed showed an initially faster or initially slower rate of healing, depending on which value is chosen as a threshold marking the wavefront location. This is consistent with the results of Maini *et al.* [115], who were using a standard Fisher's equation without a non-linear diffusion coefficient. The transitory behaviour of the wavefront is actually a point of interest, because it is something that can also be considered in the GGH model simulations presented below.

Using these values, the solution curves predicted by the PDE model can be compared to those from the GGH model, once it has also been given a physical scale both spatially and temporally. The travelling waveform (6.9) is a sharp-fronted wave and thus better represents cellular populations which are tightly packed, an expected result of the cell-cell adhesion included in the GGH model (at least when operating under its normal regime).

Individual Cell Scale

When there is no chemical effect included, the GGH model can be run according to the protocol presented in Section 6.2.4, with no ΔH modification corresponding to chemical effect ($\mu = 0$). The three different types of adhesive regime listed in Table 5.2 were each used in different scratch assay simulations, all visualised in Figure 6.2. As is common in 2D cellular automata simulations of cell fronts (for example [180]), the simulation data was easily reduced to one dimension by averaging across the vertical dimension (parallel to the direction of the scratch). This creates a one-dimensional wave profile just like those seen in population-level PDEs, and allows for comparison between the two different types of model. However, care must be taken with regard to stochastic effects, especially given that the GGH model is more computationally demanding compared to most CA approaches and thus is more restrictive in terms of how many agents can be included.

The scratch assays simulated by the GGH model showed a wave of proliferative healing no matter which adhesive regime was used, and this was confirmed to be a proliferative effect because the healing rate depended strongly on the value of $\mathcal{P}$, and indeed for the case $\mathcal{P} = 0$ no healing occurred. While it is obvious that without proliferative effect the artificial wound will not be able to completely heal because there simply won't be enough cellular material to cover the entire space, the migration of cells into the wound space can also be interpreted as a form of healing. This is indeed an important effect, given that proliferation-retarded cells have been shown to heal small scratch wounds by migrating into the open space and occupying more area by flattening out their shapes in adhering to the substrate [1]. This flattening effect is not included in the GGH implementation here, being a limitation of its 2D nature. Moreover, under the standard and non-adhesive regimes cells will not break away from the initially tightly packed cluster, even those at the wavefront with empty space free to move into. Under the 'reverse' regime, there is in fact a slight diffusive spread of cells due to the fact that in this case cell boundaries prefer to be exposed to empty space over other cells. When the simulation begins with the domain completely occupied by cells, there is no free space and the nature of the trial updates used by the CPM and GGH model means that no free space can be created. However when the scratch is made, empty space is now present, and given time this empty space does eventually find its way between the cells, thus causing the population as a whole to occupy more space (corresponding to a slight healing effect). However, even though these cells become separated, they do not show any large degree of motility. Without the inclusion of a more active migratory effect or a cell spreading effect, the 2D GGH model is unable to predict any significant healing effect in this non-proliferative case. This is a point of significant concern, given that it has been assumed here that the random fluctuations of cell membranes could be used to represent unguided motility in the GGH model.

When proliferation is included, the creation of new cellular material easily allows the domain to refill with cellular material after wounding, and indeed this occurs via an advancing wave of cells as was seen in Figure 6.2. The region behind the wavefront completely heals in the

a) Normal adhesion

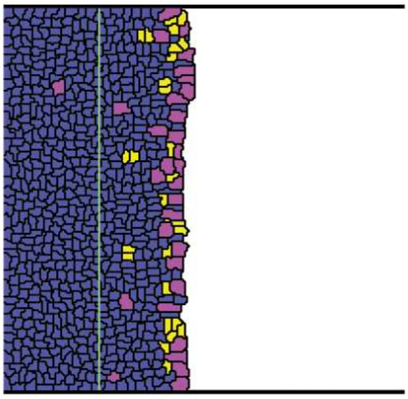

b) No adhesion

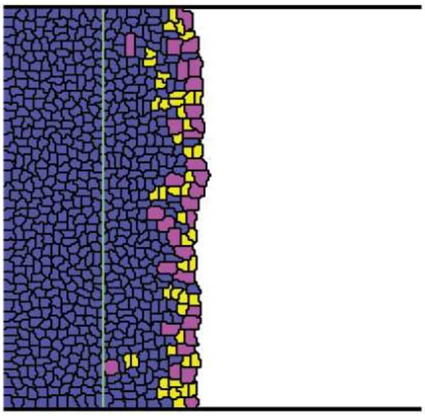

c) Reverse adhesion

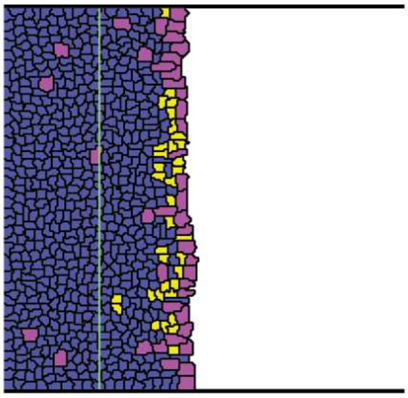

Figure 6.2: Simulated healing of an artificial wound in a monolayer using a GGH model under the three adhesive regimes, using $\mathcal{P} = 0.20$ and an elapsed time of 200 hours. The horizontal width of the domain is $1.2\,\text{mm}$ (slightly different between regimes). The scratch location is marked by the green line. Blue cells are quiescent, purple cells are proliferative and yellow cells are recent daughter cells.

same way the purely proliferative simulations in Chapter 5 did, reaching confluence. Just like in those prior simulations, when the proliferation rate is lowered and the reversely adhesive regime is used, confluence corresponds to a state with gaps between the cells beyond which proliferation occurs. Simulations using a lower value of $\mathcal{P} = 0.01$ which are visualised in Figure 6.3 demonstrate this effect and show the increased roughness of the front arising from the greater degree of stochastic variation. Several key observations remain consistent between the simulations for different values for $\mathcal{P}$. Firstly, both situations demonstrate mitosis limited almost entirely to the wavefront, healing evidently arising due to the space-filling effect of the new proliferations. This is a behaviour apparently consistent with what is suggested for chick neural crest (NC) cells [181] (and a localisation of proliferation has been confirmed with staining), but not for countless other cell types where proliferation is unnecessary for a healing effect and not at all localised to the advancing front [47, 199]. The rate of healing (in terms of MCS, a physical timeframe is discussed below) is dependent on the different surface tensions for cell-cell and cell-medium contacts, with the fastest healing occurring in the reversely-adhesive case because this encourages expansions of cells into empty space as opposed to into other cells. The ability of cells to expand into free space is the important consideration in this case because the greatest majority of proliferation only occurs at the wavefront where cells are not contact inhibited.

Averaged wave profiles for the more interesting case of the lower proliferation value $\mathcal{P} = 0.01$ are displayed in Figure 6.4. In the cases of a normally-adhesive or non-adhesive simulation, the wave profiles are very sharp, and monotonic, as can easily be surmised from the sample visualisations. It is seen that the width of the invasive profile is only several cell lengths, which does not correspond to the diffuse profiles seen in many experimental results presented by other publications featuring mathematical models of the scratch assay [26, 114, 169]. However, photographic images seen in these publications and other scratch assay experiments do for some cell types and experimental conditions show very tightly-packed wavefronts with sharp-looking fronts. In these cases the more diffuse profiles seen upon ‘zooming out’ to obtain macroscopic data might be a result of scratches that are not perfectly straight or other experimental imperfection. Alternatively, it could result from a kind of biological stochasticity inherent to cells that is not represented by the stochastic updates of the GGH model or possibly achievable via a lower value of $\mathcal{P}$ to increase the degree of stochasticity. Given these possible alternate explanations which seem to better match photographic images of healing monolayers, the sharpness of the wavefronts observed here is not considered to be a major weakness of the simulations. Nevertheless, the ability of the GGH model (as implemented here) to predict more diffuse wavefronts which heal realistically remains of critical interest.

For some choices of $\mathcal{P}$, the reversely-adhesive regime can result in a more interesting behaviour, where although a standard confluence behind the proliferation-driven invasive wavefront is observed, the cell concentration at the front is actually *larger* than the concentration immediately behind it. This sort of invasion is visualised in Figure 6.5, and the average wave profile averaged across 50 such simulations is shown in Figure 6.6. This occurs because the trend

a) Normal adhesion

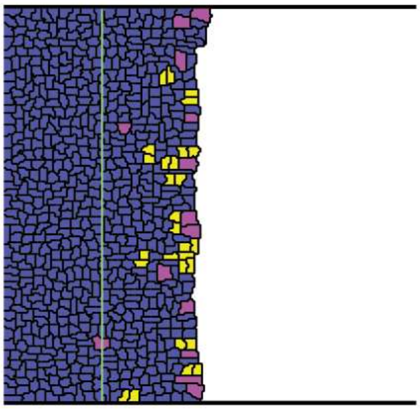

b) No adhesion

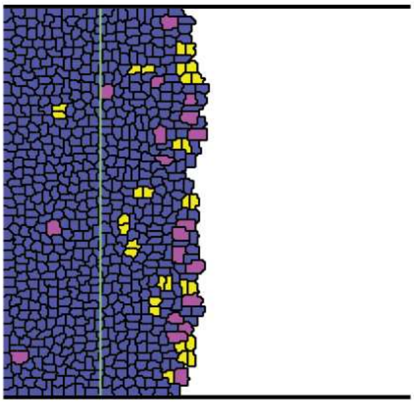

c) Reverse adhesion

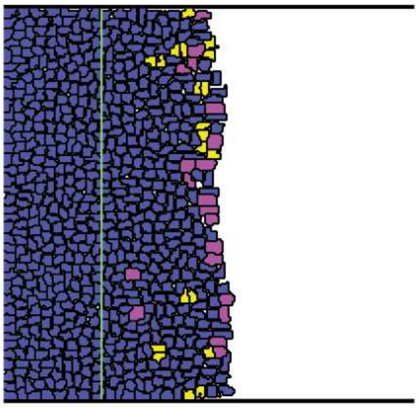

Figure 6.3: Simulated healing of an artificial wound in a monolayer using a GGH model under the three adhesive regimes, using $\mathcal{P} = 0.01$ and an elapsed time of 200 hours. The horizontal width of the domain is $1.2\,\mathrm{mm}$ (slightly different between regimes). The scratch location is marked by the green line. Blue cells are quiescent, purple cells are proliferative and yellow cells are recent daughter cells.

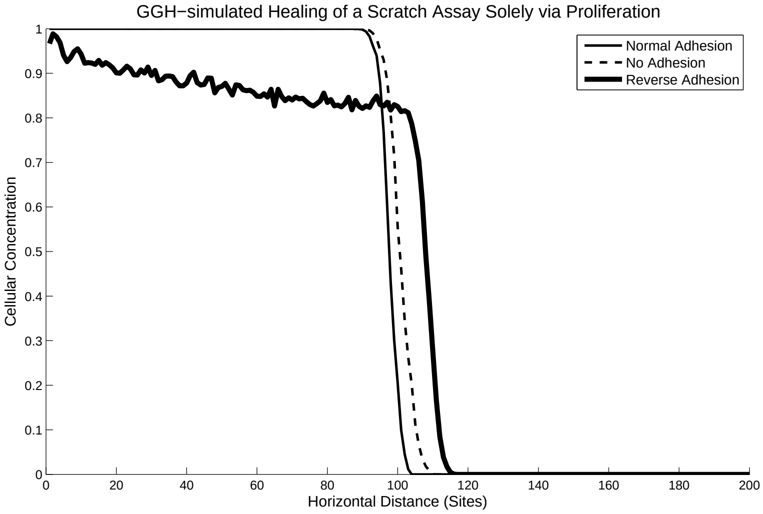

Figure 6.4: Averaged (10 simulations) wave profiles for the three different adhesive regimes, showing shape and relative speed (by comparing front position). $\mathcal{P} = 0.01$.

for cells under the reverse-adhesion framework to form gaps between each other applies only to quiescent cells (because its intention was to induce a more migratory behaviour in these non-proliferating cells), and thus it is easy for the cells at the front where proliferation occurs readily to fill the entire domain while those behind the wavefront slightly repel each other. The exact behaviour is of course rather dependent on the specific parameters chosen, and on how the reversely-adhesive regime is constructed, but despite that fact, simply changing the adhesive balance of J values has resulted in a non-monotonic wave profile that would never be observed in population-scale PDE models featuring simply proliferation and expansion into free space (equation (6.8) for example). It should be noted of course that because cell concentration is measured in terms of space, instead of cell count, it is easy for the different sizes of cells to complicate the interpretation of such a result. However, what is made clear by this case is just how important the representation of the physical shapes and sizes of cells, along with their adhesion, can be for determining their behaviour and comparing between microscopic and macroscopic scales.

It is also important to confirm that these invasive profiles do represent a travelling wave, in the previously discussed sense that they must display an *overall constant* rate of invasion. Due to the stochastic nature of the GGH model, no individual simulation will demonstrate a consistent healing rate except perhaps over very long measuring periods. Instead here, the averaged simulations also used to generate the average wave profiles in Figure 6.4 were used to plot the trend of the invasive velocity over time, taken every 100 MCS and shown in Figure 6.7. The wavespeed is measured by considering differences in the wavefront position, with the wavefront position at any moment in time calculated by averaging the horizontal locations of the rightmost cells in each row of sites in the cellular automata domain. This is arguably equivalent to using a very low threshold value to mark wavefront position in macroscopic continuum

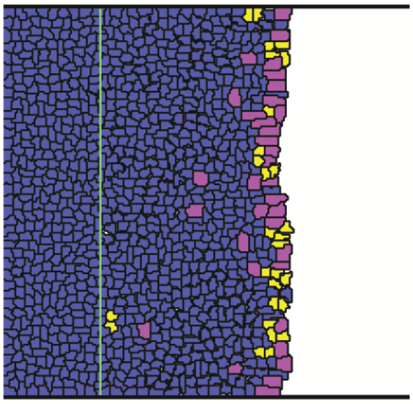

Figure 6.5: Simulated healing of an artificial wound in a monolayer using a GGH model under the reversely-adhesive regimes, using $\mathcal{P} = 0.05$ and an elapsed time of 380 hours. The horizontal width of the domain is 1.2 mm (slightly different between regimes). The scratch location is marked by the green line. Blue cells are quiescent, purple cells are proliferative and yellow cells are recent daughter cells.

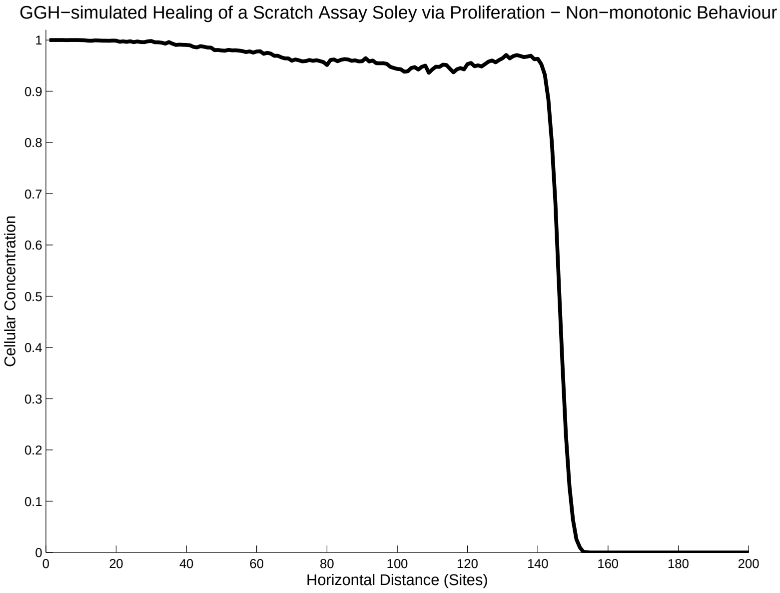

Figure 6.6: Averaged (50 simulations) wave profile for the reversely-adhesive regime, using $\mathcal{P} = 0.05$.

modelling. While the different adhesive regimes show different overall invasive wavespeeds as previously discussed, all show the same temporal trend, namely an initial period of faster invasion which then subsides into a constant rate of healing. Not only does this levelling out of the overall wavespeed trend confirm that these simulated invasions do indeed represent travelling waves and would appear to move at constant speed when observed on a macroscopic scale over longer timeframes, but an initial period of faster invasion has in fact been seen in experimental data [115], which lends a lot of credence to these simulations. Before the scratch, cells are packed into the monolayer occupying a volume lower than their target volume, and this gives the system a sort of potential mechanical energy which is released when the scratch is made and the cells have free space to expand into to reach their target volumes. It is believed that the initially faster wavespeed is a consequence of the release of this “potential energy”, an effect which could also be the biological explanation for such observations. However, despite these realistic-looking simulations and steady travelling wavespeeds, it is seen below that when a specific model cell is chosen to allow for quantitative comparison to experimental data, these proliferation-driven simulations are in fact not correctly predicting scratch assay healing.

The still rather nebulous parameters of the GGH model and the fact that simulations of a realistic number of cells are highly computationally taxing make it difficult to simulate with a physical interpretation of space and time in mind. However, the question of how velocities predicted in these GGH model simulations compare to those observed experimentally and predicted by the PDE model was considered by using the same choice of model cell, MG63 osteoblast-like cells. This is again informed by the data from the circle migration assays of Sengers *et al.* [169] which has been integrated into Table 6.1. However, the connections between the population-level observations and GGH model parameters are not obvious and a novel approach is used here in order to link the two and hence provide a physical measure of time and space to the GGH model simulations.

The experimental results of Sengers *et al.* [169] for MG63 cells suggested a cellular concentration at confluence of $1200\,\text{cells} / \text{mm}^2$, resulting in an average cell size of $8.33 \times 10^{-4}\,\text{mm}^2$. This is an area measurement and not a volume, however this is appropriate for a cell population forming a monolayer as is the case in the experiment and in the 2D GGH model here. This piece of data, along with their observed proliferation rate (from a purely-proliferative assay) of $0.023\,/\text{hr}$, is used to construct a physical interpretation of the GGH model here via comparison with the purely-proliferative simulations carried out in Chapter 5. The fact that the results of these simulations were reasonably different for different adhesive regimes and proliferation probabilities means that the physical interpretation of the GGH model must also be changed depending on which regime and proliferation probability is being used. The process for determining physical dimensions (spatial and temporal) for the GGH model is explained here using the example of the non-adhesive regime with proliferative rate $\mathcal{P} = 0.2$, though the exact same calculations are used for every combination of $\mathcal{P}$ value and adhesive regime, using the values listed in Table 5.3.

Under the non-adhesive regime, the GGH model with $\mathcal{P} = 0.2$ reached confluence with a

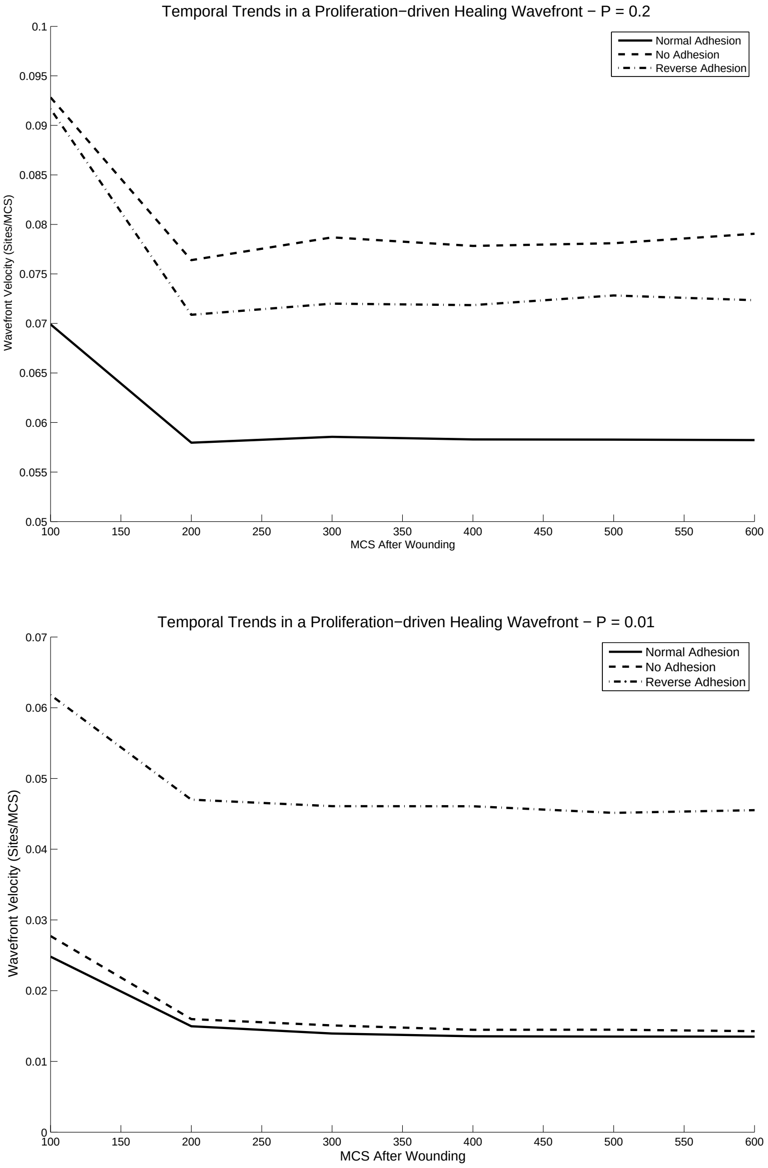

Figure 6.7: Trends in the simulated wavespeed right from the point of wounding showing the establishment of a steady wavespeed for the different adhesive regimes. For the upper figure, $\mathcal{P} = 0.2$, for the lower, $\mathcal{P} = 0.01$.

domain of 10,000 sites occupied by 380 cells, suggesting a size at confluence of 26.3 sites per cell. Thus the cell size of $8.33 \times 10^{-4}\,\text{mm}^2$ must correspond to each site in the GGH model's domain occupying an area of $3.17 \times 10^{-5}\,\text{mm}^2$ for the GGH model and purely proliferative assay experiment to be in agreement, and this means each lattice site must have a side length of $5.63 \times 10^{-3}\,\text{mm}$. This provides the GGH simulations with a physical scale, but temporal advancement is still governed by Monte Carlo steps and not any kind of physical measure of time. It is by matching the experimentally measured proliferation rate to the proliferation rate per MCS exhibited by the GGH model simulations that timesteps are also given a physical interpretation. The experimentally observed rate of 0.023 /hr must correspond to a simulated rate of 7.12×10^{-3} /MCS as listed in Table 5.3. Thus each individual MCS must correspond to 0.31 hr. With both of these physical scales defined, a wavespeed expressed in terms of sites/MCS as in Figure 6.7 can be converted into a wavespeed expressed in mm/hr and thus compared with experimental data. The wavespeed observed for the non-adhesive case is seen to be 0.077 sites/MCS, which corresponds to a physical wave velocity of ~ 0.0013 mm/hr. This is an order of magnitude difference compared to the observed velocity of MG63 cells in that circle migration assay, which was ≈ 0.012mm/hr. This discrepancy cannot easily be explained away as a result of the rather arbitrary choice of parameters like cell inelasticity, given that modifications to these parameters would also affect the ability of cells to proliferate in the purely proliferative assay and thus affect the determination of physical scales. Indeed, calculation of the associated physical healing rate under the other regimes using either $\mathcal{P} = 0.2$ or $\mathcal{P} = 0.01$ reveals very little change resulting due to these modifications. Thus it is a rather safe conclusion that a simple space-filling effect arising from proliferation-driven healing is by itself *insufficient* to result in realistic healing of a scratched monolayer, despite the initial impression given by the simulations presented above. While the specific case of MG63 cells has been used here to make this conclusion, the doubling times and wavefront speeds for other cell types which have been experimentally and mathematically considered (e.g. 3T3 fibroblasts [26] or HPMCs [115]) are not largely different.

Also interesting is how far different cells are moving as the monolayer heals, which is easily examined by visually tracking cells when simulations are visualised as animations, or by outputting data regarding the movement of cell centres of mass. Given the large number of cells each with their own unique and stochastically-affected movements, the tracking of cell movements in this case was done by noting the locations of all cells three quarters of the way through the simulation and determining the distance away from the leading edge (measured by comparing the horizontal distance between the cell's centre of mass and the centre of mass of the rightmost cell at that horizontal location). These stored cell locations are then compared to the locations of the cells at the end of the simulation to determine how far they have moved, the tracked distance being the horizontal movement (with movement in the opposite direction of healing being marked as negative). Thus the quantity being measured is actually the effective velocity in the direction of healing. When a cell being tracked proliferates, one daughter cell retains the same σ label and continues to be tracked, and the other daughter cell is not tracked at all. The amount of contact inhibition in a given simulation is somewhat represented

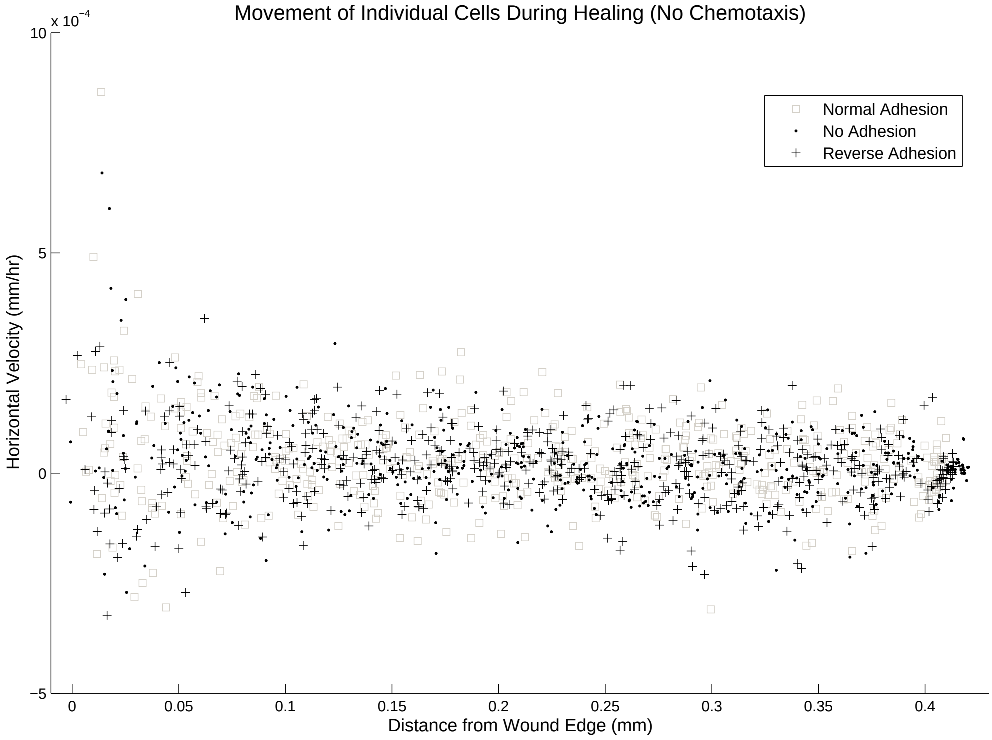

Figure 6.8: Demonstration of the trend between a cell's location relative to the wavefront and its velocity over a simulated period of proliferation-driven healing. Migration of any serious amount is seen to be limited to the wavefront.

by comparing how far cells at the wavefront migrate compared to those behind the wavefront and surrounded by other cells. Measurements for an example simulation for all three adhesive regimes are displayed in Figure 6.8, showing that in this case the velocities of cells away from the wavefront are indeed very small. This result confirms that migration of cells within the monolayer is being contact inhibited, and the movement of cells at the wavefront is larger but not always positive. The conclusion drawn here is that cells at this active region are being pushed about by proliferation events (whether forwards or backwards) until ending up behind the active region and thus essentially immobile. The net cell velocity is positive but very weakly so, confirming the fact that the healing seen here is proliferation-driven.

The observation that all proliferation and migration occurs at the wavefront agrees with observations for neural crest cells in the chick hindgut [181], where such an invasion pattern was concluded to be the most likely based on a series of experiments. However, a severe issue with this comparison is again the wavespeed, with the rate of invasion in that experiment being significantly faster than even scratch assay healing, which has already been shown to be faster than the healing being predicted here by the GGH model. This occurs despite a similar doubling time for neural crest cells [179]. Clearly even in this case an active migration effect is necessary, and neural crest invasion is *not* simply driven by proliferation. If this migration effect was highly contact-inhibited, it would indeed only be present at the wound edge. However, some of the experiments with non-proliferative donors showed that cells *can* move past each other, weakening their conclusion that migration is limited to the wavefront.

Either way, some kind of active migration effect (here chemotaxis is considered) is clearly a requirement for the GGH model as implemented here to match experimental observations and properly simulate healing of a cell monolayer. At the population scale, it has been argued via PDE models that "proliferation is the key" [179], but it is clear here that when working with a detailed individual-cell-based model the migration effect cannot simply be ignored. A simple cellular automata comparing guided and unguided invasion in wounded monolayers has suggested it is necessary to consider individual-level data to distinguish between the two types of invasion [164], demonstrating the importance of properly capturing the migratory effect in an individual-cell-based model like the GGH model used here.

In general, the way the GGH model framework naturally predicts cell clustering with some natural degree of stochastic fluctuation makes it very appealing, and the inclusion of the rather novel 'reverse' adhesion regime which causes cells to separate allows the modelling of more diffuse cell invasions also. However, the author's initial intuition that the macroscopic advance of cells could be driven solely by a proliferative pressure effect that PDE-level diffusion was capturing by chance (and tying in neatly with Maini *et al.*'s ponderings that sharper wavefronts like those seen here would better match their experimental observations [114]) has in fact been proven wrong. The need in the GGH model for an actively migratory cell behaviour (here represented by chemotaxis and explored in Section 6.3.3) has been demonstrated by comparison with experimental data. Although a specific dataset has been used, an argument regarding the lack of major variation in cell doubling times and observed wavespeeds in scratch assays using other cell types suggest this conclusion is broadly applicable.

It is the author's opinion that a very interesting modification that could be made to the GGH in order to potentially rectify the issues discovered here is a third cell phenotype, namely migratory cells. These cells would be the ones that respond to chemotactic signals, and this phenotype could be activated when free space and/or a chemical signal was detected. This would then require careful reconsideration about what causes cells to adopt a proliferative phenotype, but is expected to provide faster healing of model wounds to better match experimental observation. In the case without chemotaxis, these deliberately migratory cells could experience encouraged movement via a higher value of the simulation temperature T, or a more sophisticated process involving randomly chosen directions with a persistence effect could be adopted. These migratory cells could easily be made to break away from an adhesive cell cluster simply by using the reverse adhesion regime for them, encouraging their separation.

The other potential GGH model extension that would be very interesting even in this simple scratch assay context is a 3D model. While in the abstract case the GGH model naturally lends itself to an extension into three dimensions, in the modelling of a cell monolayer it presents a few issues for consideration. First is the observation that cells which are proliferative or inactive 'round up', whereas migrating cells spread themselves across the substrate in order to crawl across it. This could be achieved in a 3D model by modelling the substrate as a solid barrier and then prioritising contacts between cells and the underlying substrate which would cause cells to spread themselves when they have the space to do so. Inclusion of this sort of effect would also allow for some amount of healing and invasive effect to be observed even with non-proliferative cells, an issue identified here.

Regardless of whether or not these suggested extensions are made and regardless of their effectiveness, the inclusion of a chemotactic effect as explored in Section 6.3.3 remains key, given that a lack of sufficiently fast migration has been demonstrated in the non-chemotactic, purely-proliferative case. There are biological arguments for the inclusion of such a behaviour also. The importance of a wave of the signalling module MAPK which is induced by wounding has been clearly demonstrated [137], and the absence of this signal results in a greatly reduced healing effect. Observations that cells behind the wavefront move with a velocity biased in the direction of healing [26] also suggests a chemotactic effect, but could simply be derived from a contact-inhibition-driven guidance of movement. However, experimental observations of cell protrusions in the direction of healing which move under other neighbouring cells [47] suggest this biasing effect is occurring at the level of individual cells instead of simply being the macroscopic result of a bias in random cell motility introduced by cell-cell interactions. Thus the presence of some sort of chemical guidance, especially in the case of physical wounding as opposed to exposure to free space, is extremely likely.

6.3.3 Incorporation of Guided Invasion

Population Scale

The equation (6.1) is already appropriate for modelling a scratch assay including a chemical guidance effect, and thus need only be solved by the constructed finite volume implementation (Section 2.2.2) in order to simulate macroscopic healing including chemotaxis. The equation chosen here has come from a synthesis of the literature and is thus slightly different to other presented cellular chemotaxis models, however certain expectations regarding its behaviour are indeed held. Travelling waves in a model using a 'volume-filling' chemotaxis term but lacking contact inhibition of diffusion have been considered by Ou and Yuan [140] however their work used a cell-produced chemical signal and thus is not directly relevant to the case here where the signal is one which guides healing towards the wounded region via a gradient formed by cell consumption. A purely tactic cellular migration in avian neural crest cells was considered by Simpson *et al.* [179], using a mechanism like one described here where cells consume a separately supplied nutrient, but no non-linear features (saturation or contact inhibition) were included. The nutrient was membrane-bound, corresponding here to $D_s = 0$. Theoretical results using an again substrate-bound and cell-consumed chemical signal showed that non-monotonic waves could be produced only when a non-constant χ was used [105], as is the case here. The interesting question regarding the existence of non-monotonic waves is whether or not the conditions for their generation apply on the individual scale (here represented by the GGH model).

MG63 cells remain the considered model cell here, given the previous arguments. The chemotactic response of this cell line is less documented, at least as far as the author could determine, and so the 3T3 fibroblasts used in a scratch assay by Cai *et al.* [26] (which have a much better documentation in the literature of chemotactic response [61]) were also considered as an option. However, the data for the population-level mathematical modelling presented in that work suggests a doubling time of roughly six hours which does not seem feasible, and is possibly a result of their data not including the initial settling time cells experience where no proliferation occurs. Their value of a diffusive coefficient also differs by an order of magnitude compared to those suggested for other cells, although they do obtain a reasonable match with experimental data albeit over what is apparently a rather short timeframe. This is not meant as a criticism, indeed quoted diffusive coefficients for various cell types have been seen to vary wildly (see for example [23]) and Cai *et al.*'s parameter choices do predict a believable value for the wavespeed. However, given that the overall aim here is to compare cellular invasion under different mathematical frameworks as opposed to directly matching experimental data, choosing the more believable parameter set presented by Sengers *et al.* for MG63 cells is considered the best option. This maintains consistency with the results for the purely-diffusive case presented in Section 6.3.2, another reason to make this choice over the biological specificity of a given chemoattractant and documented cell response offered by a different model cell like 3T3 fibroblasts.

Given that a new migration effect is being included into a model which already predicts invasion at the correct speed, the amount of diffusion present must be reduced so that the desired wavespeed can still be observed. This does not compromise the model, for it should be recalled that the diffusion coefficient used in Section 6.3.2 was determined by Sengers *et al.* via parameter-matching with a modified Fisher's equation containing no tactic effect [169]. Two cases were considered, one where there is no diffusion at all, and one where the diffusion is decreased by a factor of 10, thus attempting to distinguish between purely unguided invasion discussed previously, purely guided invasion and a mixture of the two. However, without a specific attractant being considered, defining the parameter values governing the chemotactic response, χ_0 and K_s, and the diffusion and consumption of the chemoattractant, D_s and λ_s respectively, becomes more difficult. In the purely advective case featuring a linear gradient, the two latter parameters do not require definition because the gradient is fixed, and in this case a non-saturating chemotaxis coefficient χ_c is used instead, as argued in Section 6.2.4. The values chosen for χ_c and χ_0 in their respective problems are values which correctly predict the wavespeed observed by Sengers *et al.* for MG63 cells, with these values then being considered for realism and the wavefront shapes they generate. In the case where the chemoattractant is actively consumed by cells and possibly diffuses, parameter choices for K and λ_s were informed by other relevant works in the literature. For the consumption rate of chemical, λ_s, two values were determined. The first of these follows mathematical explorations of tactic waves [105] and haptotactic invasion of tumour cells [151] in which this rate is equal to the logistic growth of cells, $\lambda_s = \lambda = 0.023\,/\mathrm{hr}$. The second approach also sourced from the haptotactic migration of tumour cells literature used a reaction rate an order of magnitude (20 or 30 times) larger than the proliferative rate of cells [116] and thus a second value of $\lambda_s = 0.46\,/\mathrm{hr}$ was also trialled. In the case where the signalling chemical diffuses, the approach initially trialled here was that seen in Byrne *et al.*'s model of neutrophils migrating chemotactically in a Boyden chamber [23], where a chemical diffusivity 100 times the cellular diffusivity was used. The Boyden chamber model used a non-contact-inhibited cell diffusivity, and so the value of D_s was determined using the value presented by Sengers *et al.* [169] in the standard Fisher's equation case. This corresponds to a value of $D_s = 0.18\,\mathrm{mm}^2/\mathrm{hr}$, however it was found that this value resulted in a rate of diffusion far too fast to produce a significant gradient over the spatial scales used here. Thus, a value 100 times smaller, equal to linear cell diffusion $D_S = 0.0018\,\mathrm{mm}^2\mathrm{hr}$ was used instead. The same work of Byrne *et al.* [23] used the same saturating chemotaxis coefficient and thus their choice of $K = 0.5$ is also made here. Again it is stressed that these parameters were chosen to attempt a degree of loose biological realism but do not correspond to any specifically observed values. All parameter choices are summarised in Table 6.1.

The first simulations used the purely advective gradient, which as has been discussed could represent an activation of cells triggered by wounding. This case uses the non-saturating chemotactic response (6.3) and a bias of cell motion either applying to half of the unwounded region or all of it, along with the wounded region. The concentration of attractant remains fixed, and the boundary condition for cells is no-flux, which was the same boundary condition used by Sengers *et al.* [169] but should again be noted as corresponding to a circle migration assay, as opposed to a wound healing assay. If the cells behind the wavefront are allowed to respond to the gradient, it is expected that in the case where all cells are activated (gradient across the entire domain), the result will be a moving sheet of cells as opposed to a healing wound. However, the respective predictions of the GGH model and the PDE model dealing with how the sheet moves is expected to prove enlightening. It was also this case where all cells are active that was used to determine the appropriate value of χ_c in order to obtain the wavespeed of $0.012\,\mathrm{mm}/\mathrm{hr}$ as observed by Sengers *et al.* [169]. The base case used to make this determination was one where contact inhibition was included but did not entirely restrict motion, corresponding to $m = 0.9$, given this seems to best match experimental observation [26]. Diffusion was included, because the sudden beginning of the linear gradient (whether at the boundary or midway into the unwounded region) caused instabilities without the smoothing effect of the diffusion. This was the case even for a decreased timestep and using the 'safer' regime of upwinding. It should be noted here that it was found to be necessary that the boundary elements of the simulation used an upwinding method as opposed to averaging (in the cases where flux limiting could not be performed due to lacking information).

The value for healing at an appropriate rate was determined to be $\chi_c = 0.08\,\mathrm{mm}^2/\mathrm{hr}$, a value which is lower than that measured for neutrophils in a Boyden chamber [23], although given

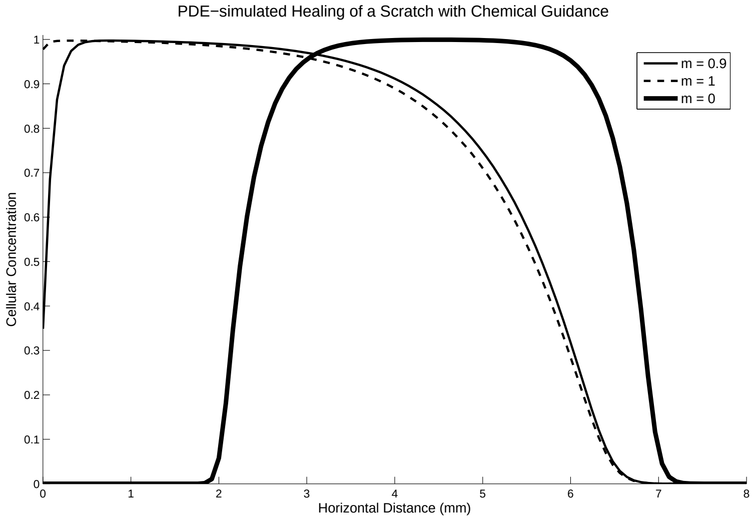

Figure 6.9: Solution profiles for PDE-simulated healing of a scratch enhanced by a chemotactic gradient ranging across the entire domain, $\chi_c = 0.08$. The results after a timeframe of 350 hours are shown for the three different considered possibilities for contact inhibition are shown. Relative position of the wavefronts can be used to judge invasive speed.

the significant chemotactic activity of that cell type this is if anything, expected. It is interesting to note that the inclusion of a chemotactic effect actually causes the healing wavefronts to become more shallow, this being somewhat unintuitive given that chemotaxis is often responsible for producing travelling shock fronts [104], and especially given that the diffusion coefficient has here been reduced. It is expected that this is a result of chemotaxis pushing leading cells into the wounded space where they are more free to respond to the signal, compensating for the fact that non-linear diffusion is lower for leading cells where the concentration is smaller. The second reason shallower chemotactic wave profiles are interesting is because it provides a simple, qualitative observation to test against GGH model simulations.

When the amount of contact inhibition present in the simulation is varied by adjusting m, keeping all other parameters constant, the effect was found to be minor when varying between strong and complete contact inhibition, with the only major difference being how much depletion could be observed at the edge where the gradient begins. However when contact inhibition was switched off by setting $m = 0$, the healing monolayer instead became a migrating cluster as initially predicted. Contact inhibition in crowded regions was indeed revealed to be the cause of chemotaxis predicting more diffuse wavefronts, with the non-contact-inhibited case displaying a wavefront even sharper than in the sharp-fronted diffusion case. These are all predictions which can be examined on an individual cell level via the different adhesive regimes in the GGH model.

The effect of starting the chemical gradient halfway into the unwounded region (such that only the half of cells closest to the wound are activated) only affected the solution profile behind the advancing wavefront, where it was seen that the location where the chemical gradient begins

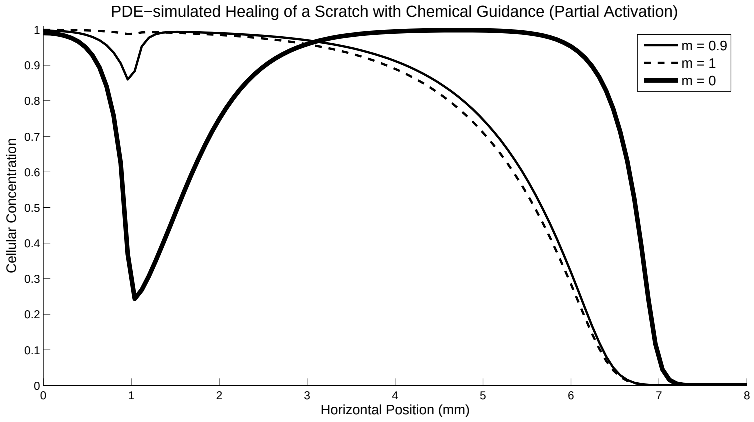

Figure 6.10: Solution profiles for PDE-simulated healing of a scratch enhanced by a chemotactic gradient ($\chi_c = 0.08$) beginning halfway into the unwounded region ($x = 1$). Again the results for the three different levels of contact inhibition after 350 hours are visualised. It can easily be seen that the invasive portion of the solution profile is entirely unchanged compared to the previous case where all cells were activated.

was populated by fewer cells. The results for this case are shown in Figure 6.10. The invasive portions of the solution profile were confirmed to exactly match those for the case where the gradient occupied the whole domain by simply overlaying them. The fact that what portion of cells are 'activated' or able to respond to the gradient doesn't affect the invasive behaviour shows that the mathematical model correctly predicts the positional invariance observed in invading monolayers [181] where inactive cells away from wounded regions do not contribute to healing.

The perhaps more realistic case where cells respond to a gradient formed by their own consumption of some kind of attractant (like a nutrient) was simulated next using the same set of PDEs. Separate values of χ must be used here to match experimentally observed wavespeeds, due to the fact that the gradients encountered in this case are much steeper, and the nature of the cell response now saturates with concentration. The new form of the chemotaxis (6.2) uses a different multiplicative constant (χ_0 as opposed to χ_s) to highlight this. First considered was the situation when the attractant is substrate-bound and does not diffuse, resulting in sharper nutrient profiles and a greater risk of numerical instability. This sharpness is of course also affected by the value of λ_s.

In the case of 'slow' nutrient consumption, where $\lambda_s = 0.023$ /hr and thus matches the logistic growth rate of cells, the value of $\chi_0 = 0.11\,\text{mm}^2/\text{hr}$ was found to produce a travelling wave with velocity $0.0125\,\text{mm/hr}$ and thus represent a realistic choice. The formation of a travelling profile under these conditions is demonstrated in Figure 6.11. The shape is seen to differ from those observed in the case of a linear gradient as could be expected, with the wavefront in this case looking similar to those observed by Landman *et al.* [105] in the case of zero diffusion and constant χ, and using initial conditions possessing compact support just as is done here.

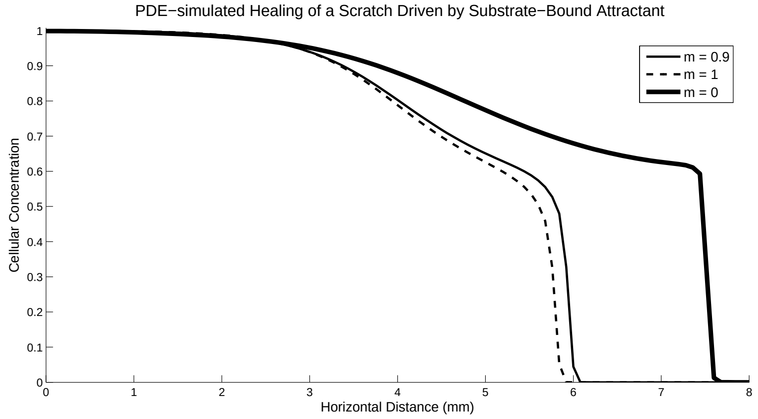

Figure 6.11: Solution profiles for PDE-simulated healing of a scratch enhanced by a cell-consumed, substrate-bound attractant. Parameter values are $D = 0.001$, $\chi_0 = 0.11$, $\lambda_s = 0.023$ and $D_s = 0$.

These waves feature a slow decrease in cell concentration implying a rather diffuse invasion of cells, but only up to a certain point at which there is a jump discontinuity down to a zero concentration. The effect of the functional dependencies in the chemotaxis term has been to slightly alter the shape behind the sharp leading edge of the healing wave, a fact which is made clear by comparing the wave profiles for the different values of m. Contact inhibition of chemotaxis here results in more diffuse fronts, in complete contrast with unguided movement where the contact-inhibition effect results in sharper invasive profiles. An invasive profile like this has not been observed experimentally, given the combination of a very sharp edge and a shallow profile behind that - if cells are spread enough that a ‘zoomed out’ profile becomes diffuse, why is there a certain region that cells manage to migrate to fill roughly 60% of space there but no cells at all manage to migrate any further?

These simulations used both a diffusive and migratory effect, with a decreased diffusion coefficient as discussed above. When the diffusion of cells was removed, the simulations seemingly suffered from numerical instability introduced by the initially sharp gradient when there is no smoothing effect of diffusion. This observation unfortunately persisted even when ‘safer’ approaches such as fully implicit timestepping or upwinding, or reducing the timestep, were taken. However, the overall trend in these results did not appear to be largely different to the cases where cellular diffusion was included, except for the oscillations introduced by that instability.

When the consumption rate of chemical was increased to the second value listed in Table 6.1, the profile of the chemical signal developed an even steeper gradient and thus the invasive speed was increased, requiring a reduction in χ_0 in order to maintain a reasonably correct invasive velocity. In this case, the travelling profile was found to move at a velocity of $0.0120\,\text{mm}/\text{hr}$ using a value of $\chi_0 = 0.02\,\text{mm}^2/\text{hr}$. Interestingly, although the profile of the chemical attractant is much steeper in this case, the reduced value of χ_0 actually resulted in a lower incidence

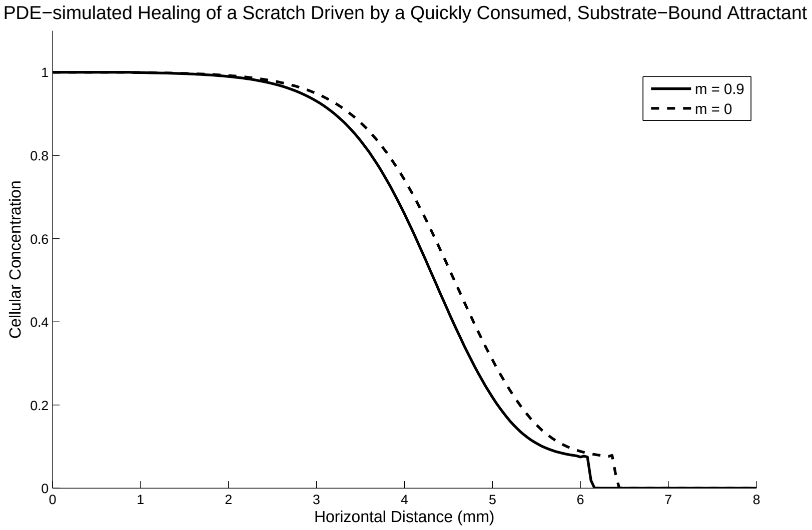

Figure 6.12: Solution profiles for PDE-simulated healing of a scratch enhanced by a cell-consumed, diffusible attractant. Parameter values are $D = 0$, $\chi_0 = 0.02$, $\lambda_s = 0.46$ and $D_s = 0$.

of numerical instability and far shorter shock fronts. The wave profiles simulated in this case are visualised in Figure 6.12, where it can be seen that the overall trend of a concave decreasing region flattening out to a plateau region behind the shock front was retained in this case. Given that cell diffusion was not included in those simulations, results for the $m = 1$ case are not displayed because without diffusion the cells initially at confluence cannot migrate at all. When diffusion of cells was turned on, it was found that the height of the wave edge actually increased but became smoother, with wave velocity almost entirely unchanged.

When the consumed gradient which drives invasion was made diffusible instead of substrate bound, its concentration profile naturally became more diffuse, causing cells to detect a less steep gradient (and thus invade more slowly) but by the same token potentially allowing more cells to respond to it. When the PDE model was simulated using a non-zero rate of nutrient diffusion ($D_s = 0.0018\,\text{mm}^2/\text{hr}$) it was found that under the 'slow' consumption regime ($\lambda_s = 0.023\,/\text{hr}$) that there was no effect on invasive wavespeed, the only change being a smoother profile that greatly resembled those seen for diffusion-driven healing discussed previously because of the lack of any pronounced 'plateau'-like regions resembling those seen in Figure 6.11. When operating under the 'fast' consumption regime ($\lambda_s = 0.46\,/\text{hr}$), the value of χ_c had to be increased ($\chi_c = 0.03\,\text{mm}^2/\text{hr}$) in order for the model to match the experimentally observed invasion rate for the chosen model cell. It is this slightly larger value which is presented in Table 6.1 because it was found that a diffusible signal works better in the GGH model (as is discussed below). In this case, with this modified parameter, the wave profile was observed to be almost exactly the same as that seen in Figure 6.12.

Overall, several key observations of how the PDE model described by equations (6.1) and (6.2) predicts cellular invasion in a scratch assay have been drawn, for comparison with the GGH model's predictions working on the scale of individual cells. It has been seen that the inclusion of a chemotactic effect can produce waves travelling at the same velocity as diffusion-driven waves but with differently-shaped profiles. Invasions driven by linear advection show a smoothing of the lower edge of the profile into a diffuse 'tail', as opposed to the sharp fronts which result from the non-linear diffusion in the model. When consumed chemical signal was driving tactic invasion, the profiles showed proper shock fronts, however these varied in height depending on the rate of chemical consumption and did not directly connect the two steady states (completely unwounded and confluent). This pattern's physical equivalent is a clearly defined wound edge but with the population at this edge showing significant gaps between cells, which is *not* something that can be experimentally observed. This suggests that chemotaxis as driven by a gradient of consumed chemical is not the behaviour at work in these experimental observations, or that the PDE model is failing to accurately represent cellular invasion (presumably because spatial effects and other intricacies of individual-cell-level effects are neglected). It is for this reason that the results of the GGH model simulations are critical.

Individual Cell Scale

The inclusion of chemotaxis into the CPM/GGH modelling framework has already been discussed in great detail in Chapter 4, where it has been shown that equation (4.4) represents the best way to achieve this, due to its compliance with the desired linear relationship (4.5) which other presented possibilities fail to demonstrate. The means of incorporating this effect has already been discussed. The only thing that should be noted is that the simulations presented in Chapter 4 involved steeper prescribed gradients than the one involved here (because the concentration is now considered scaled and varies between values of 0 and 1). Thus, the values of μ used here in the case of the specified gradient are much larger than those considered previously. Informed by the results for the unguided case that proliferation-dominated healing is seemingly incapable of matching experimental observation, the simulations here initially used a greatly reduced proliferation rate, $\mathcal{P} = 0.001$, to try to reduce the number of cells which halted chemotactic migration in order to attempt to proliferate. However, larger values of $\mathcal{P}$ were also trialled. Results of a pure proliferation study in the GGH model for this value of $\mathcal{P}$ have already been calculated and displayed in Table 5.3, and can be used to calculate the physical space occupied by each site and the physical time represented by each Monte Carlo step, just as was done for the purely proliferative GGH model in Section 6.3.2.

The first situation considered is the simplest one, in which the chemical concentration is a linear gradient established automatically and independent of the cells, ranging across either the entire problem domain or halfway into the unwounded space. For consistency with the macroscopic results, the physical length of the domain was compared to the $8\,\text{mm}$ domain used in the PDE simulations which corresponded to a gradient of $0.125\,/\text{mm}$, thus allowing the gradient's increase per site for the GGH Model to be calculated. Due to the smaller domain in the GGH model simulations, the gradient takes a much smaller value compared to the macroscopic case.

The value for the normally adhesive case was 6.85×10^{-4} /site, and these smaller gradients also necessitate an increased value of μ. As has been discussed, this case with a specified gradient is a less realistic but mathematically indicative problem, though it can possibly be related to the effects of activation caused by a passing wave of chemical signal. To reiterate, no saturation effect for chemotaxis is included when using this artificial gradient.

The primary purpose here was to determine if inclusion of a chemotactic effect could allow the GGH model simulations to predict the experimentally observed rate of healing, given the failure of the purely proliferative case. The three adhesive regimes listed in Table 5.2 were all simulated and example invasions for each case can be seen in Figure 6.13, using an equal value of μ and the same gradient to allow for direct comparison. Indeed it was found that for the the normally adhesive regime a chemotactic sensitivity of $\mu = 30000$ did predict a wavespeed roughly matching experimental observations, and was thus used for the simulations across all of the adhesive regimes. Given that an equivalent physical timeframe (different amounts of MCS) has been used for all three regimes, again the position of the healing front can be used as a rough judge of wavespeed (although it should be remembered that the physical space represented in each case is slightly different). The clear difference is with the reversely adhesive regime, which moves a lot slower due to the fact that cells in the monolayer are less able to push on other cells compared to open space and so movement of the cluster must mostly be driven by cells at the front. This effective contact inhibition of migration is also present to a lesser degree in the non-adhesive case (as shown in Section 4.3.6), but here the overall migration of the cluster has ended up largely the same as in the normally adhesive case. Cells within the cluster are less able to push on their neighbours in the non-adhesive case, but those on the periphery more readily expand into free space, and the two effects have apparently compensated for each other.

Given that cells still remain tightly clustered, the wave profiles are not largely different to those observed in the non-chemotactic case, it is simply the rate of healing that has changed. However, if the visualisations are considered carefully, it is seen that although the cells completely occupy the space at the left boundary (except in the reverse adhesion case where they break away from it), there are in fact less cells occupying this region because the cells there take on larger, stretched shapes. Indeed, the majority of proliferative cells are seen to occupy this boundary, also suggesting that a depletion is occurring in order to allow these cells the space to proliferate. Thus the effect also seen in the PDE models where a depletion (but not a breaking away) of cells at the boundary has been naturally predicted by the GGH model. In the case of the reverse adhesion regime, cells break away from the boundary completely, presumably because the rate of proliferation is too slow to counteract the chemotactic effect. This observation matches the $m = 0$ case from the macroscopic model, a very interesting fact given that this has been argued as a lack of contact inhibition of chemotaxis, and yet the reverse adhesive case which explicitly discourages cells from encroaching onto one another has proven most equivalent to the $m = 0$ case. What this demonstrates is that the conclusions drawn previously in Chapter 4 must be interpreted carefully, because the inclusion of proliferation into simulations has caused adhesion to have very different effects. In the non-proliferative simulations in

a) Normal adhesion:

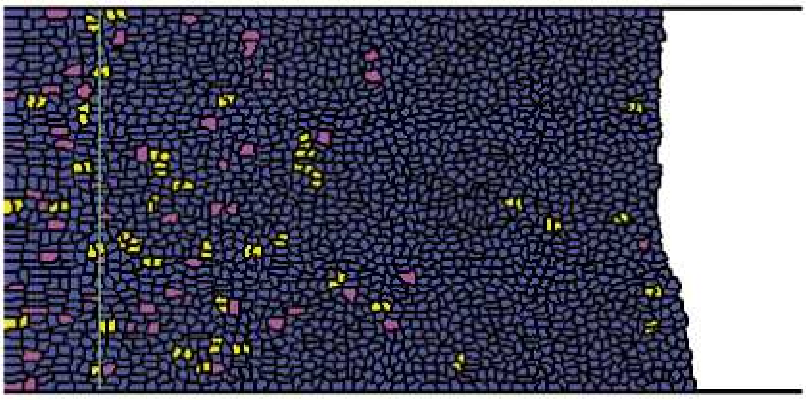

b) No adhesion:

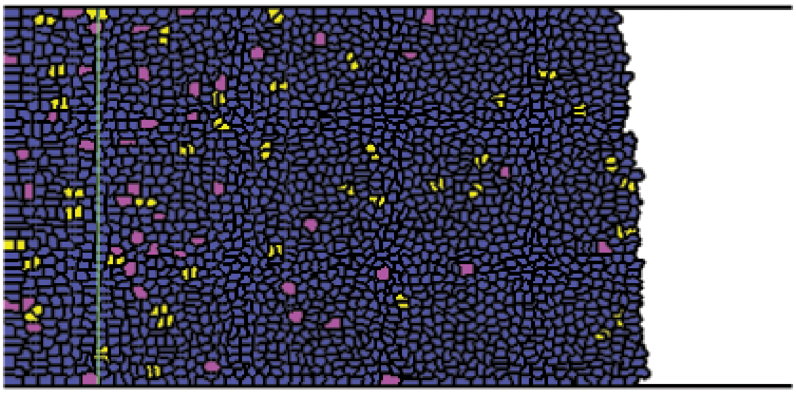

c) Reverse adhesion:

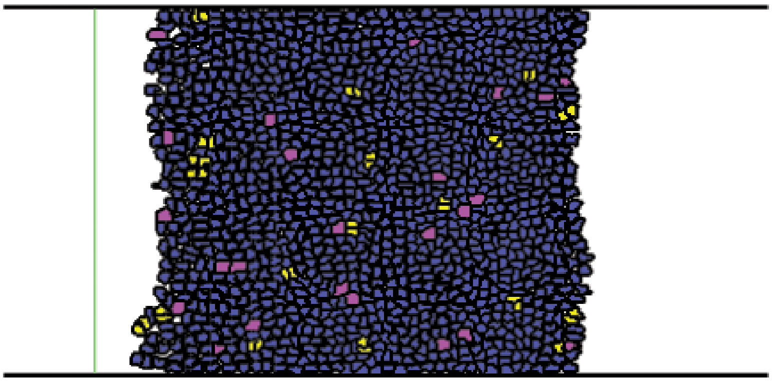

Figure 6.13: Simulated healing of an artificial wound in a monolayer using a GGH model with linear advection under the three different adhesive regimes, using $\mathcal{P} = 0.001$ and an elapsed time of 120 hours. The horizontal width of the domain is approximately 2.3 mm for the normally- and non-adhesive regimes, and 2.1 mm for the reversely adhesive regime. The scratch location is marked by the green line. Blue cells are quiescent, purple cells are proliferative and yellow cells are recent daughter cells.

Chapter 4, cells which can press onto one another show faster velocities in clusters than those in non-adhesive cases. Here though, cells which are far less able to press onto one another have demonstrated the least amount of blocking.

It should also be noted that proliferation occurs completely differently between the purely proliferation simulations and these here using linear chemotaxis. In the proliferation-dominated case, mitosis can only occur at the wavefront where the cells have room to expand to a proliferative size (reflecting the effects of contact inhibition of mitosis). However, in these chemotactic simulations here, cells are seen to proliferate largely behind the wavefront, despite those cells also being surrounded by other cells and the population being at confluence. They are able to do this because the cells around them are also moving in the direction of healing, allowing space to proliferate to be found. This is a very powerful result in itself, because neither population-level models nor typical cellular automata allow for surrounded cells to proliferate, despite the majority of proliferation occurring behind the wave in many experimental observations of healing monolayers [26, 137, 212].

As was considered for the case without chemotaxis, the velocity of individual cells over a certain timeframe of simulated healing was compared with their positions relative to the wavefront when that recorded period began. This provides a more empirical measure of which cells are indeed able to migrate, giving a more quantitative sense of how and to what extent contact inhibition of migration is present in the model. These measurements are presented in Figure 6.14. It is immediately seen that the behaviour of individual cells is entirely different here compared to the case without chemotaxis. All of the cells are far more free to move, almost equivalently so (notice how velocity is barely changed by position until the back of the unwounded region), confirming that the cluster essentially migrates as a sheet. It has already been seen that proliferation-driven healing is too slow to close the wound at a realistic rate, however here the monolayer has remained densely packed despite its faster expansion. This can occur because the migration into free space driven by the chemical gradient provides extra room to proliferate, and thus cell mitosis is less contact inhibited.

This result actually supports the thrust of works by Simpson *et al.* [178, 179] that it is the behaviours of individual cells which are key to distinguishing between different types of cellular invasion, given that the observed macroscopic wavefronts have not differed between chemotaxis-driven and proliferation-driven healing (except in invasion speed, which is parameter-controlled), but the individual cell behaviours are completely different. Proliferation-driven healing has already been shown as an insufficient predictor of experimental healing, so it remains important to determine how other types of healing which can be interpreted as a reasonable simulation of experiments can also vary in macroscopic and individual cell behaviour. This question is considered when the situation of chemotaxis driven by cell consumption of 'nutrient' is analysed below.

Cells that elect to proliferate show decreased migration, in both experiments [85] and in these simulations where they do not migrate at all. Therefore, it was expected that if the value of the

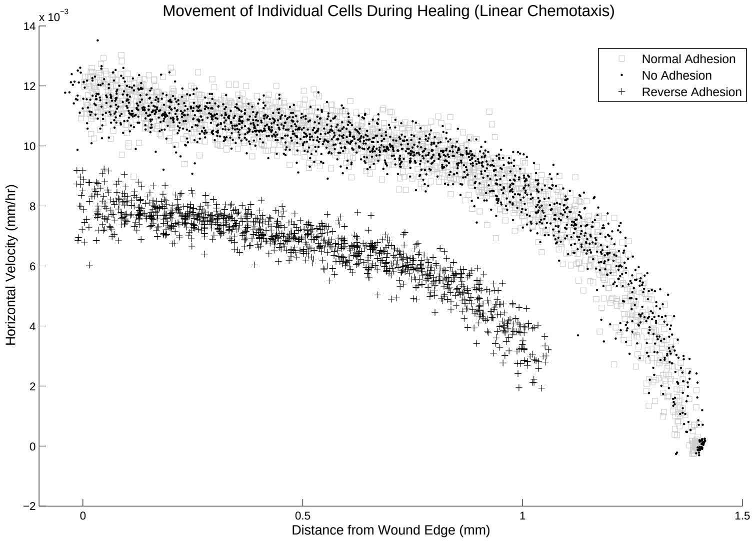

Figure 6.14: Demonstration of the trend between a cell's location relative to the wavefront and its velocity over a simulated period of advection-driven healing. Migration is strongest at the wavefront, but observed throughout.

proliferation probability $\mathcal{P}$ was made too high, the rate of healing would actually be decreased because the progression of migrating cells would be blocked by proliferating cells which do not respond to the gradient. However, it was found contrary to expectations that at least in terms of sites/MCS, the healing rate was actually increased for larger values of $\mathcal{P}$. However, when the velocity is converted into physical terms, the increased proliferation rate suggests that the time length represented by each MCS is much shorter (in order for the results to remain consistent with the purely proliferative assay) and thus the rate of physical healing is indeed decreased when $\mathcal{P}$ is higher. The effect of proliferating cells being essentially immobile has been considered by Landman *et al.* in their macroscopic modelling of a scratch assay involving detachment of proliferating cells [103], and a decrease in the physical rate of invasion has now also been demonstrated here via a relatively in-depth individual-cell-based model, albeit one that does not specifically consider detachment. Variation of $\mathcal{P}$ does not significantly affect the trend visualised in Figure 6.14, so this is not shown.

When the second linear gradient was used, which begins midway into the unwounded region, the point where the gradient began did show an evacuation of cells in a similar fashion to that observed in the PDE model, as can be seen in Figure 6.15. However, this only occurred in the non-adhesive and reverse-adhesive cases, and not in the normally adhesive case. The observation that the rate of expansion and the invasive profile was unchanged between the two different linear gradients has been observed in the GGH model just as it was seen in the PDE model. The depletion of cells at the location of the beginning of the gradient has also been seen for the models on both scales, with again the reversely-adhesive regime in the GGH model corresponding to the $m = 0$ case. It can also be seen that the non-adhesive case seems to somewhat correspond to an intermediary value of m, and the normally adhesive case to $m = 1$ when considering the depletion of cells. However, the previously noted observation that the invasive fronts predicted by the GGH model are far too sharp to match those predicted by the continuum PDE model, which showed that increasing contact inhibition of chemotaxis through m actually causes the concentration profile at the wound edge to become rather diffuse. The intention of introducing a contact inhibition effect into the GGH model by changing its adhesive regime (demonstrated as related in Chapter 4) has been complicated too severely by the inclusion of cellular proliferation, and the two effects are clearly rather distinct.

So, it has now been shown that the inclusion of this linear gradient can generate a healing effect in the GGH-model-simulated scratch assay which can match the experimentally observed speed. However, unlike the experimental results published by Cai *et al.* [26], the trend here is for cells behind the wavefront to also move at a similar speed to those further behind the wavefront, and this is observed regardless of which adhesive regime is chosen. Thus, the use of a linear advective effect (whether rationalised as resulting from a wave of activation or not) is *not* a good explanation of scratch assay healing, even though it predicts sufficiently sharp wavefronts healing at the correct rate. If an activation wave was considered in more specific detail, presumably it would exhibit some sort of dissipation which might cause cells closer to the wound edge to migrate more rapidly than those further back, thus matching those experimental observations of contact inhibition of migration. An activation wave as an important mechanism in the scratch assay thus should not be discounted (and indeed has been shown as a critical determinant of behaviour in some contexts [137]), however it clearly cannot be modelled simply by activating some portion of cells in the unwounded monolayer with a bias of motion in the direction of healing. A far stronger conclusion here is the other side of the same coin - the mathematical ideal of a pure advective effect (whether chemotactic or not) has been found to incorrectly predict contact inhibition of migration, with cells at the wavefront displaying a velocity no faster than those behind despite that trend being observed in the non-proliferative GGH model in Chapter 4. One last major point of concern with these simulations based around specified linear gradients to drive healing is that the region where the gradient begins is where the greatest majority of proliferation occurs, and given that the chemical concentration is fixed, this means the proliferative region is always at a different position relative to the wavefront as the monolayer heals, suggesting it is not a natural cell behaviour.

Given that any contact inhibition of migration inherent to the GGH model's choices of adhesive regime has been shown as insufficient, the 'stricter' contact inhibition used by Merks *et al.* [130] previously argued as heavy-handed might in fact prove beneficial, especially if it was used to simply *reduce* chemotactic effect and not completely switch it off, in a similar fashion to the parameter m used in this thesis at the macroscopic scale. This would potentially cause the trend shown in Figure 6.14 to better match experimental observations of contact inhibition of migration in healing monolayers [26]. Brief simulations tested along these lines showed that in the non-adhesive case, incorporating a reduced chemotactic response for cells pushing on others did actually allow a few individual cells to break away from the main monolayer,

a) Normal adhesion

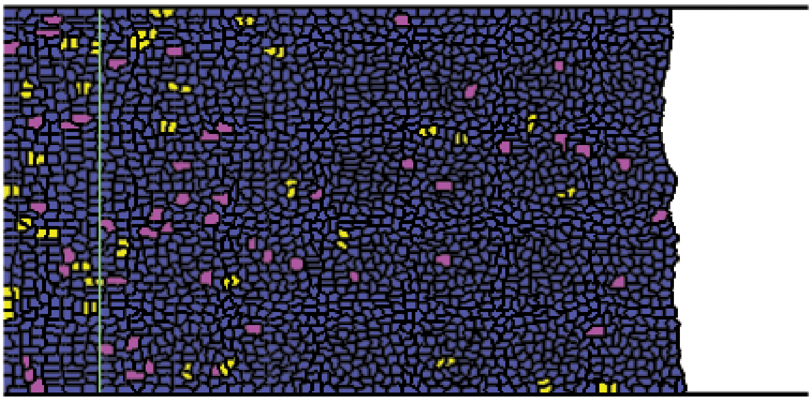

b) No adhesion

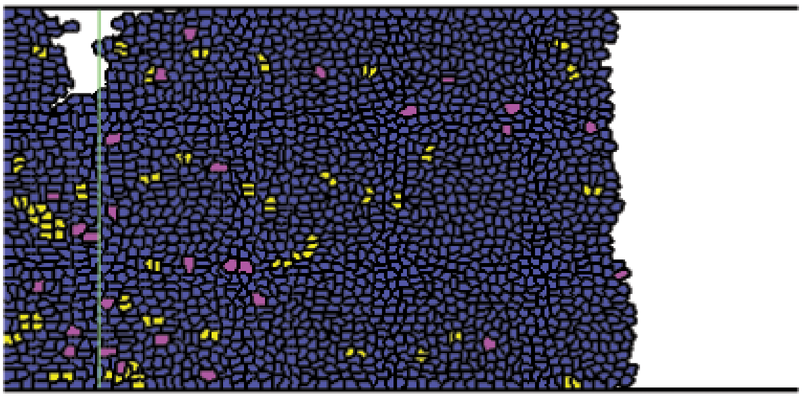

c) Reverse adhesion

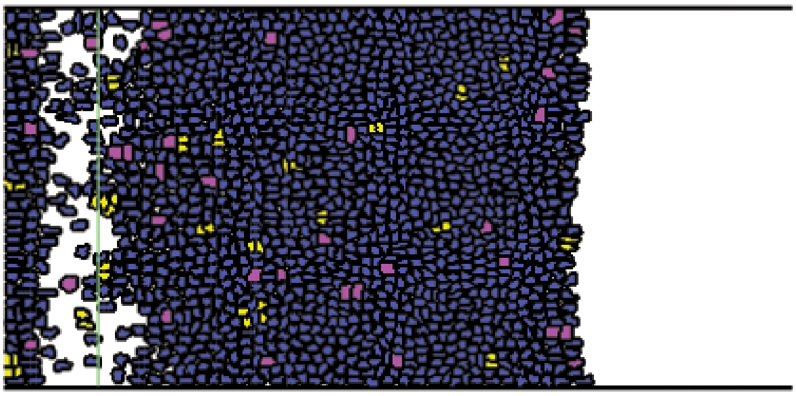

Figure 6.15: Simulated healing of an artificial wound in a monolayer using a GGH model with linear advection under a normally adhesive regime, using $\mathcal{P} = 0.001$ and an elapsed time of 120 hours. The horizontal width of the domain is approximately 2.3 mm for the normally- and non-adhesive regimes, and 2.1 mm for the reversely adhesive regime. The scratch location is marked by the green line. Blue cells are quiescent, purple cells are proliferative and yellow cells are recent daughter cells.

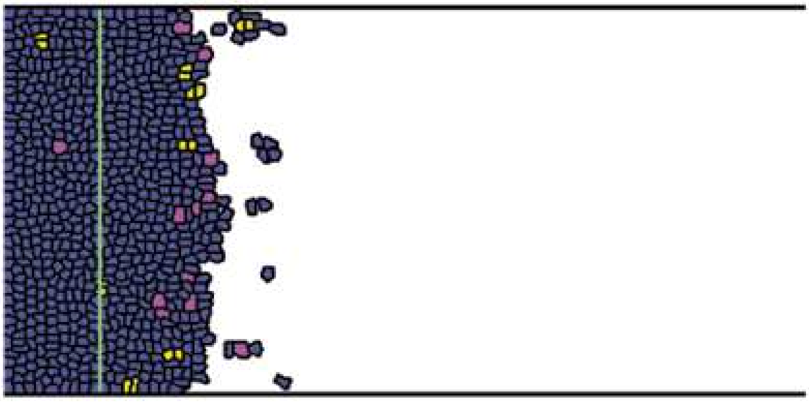

Figure 6.16: Simulated healing of an artificial wound in a monolayer using a GGH model with linear advection under a non-adhesive regime, with chemotactic response reduced to 1% when cells were attempting to encroach onto other cells. Subtle fingering of the front, along with detached 'pioneer' cells can be seen.

rushing forward to heal and hence creating a more diffuse monolayer. Therefore, situations where individual 'pioneer cells' are observed could be resulting simply from the difference in chemotactic response the very front cells can show compared to those behind them which can't immediately advance. When using a strong blocking effect (equivalent to large m), the healing front did become a little rougher also, showing some fingering. One example of this sort of result is visualised in Figure 6.16. These are certainly interesting behaviours but are still nowhere near diffuse enough to match the PDE model predictions, nor photographic results of cell types which do show specifically diffuse invasive patterns. Additionally, it is clearly seen that the rate of healing is drastically slowed by the contact inhibition of chemotactic effect, and it was found that increasing the value of μ to compensate allowed more cells to break away and the healing to occur more quickly, but with a clear distinction between the pioneer cells (now clusters) and the overall monolayer. Thus, although incorporating the contact inhibition of migration used by Merks *et al.* [130] does change the position-velocity trends in a favourable way, overall the predicted healing effect still fails to match experimental assays. The use of this enforced contact inhibition under the other adhesive regimes was also considered. In the case of normal adhesion, the adhesion prevented any cells from breaking away, however it was found that when μ was increased enough to predict appropriately fast rates of healing, the effect of the contact inhibition was limited (perhaps counteracted by adhesion to the faster-moving cells in the front) and the position-velocity trend still showed all cells responding to the gradient. In the case of reverse adhesion cells prefer to have space between them and thus a modification to how cells can press on one another had very little effect, even in the maximal case where chemotactic response was completely switched off when cells were trying to push into already occupied space.

As in the macroscopic case modelled using PDEs, in switching between a specified gradient and a naturally-forming one the value of the chemotactic sensitivity must also be adjusted due

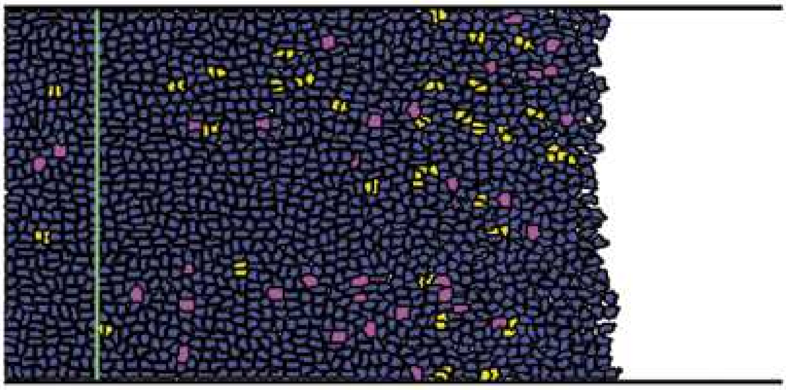

Figure 6.17: Simulated healing of an artificial wound in a monolayer using a GGH model with advection driven by a consumed chemical, under a reversely adhesive regime.

to the change in slope, otherwise the invasive velocity will no longer match that which is experimentally observed. There are also two consumption rates which are tested here, as listed in Table 6.1 and already considered in the macroscopic case, and the value of μ which results in agreement between GGH model simulations and the experimental velocity will change depending on the consumption rate of chemical signal. Whether or not the attractant chemical is diffusible or substrate-bound is also very important both for the sorts of invasion predicted, and the values of μ which can predict an appropriate rate of healing.

When the consumption rate was slow, it was seen that cells remained a single clustered monolayer and it was soon determined that, as with the introduction of a linear chemotaxis above, these monolayers were indeed capable of healing at a rate matching experimental observation. There were, however, two key differences between healing predicted by a prescribed gradient and healing predicted using a slowly-consumed chemical gradient. Firstly, proliferation was found to be better mixed throughout the domain in the latter case, and a brief examination of the individual cell velocities relative to wavefront position revealed that there was also a greater degree of contact inhibition in this case, a desired result. The trend between cell position relative to the monolayer edge, and velocity was in fact found to be essentially linear and decreasing. The second major difference between the two different types of chemical guidance was essentially a consequence of the first. When contact inhibition is a much more pronounced effect and cells at the back of the monolayer do not move, they cannot break away from the left edge of the domain, as was seen for the reversely adhesive case responding to a linear gradient (Figure 6.13c)). Here, as visualised in Figure 6.17, this unrealistic and undesired breaking away was not observed in this case even under the reversely-adhesive regime. Given that both of these two differences are positive changes, it is concluded here that a consumed chemical gradient is a better predictor of tightly-packed healing clusters with well-defined front edges.

The issue with determining an appropriate value for the chemotactic strength in these cases is made far more complicated by the fact that cell invasion patterns become far less regular in this case, causing the measure of averaging the rightmost cell position to result in a very volatile determination of wavefront position. The simulated wavefronts were found to show in some cases a spike of cell occupancy right at the very front, corresponding to non-monotonic invasive wavefronts. Such non-monotonic invasive profiles are a mathematical curiosity but have not been experimentally observed, and so while they are very interesting here they should also be interpreted as a marker of failure to properly reproduce experimental results. Due to the formation of these more complex wavefronts and the large variation in results between different adhesive regimes, the use of a threshold concentration to define wavefront location (and hence velocity) was considered too risky and the previously discussed measure (the average of the right most cell location in each row) was retained as a measure here.

Due to the fact that these simulations featuring a consumed chemical gradient typically demonstrated cells breaking away from the main monolayer when healing, the model under these circumstances was considered a prime opportunity to try to predict diffuse healing patterns such as those observed for HBMSCs by Sengers *et al.* [169]. However, to maintain comparison with the previous GGH model simulations and the population-level results, the parameter values and desired wavespeed remained those for MG63 cells. As is demonstrated in Figure 6.18, only under the reversely-adhesive regime which explicitly discourages cells from sticking together do cells break away as individuals, and so this is the regime which is focused on here. Cells invading as separate *clusters* (not individuals) which break away from the primary healing monolayer, as they do in the GGH model simulations using the normally- or non-adhesive regime, is not a trend which has been experimentally observed.

With cells inside the monolayer consuming the attractant at an equal rate, a gradient can only form between the occupied and unoccupied regions, especially in the case where the chemical is substrate-bound. This is in contrast to population-level thinking where a certain finite volume site can represent a moderate value of C and thus be partially occupied, something which can never occur in the GGH model. When the chemical attractant is substrate-bound, cells at the front of the wave always experience the strongest gradient, rushing forwards at a much faster rate than the rest of the monolayer. This does not correspond to a travelling wave, because there can be no hope of a constant profile (or even constant average profile) which persists as invasion continues.

In that case, only the foremost cells experience the gradient and then rush forward, continuing to consume the chemical and thus experience a gradient keeping them moving in the direction of healing. In the case of the lower rate of chemical consumption listed in Table 6.1 ($\lambda_s = 0.023$), the GGH model could not recreate a realistic pattern of invasion. If the value of μ was too small, then the simulated invasion was not sufficiently fast, and if the value of μ was increased then cells began to overlap one another, violating the contact inhibition clearly seen in monolayers and resulting in unrealistic cell shapes. When the higher rate of consumption ($\lambda_s = 0.46$) was used the gradient becomes sharper and cells have more opportunity to migrate along it, preventing or lessening the overlapping effect. However, even when the faster consumption rate and a high value of μ is used, it was found that the GGH model as implemented here could not predict a realistic pattern of invasion. The cells at the front which detect the

a) Normal adhesion

b) No adhesion

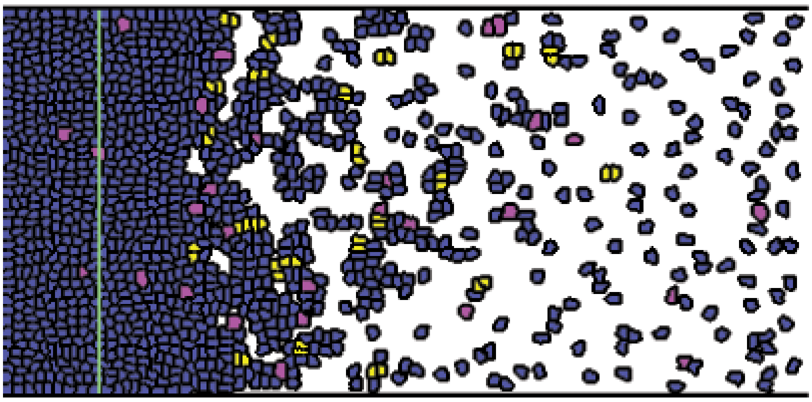

c) Reverse adhesion

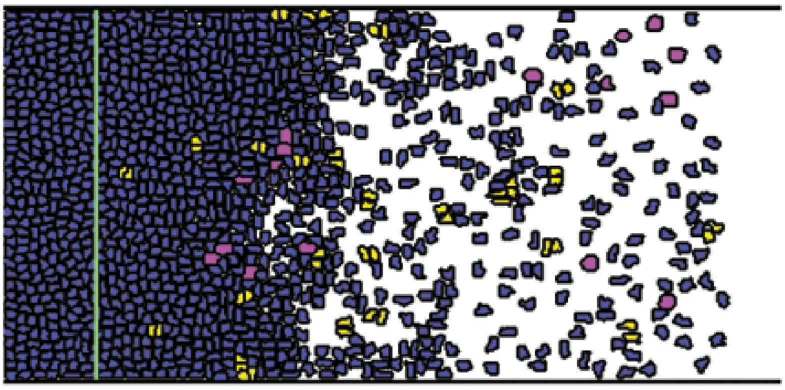

Figure 6.18: Simulated healing of an artificial wound using a GGH model with a normally-adhesive regime. Parameters are $\mathcal{P} = 0.001$, $\mu = 20000$, $\lambda_s = 0.46$ and $D_s = 0.0018$. The elapsed time is 120 hours after the moment of wounding. The horizontal width of the domain is approximately 2.3 mm for the normally- and non-adhesive regimes, and 2.1 mm for the reversely adhesive regime. Blue cells are quiescent, purple cells are proliferative and yellow cells are recent daughter cells.

gradient rush forward, but behind those invasive, 'pioneer' cells the monolayer experiences very little chemotactic effect because the chemical has already been consumed and thus the overall healing outside of the cells which rush forward is extremely similar to the previous proliferation-only simulations shown in Section 6.3.2 to not match experimental observations. Indeed if the movement of the main group of cells is on the whole slower than the pioneer cells, then the formed invasive structure does not represent an invasion wave at all, and the rate of healing cannot simply be classified according to how fast the pioneer cells move.

In the case where the attractant driving migration into the wound space is diffusible, the concentration profile remained smooth and diffuse with the general gradient oriented towards the correct direction of healing and able to affect multiple cells at a given vertical position. To the author's knowledge, there has been no direct demonstration of any specific diffusing chemical signal in a scratch assay. However, it is an easily implemented option for making GGH model cells migratory in order to reach appropriate rates of wound healing, and by comparing the predicted invasive patterns with those observed experimentally the plausibility of a diffusible attractant as an explanation can be examined, helping answer one of the primary questions of the thesis - whether or not scratch assay healing is guided or unguided.

It was determined that a diffusible chemical signal did successfully allow the GGH model to simulate a scratch assay healing in response to a chemical signal, which is why the previously displayed Figure 6.18 feature simulations using those parameter values. With appropriate choice of μ, the simulated wavespeed could indeed match that which is experimentally observed.

Example simulations demonstrating the successful case are shown in Figures 6.18c) and 6.20, giving an idea of the diffuse wavefronts that form. These simulations used a consumption rate of $\lambda_s = 0.46$ and a diffusion coefficient of $D_s = 0.0018$ as quoted in Table 6.1. The velocity of overall healing in these cases was found to indeed potentially match the experimentally observed velocity, without inducing unrealistic behaviour or deformations of individual cells. This was achieved by careful choice of the value of μ, with the value of μ required to predict an appropriate rate of healing depending on the parameter $\mathcal{P}$.

In the case of the lower proliferation rate $\mathcal{P} = 0.001$, the value of μ predicting a healing rate matching experimental observation for MG63 cells was $\mu = 20000$, which is the value used in the simulation presented in Figure 6.18c). The invasion was seen to be very diffuse, but with the monolayer also successfully healing behind the cells which surge forwards individually, in contrast to the case of the substrate-bound attractant seen above where pioneer cells do break away but the monolayer itself showed little healing. The wavefront which forms, averaged over 50 repeated simulations, is visualised in Figure 6.19, displaying a shock front at the leading edge which features a slight spike in the cell concentration, making for a non-monotonic waveform. Diffuse invasive profiles which are observed experimentally (for example the HBMSCs presented by Sengers *et al.* [169]) do not display a shock-like edge as observed here, suggesting that this healing mechanism might not be correct and casting doubt on signal-driven invasion,

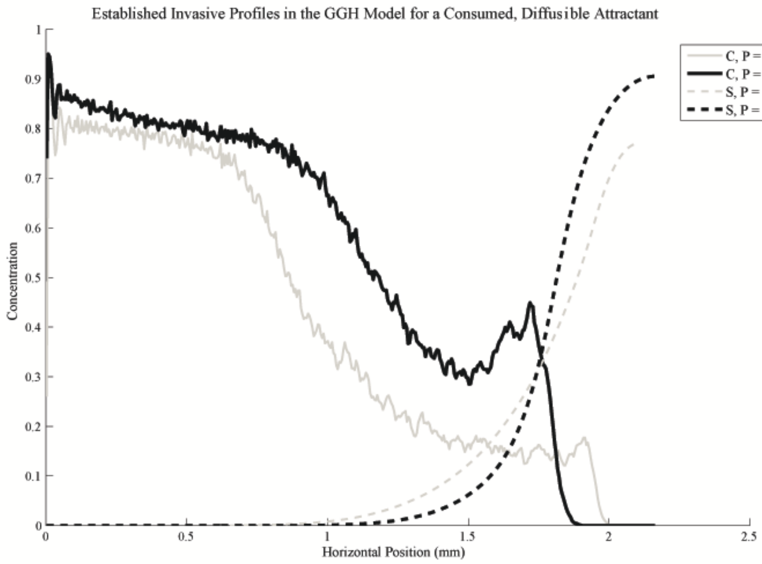

Figure 6.19: The invasive waveforms (after 120 hours) predicted by GGH model simulations with a low ($\mathcal{P} = 0.001$) and moderate ($\mathcal{P} = 0.0025$) proliferation rate. Example visualisations of invasions resulting in this profile are demonstrated in Figures 6.18 and 6.20. Parameters are $\lambda_s = 0.46$, $D_s = 0.0018$ and $\mu = 20000, 110000$ for the lower and higher $\mathcal{P}$ values respectively. The waveform has been generated using the average of 50 simulations.

at least for cell types which display a diffuse invasive pattern. However, the agreement between the GGH model and the PDE model is very surprising, with the GGH model exactly displaying a wave profile displaying a short, shock-fronted edge with a convex curve ending in a flat plateau region connecting the jump discontinuity to the stable state at confluence. Unfortunately, it must be noted that the overall width of the whole wavefront is much larger in the PDE simulations compared to the GGH model observations found here. This could simply be a matter of adjusting parameters, though simulations large enough to represent a domain of appropriate width filled up with cells (and likely given a larger vertical dimension to reduce stochastic variation) would be extremely costly computationally.

When a larger value of $\mathcal{P}$ was trialled in this case, the resulting healing naturally became more proliferation-biased, with the greatest majority of these proliferative events occurring at the travelling front and the width of the wavefront region becoming much smaller. A sample simulation along these lines is visualised in Figure 6.20, and the average invasive profile for this case has also been visualised in Figure 6.19. Due to the fact that proliferating cells do not migrate, and because an increase in $\mathcal{P}$ also significantly affects the purely proliferative assay which is used to determine the physical parameters of the GGH simulations, the chemotactic strength must be significantly increased (here to $\mu = 110000$) in order to maintain consistency with experimentally observed healing rates. Given that the value of μ is a GGH model-specific parameter linked to the strength of chemotaxis but assigned no physical definition, it can be changed freely like this. Moreover, because the physical interpretation of the model has changed to

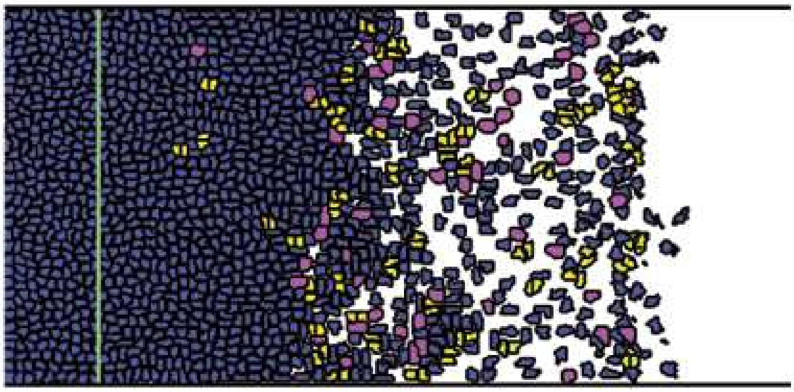

Figure 6.20: Simulated healing of an artificial wound using a GGH model with a reversely adhesive regime. Parameters are $\mathcal{P} = 0.0025$, $\mu = 110000$. The elapsed time is 120 hours after the moment of wounding, and the horizontal width of the domain is 2.2 mm. The green line marks the location of the original wound. Blue cells are quiescent, purple cells are proliferative and yellow cells are recent daughter cells.

match the new value of $\mathcal{P}$, it still successfully predicts the appropriate proliferation rate in the proliferative assay and the invasion rate in the wound healing (circle migration) assay, but with a completely different invasive behaviour (a much sharper and less diffuse profile). Thus, the GGH model implemented here has been shown as capable of predicting different healing patterns by varying the model's *internal* proliferation rate (and an internal parameter relating to chemotaxis strength) without actually changing the *physical* proliferation rate or healing velocity. This allows the GGH model as implemented and interpreted here to successfully simulate scratch assays involving cells which display varying degrees of diffusivity in their invasive pattern, even if the cells involved might have similar doubling times and display similar healing rates. The question then becomes what has effectively been changed physically between the two simulations, and the answer is thought to lie in the fact that the cell's cycle time (and also the time until a cell gives up trying to proliferate) will be different between two simulations with different $\mathcal{P}$ values, because they have been defined in terms of Monte Carlo steps as opposed to a physical length of time. While it is true that changing the value of $\mathcal{P}$ changes the physical scale of the problem and thus slightly alters the rate of diffusion, it can be seen in the figure that this effect is minor (the edges of the chemical concentration curves occur at almost, but not quite, the same location). Thus, the difference in cycle times is far more likely to be the defining factor.

A low $\mathcal{P}$ simulation is suggesting that cells can proliferate quickly once they elect to, but that they are less likely to elect to. In such a situation, cells are more free to move because proliferation causes them to cease responding to the chemotactic gradient. In a higher $\mathcal{P}$ simulation cells are more likely to try to proliferate but take longer to do so, resulting in an equivalent macroscopic proliferation rate but causing less cells to be able to respond to the chemical gradient and thus reducing how diffuse the observed healing wavefront will be. In a somewhat loose sense, the parameter $\mathcal{P}$ here can be interpreted as a parameter controlling the likelihood of migratory events over proliferative events for an individual cell. Admittedly the specifics of the cell cycle and the feasibility of the specific timing values chosen here have not been considered, and an investigation of how behaviour varied with different cell cycle times would be very interesting indeed. Perhaps far more interesting, in the opinion of the author, would be the incorporation of a migratory cell phenotype as mentioned previously, where a second probability like $\mathcal{P}$ could apply to non-contact-inhibited cells in the same fashion that proliferation does here, but this probability representing the likelihood of switching to the migratory phenotype. This would be a more in-depth means of considering the impacts of how proliferation inhibits migration (because proliferating cells round up instead of crawling).

The wave profile exhibited in this case of a higher proliferation rate $\mathcal{P} = 0.0025$ with a taller shock front and thinner wave region seems to correspond to the profile observed in the PDE model when the consumption rate was lowered (and chemotactic response increased to compensate). However, the previous issues of a very different wavefront width and a spike at the front of the wave profile which does not feature in the population-level simulations still remain. Interestingly the larger spike does correspond to the situation where numerical instabilities were observed in the finite volume solver when cell diffusion was not allowed (and indeed cell diffusion is almost negligible in these GGH model simulations). Checking the results of applying a scheme like the KT scheme to the PDE system under these conditions (which might be able to better handle this very numerically-difficult problem) for a spike in the wavefront which was not merely a result of numerical oscillation would be extremely interesting.

The extent of contact inhibition encountered in this case of diffusing chemicals was also examined using the typical means of comparing individual cell velocity to wavefront position, with the results visualised in Figure 6.21. It is seen that the results are very desirable for both $\mathcal{P}$ values, with the greatest majority of migration coming from the cells at the wavefront, but with a smaller amount of migration towards the wound still observed in cells a little way behind the wound edge, matching experimental observations of partially but not entirely contact inhibited migration in cells just behind the wavefront [26]. This general pattern was also observed for the other adhesive regimes, when simulations like those visualised in Figure 6.18 were tested for velocity-position relationships.

6.4 Conclusions

The GGH model has mostly predicted invasion occurring via a tightly-clustered monolayer even in the cases where adhesion is switched off or specifically discourages cell-cell contact. This behaviour did not match with the PDE model (where it corresponds to a travelling jump discontinuity between uninvaded and invaded steady states) but does agree with many visualisations of experimental results which do demonstrate clearly defined wavefront edges. Experimental results do show a greater deal of variance in front position along the front (indeed perhaps what allows experimental data showing a clear wound edge to result in diffuse profiles when observed macroscopically [169]) but this could potentially be achieved in the GGH

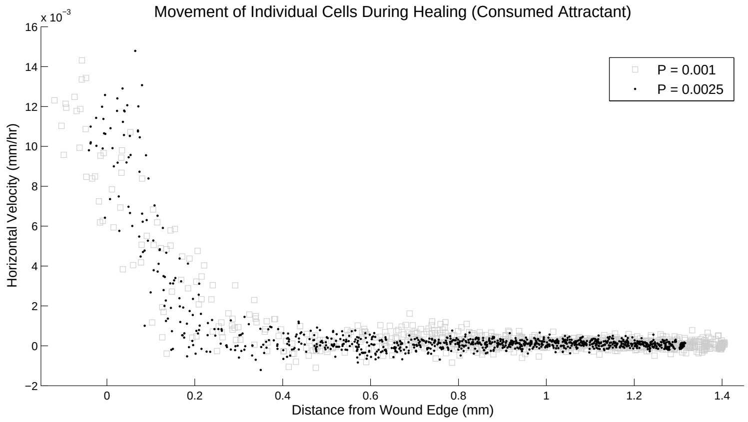

Figure 6.21: Demonstration of the trend between a cell's location relative to the wavefront and its velocity over a simulated period of healing driven by a consumed, diffusive chemical. Migration is strongest at the wavefront edge, with a small amount occurring behind that, suggesting a good match with experimental observation.

model via increasing the extent of stochastic variation somehow, possibly by changing H_{bond} or T or using a lower proliferation probability run over a longer timeframe. It was quickly discovered that although GGH model simulations featuring only proliferation did seem to generate rather realistic-looking healing which did indeed feature sharp fronts like those experimentally observed, when the physical scale of the GGH model was considered the invasion rate in these cases was far too small to match experiments. Thus the author's suspicion that proliferative pressure could drive sharp-fronted invasion which was successfully represented by diffusion at the population scale simply because diffusion introduced a movement seen only at the wavefront has been disproved.

Introducing a chemical gradient did allow for the GGH model to simulate invasive healing that did occur at a fast enough rate to match experimental simulations, unlike the purely proliferative case. Depending on the nature of this introduced chemotaxis, cells could either invade as a single cluster as in the purely proliferative case, or with individual cells or smaller clusters breaking away from the main monolayer to invade ahead of it. When chemotaxis was implemented in the most basic way, with an enforced and fixed linear gradient for cells to respond to, cells remained clustered and analysis of individual cell movements showed that all cells responded to the gradient almost equally. This is not an observation matching experimental results where migration tends to be limited to cells at the wavefront. By using a gradient which only affected half of the cells, the effects of 'partial activation' could also be examined, with the result found to be a depletion of cells at the region where the gradient began. Thus a linear chemotactic response which only applied to cells near the location of the initial scratch also could not properly predict realistic scratch assay healing. Indeed, this is quite an intuitive result and the use of a simple linear gradient is a mathematical construct without strong biological justification, but this does clearly highlight the necessity of examining the behaviours of individual cells. When this linear chemotaxis was considered at the population level the macroscopic concentration curves showed the same depletion effect and steady healing into the wounded region, albeit with rather diffuse curves. Even images of the GGH model simulations showed a healing monolayer with clear wound edge and proliferation behind the wavefront, invading at the correct speed. It is only by considering the movements of individual cells that the unrealistic features of healing driven by such a linear gradient can be exhibited.

The results for migration driven by a consumed chemical gradient were more complex, and depended strongly on the cells' consumption rate of this signal, λ_s. In both the PDE and GGH models' simulations, the effect of a larger value of λ_s (and associated reduction of chemical response to ensure the macroscopic wavespeed did not change) was found to cause the wavefront to widen and the height of the formed jump discontinuity to become shorter. Indeed, the profiles for the higher $\lambda_s = 0.46$ value for both the population scale and individual cell scale model were extremely similar except for the widths of the two corresponding profiles, and a small non-monotonic spike in the waveform for the GGH model. This was achieved in the case of the reversely-adhesive regime in the GGH model, which was the only model which predicted the cells which broke away from the main monolayer invading as individuals instead of smaller clusters. The visualisations of these GGH model results with a fast consumption rate were thought to be comparable to experimental visualisations of cell types which show diffuse invasion patterns (for example the HSBMC's studied by Sengers *et al.* [169]). However, given that both the PDE model and GGH model have agreed in predicting a shock-fronted wave with a flat profile behind it, and this does not match the profiles measured in the experiment at all (with no clear wavefront edge and a typical diffusion-like shape), the conclusion here is that a chemical consumption effect is not the driving behaviour behind cellular invasion in this case. This cannot be taken as an obvious point despite the success of Sengers *et al.* modelling the invasion of that cell type with a simple Fisher's equation [169], as this thesis repeatedly demonstrates (and others agree [178]) that the success of population-level models should not be blindly trusted.

The results for a slower rate of chemical consumption differed more significantly between the population-level and individual-cell-level models, though both displayed a sharp shock front of significant height. In the PDE case the general shape of a convex wave profile which flattens off before a jump discontinuity was still observed, but the GGH model simply predicted a tightly clustered monolayer which healed in a similar fashion to the case of linear chemotaxis. However, there were indeed key differences between the two situations. When individual cell velocities were examined, it was found that this situation better represented experimental observations, where cells behind the wavefront show a small but nonzero velocity biased towards the direction of healing [26]. The trend in this case was seen to be essentially linear (decreasing) between a cell's effective healing rate and its distance from the wavefront. Additionally, proliferation of cells in this case was seen to be better distributed throughout the entirety of the monolayer, better matching typical experimental observation [199]. Another difference between a slowly consumed gradient and a universal linear gradient was for the case of the reversely-adhesive regime, where only the linear gradient caused the cell cluster to break away from the left edge of the domain, not a biological effect but one also predicted by the PDE model when chemotaxis was not contact inhibited.

The best correspondence between population-level and individual-cell-level models was found for the reversely-adhesive GGH model, because it produced the greatest amount of cell spreading and thus corresponded better to the more diffuse profiles observed in the majority of PDE model predictions. Chosen to prevent cells from sticking together and thus thought to be representing contact inhibition of migration (which causes cells to change direction when colliding with other cells), it was actually discovered that this choice of adhesions J best corresponded to a complete *lack* of contact inhibition of chemotaxis ($m = 0$) in the PDE model. This unintuitive result highlights the need for sophisticated models on the scale of individual cells like the GGH model implemented here, because the interactions of the various cell behaviours essentially assumed separate by PDE models, and those not often considered by PDE models (adhesion, proliferative pressure) are key.

A means of representing diffusion via active, but random cell motility in the GGH model has been identified as a necessity in this chapter, with the effects of proliferative pressure and random fluctuations caused by the stochastic nature of the model to be insufficient for this purpose. Without the proper inclusion of a sufficient amount of random migration, it was difficult to use the individual-cell-level model to attempt to distinguish between guided and unguided migration as is the primary thrust of this thesis. However, this deficiency was one that could not be known before constructing the model and simulating it with a chosen model cell and physical interpretation (here provided by a simple but unique technique) in mind. The author's recommended means of including such an effect for future work is to incorporate a polarisation for each cell which could then be informed by the chemical gradient but would also allow for unbiased polarity in order to achieve random active motility in the absence of a specific chemical gradient. To prevent this active random motility from applying to all cells, the means of choosing cells to proliferate in the GGH model here might also be applied to deal with the 'activation' of cells into a migratory phenotype.

In summary, the attempt has been to distinguish between various postulated mechanisms for cell invasion, namely proliferative pressure, unguided migration and tactically guided migration. Purely proliferative healing is obviously incapable of reproducing diffuse invasive patterns, but was thought a possible explanation for healing where cells remain as a singular cluster with clearly defined wound edge. This was shown not to be the case for MG63 cells, but as previously argued the doubling times and macroscopic invasion rates for many different cell types are very similar. Population-level models with unguided migration have been seen to model invasions of tightly packed cell clusters well on a macroscopic scale, but without correctly capturing the sharp, well-defined edge of the monolayer ([115, 169]). Diffusion would also not be expected to be able to naturally predict cells just behind the healing edge showing reduced velocity in the direction of healing, either, though this unfortunately could not be tested in the GGH model implementation here because it was only after analysing the results that it was found that inherent diffusion introduced by the model's stochastic nature was insufficient. For this reason, it was concluded that some sort of chemical guidance effect must be at work for cell types which show wound healing via a single expanding monolayer. Exploration of the various types of chemotactic healing considered here demonstrated that in the individual cell model either a pure linear advection or a cellular response to a consumed attractant can produce an appropriately healing monolayer, provided this nutrient was diffusible and consumed sufficiently slowly. Examination of individual cell movements in both situations suggested that a consumed attractant was more realistic. Linearly advected cells showed almost no contact inhibition of migration and when this was inhibition was manually enforced via the method of Merks [130] the healing monolayer was lost. On the other hand, both GGH model and PDE predictions for diffusely healing scratch assays agreed that no sort of chemical response predicted waveforms which could match what has been observed experimentally [169]. While a chemical gradient consumed sufficiently rapidly did allow some cells in the GGH model to break away from the primary cluster and surge forwards to heal, visualisations and constructed average wavefronts showed a certain threshold distance which clearly marked the edge of the invasive region, in contrast to scratch assay photography. This 'threshold' effect was also predicted by the PDE model via a jump discontinuity. With simulations on both scales suggesting chemotaxis is an inappropriate predictor of diffusive healing, it is concluded here that healing monolayers displaying spaced out, individual invading cells operate simply via random motility and contact inhibition of migration. On the other hand, when a monolayer heals as a single expanding cluster of cells, the GGH model simulations have suggested that a slowly-consumed chemical gradient is actually the most reasonable explanation for this effect. To truly make that conclusion, however, a correct active but unguided migration would need to be included into the GGH model implementation to test against this.

Chapter 7

A Heterogeneous Scratch Assay

7.1 Approach and Rationale

It has been seen that some sort of migratory effect is a necessary component of healing in wounding or invading monolayers, as demonstrated clearly by non-proliferative experimental assays, and also through GGH model simulations which took into account the space-filling effect resulting from cell proliferation. However, as has been reviewed, the exact nature of this active migration is not easily quantified, but can be explained by either random motility of cells (to some degree biased in the direction of healing by the effects of contact inhibition of migration) or by a tactic response of cells to a chemical signal. The conclusion of the work in Chapter 6 was that an unguided migration effect was more likely to be the primary effect, due to inconsistencies between the invasions predicted by both macroscopic and microscopic scale mathematical models including a guided invasion effect and what is actually observed experimentally. This chapter seeks to use a novel thought experiment to suggest further experiments which could possibly be used to better determine what migratory behaviours are at work in monolayer healing for various cell types under different experimental conditions. The large differences in invasive behaviour that can be seen for different cell types [169], different chemical environments [199] and different physical triggers [137] make simple identification of dominant behaviours very desirable.

The thought experiment explored here is a scratch assay occurring over a heterogeneous domain, still representing an appropriately treated culture dish, but one in which there is now some variance of property (and thus variance in one or more simulation parameters in a corresponding mathematical model). One presumably easy approach for achieving this would be to use a substrate with a varying stiffness or roughness, both of which have been shown to affect cell motility [92, 111]. However, neither of these properties has an effect on cell migration in either of the mathematical models used here, and so instead changes to parameters which directly impact on the invasion rate are made instead, with little emphasis given to the feasibility of experimental realisation.

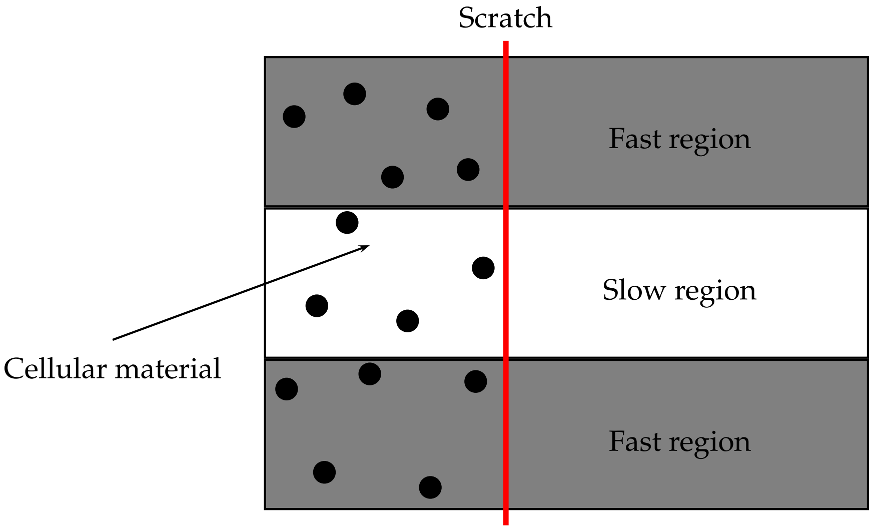

Figure 7.1: Demonstration of the heterogeneous domain.

Specifically, the non-homogeneous domain is one where there are two regions with the boundary between them running perpendicular to the scratch in the monolayer. Using the same convention as in Chapter 6, invasion is to the right, and the bands are horizontal, an upper and lower band with the rate of invasion different between the two. These are referred to as a 'fast' and 'slow' band, and the upper region is taken as the fast one without loss of generality. A graphical representation of the situation, albeit with three bands for consistency with the works of Brazhnik and Tyson [19, 20] which inspired this approach, is given in Figure 7.1. Brazhnik and Tyson explored how fast and slow regions in a generalised excitable (bistable) media could generate steady travelling wavefronts. At the macroscopic scale at least, cell invasion operates as a travelling wave connecting an unsteady and a steady stable state, and thus serves as an example of bistable media. In Chapter 6, the GGH model implementation was also demonstrated as capable of predicting waves with constant invasive velocity. However, a chemotactic effect specifically acting in a certain direction introduces an anisotropy which prevents consideration of the scratch assay as a simple excitable media (unlike having an isotropic effect which differs between several domains). The case of a consumed gradient does result in a correspondence between the direction of the chemical gradient and the invaded and uninvaded regions, and thus could perhaps be simplified into an excitable media.

A domain of form shown in Figure 7.1 presents the opportunity to observe cellular migration as it is impacted by bands of different property. Given that steady travelling waves have been mathematically predicted to exist in such a structure [20, 125], this situation provides a prime opportunity for mathematical exploration that can be tied to a potentially simple experimental setup. If a steady rate of cellular invasion for such a domain was indeed observed experimentally, then this could be an opportunity to differentiate guided and unguided invasion whilst still using a macroscopic property (wavespeed) which is easily determined experimentally. This would be in contrast to scratch assays (and their mathematical models) on homogeneous domains where the examination of individual cell data has been raised as a necessity [178]. The remainder of this thesis deals with what the two streams of mathematics considered here (population-level models driven by PDEs and individual-cell-level models driven by the GGH model) suggest about how guided and unguided migration differ in the case of this novel thought experiment and thus conclude what experimental observations would be expected when cell migration is dominated by guided or unguided migration.

It is necessary to define what exactly is the difference between the fast and slow regions of the nonhomogeneous domain, and naturally this can be achieved in several ways, potentially different for different types of modelled scratch assay (for example guided migration versus unguided migration situations presenting different parameters to be varied). Given that the suggested potential biological realisation of this thought experiment would involve modifying the substrate to modify the ability of individual cells to move, it was the parameters directly affecting migration which were chosen to be modified in order to construct regions of fast and slow invasion. This was opposed to varying proliferation, which also affects the overall rate of invasion and so could also generate fast and slow regions. However in addition to the anticipated increased biological applicability of varying migratory rates directly, the effect of proliferation is a little bit more difficult to classify given that the GGH model has actually demonstrated a reduced invasion rate for higher values of proliferation, in direct contrast to the macroscopic models which do not distinguish between migrating and proliferating cells.

Unfortunately, there is no parameter that can simply be varied to control the rate of unguided invasion in the case of the GGH model, due to the unexpected failing of its stochastic updates to appropriately generate random motility. Thus the individual-cell-level simulations here could only be used for the cases where migration was driven by a chemical gradient. Taking this into account, the PDE model was used to attempt to distinguish between guided and unguided migration via consideration of wavefront features, with the GGH model then used to attempt to verify if the interesting features seen to develop were indeed legitimate effects and not a consequence of numerical instability or an incorrect realisation of the effects of the boundary between the fast and slow regions.

In the previous chapter, a comparison with experimental results (specifically those for MG63 cells presented by Sengers *et al.* [169]) was used to inform parameter choices, most notably through a target wavespeed. This was especially important in the case of the GGH model, where interactions between parameters are less easily defined or summarised, and parameter choices themselves are a bit more nebulous. There are no known experimental results to be compared against for the non-homogeneous case, and so instead the simulations here operate as thought experiments, using the parameter values already established in Chapter 6 as a

Situation	Parameter	Fast Value	Slow Value
PDE model - diffusion-driven healing	D	0.0134	0.0034
PDE model - advection-driven healing quickly consumed signal	χ_0	0.03	0.012
PDE model - advection-driven healing slowly consumed signal	χ_0	0.10	0.015
GGH model - advection-driven healing quickly consumed signal	μ	20000	8000
GGH model - advection-driven healing slowly consumed signal	μ	20000	4000

Table 7.1: Parameter choices in order to define a fast region and slow region where cells invade at half the speed, with the fast wavespeed corresponding to the typical invasion rate for MG63 cells, $0.0124\,\text{mm/hr}$. Other parameter values used in simulations were those in Table 6.1.

basis. Preliminary simulations run without a heterogeneous domain were used to determine what extent of parameter variation was required to obtain a consistent amount of decreased migration in the slow region, with the desired level of decrease arbitrarily chosen to be 50%. The results of these simulations are presented in Table 7.1. It should be noted that the case of a linear, prescribed gradient driving invasive healing has not been considered in this chapter. This is both because of its suggested unrealistic nature and because a migration entirely in the direction of healing corresponds to no mixing between domains and thus no establishment of a steady wavefront and singular wavespeed across the whole heterogeneous domain.

The means of locating wavefront positions was chosen to match that already used for homogeneous domains in the GGH model simulations already presented. That is, the rightmost occupied location in each row (“occupied” in the PDE model corresponding to $C > 0.01$) was averaged to determine an overall location of the wavefront. This does mean that in cases where cells broke away from the cluster it was the pioneer cells which dictated the wavefront position.

7.2 Analysis

7.2.1 Population-level Simulations

It was first critical to ensure that the population-level PDEs used here were indeed capable of predicting a steady wavefront which successfully invaded the wound space at a constant rate despite a reduced cell velocity in one portion of the domain. Thus the different potential healing regimes were all tested using a simple domain of 50% fast and 50% slow medium and the wavefront position tracked to determine whether or not the wavespeed was constant. It is reiterated that especially the wave velocity is important because it represents an easily measured, macroscopic quantity.

In all cases it was found that the various PDE models did all result in constant speed-travelling waves which invaded into the wound region at a moderate velocity between the two velocities

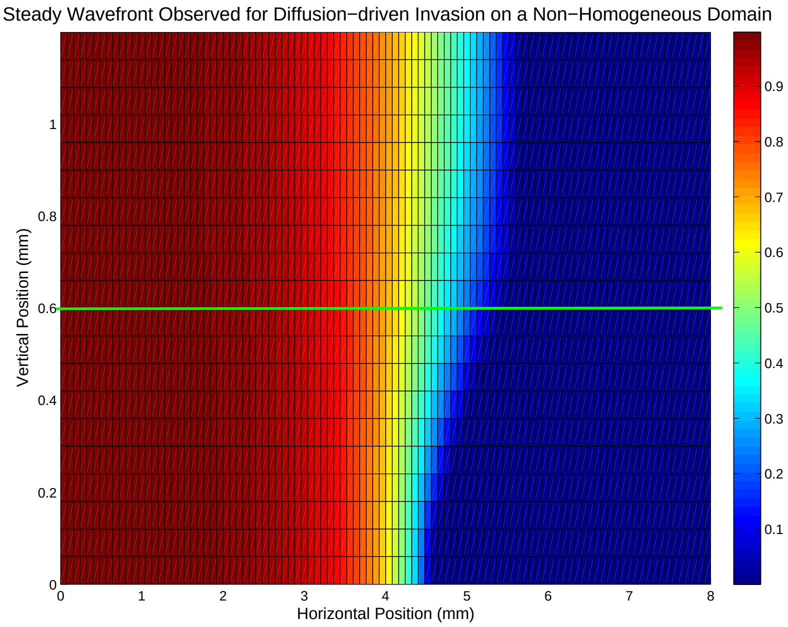

Figure 7.2: Steady wavefront which develops on a heterogeneous domain healing via random motility of individual cells (diffusion). The green line marks the domain between the two boundaries, with parameters as in Table 7.1.

corresponding to invasion waves in purely fast or purely slow domains. This demonstrated that although the lack of isotropy in the case of guided migration disallows the use of the kinematic method originally used to predict travelling waves of constant speed and shape in such media [20], invasion waves in these cases still display curvature-velocity effects which allow steady 2D waveforms to develop. The unique types of waveform found to develop for different migratory mechanisms are visualised in Figures 7.2-7.4.

The diffusion-driven simulation displayed no particularly interesting features, outside of its ability to generate a steady speed travelling wave in the first place, something which had already been demonstrated for a linear diffusive effect [125]. However, the chemotaxis-driven simulations proved much more interesting. In the case of either a substrate-bound or diffusible attractant, the actual front of cells remained largely unaffected and invaded in an expected fashion with cells in the fast region surging forward and filling in to the slow region to create a curved front invading at a moderate velocity. However, behind these typically-behaving pioneer cells the behaviour was very different between the two types of attractant, and between either type of attractant-driven and diffusion-driven invasion. It is these general, macroscopic trends (which could theoretically be experimentally observed) which are important to establish, because small-scale specificities in wavefront shape will depend more heavily on parameter choices and biological complexities. This is doubly important when it is contextualised that all simulations here have used parameter values corresponding only to a single type of cell chosen as a model species.

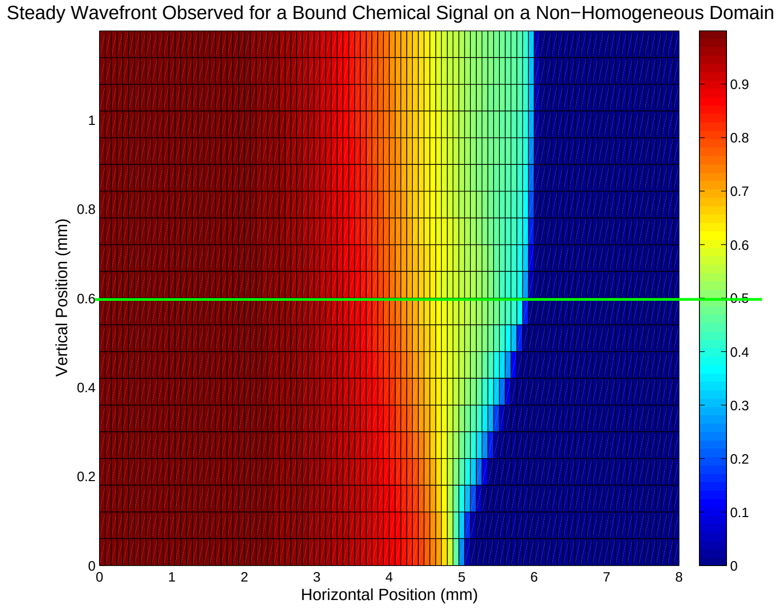

Figure 7.3: Steady wavefront which develops on a heterogeneous domain healing via a substrate-bound, consumed chemical gradient. The green line marks the domain between the two boundaries, with parameters as in Table 7.1. A trend of higher concentrations actually being observed further invaded into the wound space in the *slow* region can be observed.

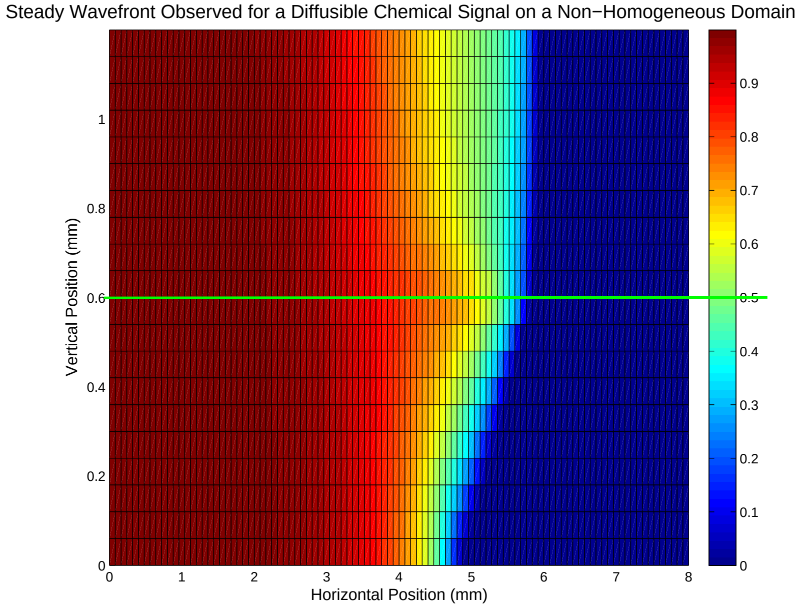

Figure 7.4: Steady wavefront which develops on a heterogeneous domain healing via a diffusible, consumed chemical gradient. The green line marks the domain between the two boundaries, with parameters as in Table 7.1. A trend of higher concentrations at the boundary between the two regions caused by cells 'piling up' in this location can be observed.

The key distinguishing behaviour for cells invading in response to a substrate-bound chemical attractant is a buildup of cells just behind the travelling front, at the distant edge of the slow region. Unfortunately this appears to be a boundary effect, which would require a specific geometry to recreate in an experimental situation. It is expected that this effect occurs because without diffusion to smooth out the concentration field of the attractive signal, cells which fill in to the slow region from the fast region continue to experience a gradient in the downwards direction, advecting them up against the solid boundary at the bottom of the domain. This effect is caused by the additional cells filling in from the fast region and thus was seen to occur near the edge of the wavefront.

When the gradient was diffusible, a similar buildup of cells in the slow region could be observed, but in this case the gradient's diffusion caused its profile to smooth out and prevent the continuous advection of cells towards the lower boundary. Instead, the 'piling up' effect was observed at the centre of the domain, with a clear ridge of increased concentration seen to run horizontally along the wavefront. This perculiarity was particularly pronounced when cells did not display random motility ($D = 0$), preventing cell diffusion from smoothing out the spike in concentration. Given that such an effect has been witnessed coming from a numeric solver for a PDE system which has displayed the potential to generate spikes due to numerical instability, *and* occurring at a boundary where there is a non-smooth switching from one parameter value to another, it is quite easy to dismiss this observation as simply a numerical artefact. However, one point arguing against that interpretation is that the concentration profile of the chemical signal driving the tactic migration which creates this effect is indeed smooth. The key test of the legitimacy of this effect lies in whether or not it can be observed in an individual-cell-based model where numerical artefacts are not a concern.

The other macroscopic property of these simulations on heterogeneous domains is the wavespeed of the travelling profile, a quantity which becomes much more interesting in this case. When the scratch assay is modelled on a homogeneous domain, parameter matching allows many different population level models to all predict the 'right' result, with no easy means of distinguishing between them to determine which is actually correctly representing cell behaviours [179]. However, when invasion occurs across a heterogeneous domain, parameter matching has already been used to ensure the correct velocities in the fast and slow regions of the domain, leaving no degrees of freedom that might be used to adjust results as required. Thus it is quite possible for the wavespeeds of steady travelling wavefronts to vary depending on the effect driving cellular invasion, presenting another means of distinguishing between the various types of guided and unguided invasion.

Indeed, a considerable difference was observed. Invasion driven by a chemical gradient showed a much larger degree of 'filling in' from the fast region, and this allowed the slow region's wave profile to effectively move much quicker too, because the influx of cells served almost as an increased value of proliferation rate λ. Indeed, even using a domain of 50% slow region where cells travel at half the speed, the velocity was found to be almost the same as if the entire domain was simply a fast region. In contrast, for unguided migration, the presence of a slow region did show a moderate slowing effect on the overall travelling wave that formed, the speed at a moderate value between those for the slow and fast region. Thus guided and unguided migration might easily be distinguished simply by performing two separate scratches on a fast substrate and a slow substrate to check for invasive velocities, and then comparing these with the healing rate observed for a heterogeneous substrate.

Physically, the waves which show 'faster' invasion for higher contour values in the slow region correspond to an overall depositing of cells in the slow region, at least behind the pioneer cells. This would be easily detected in a GGH model simulation or experimental photographic image simply by counting cells to determine densities in different regions and checking if a certain moderate density was indeed seen further advanced into the wound space in the slower region. Of course, this necessitates a non-adhesive or reverse adhesive GGH model so that cells can actually break away from one another in order to achieve any regions of moderate density at all. Observation of such a trend experimentally would be incredible given its non-intuitiveness, and these population-level results suggest the explanation could lie in a substrate-bound attractant or nutrient being consumed by cells. If a steady wavefront invading at constant speed was observed but without any cellular build up in the slow region, then this would suggest a healing driven by the random motility of cells. At this point, to contrast with the two potential results just discussed, it should be recalled that invasions driven purely by an advection in the direction of the wound space (i.e. purely to the right in the problems discussed and visualised here) do not demonstrate steady travelling wavefronts at all. Of course, the lack of a steady travelling wavefront is also an effect that might be experimentally realised, so this fact should not be forgotten. The lack of biological realism associated with the linear gradient situation does suggest that an experimental scratch assay performed on a non-homogeneous domain would be expected to evolve into a single travelling wave of constant velocity.

7.2.2 Individual-cell-level Simulations

The GGH model implementation that has been created here is important as a means of simulating the behaviour of individual cells, because it is able to more naturally capture the effects of their blocking one another and the space occupied by proliferation. Moreover, concerns like numerical instability or inaccuracy are not relevant, and thus if the interesting results demonstrated in the previous section can be replicated in this theoretically 'safer' environment the possibilities that these results arise due to numerical issues or from the implicit assumptions of a continuum model can be disregarded. For this reason, the first simulations considered here are those which seek to replicate or discredit the interesting effects which have been seen in the PDE model. Given that parameters which provide an approximately correct wavespeed in the two regions have already been defined, these could be used directly without modification. Remembering that contour lines cannot really be used to analyse the predictions of the GGH model, the goal was to identify whether or not cells did cluster in the aforementioned regions.

The results of these GGH model simulations did in fact demonstrate the desired behaviours

Figure 7.5: GGH-model-simulated healing on a heterogeneous domain where invasion is driven by a consumed chemical gradient, with the boundary between fast and slow regions marked in green. Two examples of a deposition of cells where the effective concentration is significantly larger in the slow region compared to the fast region have been circled.

on a qualitative level, suggesting that the effects on invasive behaviour which arise due to a substrate-bound or diffusible, cell-consumed attractant are not numerical artefacts but very real effects. As can be seen in the visualisations (Figures 7.5 and 7.6), clustering of cells in the expected regions is indeed naturally observed without making any additional considerations or artificial modifications to the model. Additionally, ahead of these unique behaviours the pioneer cells (somewhat corresponding to very low contour values in the results of the PDE simulations) behave just like the front edges of the invasive wavefronts in the population-level model. That is, pioneer cells behave as could be intuitively predicted, with the fast region surging forwards and then also filling into the slower region where cells lag behind. The behaviour of the wavefront behind these pioneer cells distinguishes between migration that is driven by random motility (biased towards open space) and migration that is driven by a consumed chemical signal (and whether or not this chemical signal is substrate-bound/haptotactic or diffusible). This result alone suggests a standard scratch assay executed on a non-homogeneous domain like the ones considered here could easily be checked for these key behaviours in order to provide a rather strong answer to the question of whether or not a certain cell type's invasion is guided or unguided.

The visualised simulations here used parameter values which predicted invasion of individual cells, given that this was the regime which demonstrated a good match with population-level simulations involving a consumed attractant on homogeneous domains in Chapter 6. GGH model predictions of healing monolayers which remain as a singular cell cluster could not be matched to PDE model predictions, but given that such fronts have been readily observed in scratch assay experiments this did not invalidate their consideration on non-homogeneous do-

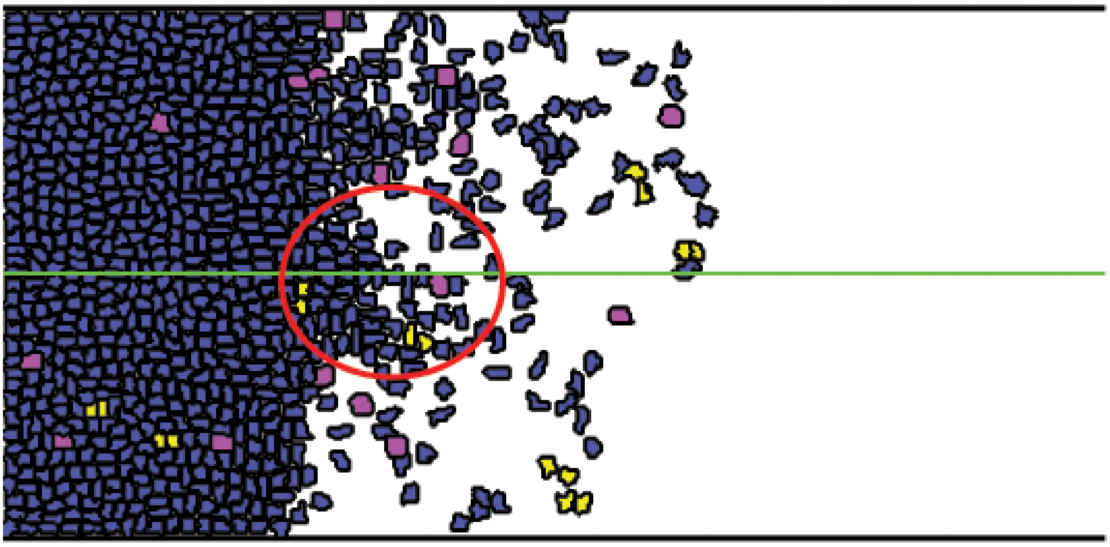

Figure 7.6: GGH-model-simulated healing on a heterogeneous domain where invasion is driven by a consumed chemical gradient, with the boundary between fast and slow regions marked in green. A deposition of cells at the centre of the domain, at the boundary between the fast and slow regions, is observed (circled).

mains here. Unfortunately, it was discovered that these wavefronts did not readily demonstrate the establishment of steady speed travelling waves of fixed shape.

7.3 Conclusions

This thought experiment has been used as a supplement to the results uncovered in Chapter 6, the use of non-homogeneous domains demonstrated here to be a potential experimental tool that could be used to determine which cell behaviours are dominant for a given cell type. Key differences between cell migration driven by random motility and that driven by a chemical gradient have been shown using both the population-level model and the individual-cell-level model with both frameworks predicting the same qualitative features which might be experimentally observed in a scratch assay. A potential simple means of establishing such an experiment has been proposed.

It was unfortunately found that healing over a non-homogeneous domain would not always lead to a single steady wavefront moving at constant velocity across both domains (despite the differing velocities of individual cells in those two domains). In the case of an enforced linear chemotaxis where there is little mixing between the two regions, this result was unsurprising. However, a lack of a steady travelling wavefront in a tightly-packed cluster in the case where the migratory response was to a consumed chemical attractant was less expected. Given that chemical will not be consumed in areas in the slow region where invasion has not yet reached, a filling in of cells from the fast region in order to generate a steady wave was thought to be a possibility. This can be explained, however. As concluded in Chapter 6, it was the reversely-adhesive regime in the GGH model which featured cells with the most willingness to move and break away from the monolayer. Here, where the establishment of a steady wavespeed relies on a movement of cells from the fast region into the slow region, this movement is insufficient when cells are not free to individually move, as dictated by their relative adhesions to each other and the medium, J. This does suggest that when attempting to observe the trends seen in this chapter and summarised below in an experimental context, the use of cells which do display a diffuse invasive pattern (e.g. HBMSCs [169]) is critical.

Simulations which did use the parameter set found to nicely predict diffuse healing with individual cells breaking away from the cluster (and its equivalent at the population level) did reveal very interesting behaviour. The PDE model showed that the invading edge of the wavefront behaved largely the same, with cells surging forward in the faster region and filling in to the slower region to create a steady wave profile which was curved in 2D, no matter which sort of effect was the driver of invasion. However, the behaviour behind the very front of the wave was found to be very different depending on whether cells migrated due to random motility or due to a cell-consumed signal that was either diffusible or substrate-bound. The key difference between guided and unguided migration in this case was that for a given horizontal location, a diffusion-driven invasion would never display a significantly larger concentration of cells in the slow region compared to the fast region. However, invasions driven by consumed chemicals exhibited exactly this, with the wave profile actually appearing to be more advanced in the slow region (apart from its edge) due to the buildup of cells. This effect can be explained by the consumption of the chemical signal by cells. When cells in the fast region surge forwards, they experience a positive gradient not only in the direction of healing, but in the direction of the slow region as well, where the nutrient has not yet been consumed. This effect is not seen for the 'pioneer cells' which make up the very front of the wave profile, because this represents those cells which are crawling in the direction of healing. This does also explain the difference in behaviour observed for a diffusible and substrate-bound attractant. In the former case, the vertical imbalance in the gradient is restored by diffusion, preventing significant invasion of cells into the slow region. However, cells are still advected towards the slow region initially, and so they end up deposited at the middle of the domain. On the other hand, a substrate-bound attractant cannot correct this vertical imbalance and so those cells which enter from the fast region continue to consume the chemical signal and thus establish a vertical gradient further into the slow region.

The PDE model simulations used a small vertical height, so that comparisons with the GGH model would be more direct. It would be interesting to explore what happens when the vertical length of the domain is actually very long compared to the horizontal length. While a diffusible gradient would likely still predict a buildup of cells on the edge between the two regions, the piling up against the boundary observed in the case of a substrate-bound chemical might instead be replaced by invasion into the slow region of a certain distance only.

There were concerns that these PDE model predictions might be consequences of the failure of the population level scheme to correctly represent the interactions of individual cells, or even numerical artefacts (especially considering there is a discontinuity in the value of the chemotaxis, χ between the two regions, the location of the concentration spike in one case). However, these concerns were alleviated by the GGH model simulations, where cell interactions are handled naturally and numerical instabilities not a concern. Without any modifications made to the GGH model, it has been seen here to correctly produce a piling up of cells at the boundary between the fast and slow regions, or the boundary of the domain in the slow region, corresponding correctly to a diffusible and substrate-bound gradient, respectively. The qualitative agreement between the two different modelling frameworks was not limited to these unique, unintuitive observations. Just like in the PDE model, the edge of the wavefront (here represented by the threshold distance reached by 'pioneer cells') did show the typical effect of an almost vertical edge in the fast region which curves back into the slow region. The interesting behaviours occurred behind these pioneer cells.

One last observation which could serve as an experimental differentiator between guided and unguided invasion over a non-homogeneous domain was the macroscopic wavespeed formed by the steady wave profiles. The different invasive regimes could be consistently compared by choosing parameters such that the velocities of healing in the fast and slow region (when considered as a separate, homogeneous domain) were the same regardless of whether cells were experiencing random motility or a guided response. Comparing the wavespeeds of the profiles formed by diffusion-driven healing and chemotaxis-driven healing, it was seen that the diffusive case was far more seriously impacted by the presence of a slow region, with the established wavespeed being a moderate value between the fast and slow speeds. In contrast, invasion driven by a consumed attractant settled into a steady speed that was almost equivalent to the case of healing on a purely 'fast' domain. This also allows for experimental design that might distinguish between these two varieties of invasion, with the location of the build up of cells (if any) used to distinguish between the two types of chemotaxis. If chemotaxis was a simple linear response, then no steady wavefront would be expected to be established. Again, this approach is thought to be applicable to cells which do show diffuse invasion patterns.

In Chapter 6 it was proposed that monolayer healing which occurs via a tightly clustered population which invades as a sheet is a tactic behaviour, due to the convincing simulation of such an invasion pattern demonstrated by the GGH model which considers individual cells, most importantly including spatial effects. This occurred via a slowly-consumed chemical attractant forming a gradient, which allowed for a good match between both an experimentally observed macroscopic healing rate and data regarding individual cell velocities. On the other hand, it was suggested that diffuse invasions occur via an unguided migration effect, given the establishment of wavefront shapes in both the macroscopic and microscopic model which do not seem to match experimental results. The results in this chapter have sought to further explore this case, demonstrating unique behaviours in chemotactically-driven, diffusely-invading cell populations which heal over a non-homogenous domain. These trends have been seen on both the level of cell populations and individual cells and would be expected to be thus easily experimentally observable. Although it was not permitted by the restrictive running times of simulating scratch assays in the manner done here, a further analysis which averaged the positions of cells across multiple GGH model simulations to determine exactly how consistent and prominent these unique patterns seen for non-homogeneous scratch assays really are would be very interesting and is a planned future work.

Consideration of clustered invasions on a non-homogeneous domain was less immediately enlightening, and again given the lack of a proper unguided migration at the individual cell level was not considered in detail here. Work which was carried out but unfortunately not to a rigorous-enough standard for inclusion was to consider how overall invasion speeds varied with the width of the bands of the two regions making up the non-homogeneous domain. If the implementations could be made more efficient (and considerable effort has already been used towards this end), then further prediction about how diffusion-driven and chemotaxis-driven invasions could be distinguished by using a series of experiments of varying band width could be made.

Chapter 8

Conclusions

This thesis has explored the modelling of cellular migration and proliferation as general behaviours, using the scratch assay as a specific biological situation because of its relative simplicity both in terms of experimental realisation and the related mathematical modelling. The mathematical tools used here have been explored thoroughly before applying them to this context, especially the GGH model, an extension of a relatively recent individual-cell-based cellular automata model, the cellular Potts model (CPM).

The GGH model is a powerful tool because it naturally incorporates deformations in cell shapes, and models these deformations as minimisations of a defined total energy of the system. This total energy is constructed in order to represent the physical forces of adhesion and elasticity of cell volumes and membranes, and the means of doing so is well accepted. The effects of these forces are very difficult to represent in PDE models and their relevance is not well known, making the GGH model a very desirable model choice for an individual-cell-level model. However, the techniques for modifying the GGH model framework to include the critical cell behaviours of mitosis and chemotaxis are less clear cut. The inclusion of both these behaviours in the CPM/GGH model has been reviewed and explored here, resulting in novel contributions to the framework of the GGH model in general.

GGH Model - Chemotaxis

In the case of chemotactic response, the models already presented in the literature have been tested to verify that the current general dogma is indeed correct, important both because modelling featuring alternate approaches can still be seen in the literature and because in this author's opinion the general trend with CPM/GGH model simulations featuring chemotaxis has been to focus on the specific situation being simulated without much in the way of basic analysis of chemotaxis as a behaviour in itself. The prevalent ΔH-based approach (4.4) has here been conclusively demonstrated as superior.

Consideration of how variation of GGH model parameters affects the ability of cells to migrate chemotactically in the framework has not been seen in the literature, but was explored here. It was found that in the sense of choosing parameter values for adhesion and inelasticity, chemotaxis can be largely ignored and these parameters selected as needed. So long as the strength of chemotaxis, μ, took on a reasonable value, there was no effect on the general shapes taken by cells and clusters, and the critical temperatures for realistic cell behaviour were unaffected. Exploration of the dependence of chemotactic velocity on simulation temperature uncovered the suggestion that chemokinesis might easily be incorporated into a CPM/GGH simulation at an individual cell level simply by using a concentration-dependent value of $T = T(S)$ for all cells. This extends the previous physical interpretation of simulation temperature (that it represents the amount of fluctuation in cell membranes [132]) by demonstrating that such thinking also applies to chemokinetic effects where sufficiently low concentrations of chemokinetic signal fail to excite cells into movement at all, and high concentrations can saturate cell receptors and break cell polarisation [192].

A linear trend between effective chemotactic velocity and the value of μ, the chemotactic strength, is desirable both for its correspondence to force-based arguments (4.5), and to population-level chemotaxis modelled using PDEs (when disregarding saturation or volume filling effects and not including cell diffusion). Such a trend had been demonstrated in the normal CPM [118] but has now also been demonstrated here for the GGH model, including confirmation that the inclusion of a dissipative bond-breaking energy up to a moderate value only affects the slope of this linear trend.

More importantly, several issues that must be addressed before chemotaxis is used in GGH modelling have been uncovered, which have not been discussed by those using this model. This does not necessarily invalidate previously published work, because chemotaxis has largely been used as a means to an end as opposed to being specifically considered, but highlights the importance of the more thorough exploration performed here. It has been shown that lattice anisotropy can affect tactic migration and this would not be rectifiable by using additional neighbours for surface calculations, necessitating a hexagonal lattice. More importantly, consideration of chemotaxis of differently-sized clusters revealed very interesting information about a natural sort of contact inhibition of migration included in the GGH model. Under standard parameters, the negative adhesive energies between cells in the GGH model actually imply that cells can more easily encroach onto one another as opposed to free space, in complete contrast to biological understanding. This effect has been explored and verified to not be an adhesive tugging, suggesting that it should be watched for in other GGH model implementations where cell-cell interaction is of high importance.

Temporal evolution in the GGH model, which is modelled via trialled updates considered by the Metropolis algorithm, has been shown here to conflate cell movement behaviours. Unlike with PDE models, diffusion and chemotaxis can not be thought of separately and one can hamper or bolster the other. This is another novel concern about the framework that must be carefully considered, especially given their assumed independence in many macroscopic models. Indeed, later simulations suggested that the anticipated diffusion was not actually being successfully implemented by the GGH model at all, despite its presence being essentially assumed by the literature.

GGH Model - Proliferation

The second major modification to the GGH framework was the inclusion of mitosis, and the means by which this has been achieved in the literature have been summarised. These approaches vary greatly, both in terms of the key factors controlling cell proliferation and the relative level of complexity. The specific situation being modelled is of key importance, explaining this wide variation and motivating the creation of the novel technique used in this thesis. The approach that was adopted here possesses two main advantages - the successful replication of contact inhibition of mitosis or an equivalent effect, and the ability to have a cell's parameters be different while it undergoes the mitotic cycle. This allowed the fact that proliferating cells stop crawling and simply swell in size to be captured in the GGH model simulations here, and to the author's knowledge no other CPM or GGH model has done this (though an existing CPM model of tumours did have only tumours cells proliferate and used different properties for the two cell types [97]). The key to the model that was used here is the creation of an additional cell phenotype, 'proliferative' cells which normal cells can change into when attempting to proliferate. This allowed a single cell species to exhibit different properties depending on its current state of being, and these transformations of individual cells from one type to properly capture the differences between proliferative and quiescent cells are novel.

The proliferation mechanism put forward in this thesis was then tested to ensure that it produced realistic behaviour. It was seen that simply seeding a single cell in the centre of a square GGH model lattice and letting it proliferate and multiply resulted in growth curves that were very similar to those seen for logistic growth, despite the effects of the square boundary. Logistic growth is both an effect that has been clearly observed experimentally for growing monolayers [194] and is also the assumed form used by population-level models, making this adherence to it in the GGH model here very important. This demonstrated the power of naturally modelling contact inhibition of proliferation via the novel means used here, and indeed this logistic growth behaviour was naturally observed without any model modification or variation of parameters to specifically attempt to obtain such an effect. Logistic growth was observed over a range of values of $\mathcal{P}$, the probability of a cell with sufficient space to divide becoming proliferative, though stochastic effects did have an impact for lower values of $\mathcal{P}$. Additionally, three adhesive regimes were also presented, two being those already discussed when dealing with chemotaxis, and a third which specifically sought to encourage expansions onto medium as opposed to into other cells, for later use in the GGH model simulations of the scratch assay. It was found that growth curves remained logistic for all the different adhesive regimes, although there was a trend of continued slow growth after 'confluence' was achieved in the reversely adhesive regime. The calculated values of the proliferation rate and carrying capacity for the different adhesive regimes, obtained via simple curve fitting, were tabulated for a few values of $\mathcal{P}$, both to demonstrate the net macroscopic effects of varying these model parameters and also for use in the next chapter where the data was used to lend a physical interpretation to the GGH model simulations via comparison with experimental data.

Finite Volume Method

On the macroscopic scale, the modelling of cell behaviours is better developed, with the greatest majority of approaches using PDEs primarily based around the continuity equation (2.1). These PDEs are then subject to mathematical analysis when that presents itself as an option, or solved approximately using numerical techniques. Here a reasonably broad literature review has been conducted, discussing the basic cell behaviours and how they have been represented in macroscopic models. This eventually led to a model used to represent monolayer healing in the scratch assay which arose from a synthesis of the literature, including a small novel modification to how contact inhibition is handled, justified by experimental observation of cell velocity trends. The chosen numerical approach implemented in the thesis to solve the formulated PDE model - the finite volume method (FVM) - was explained in detail, including an explanation of how specifically it was implemented here. The implementation as described was then applied to a series of test problems where an analytic solution was available so that an appropriate choice from the various possibilities for the scheme could be selected and justified. This included flexibility in how to apply flux limiting, how to handle non-linear diffusion, what type of sensor should be used for flux limiting either explicitly or implicitly, and how the upwind face used for flux limiting should be located. It was quickly determined that flux limiting was a necessary incorporation for its increased accuracy without loss of stability, but that the simpler kind of flux limiting (derivative-based) was more appropriate. It was determined that for this choice, calculating the sensor explicitly was not only simpler and faster, but also more accurate. Three flux limiter functions were checked, with the van Leer limiter demonstrating the best results. A simple but challenging 2D problem was used to demonstrate that the “maximum flow method” [196] was apparently inappropriate for flux-based sensors and demonstrated no benefit for derivative-based sensors.

MATLAB Implementations

Working implementations of both a FVM solver and the GGH model including both chemotaxis and proliferation have been presented in the thesis and constructed in MATLAB. These products were designed in a modular fashion, so that further modification would prove less challenging, and to allow for a greater ease of use by those less familiar with the frameworks. These implementations have been used in this thesis to model the scratch assay on both homogeneous and heterogeneous domains, however this is certainly not the only biological context to which they could be applied and with their modular nature modification would not be difficult.

The Scratch Assay

The individual-cell-level and population-level models already demonstrated as successful and appropriate were then used to simulate homogeneous scratch assays under a series of conditions, including those featuring several types of chemotactic response and a lack of chemotactic response (in which case invasion is driven by random cell motility or proliferative pressure). One of the primary goals was the distinguishing between guided and unguided invasive behaviours, a known open question in the literature, and emphasis was placed on the GGH model simulations where such questions are novel considerations.

Use of the finite volume method to solve the PDEs provided results largely consistent with previously published modelling on the topic, although the results here considered both non-linear chemotaxis and non-linear diffusion, and further extended the volume-filling effect in the chemotaxis term by allowing the extent of that behaviour to vary. Choosing parameters for their correspondence to a chosen model cell for which experimental data was readily available [169], it was found that varying the amount of contact inhibition present in chemotaxis (via the parameter m) had very little effect on the generated invasive waves, except at the back edge of an invading cluster. Interestingly, although some simulations did display invasive waveforms which were led by shock fronts, none predicted a 'pure' sharp front connecting the invaded and uninvaded steady states directly and corresponding to a clearly defined wound edge. Given sharp-fronted monolayers are observable in experimental contexts, the inability of the PDE model as considered here to predict such behaviour highlights the need for the GGH model which can naturally predict this sort of invasion. The plateau-like structures found to arise when a consumed chemical gradient drove migration have been argued as contrary to experimental data.

Unfortunately, distinguishing between guided and unguided migration in the GGH model could not be properly achieved with the model as implemented here, but only because of an issue that could not be apparent until the model was given a physical interpretation, again using model cell data. This technique of using data from the purely proliferative assay to assign concrete physical dimensions of space and time to the GGH model (often left undefined, or chosen rather more arbitrarily) actually made it clear that proliferation-driven healing was occurring too slow to match experimental observation, at a rate thus indicating a lack of active diffusive migration. This conclusively disproved the author's initial hypothesis that the presence of sharp-fronts seen in experimental scratch assays could be explained by proliferation-driven healing, with the effects of space-filling and proliferative pressure providing a passive movement that was being represented by active migration when 'zooming out' in macroscopic modelling.

The lack of active diffusion in the GGH model is actually a rather novel demonstration. Generally the inclusion of random updates has been thought of as representing diffusion, with the simulation temperature parameter controlling its prevalence. This has here been demonstrated as insufficient, at least for this context, necessitating the inclusion of an active unguided migration effect. An idea for achieving this has been suggested, namely the creation of a third cell phenotype which would be used in a very similar way to how simulations here used a proliferatory phenotype and determined which cells were contact inhibited. This new state of being for cells would represent an actively migratory state, likely achieved using polarisation vectors that could naturally generate random motility with some degree of directional persistence but might also depend on detectable chemical gradients. Polarisation of cells has rarely been considered in the CPM/GGH model framework [120], and the introduction of a separate migratory type for cells that might use this polarisation vector is a yet unseen modification to the GGH that this author is very interested in.

When chemotaxis was introduced to the GGH model simulations of the scratch assay, it was first demonstrated that by choosing an appropriate value of μ, a linear gradient representing activation of all cells did indeed allow the simulated scratch to heal at a rate matching experimental observation, and thus a realistic simulation of a scratch assay featuring densely packed cells had been achieved. Although invasions in a tumour context had been considered by the GGH model [197, 198], this could be argued as the first true realisation of a constant speed travelling wave in the GGH model, especially one that has been matched to experiments.

When the initial conditions were changed so that only half of the cells post-scratch became chemotactically active, finite volume methods predicted that the edge between the active and inactive regions shows a depletion of cells, with the invasive behaviour otherwise unaffected. In the GGH model simulations, the same trend was actually observed, with the type of adhesive regime selected affecting the extent of this depletion, analogous to the effects of varying m in the PDE model. Contrary to what was hypothesised, the reversely-adhesive regime actually matched the effects of no contact inhibition of chemotaxis ($m = 0$), despite this choice of J's specifically encouraging cells not to press against one another. The normally adhesive regime that was argued in Chapter 4 to unwittingly introduce a *reverse* contact inhibition actually showed results closest to the case of fully contact inhibited chemotaxis ($m = 1$), though it should be noted that this was observed in a simulation which had already taken measures to counteract that unrealistic effect. The disagreement between the population-level modelling, common sense and the actual observations for the GGH model operating under different adhesive regimes demonstrates the need for a robust individual-cell-level model such as the one used here.

The apparent success of a linear chemotaxis effect for predicting realistic scratch assay invasion was called into question when individual cell velocities were tracked. This analysis demonstrated that all cells were actually completely active, with very little difference in speed between cells at the wavefront and those far behind it, in complete contrast to experimental observation [26]. This implied that linear chemotaxis was *not* a realistic driver for scratch assay invasion, especially when attempting to introduce an enforced contact inhibition to prevent the internal cells from responding so strongly failed to predict realistic healing.

A quickly-consumed and diffusible chemical that forms a gradient to drive invasion was next considered in the GGH model, and it was found that cells broke away from the main healing monolayer cluster. Thus it was figured that these simulations might be able to predict the diffuse invasive patterns seen for some other cell types or experimental conditions. However, and quite surprisingly, the wavefront profiles for these simulations actually qualitatively matched those seen in the PDE model in terms of shape, with a plateau of cellular concentration leading into a shock front. Given that such a trend has not been seen experimentally but now predicted naturally by two reasonable models operating at two different scales, this suggested that diffuse invasions could not be predicted by a consumed chemical attractant. Given the similar failure of the linear chemotaxis to even predict breakaway cells, it was concluded that those diffuse invasions must be occurring via unguided migration.

Varying the proliferation probability in the GGH model (able to be done without affecting the macroscopic proliferation rate thanks to the way all results are matched to the purely proliferative assay data for the model cell type) demonstrated that the different wavefront profiles observed at the population level for different values of λ_s could be demonstrated, although these two parameters are not actually linked. An argument for how varying the proliferation probability in this uniquely interpreted GGH model should be physically interpreted was presented. More interestingly, the GGH model simulations of healing driven by a consumed chemical demonstrated non-monotonic wave profiles with a spike at the leading edge. This was observed occasionally by the population level model too, though there was considered numeric instability. These results suggest that spike-fronted waves are indeed not merely a numerical instability at all but can be a natural conclusion of healing driven by this paradigm.

When the consumption of a diffusible attractant was slower, it was seen that healing could occur as a single clustered monolayer invading into the wound space, and with proliferation occurring throughout this monolayer. Additionally, consideration of individual cell velocities did indicate that the cells behind the wavefront moved slower than those at the front, giving a qualitative match to experimental knowledge. This was actually thought to be more a consequence of the nature of the attractant profile as opposed to direct contact inhibition of migration, but given that this gradient is undefined it could indeed represent the means by which cells detect where they are in relation to the wavefront in the first place.

It should be reiterated that predictions as to the important driving behaviours behind both clustered and diffuse invasions have been presented (and are thought to be different). Diffuse invasions are suspected to be driven by unguided migration of the individual pioneer cells, as suggested by considerations of wavefront profiles compared to experimental photography. This migration could be possibly triggered by a chemo*kinetic* agent which activated cells at the time of wounding. On the other hand, clustered invasions do not allow for much diffusive movement and individual cells cannot break away, so although a truly active unguided migration effect could not be included in the GGH model (due to the unforseen clash with the literature's common interpretation of such an effect), it has been suggested here that such invasions are driven by a consumed chemical attractant.

The Heterogeneous Scratch Assay

The original driving question of distinguishing between guided and unguided invasion has been potentially answered using the homogeneous scratch assay simulations, but the original thesis concept regarding a scratch assay on a non-homogeneous domain was still investigated. This concept was treated as a thought experiment given its lack of experimental realisation in the literature, though the intention was to make predictions that might then be observed in such an experiment. The use of these domains was inspired by Brazhnik and Tyson [20], with the same set up of fast and slow regions used here. It has been argued that such a domain could be realised experimentally by varying properties of the underlying substrate, such as its stiffness or by including grooves [92, 111]. The focus was not on the exact shapes of the waves which invaded over these domains, but instead on macroscopically-observable qualities like unique wave features or healing speed, because these would be more readily observed in an experiment. Due to the inability of the GGH model to correctly predict unguided migration occurring at a sufficiently fast rate, instead the predictions of the population level PDEs on these non-homogeneous domains were used to compare the different invasion mechanisms, with the GGH model simulations used to verify the interesting behaviours which were seen in the PDE model, ensuring they were not simply a consequence of numerical instability.

The incorporation of guided invasion in simulations on non-homogeneous domains was limited to the case where cells consume the attractant, because an enforced linear advection does not allow for sufficient mixing between the two regions and thus a constant speed travelling wave was found not to readily form a constant wave shape invading at a steady velocity. However, given that it has been demonstrated here that steady travelling waveforms do evolve in invasion driven by random motility or a cell-consumed signal, if an experimental scratch assay was performed over a heterogeneous domain and *no* steady observable wavefront was formed, this evidence would point directly to a linear guiding in the direction of healing (perhaps driven by an initial activation wave of chemical signal). This would be a very simple experimental result with strong consequences to the question being re-posed and partially answered by this thesis.

Unique steady waveforms arising from migration driven by a consumed chemical attractant have been demonstrated in the numerical solution of the PDE model, forming non-intuitive shapes that would be expected to be very noticeable in experimental or GGH model simulations if they were indeed real effects. The key observations seen for these wave profiles were an expected healing of the front edge of the wave, but a clustering of cells behind the wave edge in an unexpected location. This location was different depending on whether the attractant was diffusible or substrate-bound, with the former case resulting in a ridge of increased concentration running along the middle of the wavefront and the latter case a piling up of cells causing the slower region to actually heal faster than the fast region (behind the monolayer edge, which again shows expected healing with the fast region in front). Given that the spiked ridge forming for the diffusible attractant case occurred right along the boundary between the two regions, it was suggested that this effect might simply be a numerical artefact and this encouraged the use of the GGH model for further investigation.

Incredibly, the individual cell level model did display the same qualitative observations as those resulting from the PDE model, despite their unexpected nature. Pioneer cells making up the edge of the wavefront invaded as predicted, crawling forwards more rapidly in the fast region and filling in to the region of slower movement to form a curved leading wave edge. Some cell clustering within the middle of the wavefront was displayed in the expected regions, at the middle of the domain for a diffusible attractant and at the domain edge for a substrate-bound attractant. This location was between the pioneer cells and the confluent monolayer, corresponding to moderate values of the macroscopic concentration, C, and thus matching the portions of the wavefront displaying these interesting behaviours in the PDE model.

These behaviours corresponded to cells which invade as individuals displaying a diffuse pattern, and thus it was suggested that these are the sorts of cell (or cell situation, given observations that variations in chemical presence can also switch between cells invading as a monolayer or as individuals [199]) that should be trialled on a non-homogeneous domain in a scratch assay, at least initially.

The author's proposed future work would involve using a simple statistical approach considering many repeated non-homogeneous scratch assay simulations (recalling that the GGH model is stochastic, not deterministic) in order to examine the probabilities of certain locations being filled or unfilled by cellular material. This would then demonstrate exactly to what extent these unique wavefront features are present in the GGH model simulations, and allow for much better comparison against the steady wavefronts predicted by the PDE model. It should be noted, though, that the results demonstrated as displaying those unique features were not hand-picked or 'lucky' results of stochastic variation, with repeated trialling seen to demonstrate seemingly the same basic effect. This stochastic analysis was not performed only due to the limitation of running time, given the costliness of each GGH model simulation, but the candidate believes would make for very impactful future work.

The results for the non-homogeneous case did only further highlight the need for a correct representation of random motility in the GGH model, presumably incorporated using the author's suggestion of cell polarisation vectors and potentially a specifically migratory phenotype. Given that the random ruffling of cells in the GGH model has been seen to be insufficient for generating a correct diffusive effect, some sort of extension to the implementation presented here would be needed in order to properly consider how diffusion-driven healing on an individual cell level is impacted by non-homogeneous domains. With a smaller amount of random motility in the slow domain, it might actually demonstrate a buildup of cells. The author does not expect that this effect would be as noticeable as in the case of a diffusible, consumed signal, especially given that the population scale modelling suggests that a changing diffusion coefficient would not generate such an effect. However, an individual cell level investigation to verify these suspicions is certainly preferable, especially given the numerous examples of the important differences exhibited by individual cell level models demonstrated throughout this thesis.

The macroscopically observable quantity of invasive wavespeed has also been considered here, briefly. It has been suggested that diffusion-driven invasion is slowed by the presence of a region of slow migration far more than chemotaxis-driven invasion, thus also providing a very simple determinant between the two regimes should this thought experiment be realised adequately in a laboratory. Partially-collected data regarding the effects of varying the width of the two bands of different invasive speed on these overall macroscopic velocities has not been presented here because of its lack of rigour, but this is a further direction of expansion that the author hopes to realise.

In Summary

Overall, this thesis has significantly contributed to the understanding of cell invasion in the scratch assay context by using a sophisticated individual cell level approach, the GGH model. The specific GGH model implemented here incorporated a novel means of generating cell proliferation in this framework, its appropriate performance validated by comparison to purely proliferative assay data. Several issues with the current interpretation of the GGH model have been raised, most notably the lack of 'true' diffusive migration that is supposedly captured by the randomness of Metropolis algorithm updates, and the trend for "reverse contact inhibition" where cells with typical choices for GGH parameters actually push more readily into one another as opposed to into free space.

The observations of this sophisticated individual-cell-level model have been compared and contrasted to more 'traditional' PDE models in order to demonstrate how the assumptions inherent to macroscopic modelling, and behaviours that are not easily represented at that scale, can have a serious impact on a model's predictions, even in this biological context of the scratch assay which has actually been selected for its relative simplicity. The GGH model implemented here has been shown to generate constant velocity travelling waves, the feasibility of these waves examined by determining a physical spatial and temporal scale for the GGH model, using a simple but novel approach via comparison with experimental data for a certain model cell that allows the GGH model to simultaneously correctly predict cell behaviour in the scratch assay and the purely proliferative assay.

A conclusion as to whether invasion in the scratch assay is driven by guided or unguided migration, based on the simulation results of this novel GGH model for this problem, has been presented. It has been suggested that the two primary types of invasive pattern seen (clustered monolayer and diffuse) are indeed driven by distinct behaviours, with the diffuse patterns driven by unguided migration, and clustered patterns by a guided migration. The use of guided migration allows for cells to remain as a clustered monolayer with a well-defined wound edge, something seen in visualisations of this experiment but not in the PDE models supposedly matching that data [114, 169]. This has been argued as a result of the 'zooming out' of these population-scale models managing to interpret differences in the front position (arising due to complex biological variation that can likely be thought of as stochastic, or possibly imperfectly straight scratches) as evidence of a diffuse healing profile. It is of course intuitive to trust the photography demonstrating a tightly-clustered invading monolayer over the cell-counting data which is subject to the aforementioned effects.

A new potential experiment involving a non-homogeneous domain for a scratch assay has been proposed, and considered here as a thought experiment so that it could be simulated using the PDE model and GGH model implemented in this thesis. A surprising extent of agreement between the two models operating at different scales strengthened the suggestion that these results could be used to attempt to differentiate between guided and unguided migration in a scratch assay showing diffuse healing. Better yet, this would be achieved via the identification of qualitative, macroscopic trends which would be relatively easy to observe experimentally (if present) and would require no 'fiddly' calculations of individual cell velocities, which are also more likely to be subject to the general whims of biological complexity.

It would be extremely interesting to see such a thought experiment adequately realised in the laboratory, and if the suggestions made in this thesis are capable of achieving that, then this would not require significant deviation from the current scratch assay process. The non-homogeneous assay offers a great deal both to biologists and mathematicians, predominantly because it introduces no additional cell behaviours (or equivalently mathematical parameters) and yet can generate unique, macroscopically-observable invasion patterns that have been suggested here as differentiating between guided and unguided invasion. Given that varying parameters to fit curves has already allowed several mathematical models to fit experimental scratch assay data [114, 169] without fully enlightening the issue of what cell-level behaviours are actually driving invasion, the non-homogeneous scratch assay including an extra degree of complexity that cannot be compensated for by parameter changes makes it an extremely interesting mathematical problem. Experimental and mathematical realisations of a scratch assay healing over 'fast' and 'slow' material can be compared much more fairly when the two are forced to be combined, and interact, by this unique take on the experiment.

Bibliography

[1] M. Abercrombie. The crawling movement of metazoan cells. *Proc. R. Soc. Lond. B*, 207:129–147, 1980.

[2] M. Ablowitz and A. Zeppetella. Explicit solution of fisher's equation for a special wave speed. *Bull. Math. Biol.*, 41:835–840, 1979.

[3] T. Alarcon, H. Byrne, and P. Maini. A cellular automaton model for tumour growth in inhomogeneous environment. *J. Theor. Biol.*, 225:257–274, 2003.

[4] M. Alber, N. Chen, T. Glimm, and P. Lushnikov. Multiscale dynamics of biological cells with chemotactic interactions: From a discrete stochastic model to a continuous description. *Phys. Rev. E*, 73(5):051901, 2006.

[5] M. Alber, M. Kiskowski, J. Glazier, and Y. Jiang. On cellular automaton approaches to modeling biological cells. In *IMA 134: Mathematical Systems Theory in Biology, Communication, and Finance*. Springer-Verlag, 2002.

[6] W. Alt. Biased random walk models for chemotaxis and related diffusion approximations. *J. Math. Biol.*, 9:147–177, 1980.

[7] W. Ames. *Numerical Methods for Partial Differential Equations*. Academic Press, Inc., 1992.

[8] M. Anderson, G. Grest, and D. Srolovitz. Grain growth in three dimensions: A lattice model. *Scr. Metall.*, 19:225–230, 1985.

[9] K. Anguige and C. Schmeiser. A one-dimensional model of cell diffusion and aggregation, incorporating volume filling and cell-to-cell adhesion. *J. Math. Biol.*, 58(3):395–427, 2009.

[10] N. Armstrong, K. Painter, and J. Sherratt. A continuum approach to modelling cell-cell adhesion. *J. Theor. Biol.*, 243:98–113, 2006.

[11] N. Armstrong, K. Painter, and J. Sherratt. Adding adhesion to a chemical signalling model for somite formation. *Bulletin of Mathematical Biology*, 71:1–24, 2008.

[12] R. Assoian. Anchorage-dependent cell cycle progression. *J. Cell Biol.*, 136:1–4, 1997.

[13] M. Awad and I. Turner. Flux-limiting and non-linear solution techniques for simulation of transport in porous media. *ANZIAM J.*, 42:157–182, 2000.

[14] T. Backes, R. Latterman, S. Small, S. Mattis, G. Pauley, E. Reilly, and S. Lubkin. Convergent extension by intercalation without mediolaterally fixed cell motion. *J. Theor. Biol.*, 256:180–186, 2009.

[15] A. Bagorda and C. Parent. Eukaryotic chemotaxis at a glance. *J. Cell Sci.*, 121:2621–2624, 2008.

[16] R. Baker, E. Gaffney, and P. Maini. Partial differential equations for self-organization in cellular and developmental biology. *Nonlinearity*, 21:R251–R290, 2008.

[17] A. Bauer, T. Jackson, and Y. Jiang. A cell-based model exhibiting branching and anastomosis during tumor-induced angiogenesis. *Biophys. J.*, 92:3105–3121, 2007.

[18] M. Bindschadler and J. McGrath. Sheet migration by wounded monolayers as an emergent property of single-cell dynamics. *J. Cell Sci.*, 120:876–884, 2007.

[19] P Brazhnik. Exact solutions for the kinematic model of autowaves in two-dimensional media. *Physica D*, 94:205–220, 1996.

[20] P Brazhnik and J Tyson. Steady-state autowave patters in a two-dimensional excitable medium with a band of different excitability. *Physica D*, 102:300–312, 1997.

[21] M. Brenner, L. Levitov, and E. Budrene. Physical mechanisms for chemotactic pattern formation by bacteria. *Biophys. J.*, 74:1677–1693, 1998.

[22] M. Burger, M. Di Francesco, and Y. Dolak-Struss. The Keller-Segel model for chemotaxis with prevention of overcrowding: Linear vs. nonlinear diffusion. *SIAM J. Math. Anal.*, 38(4):1288–1315, 2006.

[23] H. Byrne, G. Cave, and S. McElwain. The effect of chemotaxis and chemokinesis on leukocyte locomotion: A new interpretation of experimental results. *IMA J. Math. Appl. Med.*, 15:235–256, 1998.

[24] H. Byrne and M. Owen. A new interpretation of the Keller-Segel model based on multiphase modelling. *J. Math. Biol.*, 49:604–626, 2004.

[25] A. Cai, K. Landman, and B. Hughes. Modelling directional guidance and motility regulation in cell migration. *Bulletin of Mathematical Biology*, 68:25–52, 2006.

[26] A. Cai, K. Landman, and B. Hughes. Multi-scale modeling of a wound-healing cell migration assay. *J. Theor. Biol.*, 245:576–594, 2007.

[27] C. Carrillo, N. Britton, and M. Mogie. Coexistence of sexual and asexual conspecifics: A cellular automaton model. *J. Theor. Biol.*, 217:275–285, 2002.

[28] M. Chaplain, M. Lachowicz, Z. Symanska, and D. Wrzosek. Mathematical modelling of cancer invasion: The importance of cell-cell adhesion and cell-matrix adhesion. *Math. Models Appl. Sci.*, 21:(to appear), 2011.

[29] R. Chaturvedi, J. Izaguirre, C. Huang, T. Cickovski, P. Virtue, G. Thomas, G. Forgacs, M. Alber, G. Hentschel, S. Newman, and J. Glazier. Multi-model simulations of chicken limb morphogenesis. *Lect. Notes Comput. Sci.*, 2659:39–49, 2003.

[30] C. Chen, M. Mirksch, S. Huang, G. Whitesides, and D. Ingber. Geometric control of cell life and death. *Science*, 276:1425–1428, 1997.

[31] S. Chen, S. Dawson, G. Doolen, D. Janecky, and A. Lawniczak. Lattice methods and their application to reacting systems. *Computers Chem. Engng.*, 19 (6/7):617–646, 1995.

[32] R. Chisholm and R. Firtel. Insights into morphogenesis from a simple developmental system. *Nat. Rev. Mol. Cell Biol.*, 5:531–541, 2004.

[33] C. Chung, C. Chen, C. Chen, and C. Tseng. Enhancement of cell growth in tissue-engineering constructs under direct perfusion: Modeling and simulation. *Biotech. Bioeng.*, 97(6):1603–1616, 2007.

[34] C. Cone, Jr and M. Tongier, Jr. Contact inhibition of division: Involvement of the electrical transmembrane potential. *Journal of Cellular Physiology*, 82(3):373–386, 1973.

[35] J. Crank. *The Mathematics of Diffusion*. Oxford University Press, 1975.

[36] G. Cruywagen, P. Maini, and J. Murrary. Travelling waves in a tissue interaction model for skin pattern formation. *J. Math. Biol.*, 33:193–210, 1994.

[37] B. Cullity and C. Graham. *Introduction to Magnetic Materials*. Wiley, 2009.

[38] F. Dahlquist, P. Lovely, and D. Koshland Jr. Qualitative analysis of bacterial migration in chemotaxis. *Nat. New. Biol.*, 236:120–123, 1972.

[39] D. Dan, C. Mueller, K. Chen, and J. Glazier. Solving the advection-diffusion equations in biological contexts using the cellular Potts model. *Phys. Rev. E*, 72:041909, 2005.

[40] P. Denman, S. McElwain, and J. Norbury. Analysis of travelling waves associated with the modelling of aerosolised skin grafts. *Bull. Math. Biol.*, 69:495–523, 2007.

[41] A. Deutsch and S. Dormann. *Cellualr Automaton Modeling of Biological Pattern Formation: Characterization, Applications and Analysis*. Birkhauser, 2005.

[42] P. Devreotes and S. Zigmond. Chemotaxis in eukaryotic cells: A focus on leukocytes and *Dictyostelium*. *Annu. Rev. Cell. Biol.*, 4:649–686, 1988.

[43] Y. Dolak and C. Schmeiser. The Keller-Segel model with logistic sensitivity function and small diffusivity. *SIAM J. Appl. Math.*, 66(1):286–308, 2005.

[44] Y. Dolak and C. Schmeiser. Kinetic models for chemotaxis: Hydrodynamic limits and spatio-temporal mechanisms. *J. Math. Biol.*, 51:595–615, 2005.

[45] S. Dormann. *Pattern Formation in Cellular Automation Models*. PhD thesis, Angewandte Systemwissenschaft FB Mathematik/Informatik, Universitt Osnabrck, Austria, 2000.

[46] F. Entschladen, T. Drell IV, K. Lang, K. Masur, D. Palm, P. Bastian, B. Niggemann, and K. Zaenker. Analysis methods of human cell migration. *Exp. Cell Res.*, 307:418–426, 2005.

[47] R. Farooqui and G. Fenteany. Multiple rows of cells behind an epithelial wound edge extend cryptic lamellipodia to collectively drive cell-sheet movement. *J. Cell Sci.*, 118:51–63, 2005.

[48] A. Fernando, K. Landman, and M. Simpson. Nonlinear diffusiona nd exclusion processes with contact interactions. *Phys. Rev. E*, 81:011903, 2010.

[49] R. Fisher. The wave of advance of advantageous genes. *Annals of Eugenics*, 7:355–369, 1937.

[50] J. Flegg, S. McElwain, H. Byrne, and I. Turner. A three species model to simulate application of hyperbaric oxygen therapy to chronic wounds. *PLoS Comp. Biol.*, 5(7):e1000541, 2009.

[51] A. Fokas and Y. Yortsos. On the exactly solvable equation $s_t = [(\beta s + \gamma)^{-2} s_x]_x + \alpha(\beta s + \gamma)^{-1} s_x$ occuring in two-phase flow in porous media. *SIAM J. Appl. Math.*, 42(2):318–332, 1982.

[52] R. Ford and D. Lauffenburger. Analysis of chemotactic bacterial distributions in population migration assays using a mathematical model applicable to steep or shallow attractant gradients. *Bull. Math. Biol.*, 53:721–749, 1991.

[53] R. Foty and M. Steinberg. The differential adhesion hypothesis: A direct evaluation. *Dev. Biol.*, 278:255–263, 2005.

[54] U. Frisch, B. Hasslacher, and Y. Pomeau. Lattice-gas automata for the Navier-Stokes equation. *Phys. Rev. Lett.*, 56:1505–1508, 1986.

[55] C. Galban and B. Locke. Analysis of cell growth kinetics and substrate diffusion in a polymer scaffold. *Biotechnol. Bioeng.*, 65(2):121–132, 1999.

[56] M. Gardner. Mathematical games: The fantastic contributions of John Conway's Game of Life. *Scientific American*, 223:120–123, 1970.

[57] M. Gerhardt and H. Schuster. A cellular automaton describing the formation of spatially ordered structures in chemical systems. *Physica D*, 36:209–221, 1989.

[58] A. Gerisch and M. Chaplain. Mathematical modelling of cancer cell invasion of tissue: Local and non-local models and the effect of adhesion. *J. Theor. Biol.*, 250:684–704, 2008.

[59] G. Gerisch and U. Wick. Intracellular oscillations and release of cyclic AMP from *Dictyostelium* cells. *Biochem. Biophys. Res. Commun.*, 65:364–370, 1975.

[60] W. Geyi. *Foundations of Applied Electrodynamics*. Wiley, 2010.

[61] M. Gharaee-Kermani and S. Phan. Role of cytokines and cytokine therapy in wound healing and fibrotic diseases. *Curr. Pharm. Des.*, 7(11):1083–1103, 2001.

[62] B. Gilding and R. Kersner. *Travelling waves in nonlinear diffusion-convection-reaction*. Birkhauser, 2004.

[63] J. Glazier, A. Balter, and N. Poplawski. *Single-cell Based Models in Biology and Medicine*, chapter Magnetization to morphogenesis: A history of the GGH model, pages 79–106. Birkhauser, 2007.

[64] J. Glazier and F. Graner. Simulation of the differential adhesion driven reaarrangement of biological cells. *Phys. Rev. E*, 47(3):2128–2154, 1993.

[65] J. Glazier and A. Upadhyaya. *Dynamical Networks in Physics and Biology: At the Frontier of Physics and Biology*, chapter First steps towards a comprehensive model of tissues, or: A physicist looks at development, pages 149–160. EDP Sciences/Springer Verlag, 1998.

[66] J. Glazier and D. Weaire. The kinetics of cellular patterns. *J. Phys. Condens. Matter*, 4:1867–1894, 1992.

[67] I. Golding, Y. Kozlovsky, I. Cohen, and E. Ben-Jacob. Studies of bacterial branching growth using reactiondiffusion models for colonial development. *Physica A*, 260:510–554, 1998.

[68] J. Goodman and R. LeVeque. On the accuracy of stable schemes for 2d scalar conservation laws. *Mathematics of Computation*, 45:15–21, 1985.

[69] N. Gov. Collective cell migration patterns: Follow the leader. *PNAS*, 104(41):15970–15971, 2007.

[70] F. Graner and J. Glazier. Simulation of biological cell sorting using a two-dimensional extended Potts model. *Phys. Rev. L*, 69(13):2013–2016, 1992.

[71] S. Grasso, J. Hernandez, and S. Chifflet. Roles of wound geometry, wound size, and extracellular matrix in the healing response of bovine corneal endothelial cells in culture. *Am. J. Physiol. Cell Physiol.*, 293:1327–1337, 2007.

[72] L. Gray. A mathematician looks at Wolframs New Kind of Science. *Notices of the AMS*, 50(2):200–211, 2003.

[73] C. Hall. *Modelling of some biological materials using continuum mechanics*. PhD thesis, Queensland University of Technology, 2008.

[74] J. Hardy, O. de Pazzis, and Y. Pomeau. Molecular dynamics of a classical lattice gas: Transport properties and time correlation functions. *Phys. Rev. A*, 13:1949–1961, 1976.

[75] A. Harten. High resolution schemes for hyperbolic conservation laws. *J. Comput. Phys.*, 49:357–393, 1983.

[76] C. Harwood, K. Fosnaugh, and M. Dispensa. Flagellation of *pseudomonas putida* and analysis of its motile behavior. *J. Bacteriol.*, 171:4063–4066, 1989.

[77] T. Hillen and K. Painter. Global existence for a parabolic chemotaxis model with prevention of overcrowding. *Adv. Appl. Math.*, 26:280–301, 2001.

[78] T. Hofer, P. Maini, J. Sherratt, M. Chaplain, P. Chauvet, D. Metevier, P. Montes, and J. Murray. A resolution of the chemotactic wave paradox. *Appl. Math. Lett.*, 7(2):1–5, 1994.

[79] P. Hogeweg. Evolving mechanisms of morphogenesis: On the interplay between differential adhesion and cell differentiation. *J. Theor. Biol.*, 203:317–333, 2000.

[80] T. Holy, M. Dogterom, B. Yurke, and S. Leibler. Assembly and positioning of microtubule asters in microfabricated chambers. *Proc. Natl. Acad. Sci. USA*, 94:6228–6231, 1997.

[81] D. Horstmann. From 1970 until present: the keller-segel model in chemotaxis and its consequences i. *Jahresber. Deutsch. Math.-Verein.*, 105(3):103–165, 2003.

[82] D. Horstmann. From 1970 until present: the keller-segel model in chemotaxis and its consequences ii. *Jahresber. Deutsch. Math.-Verein.*, 106:103–16551–69, 2004.

[83] B. Hu, W. Chen, W. Rappel, and H. Levine. How geometry and internal bias affect the accuracy of eukaryotic gradient sensing. *Phys. Rev. E*, 83:021917, 2011.

[84] S. Huang and D. Ingber. The structural and mechanical complexity of cell growth control. *Nature Cell Biology*, 1:E131–138, 1999.

[85] F. Hughes and C. McCulloch. Quantification of chemotactic response of quiescent and proliferating fibroblasts in boyden chambers by computer-assisted image-analysis. *J. Histochem. Cytochem.*, 39:243–246, 1991.

[86] A. Huttenlocher, M. Lakonishok, M. Kinder, S. Wu, T. Truong, K. Knudsen, and A. Horwitz. Integrin and cadherin synergy regulates contact inhibition of migration and motile activity. *J. Cell Biol.*, 141(2):515–526, 1998.

[87] R. Motta Jalefice, B. Bechara, L. Barros, R. Bassanezi, and F. Gomide. Cellular automata with fuzzy parameters in microscopic study of positive hiv individuals. *Math. Comput. Mod.*, 50:32–44, 2009.

[88] Y. Jiang, H. Levine, and J. Glazier. Possible cooperation of differential adhesion and chemotaxis in mound formation of dictyostelium. *Biophysical J.*, 75:2615–2625, 1998.

[89] Y. Jiang, J. Pjesivac-Grbovic, C. Cantrell, and J. Freyer. A multiscale model for avascular tumor growth. *Biophys. J.*, 89:3884–3894, 2005.

[90] J. Kafer, T. Hayashi, A. Maree, R. Carthew, and F. Graner. Cell adhesion and cortex contractility determine cell patterning in the Drosophilia retina. *PNAS*, 104(47):18549–18554, 2007.

[91] J. Kafer, P. Hogeweg, and A. Maree. Moving forward moving backward: Directional sorting of chemotactic cells due to size and adhesion differences. *PLoS Comp. Biol.*, 2(6):e56, 2006.

[92] J. Kaiser, A. Reinmann, and A. Bruinink. The effect of topographic characteristics on cell migration velocity. *Biomaterials*, 27:5230–5241, 2006.

[93] Y. Kalinin, L. Jiang, Y. Tu, and M. Wu. Logarithmic sensing in *Eschericia coli* bacterial chemotaxis. *Biophys. J.*, 96:2439–2448, 2009.

[94] E. Keller and L. Segel. The initiation of slime mold aggregation viewed as an instability. *J. Theor. Biol.*, 26:399–415, 1970.

[95] E. Keller and L. Segel. Travelling bands of chemotactic bacteria: A theoretical analysis. *J. Theor. Biol.*, 30(2):235–248, 1971.

[96] C. Kelley. *Solving Nonlinear Equations with Newton's Method*. Number 1 in Fundamentals of Algorithms. SIAM, 2003.

[97] M. Knewitz and J. Mombach. Computer simulation of the influence of cellular adhesion on the morphology of the interface between tissues of proliferating and quiescent cells. *Computers in Biology and Medicine*, 36:59–69, 2006.

[98] A. Koch and H. Meinhardt. Biological pattern formation: From basic mechanisms to complex structures. *Reviews of Modern Physics*, 66:1481–1507, 1994.

[99] B. Koren. *Numerical Methods for AdvectionDiffusion Problems*, chapter A robust upwind discretisation method for advection, diffusion and source terms, pages 117–138. Braunschweig, Vieweg, 1993.

[100] R. Kowalczyk. Preventing blow-up in a chemotaxis model. *J. Math. Anal. Appl.*, 305:566–588, 2005.

[101] A. Kurganov and E. Tadmor. New high-resolution central schemes for nonlinear conservation laws and convection-diffusion equations. *J. Comput. Phys.*, 160:241–282, 2000.

[102] A. Lanas, A. Garcia-Gonzalez, F. Esteva, E. Piazuelo, P. Jimenez, and J. Morandeira. Collagen secretion by human gastric and skin fibroblasts: Implications for ulcer healing. *Eur. Surg. Res.*, 30:48–54, 1998.

[103] K. Landman, A. Cai, and B. Hughes. Travelling waves of attached and detached cells in a wound-healing cell migration assay. *Bull. Math. Biol.*, 69:2119–2138, 2007.

[104] K. Landman, G. Pettet, and D. Newgreen. Chemotactic cellular migration: Smooth and discontinuous travelling wave solutions. *SIAM J. Appl. Math.*, 63(5):1666–1681, 2003.

[105] K. Landman, M. Simpson, and G. Pettet. Tactically-driven nonmonotone travelling waves. *Physica D*, 237:678–691, 2007.

[106] K. Landman, M. Simpson, J. Slater, and D. Newgreen. Diffusive and chemotactic cellular migration: Smooth and discontinuous traveling wave solutions. *SIAM J. Appl. Math.*, 65(4):1420–1442, 2005.

[107] R. Lapidus and R. Schiller. Model for the chemotactic response of a bacterial population. *1976*, 16:779–789, Biophys. J.

[108] B. Van Leer. Towards the ultimate conservative difference scheme ii: Monotonicity and conservation combined in a second-order scheme. *J. Comput. Phys.*, 14(4):361–370, 1974.

[109] R. LeVeque. *Finite volume methods for hyperbolic problems*. Cam, 2002.

[110] C. Liang, A. Park, and J. Guan. In vitro scratch assay: A convenient and inexpensive method for analysis of cell migration in vitro. *Nature Protocols*, 2(2):329–333, 2007.

[111] C. Lo, H. Wang, M. Dembo, and Y. Wang. Cell movement is regulated by the rigidity of the substrate. *Biophys. J.*, 79:144–152, 2000.

[112] P. Lushnikov, N. Chen, and M. Alber. Macroscopic dynamics of biological cells interacting via chemotaxis and direct contact. *Phys. Rev. E.*, 78:061904, 2008.

[113] R. Macnab and D. Koshland Jr. The gradient-sensing mechanism in bacterial chemotaxis. *Proc. Nat. Acad. Sci. USA*, 69(9):2509–2512, 1972.

[114] P. Maini, D. L. S. McElwain, and D. Leavesley. Travelling wave model to interpret a wound-healing cell migration assay for human peritoneal mesothelial cells. *Tissue Engineering*, 10(3/4):475–482, 2004.

[115] P. Maini, D. L. S. McElwain, and D. Leavesley. Travelling waves in a wound healing assay. *Applied Mathematics Letters*, 17:575–580, 2004.

[116] D. Mallet and G. Pettet. A mathematical model of integrin-regulated haptotactic cell migration. *Bull. Math. Biol.*, 68:231–253, 2006.

[117] D. Mallet and L. De Pillis. A cellular automata model of tumor-immune system interactions. *J. Theor. Biol.*, 239:334–350, 2006.

[118] A. Maree, V. Grieneisen, and P. Hogeweg. *Single-cell Based Models in Biology and Medicine*, chapter CPM and properties of cells, tissues and morphogenesis, pages 107–136. Birkhauser, 2007.

[119] A. Maree and P. Hogweg. How amoeboids organize into a fruiting body: Multicellular coordination in dictyostelium discoideum. *Proc. Natl. Acad. Sci. USA*, 98(7):3879–3883, 2001.

[120] A. Maree, A. Jilkine, A. Dawes, V. Grieneisen, and L. Edelstein-Keshet. Polarization and movement of keratinocytes: A multiscale modelling approach. *Bulletin of Mathematical Biology*, 68:1169–1211, 2006.

[121] A. Maree, A. Panfilov, and P. Hogeweg. Migration and thermotaxis of *dictyostelium discoiduem* slugs, a model study. *J. Theor. Biol.*, 199:297–309, 1999.

[122] M. Markus, D. Bohm, and M. Schmick. Simulation of vessel morphogenesis using cellular automata. *Mathematical Biosciences*, 156:191–206, 1999.

[123] J. Martiel and A. Goldbeter. A model based on receptor desensitization for cyclic AMP signalling in Dictyostelium cells. *Biophys. J.*, 52:807–828, 1987.

[124] E. Martin. John conway's game of life, 2006.

[125] L. Martino, A. Osella, C. Dorso, and J. Lanata. Fisher equation for anisotropic diffusion: Simulating South American human dispersals. *Phys. Rev. E*, 76:031923, 2007.

[126] E. Martz and M. Steinberg. The role of cell-cell contact in contact inhibition of cell division: A review and new evidence. *Journal of Cellular Physiology*, 79(2):189–210, 1972.

[127] J. Mazoyer. A six-state minimal time solution to the firing squad synchronization problem. *Theor. Comput. Sci.*, 50(2):183–238, 1987.

[128] R. Merks, S. Brodsky, M. Goligorsky, S. Newman, and J. Glazier. Cell elongation is key to in silico replication of in vitro vasculogenesis and subsequent remodeling. *Developmental Biology*, 289:44–54, 2006.

[129] R. Merks and J. Glazier. A cell-centred approach to developmental biology. *Physica A*, 352:113–130, 2005.

[130] R. Merks, E. Perryn, A. Shirinifard, and J. Glazier. Contact-inhibited chemotaxis in de novo and sprouting blood-vessel growth. *PLoS Comp. Biol.*, 4(9):e1000163, 2008.

[131] N. Metropolis, A. Rosenbluth, M. Rosenbluth, A. Teller, and E. Teller. Equations of state calculations by fast computing machines. *J. Chem. Phys.*, 21 (6):1087–1092, 1953.

[132] J. Mombach and J. Glazier. Single cell motion in aggregates of embryonic cells. *Phys. Rev. Lett.*, 76(16):3032–3035, 1996.

[133] J. Mombach, J. Glazier, R. Raphael, and M. Zajac. Quantitative comparison between differential adhesion models and cell sorting in the presence and absence of fluctuations. *Phys. Rev. Lett.*, 75(11):2244–2247, 1995.

[134] J. Murray. *Mathematical Biology I: An Introduction*. Springer-Verlag, 2002.

[135] J. Murray. *Mathematical Biology II: Spatial Models and Biomedical Applications*. Springer-Verlag, 2002.

[136] G. Ngwa and P. Maini. Spatio-temporal patterns in a mechanical model for mesenchymal morphogenesis. *J. Math. Biol.*, 33:489–520, 1995.

[137] D. Nikolic, A. Boettiger, D. Bar-Sagi, J. Carbeck, and Y. Shvartsman. Role of boundary conditions in experimental model of epithelial wound healing. *Am. J. Physiol. Cell Physiol.*, 291:C68–C75, 2006.

[138] L. Onsager. Crystal statistics. i. a two-dimensional model with an order-disorder transition. *Phys. Rev. (2)*, 65(3-4):117–149, 1944.

[139] H. Othmer and A. Stevens. Aggregation, blowup and collapse: The ABC's of taxis in reinforced random walks. *SIAM J. Appl. Math.*, 57(4):1044–1081, 1997.

[140] C. Ou and W. Yan. Traveling wavefronts in a volume-filling chemotaxis model. *SIAM J. Appl. Dyn. Syst.*, 8(1):390–416, 2009.

[141] G. Ouaknin and P. Bar-Yoseph. Stochastic collective movement of cells and fingering morphology: No maverick cells. *Biophys. J.*, 97:1811–1821, 2009.

[142] N. Ouchi, J. Glazier, J. Rieu, A. Upadhyaya, and Y. Sawada. Improving the realism of the cellular Potts model insimulations of biological cells. *Physica A*, 329:451–458, 2003.

[143] K. Painter, N. Armstrong, and J. Sherratt. The impact of adhesion on cellular invasion processes in cancer and development. *J. Theor. Biol.*, 264(3):1057–1067, 2010.

[144] K. Painter and T. Hillen. Volume-filling and quorum-sensing in models for chemosensitive movement. *Can. Appl. Math. Q.*, 10(4):501–543, 2002.

[145] K. Painter and T. Hillen. Spatio-temporal chaos in a chemotaxis model. *Physica D*, 240:363–375, 2011.

[146] K. Painter and J. Sherratt. Modelling the movement of interacting cell populations. *J. Theor. Biol.*, 225:327–339, 2003.

[147] E. Palsson and H. Othmer. A model for individual and collective cell movement in Dictyostelium Discoideum. *PNAS*, 97(19):10448–10453, 2000.

[148] C. Parent and P. Devreotes. A cell's sense of direction. *Science*, 284:765–769, 1999.

[149] J. Parker and F. McQuiston. *Introduction to Fluid Mechanics and Heat Transfer*. Kendall/Hunt, 1988.

[150] C. Patlak. Random walk with persistence and external bias. *Bull. Math. Biophys.*, 15:311–338, 1953.

[151] A. Perumpanani and H. Byrne. Extracellular matrix concentration exerts selection pressure on invasive cells. *Eur. J. Cancer*, 35(8):1274–1280, 1999.

[152] A. Perumpanani, J. Sherratt, J. Norbury, and H. Byrne. Biological inferences from a mathematical model for malignant invasion. *Invasion Metastasis*, 16(4-5):209–221, 1996.

[153] A. Perumpanani, D. Simmons, A. Gearing, K. Miller, G. Ward, J. Norbury, M. Schneemann, and J. Sherratt. Extracellular matrix-mediated chemotaxis can impede cell migration. *Proc. R. Soc. Lond. B*, 265:2347–2352, 1998.

[154] G. Pettet, S. McElwain, and J. Norbury. Lotka-Volterra equations with chemotaxis: Walls, barriers and travelling waves. *IMA J. Math. Appl. Med.*, 17:395–413, 2000.

[155] G. Pettet, C. Please, M. Tindall, and S. McElwain. The migration of cells in multicell tumour spheroids. *Bulletin of Mathematical Biology*, 63:231–257, 2001.

[156] N. Poplawski. Volume and surface constraints in the cellular potts model. Technical Report physics/0512129, arXiv:physics, Dec 2005.

[157] N. Poplawski, U. Agero, J. Gens, M. Swat, J. Glazier, and A. Anderson. Front instabilities and invasiveness of simulated avascular tumors. *Bull. Math. Biol.*, 71:1189–1227, 2009.

[158] N. Poplawski, A. Shirinifard, U. Agero, J. Gens, M. Swat, and J. Glazier. Front instabilities and invasiveness of simulated 3D avascular tumors. *PLoS One*, 5(5):e10641, 2010.

[159] N. Poplawski, A. Shirinifard, M. Swat, and J. Glazier. Simulation of single-species bacterial-biofilm growth using the Glazier-Graner-Hogeweg model and the Compucell3D modeling environment. *Math. Biosci. Eng.*, 5(2):355–388, 2008.

[160] N. Poplawski, M. Swat, J. Gens, and J. Glazier. Adhesion between cells, diffusion of growth factors, and elasticity of the AER produce the paddle shape of the chick limb. *Physica A*, 373:521–532, 2007.

[161] M. Potel and S. Mackay. Preaggregative cell motion in *dictyostelium*. *J. Cell. Sci.*, 36:281–309, 1979.

[162] R. Potts. Some generalized order-disorder transformations. *Mathematical Proceedings*, 48(1):106–109, 1952.

[163] M. Poujade, E. Grasland-Mongrain, A. Hertzog, J. Jouanneau, P. Chavrier, B. Ladoux, A. Buguin, and P. Silberzan. Collective migration of an epithelial monolayer in response to a model wound. *PNAS*, 104(41):15988–15993, 2007.

[164] N. Rashevsky. *Mathematical Biophysics: Physico-Mathematical Foundations of Biology*. Dover, 1960.

[165] M. Rivero, R. Tranquillo, H. Buettner, and D. Lauffenburger. Transport models for chemotactic cell populations based on individual cell behaviour. *Chem. Eng. Sci.*, 44(12):2881–2897, 1987.

[166] N. Savill and P. Hogweg. Modelling morphogenesis: From single cells to crawling slugs. *J. Theor. Biol.*, 184(3):229–235, 1997.

[167] T. Scribner, L. Segel, and E. Rogers. A numerical study of the formation and propagation of traveling bands of chemotactic bacteria. *J. Theor. Biol.*, 46:189–219, 1974.

[168] J. Semple, N. Woolridge, and C. Lumsden. In vitro, in vivo, in silico: Computational systems in tissue engineering and regenerative medicine. *Tissue Engineering*, 11(3/4):341–355, 2005.

[169] B. Sengers, C. Please, and R. Oreffo. Experimental characterization and computational modelling of two-dimensional cell spreading for skeletal regeneration. *J. R. Soc. Interface*, 4:1107–1117, 2007.

[170] V. Shamanskii. On a modification of newtons method. *Ukrainskyi Matematychnyi Zhurnal*, 19:133–138, 1967.

[171] J. Sherratt. Cellular growth control and travelling waves of cancer. *SIAM J. Appl. Math.*, 53:1713–1730, 1993.

[172] J. Sherratt. Chemotaxis and chemokinesis in eukaryotic cells: The Keller-Segel equations as an approximation to a detailed model. *Bull. Math. Biol.*, 56(1):129–146, 1994.

[173] J. Sherratt. Wavefront propagation in a competition equation with a new motility term modelling contact inhibition between cell populations. *Proc. R. Soc. Lond. A*, 456:2365–2386, 2000.

[174] J. Sherratt and B. Marchant. Nonsharp travelling wave fronts in the Fisher equation with degenerate nonlinear diffusion. *Appl. Math. Lett.*, 9(5):33–38, 1996.

[175] S. Sick, S. Reinker, J. Timmer, and T. Schlake. Wnt and dkk determine hair follice spacing through a reaction-diffusion mechanism. *Science*, 314:1447–1450, 2006.

[176] M. Simpson, R. Baker, and S. McCue. Models of collective cell spreading with variable cell aspect ratio: A motivation for degenerate diffusion models. *Phys. Rev. E*, 83:021901, 2011.

[177] M. Simpson, K. Landman, and T. Clement. Assessment of a non-traditional operator split algorithm for simulation of reactive transport. *Mathematics and Computers in Simulation*, 70:44–60, 2005.

[178] M. Simpson, K. Landman, and B. Hughes. Distinguishing between directed and undirected cell motility within an invading cell population. *Bulletin of Mathematical Biology*, 71:781–799, 2009.

[179] M. Simpson, K. Landman, B. Hughes, and D. Newgreen. Looking inside an invasion wave of cells using continuum models: Proliferation is the key. *J. Theor. Biol.*, 243:343–360, 2006.

[180] M. Simpson, A. Merrifield, K. Landman, and B. Hughes. Simulating invasion with cellular automata: Connecting cell-scale and population-scale properties. *Phys. Rev. E*, 76:021918, 2007.

[181] M. Simpson, D. Zhang, M. Mariani, K. Landman, and D. Newgreen. Cell proliferation drives neural crest cell invasion of the intestine. *Dev. Biol.*, 302:553–568, 2007.

[182] S. Spekreijse. Multigrid solution of monotone second-order discretizations of hyperbolic conservation laws. *Mathematics of Computation*, 49:135–155, 1987.

[183] M. Steinberg. Does differential adhesion govern self-assembly processes in histogenesis? equilibrium configurations and the emergence of a hierarchy among populations of embryonic cells. *J. Exp. Zool.*, 173:395–434, 1970.

[184] A. Stevens. The derivation of chemotaxis equations as limit dynamics of moderately interacting stochastic many-particle systems. *SIAM J. Appl. Math.*, 61(1):183–212, 2000.

[185] E. Stott, M. Britton, J. Glazier, and M. Zajac. Stochastic simulation of benign avascular tumor growth using the Potts model. *Math. Comput. Mod.*, 30:183–198, 1999.

[186] P. Sweby. High resolution schemes using flux limiters for hyperbolic conservation laws. *SIAM. J. Numer. Anal.*, 21(5):995–1011, 1984.

[187] K. Takamizawa, S. Niu, and T. Matsuda. Mathematical simulation of unidirectional tissue formation: in vitro transanastomotic endothelialization model. *J. Biomater. Sci. Polym. Ed.*, 8:323–334, 1997.

[188] W. Tam. Evolution of a single defect in an ideal two-dimensional hexagonal soap froth. *Phys. Rev. E*, 58(6):8032–8035, 1998.

[189] J. Thackham, S. McElwain, and I. Turner. Computational approaches to solving equations arising from wound healing. *Bull. Math. Biol.*, 71:211–246, 2009.

[190] L. Timpe, E. Martz, and M. Steinberg. Cell movements in a confluent monolayer are not caused by gaps: Evidence for direct contact inhibition of overlapping. *J. Cell Sci.*, 30:293–304, 1978.

[191] M. Tindall, P. Maini, S. Porter, and J. Armitage. Overview of mathematical approaches used to model bacterial chemotaxis ii: Bacterial populations. *Bull. Math. Biol.*, 70:1570–1607, 2008.

[192] R. Tranquillo. *Biology of the Chemotactic Response*, chapter Theories and models of gradient perception, pages 33–75. Cambridge University Press, 1990.

[193] R. Tranquillo and J. Murray. Continuum model of fibroblast-driven wound contraction: Inflammation mediation. *J. Theor. Biol.*, 158:135–172, 1992.

[194] A. Tremel, A. Cai, N. Tirtaatmadja, B. Hughes, G. Stevens, K. Landman, and A. O'Connor. Cell migration and proliferation during monolayer formation and wound healing. *Chemical Engineering Science*, 64:247–253, 2009.

[195] A. Turing. The chemical basis of morphogenesis. *Phil. Trans. R. Soc.*, 237:37–72, 1952.

[196] I. Turner and P. Perr. The use of implicit flux limiting schemes in the simulation of the drying process: A new maximum flow sensor applied to phase mobilities. *Appl. Math. Model.*, 25(6):513–540, 2001.

[197] S. Turner and J. Sherratt. Intercellar adhesion and cancer invasion: A discrete simulation using the extended Potts model. *J. Theor. Biol.*, 216:85–100, 2002.

[198] S. Turner, J. Sherratt, and D. Cameron. Tamoxifen treatment failure in cancer and the nonlinear dynamics of TGF-β. *J. Theor*, 229:101–111, 2004.

[199] H. Ura, F. Takeda, and H. Okochi. An in vitro outgrowth culture system for normal human keratinocytes. *J. Derm. Sci.*, 35:19–28, 2004.

[200] J. Velazquez. Point dynamics in a singular limit of the Keller-Segel model 1: Motion of the concentration regions. *SIAM J. Appl. Math.*, 64(4):1192–1223, 2004.

[201] P. Verhulst. ″notice sur la loi que la population poursuit dans son accroissement. *Correspondance Mathmatique et Physique*, 10:113–121, 1838.

[202] K. Vermeulen, D. Bockstaele, and Z. Berneman. The cell cycle: A review of regulation, deregulation and therapeutic targets in cancer. *Cell Prolif.*, 36:131–149, 2003.

[203] P. Vitanyi. Sexually reproducing cellular automata. *Math. Biosc.*, 18:23–54, 1973.

[204] J. von Neumann. *The general and logical theory of automata*, chapter 9, pages 288–328. Pergamon Press, 1961.

[205] D. Walker, G. Hill, S. Wood, H. Smallwood, and J. Southgate. Agent-based computational modelling of wounded epithelial cell monolayers. *IEEE Trans. Nanobiosci.*, 3(3):153–163, 2004.

[206] D. Walker and J. Southgate. The virtual cell: A candidate co-ordinator for ′middle-out′ modelling of biological systems. *Brief. Bioinform.*, 10(4):450–461, 2009.

[207] Z. Wang. On chemotaxis models with cell population interactions. *Math. Model. Nat. Phenom.*, 5(3):173–190, 2010.

[208] Z. Wang and T. Hillen. Classical solutions and pattern formation for a volume filling chemotaxis model. *Chaos*, 17:037108, 2007.

[209] N. Waterson. A symmetric formulation for flux-limited convection schemes. *Int. J. Numer. Meth. Fluids*, 56:1575–1581, 2008.

[210] S. Wolfram. *A New Kind of Science*. Wolfram Media, Inc., 2002.

[211] L. Wu, J. Franke, R. Blanton, G. Podgorski, and R. Kessin. The phosphodiesterase secreted by prestalk cells is necessary for *dictyostelium* morphogenesis. *Developmental Biology*, 167:1–8, 1995.

[212] J. Zahm, H. Kaplan, A. Herard, F. Doriot, D. Pierrot, P. Somelette, and E. Puchelle. Cell migration and proliferation during the in vitro wound repair of the respiratory epithelium. *Cell Motil. Cytoskel.*, 37:33–43, 1997.

[213] M. Zajac, G. Jones, and J. Glazier. Simulating convergent extension by way of anisotropic differential adhesion. *J. Theor. Biol.*, 222:247–259, 2003.

[214] W. Zeng, G. Thomas, and J. Glazier. Non-Turing stripes and spots: a novel mechanism for biological cell clustering. *Physica A*, 341:482–494, 2004.